4-14-2017

Friction Reduction in Powertrain Materials: Role of Tribolayers

Anindya Banerji
University of Windsor

Friction Reduction in Powertrain Materials: Role of Tribolayers

By

Anindya Banerji

A Dissertation

Submitted to the Faculty of Graduate Studies

through the Department of Mechanical, Automotive & Materials Engineering

in Partial Fulfillment of the Requirements for

the Degree of Doctor of Philosophy

at the University of Windsor

Windsor, Ontario, Canada

2017

Friction Reduction in Powertrain Materials: Role of Tribolayers

by

Anindya Banerji

APPROVED BY:

_____

L. Martinu, External Examiner
École Polytechnique de Montréal

_____

H. Eichhorn
Department of Chemistry and Biochemistry

_____

H. Hu
Department of Mechanical, Automotive and Materials Engineering

_____

R. Riahi
Department of Mechanical, Automotive and Materials Engineering

_____

Michael Lukitsch, Special Committee Member

_____

A. Alpas, Advisor
Department of Mechanical, Automotive & Materials Engieering

March 22, 2017

DECLARATION OF CO-AUTHORSHIP / PREVIOUS PUBLICATION

Co-Authorship Declaration

I hereby declare that this dissertation incorporates documentation of research performed by the author under the supervision of Prof. Ahmet T. Alpas. Dr. M. J. Lukitsch (General Motors R&D) assisted in obtaining samples and provided insights into impact of experimental results on the industry. Mr. V. Francis (former student of University of Windsor) assisted the author in performing some of the experiments reported in Chapter 3 which includes comments from Dr. A. Edrisy (University of Windsor). Mr. B. McClory (General Motors Powertrain) and Mr. D. R. White (General Motors Powertrain) assisted with the provision of samples for the experiments performed in Chapter 4 and brought an industrial perspective during the discussions of the results analyzed by the author. The experiments in Chapters 5-8 were performed in collaboration with Dr. S. Bhowmick (University of Windsor).

I am aware of the University of Windsor Senate Policy on Authorship and I certify that I have properly acknowledged the contribution of other researchers to my thesis, and have obtained written permission from each of the co-author(s) to include the above material(s) in my thesis.

I certify that, with the above qualification, this thesis, and the research to which it refers, is the product of my own work.

Declaration of Previous Publication

This dissertation includes material from six original peer reviewed journal articles that have already been published and one journal article that has been accepted in a peer reviewed journal.

Dissertation	Publication title and citation information	Publication Status
Chapter 2	A. Banerji, M. J. Lukitsch, A. T. Alpas, "Friction reduction mechanisms in cast iron sliding against DLC: Effect of biofuel (E85) diluted engine oil", Wear 368 (2016) 196-209	Published
Chapter 3	A. Banerji, A. Edrisy, V. Francis, A. T. Alpas, "Effect of bio-fuel (E85) addition on lubricated sliding wear mechanisms of a eutectic Al–Si alloy", Wear, 311 (1) (2014) 1-13	Published
Chapter 4	A. Banerji, M. J. Lukitsch, B. McClory, D. R. White, A. T. Alpas, "Effect of iron oxides on sliding friction of thermally sprayed 1010 steel coated cylinder bores", http://dx.doi.org/10.1016/j.wear.2017.02.032	In Press
Chapter 5	A. Banerji, S. Bhowmick, A. T. Alpas, "High temperature tribological behavior of W containing diamond-like carbon (DLC) coating against titanium alloys", Surface and Coatings Technology, 241 (2014) 93-104	Published
Chapter 6	A. Banerji, S. Bhowmick, A. T. Alpas, "Role of temperature on tribological behaviour of Ti containing MoS_2 coating against aluminum alloys", Surface and Coatings Technology, 314 (2016) 2-12.	Published
Chapter 7	S. Bhowmick, A. Banerji, A. T. Alpas, "Role of humidity in reducing sliding friction of multilayered graphene", Carbon 87 (2015) 374-384	Published
Chapter 8	A. Banerji, S. Bhowmick, M. J. Lukitsch, A. T. Alpas, Friction Behaviour of Multilayered Graphene against Steel, MRS Proceedings, 1812 (2016) imrc2015s6b-o001, Cambridge University Press.	Published

I certify that I have obtained a written permission from the copyright owner(s) to include the published material(s) in my thesis. I certify that the above material describes work completed during my registration as graduate student at the University of Windsor. I declare that, to the best of my knowledge, my thesis does not infringe upon anyone's copyright nor violate any proprietary rights and that any ideas, techniques, quotations, or any other material from the work of other people included in my thesis, published or otherwise, are fully acknowledged in accordance with the standard referencing practices. Furthermore, to the extent that I have included copyrighted material that surpasses the bounds of fair dealing within the meaning of the Canada Copyright Act, I certify that I have obtained a written permission from the copyright owners to include such materials in my thesis.

I declare that this is a true copy of my thesis, including any final revisions, as approved by my thesis committee and the Graduate Studies office, and that this thesis has not been submitted for a higher degree to any other University or Institution.

ABSTRACT

This study aims at understanding the micromechanisms responsible for reduction in friction and wear in the engine cylinder bore/liner materials when tested under lubricated and unlubricated conditions. The tribolayers formed in-situ during sliding contact are unique to each tribosystem and a detailed study of these tribolayers will shed light on the friction reduction mechanisms in powertrain materials.

Boundary lubricated tribological performance of grey cast iron (CI) tested against non-hydrogenated diamond-like carbon coating (NH-DLC) resulted in 21% lower coefficient of friction (COF) and an order of magnitude lower volumetric wear compared to CI and steel counterfaces. Dilution of the engine oil by ethanol containing E85 biofuel, consisting of 85% ethanol and 15% gasoline, was beneficial as COF and volumetric wear losses were further reduced. TEM/EELS studies of the NH-DLC counterface provided evidence for OH adsorption of the dangling carbon bonds at the coating surface leading to low friction. Advantage of E85/engine oil blend was also evident during boundary lubricated sliding of eutectic Al-12.6% Si alloy against AISI 52100 steel. The oil residue layer (ORL) formed during boundary lubricated sliding incorporated nanocrystalline regions of Al, Si, ZnS, $AlPO_4$ and ZnO surrounded by amorphous carbon regions. Higher proportions of Zn, S, and P antiwear compounds formed in the ORL when tested using the E85/oil (1:1) blend compared to the unmixed engine oil as the hydroxyl groups in ethanol molecules facilitated ZDDP degradation. Mico-Raman spectroscopy indicated two types of tribolayers formed during unlubricated sliding

of thermally sprayed low carbon steel 1010 coating deposited on linerless Al 380 cylinder bore: i) Fe_2O_3 layer transformed from FeO during dry sliding and ii) Fe_2O_3 layer with a top amorphous carbon transfer layer when run against H-DLC coated TCR with COF of 0.18. The NH- and H-DLC coatings, that provide low friction under room temperature conditions, fail at temperatures > 200 °C. It was shown that W containing DLC (W-DLC) coatings offered low and stable COF of 0.07 at 400 °C while a Ti incorporated multilayer MoS_2 (Ti-MoS_2) coating maintained COF between 0.11 at 25 °C to 0.13 at 350 °C. The low friction provided by these coatings was attributed to formation of high temperature lubricious oxides: tungsten trioxide (WO_3) in case of W-DLC and MoO_3 in case of MoS_2, as revealed by Raman analyses of the tribolayers formed on counterface surfaces. Tribolayer formation during sliding friction of multuilayered graphene (MLG), a potential lubricant, depended on the material transfer and relative humidity (RH). Sliding friction tests performed on MLG in air (10- 45% RH) and under a dry N_2 atmosphere showed that progressively lower friction values were observed when the RH was increased, with maximum COF of 0.52 in dry N_2 and lowest COF of about 0.10 at 45% RH. Microstructural studies including cross-sectional FIB/HR-TEM determined that sliding induced defects which comprised of edge fracture, fragmented/bent graphene stacks compared to pristine graphene and disordered regions between them.

In summary, this work shows that delineating the micromechanisms responsible for reduction in friction and wear is critical for development of appropriate materials and coatings for powertrain components.

This dissertation is dedicated to

my grandfathers (late),

Mr. P. Banerjee, Mr. A. C. Mukherjee, Mr. R. C. Mukherjee,

my parents,

Mr. Srikumar Banerjee and Mrs. Anulekha Banerjee

and

my wife,

Aiswarya.

ACKNOWLEDGEMENTS

First and foremost, I would like to thank and express sincere gratitude to my advisor Prof. A. T. Alpas for his support, patience and enthusiasm throughout my Ph.D. study. It is entirely due to his constant motivation, encouragement and experienced guidance that I was able to perform to the best of my abilities and achieve good quality research work.

I also wish to extend my heartfelt thanks to Dr. M. J. Lukitsch for his valuable comments and suggestions during my research and for sharing his expertise and knowledge. Sincere thanks to my committee members, Dr. H. Hu, Dr. R. Riahi and Dr. S. Holger Eichhorn for their insightful discussions and helpful suggestions. I would like to thank Mr. B. McClory and Mr. D. R. White of the General Motors Powertrain for their support and invaluable suggestions which improved the industrial relevance of the current study.

I would like to thank Dr. Glynis de Silveira for providing access to the Canadian Center of Electron Microscopy at McMaster University, Hamilton, Canada, in particular Mr. Travis Casagrande and Dr. Andreas Korinek for taking wonderful FIB and TEM images. I would like to thank Dr. Mark Biesinger from Surface Science group at the University of Western Ontario for his invaluable help in XPS analyses. Special thanks to Ms. Sharon Lackie for her help and allowing access for operating the environmental SEM located in the Great Lakes Institute for Environmental Research. Technical assistance from Mr. Andrew Jenner, Mr. Steve Budinsky and the members of technical support centre is greatly acknowledged.

I would like to acknowledge my sincere appreciation to Dr. S. Bhwomick for his support, for providing confidence and for pushing me to perform better. I am thankful to the faculty and staff at the Department of Mechanical, Automotive and Materials Engineering of the University of Windsor, and particularly to my colleagues, former and current, at the Tribology of Materials Research Centre, for their support, encouragement and tolerance.

Sincere thanks to the Natural Sciences and Engineering Research Council of Canada (NSERC) for providing financial support. I would also like to acknowledge the Ontario Government for providing Ontario Graduate Scholarship (OGS) and the University of Windsor for providing in-program Doctoral Scholarship.

I would like to thank my parents, Mr. and Mrs. Banerjee, for their unconditional love, support and motivation. I would like to thank my parents-in-law, Mr. and Mrs. Balamurali for their love and for having so much faith in me. Last but not the least, my deepest gratitude to my wife, Aiswarya, for her love, encouragement, for tolerating me and for providing support throughout.

TABLE OF CONTENTS

DECLARATION OF CO-AUTHORSHIP / PREVIOUS PUBLICATION..... iii

ABSTRACT..... vi

ACKNOWLEDGEMENTS ix

LIST OF TABLES..... xix

LIST OF FIGURES.....xx

NOMENCLATURE xxxii

CHAPTER 1 Introduction.....1

1.1 Background and Motivation.....1

1.2 Scope & Organization of Dissertation 3

1.3 Objectives.....8

1.4 Literature Survey.....10

1.4.1 Fundamentals of Friction and Wear 10

1.4.2 Micromechanisms of Tribolayer Formation.....18

1.4.3 Micromechanisms of Tribolayer Formation.....25

1.4.3.1 Need for additives.....26

1.4.3.2 Mechanisms of ZDDP Degradation.....27

1.4.3.3 Action of ZDDP on Al Alloys 30

1.4.4 Tribolayers Formed During Sliding against Diamond-like Carbon Coatings.....33

1.4.4.1 Environmental Effects 33

1.4.4.2 High Temperature Effects.....36

1.4.5 Tribolayers Formed During Sliding against Graphene 41

1.5 Friction in Automotive Powertrain 46

Bibliography.....55

CHAPTER 2.....61

Friction Reduction Mechanisms in Cast Iron Sliding against DLC: 61

Effects of Biofuel (E85) Diluted Engine Oil.....61

2.1. Introduction.....61

2.2. Experimental 65

2.2.1 Materials and Coatings.....65

2.2.2 Tribological Tests.....67

2.2.3 Examination of Worn Surfaces 68

2.3. Results.....71

2.3.1 Effect of Moisture on Unlubricated Sliding during Tests with Varying RH.....71

2.3.2. Continuous Sliding Tests at constant RH: COF vs. Volumetric Wear Loss Diagram.....74

2.3.3. Lubricated Tests Using Engine Oil and Diluted Oil 78

2.3.4 Microscopic and Spectroscopic Analyses of Contact Surfaces.....82

2.3.4.1 Cross-sectional TEM and micro-Raman examinations of NH-DLC coating.....82

2.3.4.2 SEM and XPS Examinations of CI contact Surfaces 85

2.4. Discussion 89

2.4.1 Micromechanisms of Wear 90

2.4.2 Micromechanisms of Friction 96

Summary and Conclusions 98

Bibliography 99

CHAPTER 3 105

Effect of Biofuel (E85) Addition on Lubricated Sliding Wear Mechanisms 105

of a Eutectic Al-Si Alloy 105

3.1. Introduction 105

3.1.1. Micromechanisms of UMW in Al-Si Alloys 105

3.1.2. Effect of E85 Mixed Fuel on Wear 107

3.2. Experimental 109

3.2.1 Description of the Alloy's Microstructure 109

3.2.2 Wear Test Procedure 111

3.2.3 Volumetric Wear Loss 111

3.2.4 Examination of Worn Surfaces 114

3.3. Results 114

3.3.1 Volumetric Wear Loss 114

3.3.2 Ultra-Mild Wear Stage I 118

3.3.3 Ultra-Mild Wear Stages II and III 120

3.3.4. TEM Analyses of ORL and Subsurface Microstructure 126

3.3.5 XPS Analyses of ORL.....131

3.3.5.1 XPS Spectra of Negatively Charged Radicals.....131

3.3.5.2 XPS Spectra of Compounds Formed by Zn, Ca and C.....133

3.4. Discussion.....137

3.4.1 Role of Microstructure on ORL Formation.....137

3.4.2 Role of E85 Addition on ORL Formation Mechanisms.....139

Summary and Conclusions.....145

Bibliography.....146

CHAPTER 4.....150

Effect of Iron Oxides on Sliding Friction of Thermally Sprayed.....150

1010 Steel Coated Cylinder Bores.....150

4.1. Introduction.....150

4.2. Experimental.....153

4.2.1 Spray Coatings.....153

4.2.2 Tribological Tests.....154

4.2.3 Examination of Worn Surfaces during and After Sliding.....155

4.3. Results and Discussion.....156

4.3.1 Characterization of 1010 Coatings.....156

4.3.2 Oxide Formations during Unlubricated Sliding: Microscopic and Spectroscopic Observations.....161

4.3.3 Role of Oil Degraded Tribolayers during Lubricated Sliding Contact....171

4.3.3.1 Continuous Lubricated Tests 171

4.3.3.2 Unlubricated-Lubricated Tests 176

4.3.4 Wear and Friction Reduction Mechanisms during Lubricated Sliding.....178

Conclusions.....181

Bibliography.....182

CHAPTER 5.....185

High Temperature Tribological Behaviour of W Containing Diamond-Like Carbon (DLC) Coating against Titanium Alloys.....185

5.1. Introduction.....185

5.2. Experimental Details.....188

5.2.1 N- Based Coatings: TiN, TiAlN and TiCN.....188

5.2.2 C-Based Coatings: H-DLC and W-DLC.....189

5.2.3. Pin-on-Disk tests and Wear Rate Calculations.....192

5.3. Results and Analyses 194

5.3.1 Evaluation of Coatings and Ranking of their Performance.....194

5.3.2 Changes in Tribological Behaviour of H-DLC with Temperature.....198

5.3.3 Changes in Tribological Behaviour of W-DLC with Temperature.....204

5.4. Discussion 217

5.4.1 Titanium Adhesion Mitigation by H-DLC and W-DLC (25 ˚C to 200 ˚C).....217

5.4.2 Titanium Adhesion Mitigation by W-DLC (400 ˚C to 500 ˚C) 218

Summary and Conclusions.....223

Bibliography.....224

CHAPTER 6 Role of Temperature on Tribological Behaviour of Ti containing MoS_2 Coating.....229

against Aluminum Alloys.....229

6.1. Introduction.....229

6.2. Experimental Procedure.....231

6.2.1. Materials.....231

6.2.2. Pin-on-Disk Tests: COF Measurements and Wear Rate Calculations.....233

6.2.3. Determination of Morphological and Compositional Features of Transfer Layers.....233

6.3. Results.....234

6.3.1 Microstructure of Ti-MoS_2 Coating.....234

6.3.2. Variation of Coefficient of Friction with Temperature.....235

6.3.3. Transfer Layer Formation on 319 Al Counterfaces.....245

6.3.4. Characterization of Contact Surfaces using Raman and XPS.....249

6.4. Discussion: Friction and Wear mechanisms of Ti-MoS_2 Coating at Different Temperatures.....255

Summary and Conclusions.....260

Bibliography.....260

CHAPTER 7 Role of Humidity in Reducing Sliding Friction of Multilayered Graphene.....264

7.1. Introduction.....264

7.2. Experimental Procedure.....266

7.3. Results.....268

7.3.1. Deposition and Characterization of CVD Grown Graphene.....268

7.3.2. COF Behaviour of Graphene under Different Test Environments.....270

7.3.3. Microscopic Observations of Wear Tracks.....271

7.3.4. Characterization of Transfer Layers.....275

7.3.5. Micro-Raman Analyses of Graphene in Transfer Layer and Wear Tracks.....283

Conclusions.....290

Bibliography.....290

CHAPTER 8 Friction Behaviour of Multilayered Graphene against Steel.....294

8.1. Introduction.....294

8.2. Materials and Experiments.....295

8.3. Results.....297

8.4. Discussion.....303

Conclusions.....307

Bibliography.....308

CHAPTER 9 General Summary and Conclusions 312

9.1 Summary and Impact of the Studies Undertaken.....312

9.2 Original/Important contributions made by the author.....315

9.3 General Conclusions 317

9.4 Future Work 319

APPENDIX: Copyright Releases from Publications.....321

VITA AUCTORIS 353

LIST OF TABLES

Table 2.1. Parameters used to calculate the lubrication conditions (λ=hmin/r*) values for tests of CI in contact with NH-DLC in SAE 5W-30 engine oil and diluted oil. R is the radius of the counterface ball in m, V is the sliding velocity in m/s, P is the normal load in N, E* is the composite elastic modulus (in GPa) could be calculated by equation 1, η0 is the viscosity constant of lubricants, α is the lubricant pressure viscosity coefficient, and r* is the r.m.s. surface roughness of the contacting surfaces. The minimum lubrication thickness hmin and r* of CI in contact with NH-DLC coating were calculated using equations 2 and 3, respectively: 70

Table 3.1. Atomic percentages of the elements detected by XPS in the ORL formed on Al-12.6% Si when using E85/oil (1:1) blend and unmixed (without E85) synthetic oil. 135

Table 4.1: Variation of linear speeds, h_{min} and λ values with changes in the stroke length and/or frequency 175

LIST OF FIGURES

Figure 1.1.Variation of coefficient of friction with load and speed [23].....11

Figure 1.2. Variation of coefficient of friction with relative humidity [27]. 12

Figure 1.3. Variation of coefficient of friction with relative humidity for steel and aluminum [27]. 13

Figure 1.4.Wear mechanism map for for 6061 Al alloy showing different wear regimes [32]. 16

Figure 1.5. Tribolayers formed on top of Al-Si alloy after wear [34]. 17

Figure 1.6. Formation of mechanically mixed layer and its elemental composition detection using EDS [38]. 20

Figure 1.7. Back scattered SEM image of cross-section of worn A356 Al-10% SiC-4% Gr worn and schematic representation of constituents of tribolayer in graphitic metal matrix composite [40]. 21

Figure 1.8. Schematic representation of processes leading to the formation of metallic aluminum layer (for A390) within tribolayers in MW-2. (a) Tribolayer supporting the load; (b) Removal of tribolayer exposing Al to counterface; (c) Extrusion of Al accompanied by metal transfer and back transfer processes [41].....24

Figure 1.9. Stribeck curve showing three lubricated regimes:Boundary lubrication,Mixed lubricated and Hydrodynamic lubrication. Z=lubricant viscosity; N=sliding speed; P=applied load [42]. 26

Figure 1.10. Structure of zinc dithiophosphate. The 'R' group indicates whether it's an alkyl or an aromatic dithiophosphate [44]. 27

Figure 1.11. Infrared spectra for (a) tribologically derived ZDDP antiwear film; (b) a simulated spectrum of tribochemical film; (c) amorphous calcium pyrophosphate and (d) amorphous magnesium orthophosphate. [45]. 28

Figure 1.12. XANES spectra of model compounds and antiwear films formed on different Al-Si and steel couples. (a) P L-edge XANES spectra; (b) P K-edge XANES spectra [51]. 32

Figure 1.13. Effect of environment on friction of NH-DLC tested against Al-6.5% Si alloy in vacuum and in ambient air [57]. 35

Figure 1.14. Variation of coefficient of friction of W-DLC tested against 319 Al at different temepratures [64].....39

Figure 1.15. comparison of a-C:H/a-Si:O with other DLC coatings as a function of temeprature [78]. 40

Figure 1.16. Friction of mechanically steel vs steel tests lubricated by exfoliated graphene processed in ethanol used under unlubricated sliding [16]. 42

Figure 1.17. High resolution cross-sectional TEM (HR-TEM) images of worn surface of graphene run against H-DLC showing (a) fragmented graphene and (b) curved and bent graphene stacks [93]. 45

Figure 1.18. Schematic diagram of a basic overhead cam engine showing various engine parts:camshaft, valve-train, piston ring, piston skirt, cylinder block, crankshaft [65]. 47

Figure 1.19. Schematic representation of UMW mechanisms in eutectic Al-Si alloy. (a)Exposure of Si particle above the Al-matrix; (b) Particle sink-in and AL-matrix pile up; (c) Micro scratch and damage on the elevated matrix [105]. 50

Figure 1.20. The calculated contact pressure distribution on the particles for Al–25% Si. The Hertzian contact pressure distribution is also shown; (b) variation of the maximum contact pressure applied on the particles in Al–25% Si and Al–11% Si with the applied load [103].....51

Figure 1.21. (a) Cross-sectional low magnification and (b) HR-TTEM image of the ORL formed on AM60-9%$(Al_2O_3)_f$ under the wear track tested at 1.0 N load and 100 °C [106]. 54

Figure 2.1. (a) Low and (b) high magnification cross-sectional secondary electron images of cast iron with graphite flakes embedded in a pearlitic matrix; (c) Bright-field TEM image of the α-Ferrite and the Fe_3C lamellae adjacent to a graphite flake. 67

Figure 2.2. Variations of COF values with the relative humidity (% RH) for unlubricated sliding tests performed on CI against NH-DLC, CI and uncoated steel. COF of steel sliding against itself is shown for comparison. Load = 5.0 N and sliding velocity = 0.05 m/s for all tests. 73

Figure 2.3.(a) Typical COF vs sliding cycles plots of CI tested against NH-DLC, CI and steel. COF plot of steel run against steel is COF plot is also shown; (b) COF vs volumetric wear plot for CI tested against NH-DLC, CI and steel as well as steel vs steel in 34% RH for 5×10^3 cycles. The 3-D optical profilometer images in the inset show wear surfaces of CI/NH-DLC, CI/CI and steel/steel tribo-couples. 76

Figure 2.4. Typical COF vs. sliding cycles plots for CI / CI and CI / NH-DLC in engine oil (SAE 5W-30) and in diluted oil. Load = 5.0 N and sliding velocity = 0.05 m/s for all tests. 78

Figure 2.5. (a) Average steady state COF values obtained from CI vs CI and CI vs NH-DLC tests in oil (SAE 5W-30) and in diluted oil at different sliding cycles. Each point on this plot represents average COF value obtained from tests on fresh samples performed for that sliding cycle. The error for an average COF data point for each sliding cycle is about 10%; (b) Volumetric wear loss of CI samples plotted against sliding cycles for tests against CI and NH-DLC in oil (SAE 5W-30) and in diluted oil. Each point on this plot represents average volumetric wear loss value obtained from tests on fresh samples performed for that sliding cycle. 80

Figure 2.6. (a) Cross-sectional FIB/SEM image of the NH-DLC used as counterface against CI in unlubricated sliding test for 5×10^3 cycles (34 % RH) showing adhered material (iron oxide) as well as through thickness and interface fracture at a section subjected to significant wear damage and (b) micro-Raman spectra of worn NH-DLC after unlubricated tests for 5×10^3 cycles against CI; (c) Cross-sectional FIB/SEM image of the NH-DLC tested against CI under the boundary sliding condition for 2×10^5 cycles showing no coating damage and (d) micro-Raman spectra worn NH-DLC after boundary lubricated sliding for 2×10^5. (Raman spectra of as-deposited NH-DLC are given in figure b and d as reference). 84

Figure 2.7. (a) Backscattered SEM image of CI worn surface after sliding against NH-DLC coating in diluted oil for 2×10^5 cycles; (b) Elemental EDS maps taken from (a) showing the distributions of (b) Zn, (c) S, (d) P, (e) Ca, (f) O (g) Fe and (h) C. Arrows in figure a show different pockets of the ORL. 86

Figure 2.8. High-resolution XPS spectra showing deconvoluted peaks of (a) Zn 2p, (b) S 2p, (c) P 2p, (d) Ca 2p, (e) C 1s and (f) O 1s obtained of ORL formed on CI subjected to sliding tests using diluted oil for 2×10^5 cycles. 88

Figure 2.9. (a) Cross-sectional TEM image showing the microstructure of subsurface of CI under the worn surfaces with pockets of ORL when tested against NH-DLC for 1×10^4 cycles in diluted oil; (b) Higher magnification image of the region indicated by a dotted rectangle shown in (a). Dark strips represent Fe_3C (cementite) phase (~54 nm wide) between the lighter and thicker (~200 nm) bands of α (Ferrite) phase. The pearlite (cementite and ferrite) colonies, with two distinct orientations one nearly parallel to the sliding direction and the other nearly perpendicular, were allocated at each side of a prior γ (austenite) grain boundary; (c) schematic representation of the subsurface deformation features. 91

Figure 2.10. (a) Cross-sectional TEM image showing ORL on CI surface tested against NH-DLC for 1×10^4 cycles in diluted oil; (b) High resolution TEM image of the crystalline ZnS region from the ORL with interplanar spacing measured as 0.31 nm; (c) selected Area diffraction pattern of the HR-TEM area shown in (b). 93

Figure 2.11. (a) Cross-sectional FIB/SEM image showing different antiwear components of the ORL two regions of ORL formed on CI surface tested against

NH-DLC for 2×10^5 cycles in diluted oil; (b) brightfield TEM, (c) HR-TEM image and (d) FFT-derived diffraction pattern of the of the region marked as zinc pyrophosphate in (a) showing nano-crystalline structure with interplanar spacing 0.30 nm. 95

Figure 2.12. EELS O-K edge spectra obtained from the top surface of the NH-DLC coating after testing against CI for 2×10^5 cycles in diluted oil showing peaks at 528 eV, attributed to OH adsorption on NH-DLC, and in the oxygen K edge peaks in the range 534-538 eV.....97

Figure 3.1. (a) Optical micrograph showing the microstructure of Al–12.6% Si alloy etched with 10% NaOH solution. (b) Backscattered electron image (tilted at 45o to the beam) of etched Al–12.6% Si alloy. (c) EDS map of image (b) showing the distribution of Si and Ni, Fe in intermetallic phases.....110

Figure 3.2. (a) 3-D surface profilometer image of Al-12.6% Si alloy showing surface damage after sliding for 1×10^5 cycles. The line profile indicated by A-A' shows the location of Si particles and Al ridges (R) inside the wear track. Si particles and Al matrix in the unworn region are also marked. (b) Cross-sectional profile along A-A' showing matching locations of Si particles and Al ridges (R) corresponding to their locations labelled in Figure 2(a). 113

Figure 3.3. Variation of volumetric wear of Al-12.6% Si with sliding cycles tested using E85/oil (1:1) blend (solid lines) and unmixed oil (dashed lines) at a constant load of 2.0 N and sliding speed of 5.0 cm/s. The three stages of UMW are identified for both conditions.....115

Figure 3.4. (a) Variation of volumetric wear of Al-12.6% Si with sliding cycles using unmixed ethanol at 2.0 N load and a sliding speed of 5 cm/s. Wear of the alloy tested using E85/oil (1:1) blend and unmixed oil are shown for comparison. (b) Secondary electron image (SEI) of the wear track after sliding for 10^4 cycles and (c) 3-D surface profilometry image of the wear track after sliding for 10^5 cycles for tests with ethanol.....117

Figure 3.5. . Typical surface damage features of Al–12.6% Si after sliding for 5 103 cycles (UMW I) tested using E85/oil (1:1) blend. (a) SEI image showing wear scar on a Si particle (in the middle) without fracture and also sunken-in fractured Si particles (middle–top and top-right). (b) BSI of the same area showing sunken-in Si particles and adjacent Al pile-ups. Fractured Si particles are marked on both images. 119

Figure 3.6. 3-D surface profilometry images of Al-12.6% Si tested in E85/oil (1:1) blend showing surface evolution after sliding for characteristic cycles representing each UMW regime (WT shows the width of wear track). (a) 10^4 cycles showing the protruded Si particles (in red) outside the wear track become embedded in the Al matrix within the wear track. (b) 10^5 cycles showing that wear marks on the Al and sunken-in Si particles. (c) 6×10^5 cycles showing the

wear track with smoother appearance compared to (b). The micron bar shown in (c) and the height bar shown on the right apply to all figures. 122

Figure 3.7. (a) BSI image of wear surface morphology of Al–12.6% Si tested using E85/oil (1:1) blend after sliding for 3 105 cycles showing formation of ORL on the wear track. (b) SEI image of wear surface morphology of Al–12.6% Si tested in unmixed oil after sliding for 3 105 cycles also showing ORL. (c) Higher magnification BSI image of wear surface morphology of Al–12.6% Si tested in E85/oil (1:1) blend. (d) EDS spectrum of the ORL taken from region marked (d) in (c). (e) EDS spectrum of the ORL taken from region marked (e) in (c) which additionally shows the presence of Fe, possibly due to abrasion of counterface by Si particles.....125

Figure 3.8. (a) SEI of the wear track (tilted at 54o to the beam) of a sample tested for 3 105 sliding cycles using E85/oil (1:1) blend. (b) Cross-sectional TEM micrograph taken from A–A0 in (a) showing the ORL that covered Si surfaces and the nanocrystalline Al grains. (c) HR-TEM image obtained from the interface region indicated in plate (b). The dashed line demarcates the approximate boundary between nanocrystalline Al and ORL. (d) FFT derived diffraction patterns of the regions marked as (d) in plate (c) revealing some components of ORL. (e) HR-TEM image obtained from ORL showing an amorphous region (from (e) in plate b) on top left marked as (f) and crystalline region marked as (g). (f) FFT derived diffraction patterns of the regions marked as (f) in plate (e) showing a diffuse halo indicative of amorphous regions in ORL. (g) FFT derived diffraction patterns of the regions marked as (g) in plate (e). Interplanar distances in the plates (c), (d) and (g) are in nanometers. 130

Figure 3.11. (a) OH^- induced ligand exchange of dithiophsophate. (b) Proposed reaction route for ZDDP degradation and possible reaction products leading to antiwear compounds. 141

Figure 3.12. (a) Schematic representation of the ethanol induced ZDDP degradation mechanism leading to the formation of zinc, calcium and Al phosphates, sulphides, sulphates and oxides in ORL. It is to be noted that the ORL also comprises of amorphous carbon. (b) Schematic representation of the ORL formed on a sunken Si particle and Al matrix supported by a highly deformed subsurface zone comprised of nanocrystalline Al grains. . Elongated grains became divided into cells as a result of high strains, leading to the formation of equiaxed grains in the subsurface proximal to the ORL. 144

Figure 4.1. (a) Optical profilometry image showing cross-hatched honing marks on the 1010 spray coated engine bore with roughness parameters R_a=195±20 nm, R_q=250±20 nm and R_t=2.5±0.5 µm; (b) Backscattered SEM image of the cross-section of 1010 spray coating (inset shows Raman spectrum of FeO); (c) higher magnification backscattered SEM image of the 1010 spray coating. 158

Figure 4.2: (a) Low magnification TEM image of cross-section of as deposited 1010 coating showing differences in the grain sizes and orientations; (b) Brightfield TEM image of a FeO vein separating α-Fe matrix; (c) High resolution TEM (HR-TEM) image of the region marked within a box in (b) showing crystalline regions corresponding to FeO vein and α-Fe; Selected area diffraction pattern (SAED) analyses revealed different phases of the as-deposited 1010 steel coating (d) FeO veins and (e) α-Fe substrate; (f) High-magnification TEM image and (g) corresponding SAED analyses of unmolten Fe. 160

Figure 4.3. (a) Representative coefficient of friction plots for unlubricated tests; b) Average COF vs volumetric wear (mm^3) for unlubricated tests conducted on 1010 spray coating against CrN and DLC coated piston rings (load= 5.0 N, sliding velocity 0.02 m/s). Tests against each piston ring coating were performed three times and the average COF and wear rate values are reported. 162

Figure 4.4. (a) Typical secondary electron image of wear track formed on the 1010 coating surface tested against DLC coated piston ring under unlubricated conditions for 5000 cycles; (b) Micro-Raman spectra obtained from the areas indicated by (1), (2) and (3) in (a) corresponding to FeO, Fe_2O_3 and amorphous carbon; (c) Typical secondary electron image of wear track formed on the 1010 spray coated engine bore surface when tested against CrN piston ring under unlubricated conditions for 5000 cycles (load= 5.0 N, sliding velocity 0.02 m/s); (d) Micro-Raman spectra obtained from the areas indicated by (1), and (2) in (c) corresponding to FeO and Fe_2O_3. 164

Figure 4.5: In-situ micro-Raman observations of progression of oxide on 1010 coating during siding contact against CrN TCR. 166

Figure 4.6: Progression of oxide formation during unlubricated tests of (a) 1010 vs CrN TCR and (b) 1010 vs DLC TCR.....167

Figure 4.7. SEM images of (a) DLC coated piston ring and (b) wear debris formed on the DLC coated piston ring when tested against 1010 spray coated engine bore surface under unlubricated conditions for 5000 cycles; SEM images of (c) CrN piston ring and (d) oxide debris formed on the CrN piston ring when tested against 1010 spray coated engine bore surface under unlubricated conditions for 5000 cycles (load= 5.0 N, sliding velocity 0.02 m/s). 168

Figure 4.8: Cross-section TEM image of tribolayers formed on 1010 steel coating surface after test against DLC TCR and corresponding diffraction patterns identifying the various phases.....170

Figure 4.9. Representative coefficient of friction plots for continuous lubricated tests conducted on 1010 spray coating against uncoated CI and DLC coated piston rings (load= 5.0 N, sliding velocity 0.02 m/s). 172

Figure 4.10. Comparison of coefficient of friction for 1010 spray coating tested DLC coated piston ring in oil (5W30) at λ values. The lubrication regime λ

is determined from the ratio of minimum film thickness (hmin) to the r.m.s roughness (r*) of the contacting surfaces. The COF=0.18 at λ=0 was obtained from the unlubricated test results and was re-plotted here. 174

Figure 4.11. (a) Representative COF plots and (b) average COF vs volumetric wear (mm^3), for three tests, of 1010 spray coating tested against CrN and DLC coated piston rings under unlubricated-lubricated sliding conditions (load= 5.0 N, sliding velocity 0.02 m/s).....177

Figure 4.12. (a) Low magnification TEM image of the cross-section of the 1010 surface tested against DLC coated piston ring under boundary lubricated conditions; (b) high magnification, HR-TEM image of the amorphous layer transferred from DLC coating formed on top of ORL. The top tungsten (W) layer was deposited prior to FIB milling to protect the features of interest; (c) HR-TEM image of the interface between the ORL and the FeO vein—inset shows the SAED pattern corresponding to the FeO crystals; (d) HR-TEM image of the ORL showing nano-crystalline regions within an amorphous matrix; (e) FFT-derived diffraction pattern of the regions indicated in white circles in (d) showing the formation of $FePO_4$ and ZnS.....180

Figure 5.1. Cross-sectional micrographs of W-DLC: (a) FIB/SEM micrograph showing the W-DLC and the Cr interlayer deposited on M2 steel substrate; (b, c) EDS maps of C and W; (d) HR-TEM micrograph showing FCC crystalline structure of nano scale WC particles dispersed in an amorphous matrix; (e) selected area diffraction pattern showing WC particles in an amorphous matrix. 191

Table 5.1: Summary of average coefficient of friction of H-DLC and W-DLC coatings against Ti-6Al-4V at different test temperatures.....194

Figure 5.2. (a) Variations of the COF with the number of revolutions for uncoated M2 steel, TiN, TiAlN, PCD and H-DLC tested against Ti–6Al–4V at 25 °C in ambient air atmosphere. (Load = 5.00 N and speed = 0.12 m/s). (b) The variation of the average COF and standard deviation values for uncoated M2 steel, TiN, TiAlN, PCD, H-DLC, W-DLC and TiCN against Ti–6Al–4V-as determined from three tests performed for each coating. 197

Figure 5.3. Variations of the COF with the number of revolutions when the H-DLC coating was tested against Ti–6Al–4V at 25 °C, 100 °C, 200 °C, 300 °C and 400 °C. 200

Figure 5.4. Typical secondary electron images of wear tracks formed on the H-DLC surface when tested against Ti–6Al–4V at (a) 25 °C, (b) 100 °C, (c) 200 °C, (d) 300 °C and (e) 400 °C.....202

Figure 5.5. (a) Secondary electron image of the Ti–6Al–4V pin surface taken after sliding against H-DLC coating at 200 °C. The elemental EDS maps taken from the whole area shown in (a) are for (b) Ti, (c) Al, (d) V, (e) C, (f) O and (g) Fe. (h) Secondary electron image of Ti–6Al–4V pin surface after the sliding test

against H-DLC coating at 400 °C. The elemental EDS maps taken from the whole area shown in (h) are for (i) Ti, (j) Al, (k) V, (l) C, (m) O and (n) Fe. 203

Figure 5.6. Variation of the COF with the number of revolutions when the W-DLC coating was tested against the Ti–6Al–4V pin at (a) 25 °C, 100 °C and 200 °C; (b) 300 °C, 400 °C and 500 °C. 206

Figure 5.7. Variation of average steady state COF with the test temperature for H-DLC and WDLC coatings. The sliding wear tests were performed at a temperature interval of 25 °C up to 400 °C for H-DLC and up to 500 °C for W-DLC. 207

Figure 5.8. Typical secondary electron images of sections of W-DLC wear tracks when W-DLC was tested against Ti–6Al–4V at (a) 25 °C, (b) 100 °C, (c) 200 °C, (d) 300 °C, (e) 400 °C, (f) 500 °C. 210

Figure 5.9. (a) Percentage of area covered of the H-DLC and W-DLC wear tracks (by material transferred from Ti–6Al–4V as estimated from EDS maps of titanium (see Sections 3.2 and 3.3)) as a function of temperature. Insets show secondary electron images of wear tracks of H-DLC at 300 °C and corresponding EDS map of adhered titanium. (b) The variation of steady state COF with the percent area of the coating wear track covered by adhered material transferred from Ti–6Al–4V. Sliding wear tests were performed at an interval of 25 °C in the temperature range of 25–400 °C for H-DLC and in the temperature range of 25–500 °C for W-DLC. For H-DLC at N300 °C no steady state COF was obtained and the average COFs from the friction curves recorded up to 15.00×10^2 revolutions are reported. 214

Figure 5.10. The variations of wear rates (mm3 /N-m) of H-DLC and W-DLC against Ti–6Al–4V with test temperature. Insets show 3-D surface profile images of the wear tracks of W-DLC tested at 25 °C and 400 °C. 215

Figure 5.11. (a) Secondary electron image of Ti–6Al–4V pin surface taken after sliding against W-DLC coating at 300 °c. the elemental eds maps taken from the whole area shown in (a) are for (b) Ti, (c) Al, (d) V, (e) C, (f) O and (g) Fe. (h) secondary electron image of pin surface after the sliding against w-dlc coating at 500 °c. the elemental EDS maps taken from the whole area shown in (h) are for (i) Ti, (j) Al, (k) V, (l) C, (m) O and (n) W. 216

Figure 5.12. Micro-Raman spectra of the transfer layer formed on Ti–6Al–4V pins tested against W-DLC coating (a) at 25 °C, 100 °C, 200 °C and (b) at 400 °C and 500 °C. 219

Figure 5.13. Micro-Raman spectra of W-DLC coating surface (taken outside the wear track corresponding to an annealing time of 180 s) at (a) 25 °C, 100 °C, 200 °C and (b) at 400 °C and 500 °C. 222

Figure 6.1: (a) Cross-sectional FIB/SEM (secondary electron) image of Ti-MoS_2 coating with a Ti interlayer and the M2 steel substrate; (b) bright-field cross-sectional TEM image of the Ti-MoS_2 coating and EDS line scans showing the distributions of the Mo, S, Ti and Fe (in the substrate); (c) high magnification bright-field TEM image showing the different layers of the Ti-MoS_2 coating with interlayer spacing of 5 nm; (d) HR-TEM image of the interface between the Ti-MoS_2 coating and the Ti interlayer. The FFT generated SAED shown in the inset is obtained from the marked region within the Ti interlayer showing a crystalline structure in contrast to the Ti-MoS_2 layers which have an amorphous appearance. 235

Figure 6.2: Variations of the COF of Ti-MoS_2 coating at different testing temperatures. The maximum running-in COF is designated as μ_R and steady state COF as μ_S. Each data point corresponds to average value determined from friction results of three tests performed on Ti-MoS_2 coating at each temperature. A 50 °C interval was maintained between each test for temperatures up to 200 °C whereas a 25 °C interval was maintained between 250 °C - 350 °C to measure the accurately changes in COF at elevated temperatures. At temperatures higher than 400 °C no μ_R or μ_S could be detected as the COF curves showed large fluctuations. 237

Figure 6.3: (a) Variation of the COF with the number of revolutions when the Ti-MoS_2 coating was tested against the 319 Al pin at 25 °C, 100 °C and 200 °C. Typical secondary electron images of wear tracks formed on the Ti-MoS_2 surface when tested against 319 Al at (b) 25 °C and (c) 200 °C. 239

Figure 6.4: (a) Variation of the COF with the number of revolutions when the Ti-MoS_2 coating was tested against the 319 Al pin at 250 °C, 300 °C and 350 °C. (b) Typical secondary electron images of wear tracks formed on the Ti-MoS_2 surface when tested against 319 Al at 350 °C. The elemental EDS maps taken from the area shown in (b) are for (c) Mo, (d) S, (e) O and (f) Al. 243

Figure 6.5: (a) Variation of the COF with the number of revolutions when the Ti-MoS_2 coating was tested against the 319 Al pin at 400 °C, 450 °C and 500 °C. (b) Typical secondary electron images of wear tracks formed on the Ti-MoS_2 surface when tested against 319 Al at 450 °C. The elemental EDS maps taken from the area shown in (b) are for (c) Mo, (d) S, (e) O and (f) Al. 245

Figure 6.6: (a) Secondary electron image of the 319 Al pin surface taken after sliding against Ti-MoS_2 coating at 25 °C. The elemental EDS maps taken from the area shown in (a) are for (b) Mo, (c) S and (d) O. (e) Secondary electron image of 319 Al pin surface after the sliding against Ti-MoS_2 coating at 200 °C. The elemental EDS maps taken from the area shown in (e) are for (f) Mo, (g) S and (h) O.....247

Figure 6.7: (a) Secondary electron image of the 319 Al pin surface taken after sliding against Ti-MoS_2 coating at 350 °C. The elemental EDS maps taken from the area shown in (a) are for (b) Mo, (c) S and (d) O. 249

Figure 6.8: Raman spectra of (a) the wear tracks (WT) formed on Ti-MoS_2 and (b) transfer layers (TL) formed on 319 Al surface at 200 °C, 350 °C and 450 °C. The Raman spectrum of unworn Ti-MoS_2 is given for comparison. At 200 °C the Raman spectra of the WT and the TL appeared to be similar to that of the as-deposited coating and corresponded to MoS_2 layers. At 350 °C the Raman peaks corresponded to MoO_3 layers. The Raman spectrum at 450 °C showed prominent Si peaks which were attributed to Al-Si adhesion to WT in (a) and Si particles exposed on the 319 counterface surface in (b) as the transfer layer was not well formed. 252

Figure 6.9: X-ray photoelectron spectroscopy (XPS) spectra of transfer layers (TL) formed on 319 Al during sliding against Ti-MoS_2 at (a) 200 °C and (b) 350 ˚C.....254

Figure 6.10: Variation of COF (μ) with the test temperature for H-DLC, NH-DLC and Ti-MoS_2 coatings subjected to high temperature tests at constant temperatures between 25 and 500 °C. Note that $\mu = \mu_S$ (steady state COF) up to 400 °C for Ti-MoS_2, up to 200 °C for H-DLC and up to 100 °C for NH-DLC. 256

Figure 6.11: COF vs wear rate plot for Ti-MoS_2 tested against 319 Al at different temperatures. Low COF and wear rates were observed for temperatures between 25 °C and 200 °C where a MoS_2 transfer layer formed. In the temperature range of 200-350 °C the increase in COF and wear rates were attributed to formation of MoO_3 and transfer to counterface. At above 400 °C localized areas of coating removal and Al-Si adhesion led to significant increase in COF and wear rates. 258

Figure 7.1—Micro-Raman spectra of the graphene on Ni substrate taken at three different locations shown in the secondary electron image in the inset. The ratio of G and 2D bands indicate the graphene flakes deposited by the CVD process form more than single layer. (The ambient atmosphere consisted of 45 % RH).....269

Figure 7.2—Variation of the coefficient of friction (COF) with the number of revolutions when the graphene was tested against the Ti-6Al-4V ball at (a) dry N_2 and ambient air with 10% RH (b) 10%, 32% and 45% RH. The data obtained 10% RH are re-plotted in Figure 3 (b) for comparison. (c) Variation of peak running in (μ_r) and steady state COF (μ_s) with RH. Each point in the plot represents the average value of three tests performed at a particular RH. The error bars represent the variation about the mean COF values from the three tests. 271

Figure 7.3—Secondary electron images of typical sections of graphene wear tracks when graphene was tested against Ti-6Al-4V at (a) dry N_2, (b) 10% RH, (c) 32% RH, and (d) 45% RH. Extensive transfer and adhesion of Ti-6Al-4V occurred within the wear track when the sliding tests were conducted in dry N_2. Graphene flakes were still evident within the wear track after the sliding tests at 10%, 32%

and 45% RH. The white boxes in each figure indicate the specific locations from which Raman spectra (Figure 7a) were obtained.....274

Figure 7.4—(a) Secondary electron image of Ti-6Al-4V ball contact surface taken after sliding against graphene in a dry N_2 atmosphere. The elemental EDS maps taken from the whole area shown in (a) are for (b) C, (c) Ti and (d) Ni. (e) Secondary electron image of ball contact surface after the sliding against graphene at 45% RH. The elemental EDS maps taken from the area shown in (e) are for (f) C, (g) Ti and (h) Ni. The white boxes in each SEM figure indicate the specific locations from which Raman spectra (Figure 7b) were obtained. 276

Figure 7.5—a) Cross-sectional FIB image of the transfer layer (TL) on Ti-6Al-4V contact surface for a test performed in 45% RH atmosphere, obtained using a Ga^+ ion source sputtered at 30 kV and a beam current of 80 pA. (b) Cross-sectional TEM image of the transfer layer, acquired from the region indicated as (b) in (a), showing a network of graphene stringers. (c), High magnification image of graphene stacks forming the stringers extending in an amorphous C matrix. (d) High resolution TEM (HR-TEM) image of graphene layers consisting of 4-5 stacks with d spacings of 0.38 nm within an amorphous matrix. (e) HR-TEM image showing graphene layers consisting of 21 stacks with d spacing of 0.34 nm within an amorphous matrix. (f) HR-TEM image of the interface between transferred graphene layer and top surface of the Ti-6Al-4V counterface. The images in the inset shows the Fast Fourier Transform (FFT) derived diffraction patterns indicating graphene in transfer layer and α-Ti counterface. 281

Figure 7.6—X-ray photoelectron spectroscope (XPS) spectra of transfer layers that formed on Ti-6Al-4V ball surface during sliding against graphene in ambient air with 45% RH for (a) O 1s and, (b) C 1s. High-resolution scan of Ti (not shown in the manuscript) $2p_{1/2}$ and $2p_{3/2}$ shows binding energy values of 463.98 eV and 458.26 eV, which when considered together with O 1s value of 529.74 eV corresponds to TiO_2 [29].....282

Figure 7.7—(a) Micro-Raman spectra of the transfer layer formed on counterface sliding against graphene at dry N_2, 10% RH, 32% RH and 45% RH conditions. (b) Micro-Raman spectra of the graphene wear track after the sliding tests at dry N2, 10% RH, 32% RH and 45% RH conditions. (Compare the wear track spectra generated at 45% RH with Figure 7.1, of unworn graphene surface before the sliding test).....285

Figure 8.1: Variation of the coefficient of friction (COF) with the number of revolutions when (a) multilayered graphene (b) NH-DLC were tested against the M2 steel counterface in ambient air with 10%, 25% and 52% RH. 298

Figure 8.2: Variations of (a) peak running in (μ_R); (b) duration of running-in COF (t_R) and (c) steady state COF (μ_s) with RH (no steady state COF was reached for NH-DLC at 10% RH).....299

Figure 8.3: (a) Secondary electron image of the M2 steel pin surface taken after sliding against graphene at 25% RH. The elemental EDS maps taken from the whole area shown in (a) are for (b) C, (c) O and (d) Fe. 301

Figure 8.4: (a) Secondary electron image of the M2 steel pin surface taken after sliding against NH-DLC at 25% RH. The elemental EDS maps taken from the whole area shown in (a) are for (b) C, (c) O and (d) Fe.....302

Figure 8.5: a) Micro-Raman spectra of the transfer layer formed on M2 counterface sliding against graphene in air with 52% RH. Micro-Raman of unworn graphene surface before the sliding test was also provided for the comparisons. An enlarged view of the D and G peaks is shown in inset; (b) Micro-Raman spectra of the transfer layer formed on counterface sliding against NH-DLC in air with 52% RH. Micro-Raman of unworn NH-DLC was also provided for the comparisons. The Raman spectrum of iron oxide is showing in inset. 305

Figure 8.6: Comparisons of (a) maximum running-in COF (b) average duration of running-in COF of M2 steel and Ti-6Al-4V against graphene at different humidity levels. 306

NOMENCLATURE

α Viscosity constant of lubricating oil

η_0 Viscosity constant of lubricating oil

λ Film thickness ratio

μ_R Average steady state coefficient of friction

μ_S Maximum running-in coefficient of friction

h_{min} Lubrication film thickness

r* Composite surface roughness of two contacting bodies

a.u. Arbitrary units

BE Binding energy

COF Coefficient of friction

CVD Chemical vapour deposition

DLC Diamond-like Carbon

E* Composite elastic modulus between two bodies

EDX Energy Dispersive X-ray spectroscopy

FIB Focussed ion beam

H-DLC Hydrogenated DLC

MW Mild Wear

NH-DLC Non-hydrogenated DLC

ORL Oil-residue layer

PVD Physical vapour deposition

SEM Scanning electron microscope

TCR Top compression rings

UMW Ultra-Mild Wear

WT Wear Track

XPS X-ray Photoemission Spectroscopy

ZDDP Zinc Dialkyl-DithioPhosphate

CHAPTER 1

Introduction

1.1 Background and Motivation

"As for climate change, it's by now widely accepted by the scientific community that we have entered a new geological era, the Anthropocene, in which the Earth's climate is being radically modified by human action, creating a very different planet, one that may not be able to sustain organized human life in anything like a form we would want to tolerate."

Noam Chomsky.

The alarming threats of global climate changes have duly prompted stringent regulations on fuel emissions from automotive vehicles. The 2009 modifications of the Corporate Average Fuel Economy (CAFE) regulations [1, 2] hopes to reduce the use of petroleum and greenhouse gas (GHG) emissions, by stipulating auto industry's mandatory overall fleet mpg from 25.3 in 2010 to 34.1 by 2016. In order to achieve the emission standards, it is imperative for the automotive manufacturers to look into internal combustion (IC) engine friction reduction strategies. Due to the parasitic friction loss that occurs in the IC engine, only a small fraction of the fuel energy is expended in running the vehicle. The frictional losses in engine components (mainly in powertrain and valve train assemblies) can consume as much as 20% of the available energy [3]. In order to address the frictional losses in the tribological components of an automobile engine, it is important to have a clear understanding of the tribolayer formation mechanisms and underpinning surface damage mechanisms at the microstructural level. The morphology, microstructure and composition of tribolayers formed during cylinder bore/piston ring interactions depend on the lubricant additives as well as the applied material coatings.

Lubricants play a key role in reducing friction in IC engine powertrain. An automotive engine lubricant commonly contains base oil and a mixture of various additives, incorporated for the purpose of minimizing wear, improving efficiency and consequently prolonging engine life [4]. Under normal operating conditions, the interaction between cylinder bore/liner and piston ring is expected to occur under boundary and/or mixed lubrication conditions [5]. Sliding surfaces under these lubrication regimes often lead to formation of solid tribolayers on the surfaces. The scientific approach towards understanding of these tribolayers would comprise of microstructural and compositional analyses of the lubricant derived tribolayers and tracing it's' origin back to the additives in the engine lubricant.

The motivation for using ethanol based bio-fuels in modern powertrains is to provide a clean energy source with reduced carbon and sulphur content and consequently decreasing atmospheric emissions [6]. A common ethanol-gasoline blend that consists of 85% ethanol and 15% gasoline, E85, is known to improve fuel quality by increasing its octane value [7]. The possible expansion of the use of ethanol based fuels in near future prompts the need for a systematic study of the role of ethanol/gasoline blends (with engine oil) on wear of the IC engine materials intended for powertrain applications.

The bore geometry and service environment pose challenges to the development of durable bore coatings, some of which have are yet to be addressed by the industry. Select automobile manufacturers have started to introduce products with applied coatings, but the technology's potential for friction reduction suggests increasing market penetration of these coated products in coming years. Thus coatings applied to engine bores and/or piston rings are important while considering friction reduction strategies in IC engine powertrain. Amorphous diamond-like carbon coatings (DLC) coatings have garnered attention in the last decade as popular low friction

adhesion mitigating coatings [8 ,9]. The DLC coatings consist of a mixture of sp^2:sp^3 hybridized carbon atoms and have two principal grades: hydrogenated DLC (H-DLC) with typically 40 at.% H and non-hydrogenated DLC (NH-DLC) with <2 at.% H [10]. A clear understanding of the tribolayer formation and surface passivation mechanisms in DLC coatings are critical in choosing appropriate grade of DLC. These coatings are also sensitive to the environment in which they will be used. Therefore, once again, the focus should be on designing tribological experiments that will simulate the material transfer processes that control the friction properties of a DLC coating. A comparative study with standard production ring coatings, such as uncoated cast iron (CI) and steel rings as well as CrN coated ring will provide a suitable roadmap for choosing appropriate ring coatings.

Numerous works in the literature have reviewed these aspects of tribology, although they are usually never looked altogether as a tribosystem. For example, scuffing resistance of a cylinder material cannot be fully described without taking into account the counterface material as it would directly influence the friction behviour. The aim of this study is to adopt a holistic approach to the individual tribosystems and consider every component therein to get a complete overview of the sequence of events occurring during the tribological sliding process based on which recommendations will be made to further improve the system for achieving the goal of maximizing friction reduction.

1.2 Scope & Organization of Dissertation

The tribolayer formed during sliding interactions exhibit different structural morphology and chemical composition compared to the bulk material. The microstructure and composition of tribolayers depend intimately with the tribosystem within which it is generated. During

unlubricated sliding the formation of tribolayers may be attributed to plastic deformation, transfer of materials, interactions with the environment and mechanical mixing [11] while during lubricated sliding the tribolayers formed depend on the lubricant and it's addtives. Careful characterization of the tribolayers has been performed, using spectroscopic and microscopic tools to shed light on the sequence of events leading to the formation of the tribolayer.

The study of friction reduction in engine materials usually comprises of the lubricated tests wherein standard engine oils have been tested and the friction and or wear have been recorded. The degradation of the zinc dialkyl dithiophosphate (ZDDP) additive in the oil has been studied in details in the literature [12–14]. The study of the ZDDP degradation and subsequent formation of tribloayers have been characterized using spectroscopic techniques. However, the changes in the near-surface regions due to sliding induced strains during these lubricated sliding interactions and their effects on the stability of the tribolayer is often overlooked. In this thesis both the microstructural as well as the chemical aspects of tribolayer formation have been studied with equal weightage in order to fully appreciate the role that various components in the tribosystem plays in formation of the final tribolayer. This approach, in delineating the events forming the tribolayer provides a roadmap for potential improvements in the stability of tribolayers by incorporating certain new factors such as catalytic additives and/or surface activated coatings.

Friction reducing coatings like diamond-like carbon (DLC) coatings have great potential in reducing friction. The material transfer processes as well as the test environments play significant role in determining the particular grade of DLC that ought to be used. While hydrogenated DLC (H-DLC) performs well under dry sliding conditions in presence of standard engine oils these coatings show higher friction. On the other hand, non-hydrogenated DLC (NH-DLC) shows low friction under unlubricated sliding with high relative humidity (RH) as well as

under lubricated sliding with engine oils. Accordingly, these coatings will be evaluated for their potential in reducing friction over other standard non-carbonaceous piston ring coatings, such as CrN and steel TCRs. During starved lubrication conditions, the temperatures in an engine might reach as high as 250-400 °C. Under these conditions, the conventional H- and NH-DLC coatings do not provide low friction. The incorporation of W in H-DLC may potentially make the DLCs suitable for use at elevated temperatures. On the other hand, lamellar MoS_2 coatings with Ti additions also have potential for providing low friction at elevated temperatures. The different coatings and their unique properties have been investigated thoroughly to demonstrate the critical differences in the friction reduction mechanisms that are directly related to the steps leading to the formation of tribolayers in each case.

The friction behaviour of graphene, a new carbon based material, has attracted interest and is currently being studied. In the literature, graphene has been mainly studied at a microscopic scale although there lays great potential for macroscopic applications of graphene as lubricant [15–18]. In the studies performed on graphene tribology major emphasis has been given on the effect of graphene layers and the graphene/substrate adhesion. However, none studied the effect of atmospheric humidity as an independent variable although it is known that the wear and friction behaviour of carbon based materials, namely graphite and amorphous diamond-like carbon surfaces are strongly influenced by the humidity in the test environment, as mentioned above.

In summary, this thesis adopts three different strategies to reduce friction in engine materials and in ache case the test methodology and analyses have been designed as per the needs of the particular tribosystem. The strategies that have been considered for friction reduction in engine powertrain involves: i) use of linerless Al-Si engine with and without coatings; ii) use of engine

oil blends that would facilitate tribolayer formation lowering friction and iii) application of appropriate coatings and lubricants for friction reduction. Accordingly the different chapters have been put together although the themes often overlap each other. This thesis is organized as such that it starts with an introductory chapter (Chapter 1) which presents some brief background information and our motivation to carry out this work (Section 1.1). Section 1.2 mentions the scope of this dissertation and its' organization. Section 1.3 follows by defining the objectives, and in Section 1.4 a general literature review is provided. This thesis continues with the studies that were published or submitted in peer reviewed journals, such that the Chapter 2 includes results of friction and wear of cast iron when tested against NH-DLC coating under unlubricated and boundary lubricated conditions, with particular focus on the evolution of microstructural and morphological features of the contact surfaces during sliding. Cross-sectional microscopy and surface spectroscopic observations indicated the ethanol diluted engine oil would facilitate tribolayer formation as well as passivation of the coating. In Chapter 3, the role of ethanol-fuel blends on the wear behaviour of an Al-12.6% Si alloy were studied, with a particular focus on the evolution of microstructural and morphological features of the contact surface during sliding. Sliding tests were conducted under ultra-mild wear conditions, similar to low wear that should be maintained in linerless eutectic Al–Si powertrain components. In this way the effect addition of E85 fuel blend to the engine oil, at 1:1 ratio, on the formation and stability of the tribolayers that formed on the Al-Si surfaces was delineated. In Chapter 4, another linerless Al-Si engine material was considered but with a thermal sprayed ferrous coating on it. 1010 steel coatings deposited on Al 380 engine bore were subjected to reciprocating sliding experiments against various top compression ring (TCR) materials under unlubricated and boundary lubricated conditions. In-situ Raman spectroscopy performed during unlubricated sliding experiments

provided evidence for progression of iron oxide formation during sliding. Cross-sectional microscopy and surface spectroscopic observations on 1010 steel coatings tested against DLC tested under boundary lubricated conditions showed that a composite tribolayer consisting of an amorphous carbon layer on top of an oil degraded tribolayer or an oil residue layer (ORL), formed on the sliding surfaces. Chapters 5 and 6 include the friction results of the tribological coatings suitable for elevated temperatures. Chapter 5 includes results of friction performances of H-DLC and W-DLC coatings in comparison with the traditional N-based hard coatings focussing on the rationalization of the mechanisms responsible for material transfer. The compositions of the transfer layers were identified and discussed as a function of test temperature. Chapter 6 describes the friction and adhesion mechanisms of a Ti incorporated multilayer MoS_2 (Ti-MoS_2) coating intended for use in elevated temperature applications of lightweight Al-Si alloys. Electron microscopy and spectroscopy based results shed light on the micro-mechanisms controlling the tribological behaviour of the Ti-MoS_2 at different test temperatures. A comparison of the high temperature friction mechanisms of Ti-MoS_2 and DLC coatings against Al-Si alloys has also been made. In Chapters 7 and 8 the fundamental analyses of the role of moisture in passivating the graphene surface have been discussed by including of results multi-layered graphene tested in humid atmospheres. Sliding induced structural changes, defect formations (transformations in the C atom hybridizations), amorphization and formation of transfer layers were analyzed using a combination of analytical techniques. Finally Chapter 9 includes an overall summary and the conclusions of this dissertation.

1.3 Objectives

The general objectives of this thesis were:

- The elucidation of friction mechanisms in engine materials for automotive applications using laboratory scale tribological experiments via characterization of tribolayers formed in each case
- The selection of appropriate lubricant additive, lubricant and coatings materials as solution to the friction problem based on the derived mechanisms.

These objectives were achieved by undertaking four different sub-studies, each with its own set of objectives. The objectives of the study to investigate role of lubricant additives in tribolayer formation on IC engine materials were:

- Role of ethanol dilution of standard engine oil in facilitating tribolayer formation as well as friction reduction
- Determination of lubricant additive degradation tribochemical mechanisms in presence of ethanol via microscopic and spectroscopic characterization
- Determination of surface passivation mechanisms of DLC in presence of ethanol based additive in engine oil using near surface spectroscopic techniques.

The objectives of the study to investigate role of oxide transformations on friction behaviour of a thermally sprayed linerless Al-Si engine material run against DLC counterface material were:

- Determination of oxide phase transformations during sliding using in-situ Raman technique
- Determination of dry scuffing resistance of spray coated linerless engine run against DLC counterface material

- Determination of friction behaviour and characterization of tribolayers formed during of unlubricated-lubricated sliding of linerless engine simulating engine start conditions

The objectives of the study to investigate coating materials suitable for sliding at elevated temperatures (100-450 °C) were:

- Determination of elevated temperature friction behaviour due to incorporation of W in DLC
- Determination of elevated temperature friction reduction mechanisms of MoS_2 incorporating Ti
- Raman characterization of tribolayers formed at elevated temperature elucidating the material transfer events

The objectives of the study to investigate tribology of graphene and its friction mechanisms were:

- Determination of role of humidity in macroscale sliding friction mechanisms in graphene
- Determination of role of defects introduced in the carbon lattices during sliding on the friction behaviour of graphene
- Determination of role of counterfaces on material transfer mechanisms of graphene.

1.4 Literature Survey

1.4.1 Fundamentals of Friction and Wear

Friction has been defined as the resistance to relative motion of two bodies in contact [19] and is essentially a surface and interfacial phenomenon. Leonardo da Vinci (1452–1519), the brilliant polymath, stated the three laws describing the frictional force, when two solid bodies are placed in sliding contact with each other, as: (1) proportional to the load, or pressure of one applied, (2) independent of the area of contact, and (3) independent of the sliding velocity [19–21]. However, while the first two laws are generally followed the third law doesn't hold most of the times due to the stick-slip motion [21]. The friction forces are continuously evolving as the asperities of the sliding surfaces come into contact with each other [22]. The coefficient of friction, COF, which is the ratio of the tangential friction force to the normal force, also depends on i) the counterface material, ii) the test environment, iii) the lubricants used as well as the iv) tribochemical interactions prevalent in the tribosystem. Therefore, it is meaningless to report the COF values obtained from a sliding experiment without reporting all of the above mentioned test parameters.

Chowdhury et al. [23] performed pin-on-disk sliding friction tests on aluminum disks sliding against stainless steel (SS-304) pins to assess the effect of load and speed on COF. Unlubricated friction tests carried out under normal load 10-20 N, speed 500-2500 rpm and relative humidity (RH) 70% showed that COF decreased with increase in load and increase in sliding velocity. Figure 1.1a shows that on increasing the sliding speed from 500 to 3000 rpm the COF decreases from 0.58 to 0.45. Figure 1.1b shows that an increase in load from 10 N to 20 N led to a decrease in COF from 0.5 to 0.3. Other studies [24–27] have illustrated the effect of

humidity on unlubricated sliding friction of metals. Goto and Buckley [24] illustrated the influence of humidity on the different metals and found that at low RH water interferes with the adsorption of oxygen reducing the rate of oxidation and so permit a greater amount of intermetallic contact. At higher RH values a greater amount of water adsorbed becomes sufficient to augment the protection against intermetallic contact provided and the COF decreases.

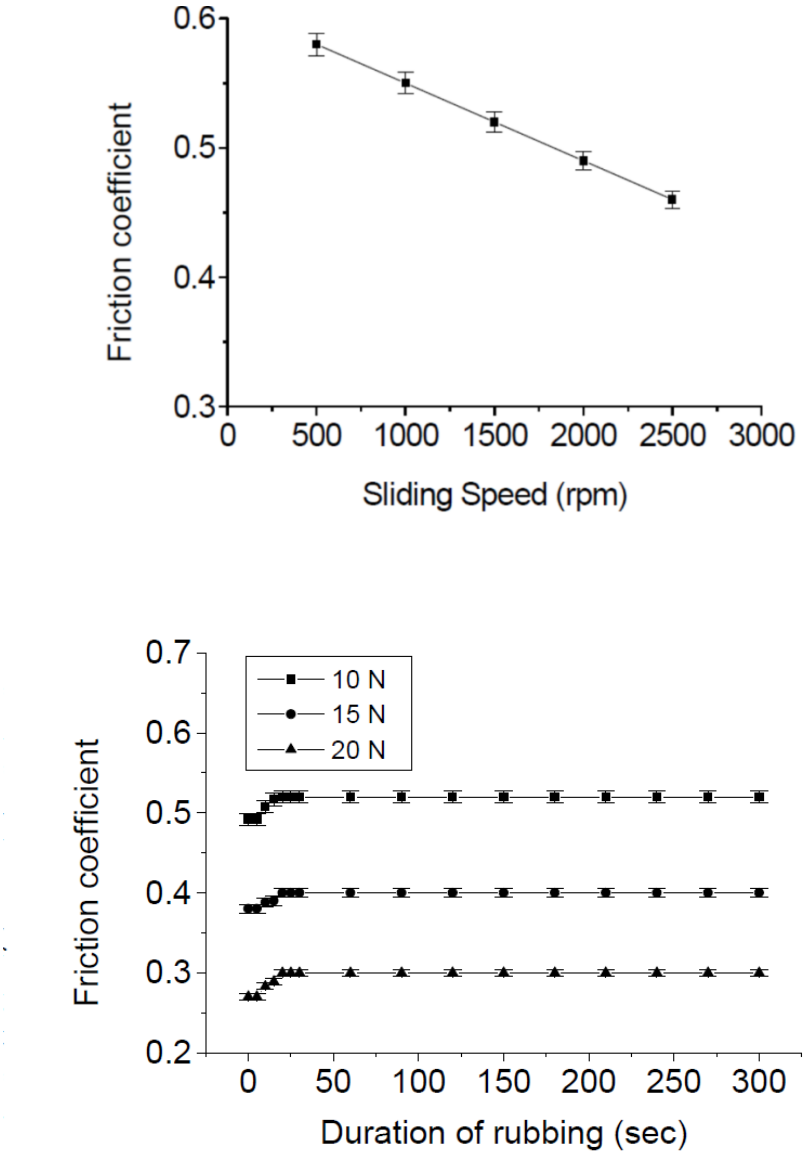

Figure 1.1.Variation of coefficient of friction with load and speed [23].

Bregliozzi et al. [27] performed ball-on-disk tests on austenitic stainless steel AISI 304 run against sapphire balls and found that at 2.0 N load, high COF and severe wear was evident at low RH (20%) while relatively lower COF and wear was observed at high RH (80%), as shown in Figure 1.2, indicating a lubricating effect of water. In case of steel the COF varied with RH as a result of surface tribochemical reaction involving formation of iron oxides and physisorbed layer of water on the surface [24, 28] although no direct evidence for these tribolayer formations was not provided. No direct relation was found between the humidity and the COF of sliding of aluminium run against itself as shown in the pin-on-disk test results presented in Figure 1.3.

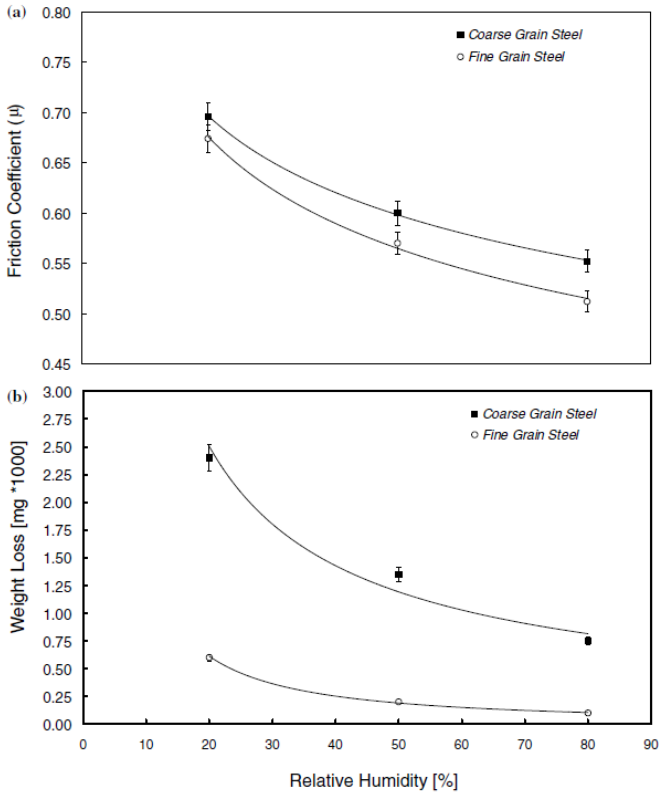

Figure 1.2. Variation of coefficient of friction with relative humidity [27].

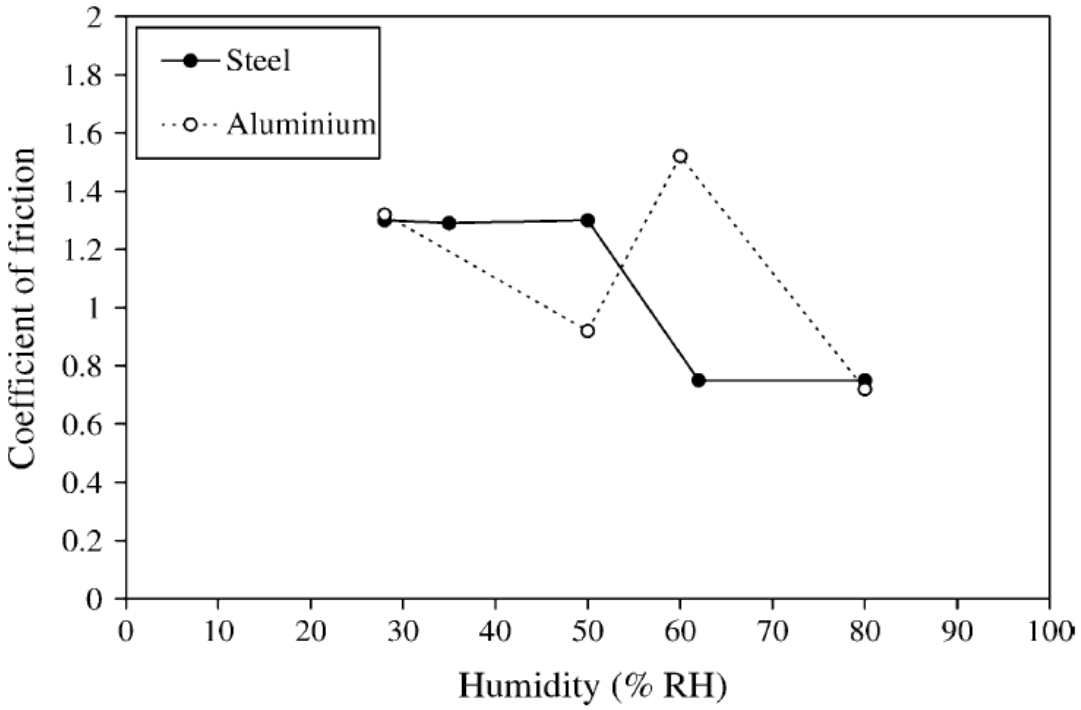

Figure 1.3. Variation of coefficient of friction with relative humidity for steel and aluminum [27].

Wear has been defined as the "alteration of a solid surface by progressive loss or progressive displacement of material due to relative motion between that surface and a contacting substance or substances" [29]. When two surfaces in contact slide over one another, one or both the surfaces will suffer wear. An empirical rule, assuming asperity (high spots) contact only, was given by Archard and Hirst [30]:

$$Q=KW/H \tag{1-1}$$

where, Q=volume worn per unit distance; W=normal load; K=coefficient of wear, a dimensionless quantity; H=hardness of the softer surface. The value of K, wear coefficient, is of great importance as it allows the comparison of severity of different wear processes. It must be noted that this equation, though one of the fundamental equations of wear predicts a linear relationship between the volume worn away to the applied load, which might not be the case in

many instances. Archard and Hirst [30], had conducted unlubricated wear tests on steel bodies and had observed two different mechanisms of wear: mild wear and severe wear. Lim and Ashby [31] constructed an empirical wear map for steel sliding on steel by summarizing wear rate and wear mechanism data for steel included in literature, further modeling it with theoretical calculations to calibrate the experimental data to illustrate different wear regimes: ultramild wear, delamination wear, mild and severe oxidational wear, melt wear and seizure. Construction of such a wear map provides the relationship between various wear mechanisms dominant under different sliding conditions and their anticipated wear rates. Mild wear (MW) and severe wear (SW) have been studied extensively for Al metal matrix composites against steel counterface under unlubricated conditions. In the mild wear regime mainly oxidational wear occurs. The wear rates are low (10^{-4}-10^{-3} mm^3/m) in this regime and wear occurs predominantly from the oxide layer formed leading to dark compacted wear debris consisting of aluminum oxide and some transferred steel. The transition from mild to severe wear, showing higher wear rates ($\geq 10^{-2}$ mm^3/m) occurs at increased load, velocity and temperature. Liu et al. [32] adopted similar methodology as Lim and Ashby to construct a wear mechanism map for aluminum alloys (Figure 1.4).

Apart from the causes mentioned above other factors like humidity, atmosphere and the counterface also affect wear of materials. Yen et al. [33] conducted unlubricated sliding wear tests with eutectic Al-Si alloy against cast iron counterface at relative humidity (RH) range 1-95%. It was observed that upto 70% RH mild wear was characterized by formation of iron-rich compacted surface layer while from 70%-95% RH the wear rate decreased two fold due to the formation of iron oxide rich surface film facilitated by increase in moisture content. The effects of atmosphere and counterface were studied by Elmadagli and Alpas [34]. The authors

investigated unlubricated wear of A390 (Al-18.5 wt% Si) alloy against SAE 52100 bearing steel in dry air and argon atmosphere. It was observed that wear rates in argon atmosphere were always less than that in dry air (5% RH). EDS results show that worn surfaces in dry air were covered with oxidized tribolayers whereas no peak for oxygen was identified in the EDS spectrum of tribolayers formed in argon atmosphere (Figure 1.5). The above review thus shows that the surface layers, or tribolayers, formed during sliding tests are responsible for the friction and wear behaviour of the tribosystem while the composition and microstructure of the tribolayers in turn are influenced by the test parameters and environment.

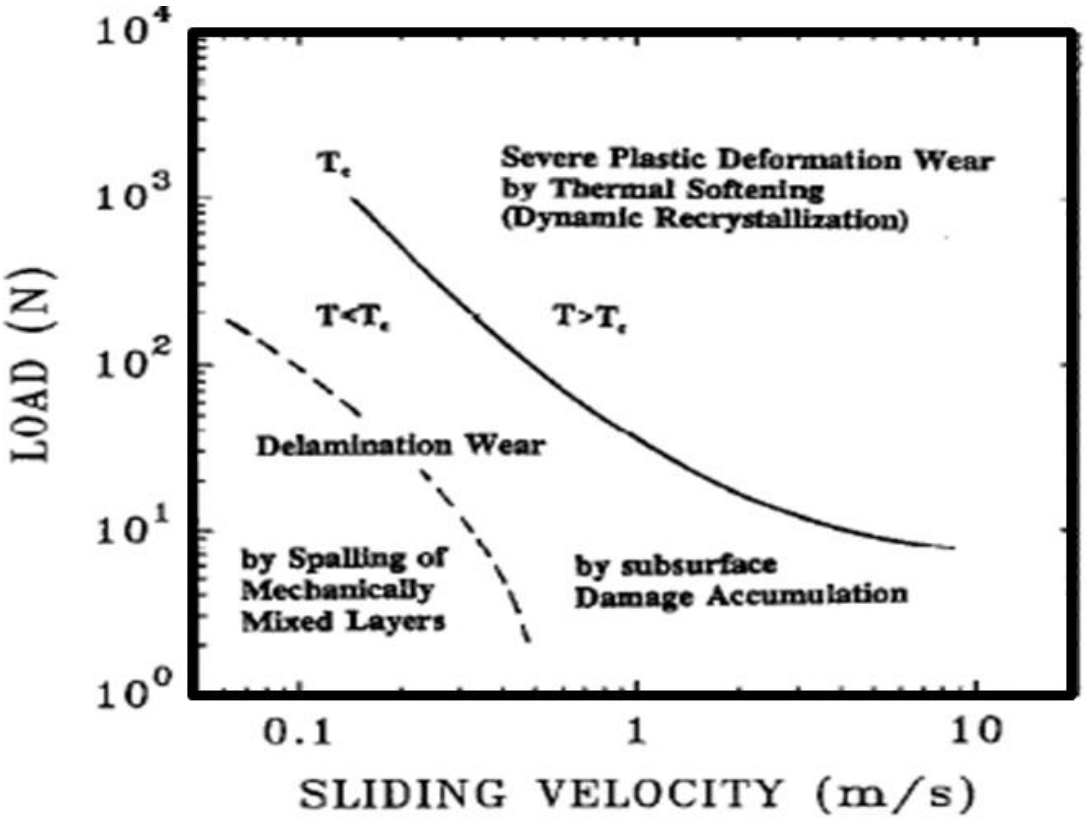

Figure 1.4.Wear mechanism map for for 6061 Al alloy showing different wear regimes [32].

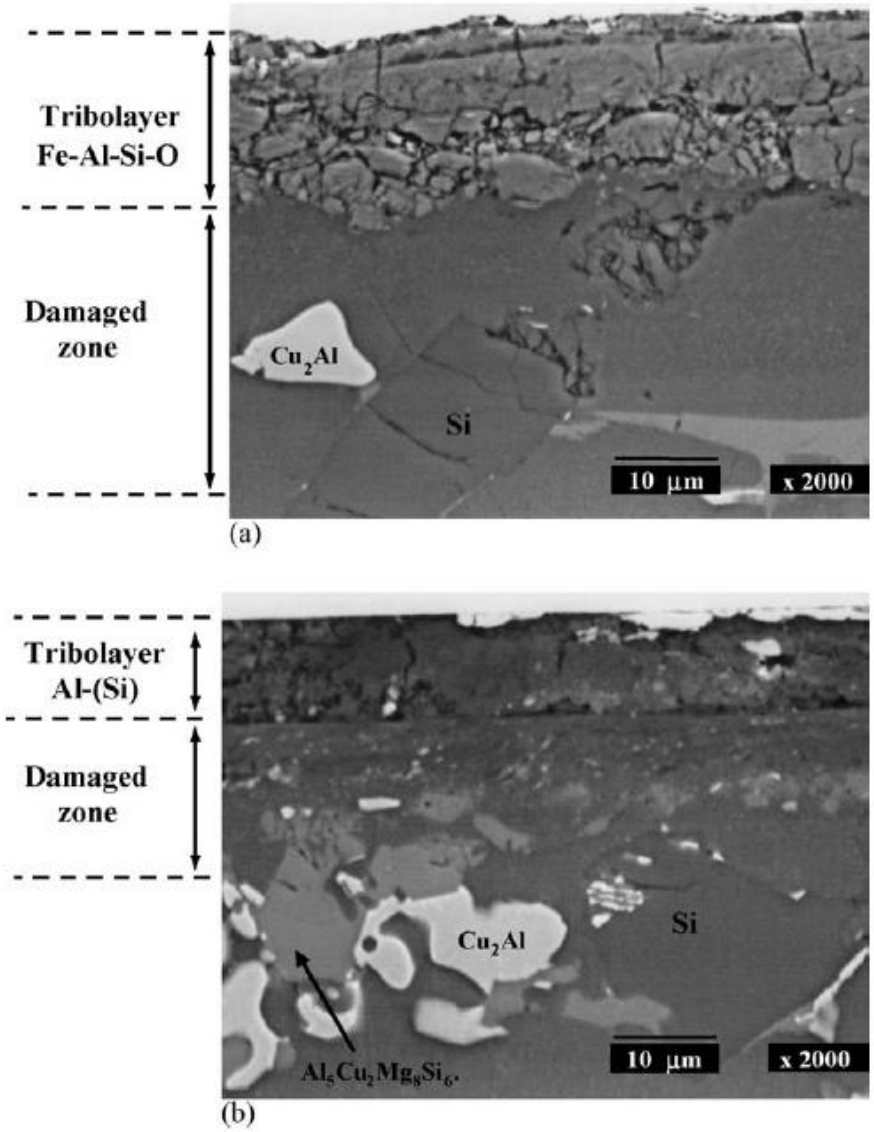

Figure 1.5. Tribolayers formed on top of Al-Si alloy after wear [34].

1.4.2 Micromechanisms of Tribolayer Formation

Tribolayer formation may be affected by counterpart material, temperature, abrasives, lubricants and other parameters. The origin of tribolayer formations maybe understood from the following observations: (i) transfer layers formation when the worn surface shows the same chemical composition as that of the mating surface where oxidation does not take place; (ii) mechanically mixed layers are formed when the chemical composition of the debris is a mixture of the wearing and the mating materials, and no oxidation takes place; (iii) composite layers build up in combination with wear and oxidation at higher temperatures [34, 35]. In this section, the role of tribolayers in controlling wear and friction of Al alloys and composites during unlubricated sliding will be reviewed whereas in subsequent sections tribolayers formed during use of coatings and lubricants will be illustrated.

Aluminum matrix composites have been developed for potential applications in automotive engines, in particular for cylinder liners where scuffing resistance during lubrication starvation conditions is very significant. Development of Al-Si alloys reinforced with SiC particles and graphite flakes or particles have increased the loads and velocities at which seizure took place under boundary lubricated and dry conditions. This can be attributed to the formation of tribolayer or mechanically mixed layers which protect the worn surfaces thus resulting in lower wear rates. The extent to which these films (oxide, adsorbed boundary lubricant, etc.) prevent intermetallic contact influences the relationship between the wear rate and the applied load. The transition between mild and severe wear regimes is associated with the breakdown of this protecting surface film [37]. Thus characterization and analysis of tribolayers for their chemical composition and mechanism of formation would be of great value. The tribolayer usually formed on the wear tracks, exhibiting different chemical composition and structural morphology

compared to the bulk material, as a result of plastic deformation, transfer, interactions with the environment and mechanical mixing [11].

Characterization of the tribolayer, also known as the mechanically mixed layer (MML), formed on the worn surface during dry block-on-ring wear tests performed on an Al-Si alloy (A356) reinforced with 20% SiC particles against tempered M2 tool steel was done using electron microscopy along with EDS, XRD and Mossbauer spectroscopy [38,39]. Figure 1.6 shows the longitudinal cross-section of the worn surface indicating that the microstructural features varied along the depth below the worn surface [38]. As shown in Figure 4, the eutectic Si colony bent towards the sliding direction, indicating plastic deformation and shear gradient in the subsurface generated during the sliding wear. The prominent feature was the morphology of the top tribolayer where extensive fracture and fragmentation of materials was evident. SEM observations of worn surfaces of A356 Al-10% SiC-4% Gr and A356 Al-5% Al_2O_3-3% Gr [40] during dry block on ring wear tests against AISI 52100 steel show that a protective tribolayer was formed at nearly all sliding speed and load in the mild wear regime for both graphitic cast aluminum composites. The top surface of the tribolayer comprised of iron oxide layers which were much more compact and hard (800 kg/mm^2) compared to the bulk material while the rest of the tribolayer consists of fractured SiC, Al_3Ni and Si particles (Figure 1.7) mixed with aluminum as indicated by EDS results. The presence of lamellar graphite films were detected within the tribolayer indicating the demarcation between the highly deformed tribolayer and the relatively undeformed bulk material.

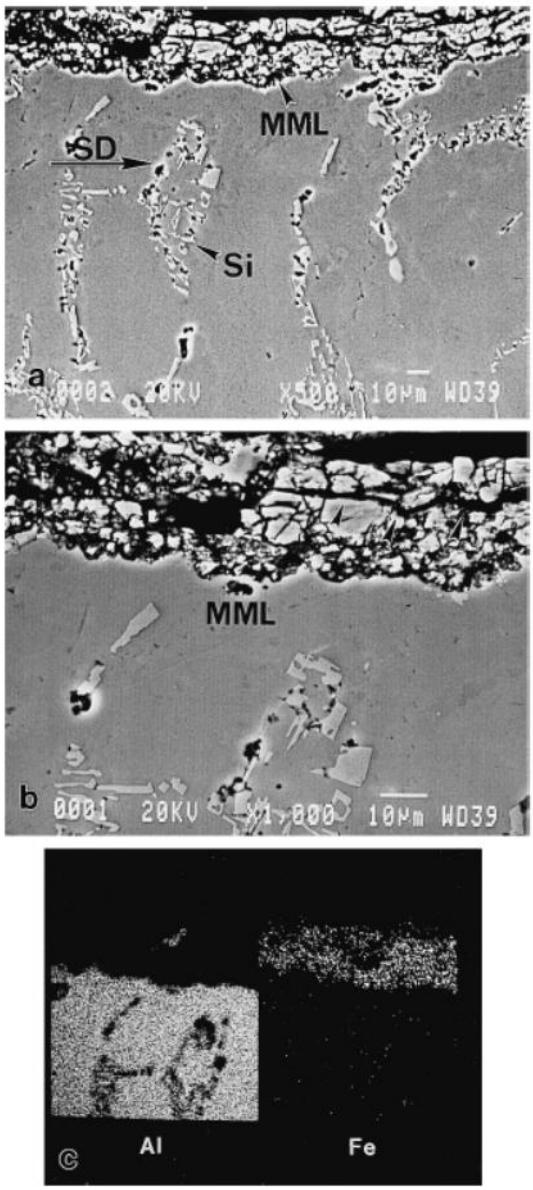

Figure 1.6. Formation of mechanically mixed layer and its elemental composition detection using EDS [38].

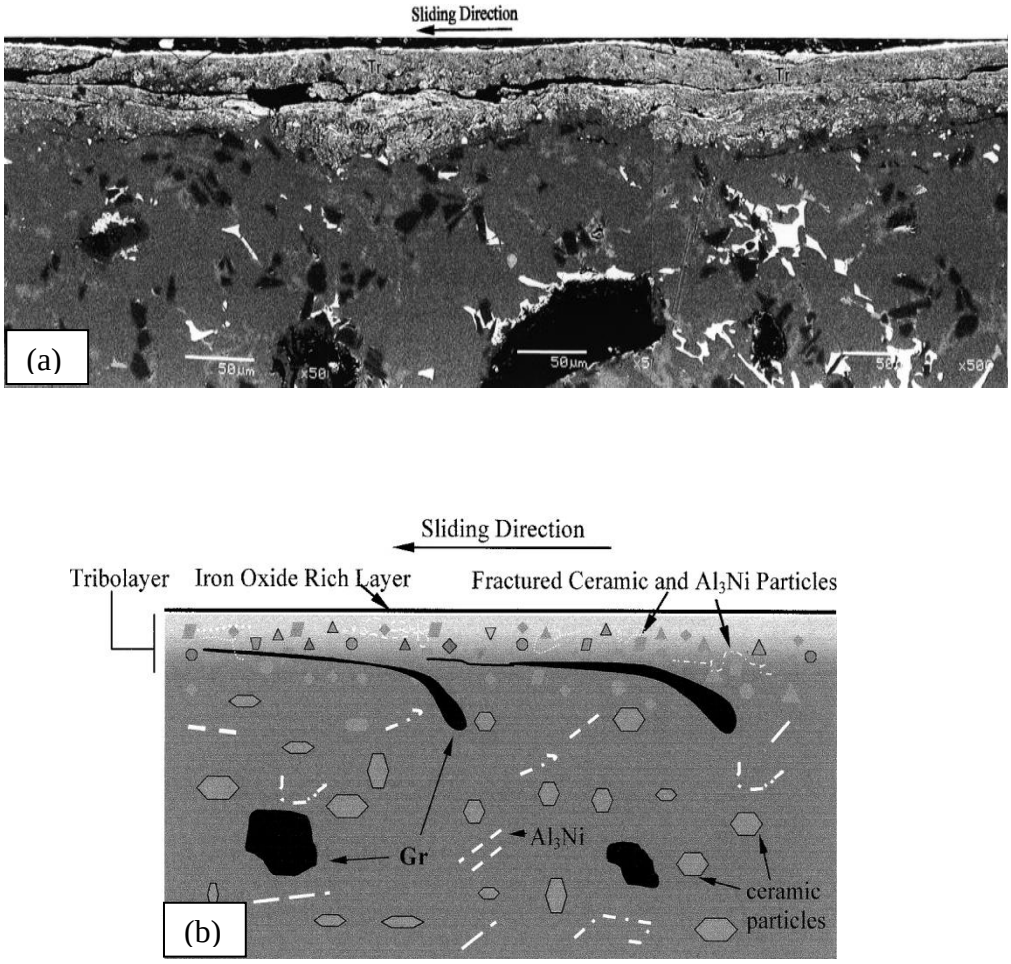

Figure 1.7. Back scattered SEM image of cross-section of worn A356 Al-10% SiC-4% Gr worn and schematic representation of constituents of tribolayer in graphitic metal matrix composite [40].

The fractured particles and thin graphite films, elongated in the sliding direction, contributed in the formation of thicker and more stable tribolayer thus delaying the mild-severe wear transition as compared to the A356 aluminum alloy and the non-graphitic aluminum matrix composites. It was also observed, however, that the steel counterface was subjected to scuffing or local material transfer from the composite as a result of abrasive action of the hard SiC carbide particles in the tribolayer and the friction heating induced softening of aluminum. The authors concluded that

such graphitic composites would be well suited for use in the cylinder liners in an IC engine where scuffing resistance is significant. Unlubricated block-on-ring wear tests performed on A390 (Al-18.5% Si) in dry air as well as in argon environment at different test loads against AISI 52100 steel counterface show that wear rates were always lower in argon atmosphere as compared to dry air (5% relative humidity) [34]. Cross-sectinal SEM observations reveal that tribolayer formation occurred on the worn surfaces under various testing conditions. The authors observed that in argon atmosphere at the initiation of sliding wear transfer of iron-rich layers occurred from the counterface to the exposed Si-particles while as sliding progressed the composition of tribolayer changed to Al-rich layer. Moreover material detached from the tribolayers was also transferred to the counterface at a high rate. In air the A390 surface was covered with iron rich oxidized tribolayers at sliding distances over 50 m. Thus it can be concluded that the tribolayer composition and depth of the damaged zone below it varies with testing conditions-the depth of the damaged zone and the magnitude of subsurface plastic strains being lower as compared to the results obtained in air. Elmadagli and Alpas [41] observed two subregimes in the mild wear regime as a function of applied loads-MW1 and MW2 for wear tests with A390 in dry air (RH 5%). Although tribolayers formed in both the subregimes the transition from MW-1to MW-2 coincided with sharp increase in amount of material transferred to the counterface. The high wear rate observed in MW-2 suggests that the aluminum matrix came in contact with the counterface through the fractured portions of the tribolayer in MW-2. Presence of Al layers on the tribolayer was observed in the MW-2.Spallation of the thick tribolayers formed in MW-2 causing transfer and back-transfer of the aluminum from the counterfce (Figure 1.8) along with the extrusion of the exposed aluminum surface over the tribolayers was the main reason behind the increased wear rate in MW-2 as compared to MW-1. These contrasting

compositions in the MW regime thus can be attributed of the tribolayers formed to different testing environments and applied load.

Tribolayer formation under dry sliding conditions is thus found to be effective in prolonging the transition to severe wear regime. Similar protective film formation is observed during lubricated sliding wear. This protective film formation can be attributed to the chemical degradation of additives used in the lubricant. Hence the next segment is the study of lubricant and its additives.

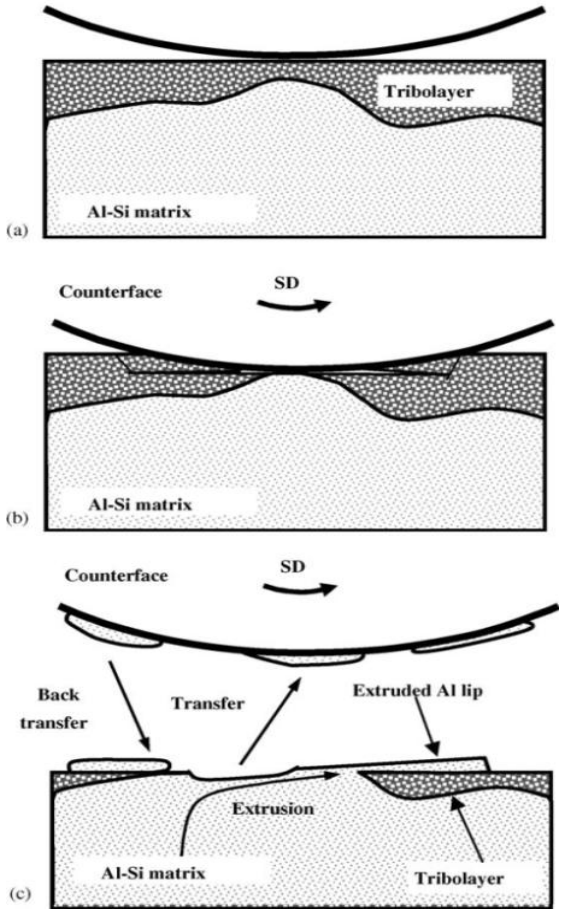

Figure 1.8. Schematic representation of processes leading to the formation of metallic aluminum layer (for A390) within tribolayers in MW-2. (a) Tribolayer supporting the load; (b) Removal of tribolayer exposing Al to counterface; (c) Extrusion of Al accompanied by metal transfer and back transfer processes [41]

1.4.3 Micromechanisms of Tribolayer Formation

Surface lubrication involves several aspects of the physical and chemical properties of the surface material and the lubricant. The viscosity of the lubricant and some of its other rheological properties determine the thickness of the lubricant fluid film. A thicker lubricant fluid film leads to better lubrication. The lubricant film thickness is often an indicator of the lubrication regime. The lubrication regimes may be characterized as hydrodynamic, mixed, or boundary lubricated according to the stribeck curve [42] as shown in Figure 1.9. Z represents the lubricant viscosity, while N is the measure of sliding speed between surfaces, P being the applied load. In hydrodynamic lubrication the surfaces are separated by a fluid film which is thick in comparison to the asperity heights on the bearing surfaces. As ZN/P decreases fluid film between the two solid surfaces become thinner and at low values the two bodies begin to interact. The region where the load is shared between the lubricant film and solid surfaces is known as mixed lubrication and is characterized by sharp increase in the COF as ZN/P decreases. At sufficiently low value of ZN/P, COF value rises to a maximum, marking the boundary lubricated condition. In boundary lubrication condition the oil film thickness is too small to provide a film separation between the surfaces [43].

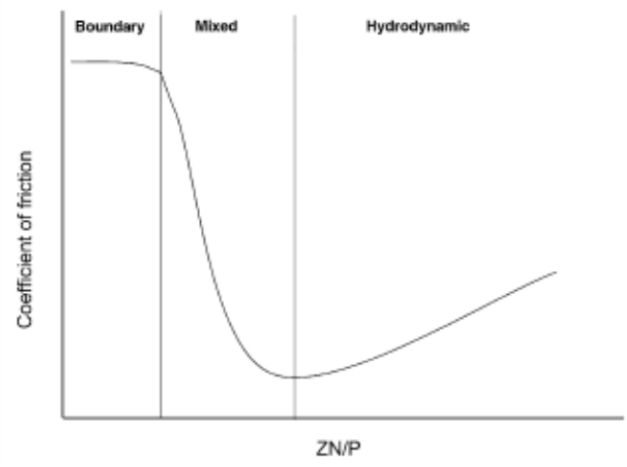

Figure 1.9. Stribeck curve showing three lubricated regimes:Boundary lubrication,Mixed lubricated and Hydrodynamic lubrication. Z=lubricant viscosity; N=sliding speed; P=applied load [42].

An automotive engine oil lubricant commonly contains hydrocarbon base oil and a mixture of various additives, incorporated for the purpose of minimizing friction and wear. Most of the sliding surfaces in an IC engine operate in a lubricated environment. Hydrodynamic lubrication in an automotive engine is achieved by the movement of the oil and dynamic viscosity as well as the tribolayers formed from to additives becomes critical.

1.4.3.1 Need for additives

Degradation of oil inside the internal combustion engine (IC engine) may be attributed to various factors [44]:

- Degradation by oxidation: The chemical components in the lubricant may react with oxygen in the engine to form oxides (often acidic oxides) to form sludge. This sludge formation may affect the heat transfer between the piston and cylinder and might also cause seizure of piston under extreme conditions. This problem can be solved by using antioxidants as additives in the base oil.

- Thermal degradation: Highly increased temperature conditions might lead to thermal breakdown of the oil. Use of synthetic oil might solve the problem.
- Corrosion: The oxidational by-products attack the internal parts of the engine and the bearing materials causing corrosion of these parts. Water present, due to condensation as a result of temperature and humidity changes, might also cause corrosion.

All the aforementioned problems may be addressed by use of additives which may chemically bond to the internal parts forming a sacrificial barrier, and/or neutralize the harmful by-products.

1.4.3.2 Mechanisms of ZDDP Degradation

The most effective class of antiwear, antioxidant and anticorrosive additive used in engine oil is Zincdialkyldithiophosphate (ZDDP). A simple representation (Figure 1.10) of the structural formula of ZDDP is as shown below although molecular nature of ZDDP is more complex [44]. Already established surface analysis techniques like X-ray photoelectron spectroscopy (XPS), infrared spectroscopy (IR), X-Ray absorption near edge (XANES) etc. have revealed the chemical composition of the surface films (between the two bodies in contact) as shown in Figure 1.11 [45]. The study of chemical composition is the key to understand the anitwear, anticorrosive properties of ZDDP.

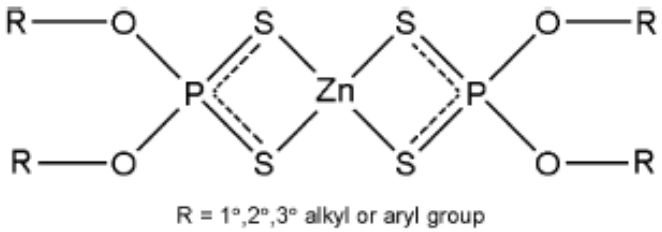

Figure 1.10. Structure of zinc dithiophosphate. The ‘R’ group indicates whether it’s an alkyl or an aromatic dithiophosphate [44].

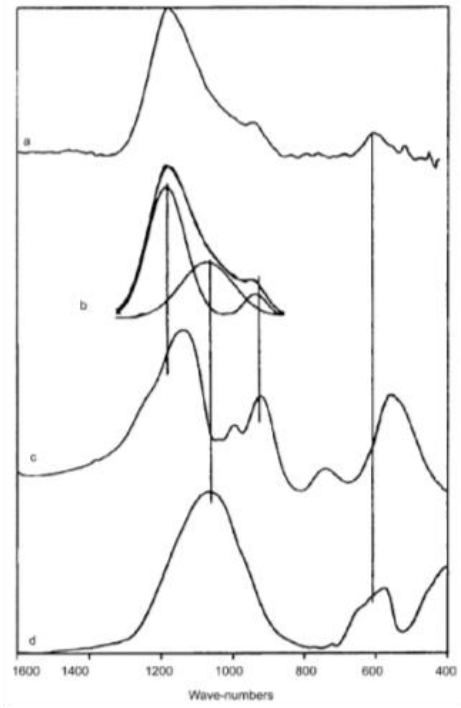

Figure 1.11. Infrared spectra for (a) tribologically derived ZDDP antiwear film; (b) a simulated spectrum of tribochemical film; (c) amorphous calcium pyrophosphate and (d) amorphous magnesium orthophosphate. [45].

Bancroft et al. [45] have found that ZDDP tribofilms, 5 μm across and 100 nm thick [46] formed on steel surfaces are chemically and mechanically stable. These films were composed of a mixture of long and short chains of polyphosphates, which were inter-grown with the metal oxide surface. This intergrowth provides strong attachment with the metal surface. It was further determined [47] that the layered short chain polyphosphates are present in the bulk whereas the layered longer-chain polyphosphates were present at the surface. The tribologically derived ZDDP antiwear film differs from their thermally derived counterparts with respect to the fact that the former has a layered structure while latter lacks the same despite possessing similar chemical composition. Also the tribofilms are formed at much lower temperatures than thermal films.

Various proposed mechanisms exist regarding the ZDDP antiwear, antioxidant and anticorrosive films formation on the steel surface. In solution ZDDP might undergo following reactions:

- Ligand exchange [48]: Labile dithiophosphate ligands can exchange the central metal cation (Zn in this case) with other divalent metal ion like Fe following Eqn.1.

$$((RO)_2\,PSS)_2Zn + M^{2+} \longrightarrow ((RO_2)PSS)_2M + Zn^{2+} \qquad (1)$$

Thus ligand exchange plays an important role in the antiwear property of ZDDP.

- Reaction with peroxides and hydroperoxides: Yin et al [30] developed a five step pathway for the decomposition of ZDDP on steel surface:

  i) ZDDP is absorbed onto the metal surface.

  ii) ZDDP in solution is converted to linkage isomer (LI).

  iii) Thermal oxidation of ZDDP by either peroxide (-O-O-) or hydroperoxide (O-O-H) leads to formation of long chain polyphosphates which are highly efficient oxidation inhibitors. Consequent hydrolysis of these long chain polyphosphates leads to the formation of short chain polyphosphates.

- Thermal degradation of ZDDP: In the absence of hydroperoxides/peroxy-radicals, and ligand exchange ZDDP reacts in a different way at high temperature (130-230ºC). The mechanism of thermal degradation is described as the exchange of alkyl groups between O and S in the ZDDP molecule finally leading to the formation of polyphosphates according to the following reactions [49]:

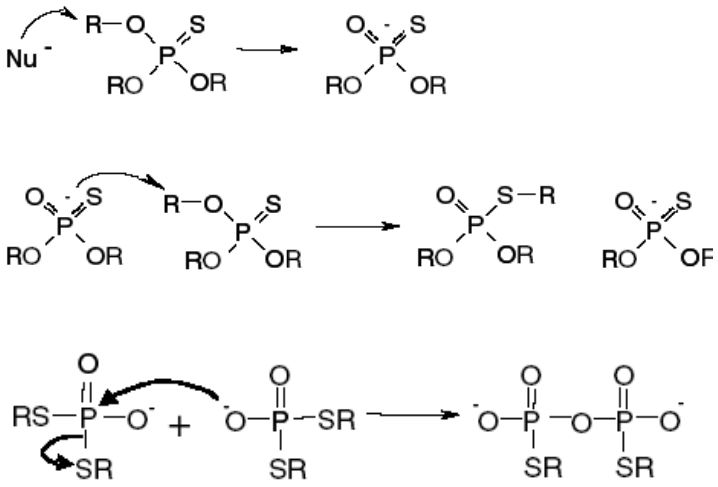

For steel surface, formation of protective and sacrificial glassy-polyphosphate film, as a result of breakdown of ZDDP, limits the contact between two rubbing surface. However, the exact mechanism resulting in formation of polyphosphates from degradation of ZDDP is yet to be determined. Some in situ analytical techniques along with vibrational and raman spectroscopy might be useful in this regard.

1.4.3.3 Action of ZDDP on Al Alloys

Tribochemical degradation of ZDDP during lubricated sliding of Al-Si alloys have led contradictory implications in the literature. Wan et al. [49] performed ball-on-block experiments on A2024 against AISI 52100 as counterface under lubricated conditions at room temperature. The authors observed that the COF do not change with increasing concentration of base oil. Moreover it was reported that although ZDDP reduces adhesive wear it produces chemical wear. Hence the authors concluded that addition of ZDDP in base stock is not beneficial in reducing wear and damage of aluminum alloys. As a reason they stated surface film produced by ZDDP is fragile and gets easily detached from the substrate and hence low concentration of phosphorus, sulphur and zinc is observed in the surface film. However, the authors have provided no supporting data for this observation. On the other hand, Fuller et al. [50] performed boundary

lubricated tests on Al alloys 6061 and A-390 with ZDDP oil blend as the lubricant at 60°C and 100°C and concluded that addition of ZDDP to the base stock results in improvement of wear performance. The authors reported that ZDDP tribofilms formed on the worn surfaces of the Al alloys consist of polyphosphate structure identical to those formed on steel. This protective film formation occurred only after extended period of rubbing. At 100°C severe wear occurs thus resulting in metal loss with insufficient tile for tribofilm formation. Nicholls et al. [51] reported similar results of tribofilm formation with identical composition as that of steel using XANES spectroscopy as shown in Figure. 1.12 [51]. Of the two alloys studied, Al 6061 and Al 319, the latter showed increased efficiency of beneficial surface formation probably because of the increased Si content providing platform for the surface film formation. While the above segment discusses the tribolayers formed as a result of degradation of ZDDP additive in engine oil, the counterface material, especially carbon based friction mitigating coatings also play a critical role in determining the tribolayer formation and composition.

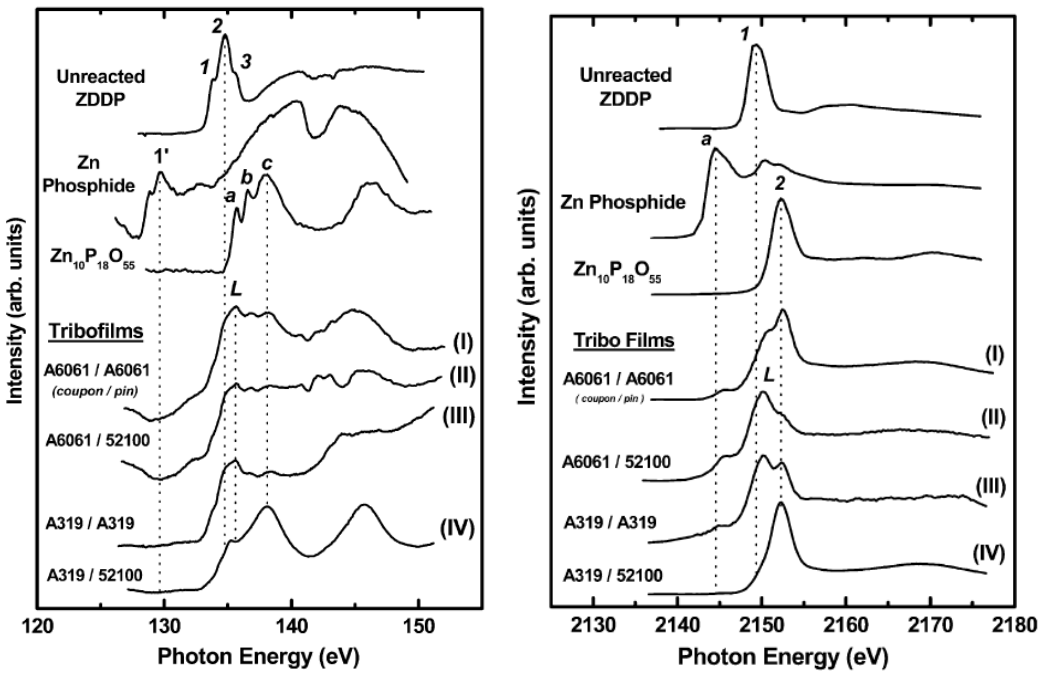

Figure 1.12. XANES spectra of model compounds and antiwear films formed on different Al-Si and steel couples. (a) P L-edge XANES spectra; (b) P K-edge XANES spectra [51].

1.4.4 Tribolayers Formed During Sliding against Diamond-like Carbon Coatings

Diamond-like carbon (DLC) coatings have consistently displayed low COF values when tested against lightweight aluminum, magnesium and titanium alloys. Several studies, involving tribological applications that used counterfaces coated with DLC—restricting material transfer from the surfaces of these alloys, have shown that DLC coatings minimized adhesion [52–55]. Thus, due to their low COF and adhesion mitigating properties, the DLC coatings provide significant opportunities for expanding the applications of lightweight materials by improving their performance in components operating under sliding contact conditions (e.g. powertrain elements in combustion engines).

1.4.4.1 Environmental Effects

A shortcoming of DLC coatings is the fact that their tribological properties are highly sensitive to the environmental conditions as their friction, wear, adhesion behaviour may change drastically with small changes in the composition of the gas or liquid atmospheres present in the tribosystem. The friction behaviour of the hydrogenated (a-C:H or H-DLC) and non-hydrogenated DLC (a-C or NH-DLC) coatings were found to exhibit almost opposite trends under vacuum and inert (i.e. N_2 or Ar) atmospheres. Among the studies conducted on ferrous materials, Erdemir [56] showed that H-DLC coatings tested in dry N_2 atmosphere against H-DLC coated H13 grade steel disks generated a COF of 0.005, while the NH-DLC produced a COF of 0.75. The very low COF value in case of H-DLC was attributed to termination of the dangling carbon bonds at the surface by the hydrogen atoms inhibiting the formation of carbides upon contact with the counterface. For aluminum alloys, Konca et al. [57] reported a high COF of 0.52 for NH-DLC against an Al-6.5% Si alloy, under vacuum (6.65×10^{-4} Pa). The same NH-DLC when tested in an ambient atmosphere (47% RH) produced a low COF of 0.16 (Figure

1.13). The COF of Al alloys were shown to decrease with increasing the moisture in the surrounding environment [58,59]. The decrease in COF of the NH-DLC coating in moist air was attributed to the passivation of the dangling carbon bonds by the OH groups dissociated from the water vapour in the atmosphere during the tribological contact. A first principles atomistic study [60] provided quantitative support for this mechanism, by showing that the dissociation of water to OH molecules at the interface is possible and the static work of separation between the OH–C (111)/OH–C(111) atoms is considerably lower than Al/non-passivated coating surface thus resulting in lower magnitudes of COF in case of OH passivated surfaces. An ab initio study [61] based on density-functional theory (DFT) and generalized gradient approximations (GGA) of two (2×1)-C(001) surfaces terminated by hydroxyl groups showed repulsive interactions (greater than termination due to H groups) which accounts for the low friction experimentally observed in [57].

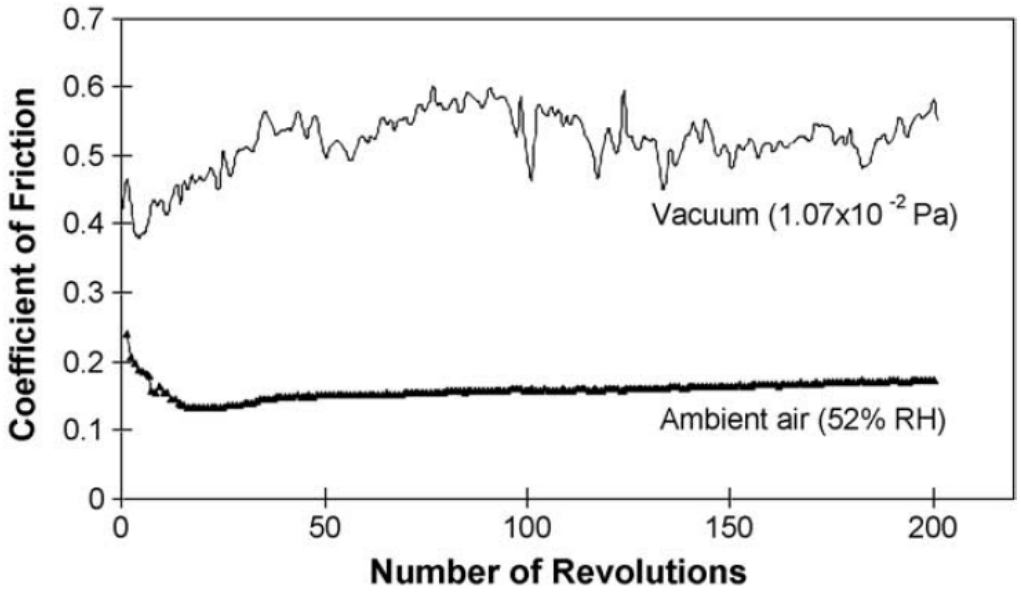

Figure 1.13. Effect of environment on friction of NH-DLC tested against Al-6.5% Si alloy in vacuum and in ambient air [57].

1.4.4.2 High Temperature Effects

As reviewed in the previous section, the COF of both H-DLC and NH-DLC coatings are sensitive to moisture which makes them unpredictable when used in conjunction with powertrain components [60,62]. It is also important to note that the low COFs of H- and NH-DLC can be maintained up to 200°C [63,64]. Thus an impediment to the wider application of DLC coatings in powertrain systems is their poor elevated-temperature friction performance. During sliding contact the interface temperatures at the cylinder-piston interface is usually around 150°C. Yet in other engine components the interface temperatures may easily exceed 300°C [65]. At 300 °C and above, sliding induced graphitization of DLC occurs, consistent with findings from other studies [66,67]. Prospective DLC coatings intended for these applications should, therefore be able to sustain low COF properties at elevated temperatures. Changes in the DLC coating hybridization [68] or carbon structure modified by W, Si and other elements have shown to promote high temperature and environmental stability [69–73].

Micromechanisms of friction and wear reduction observed in thermally stable ta-C and fluorinated ta-C (ta-C-F) with high sp^3 content tested against 319 Al have been studied [68]. In ta-C coatings the steady state COF decreased from 0.39 at 25 °C to 0.15 at 400 °C. Sliding-induced sp^2 transformation at the contact surface of ta-C contributed to the reduction of friction. The ta-C–F coatings showed further reduction in COF and wear rates due to the F incorporation in the transfer layers. Room temperature ball (WC)-on-disk (W-DLC) tests resulted in a a low COF of 0.10 of W-DLC due to the WC precipitates present on the coating surface as determined using XRD and X-ray photoelectron spectroscopy (XPS) studies [70]. Mechanical properties of

W-DLC coating were studied using transmission electron microscopy revealed the presence of nanocrystalline (nc) WC embedded in an amorphous carbon matrix of the coating. The WC-DLC system maintained a good compatibility between the mechanical properties (Hardness=15-20 GPa) and tribological properties (COF~0.2; wear rates 10-7-10-8 mm3/Nm). Voevodin et al. [73] observed that the COF of coatings with nanocrystalline (nc) WC embedded in a DLC matrix decreased from 0.70 to 0.30 as the carbon content of DLC increased from 30 at.% to 90 at.% when tested in an ambient air atmosphere (50% RH) at 25 °C. Raman analyses found evidence for the formation of tungsten oxide and the authors noted that the oxide layer led to self-lubrication of coatings. In a study on the tribological behaviour W-DLC tested against 319 Al counterface a similar low COF of 0.18 was observed at 400 ˚C [64] whereby the COF remained low (0.12) at 500 ˚C when tested against 319 Al counterface (Figure 1.14). Micro-Raman analyses indicated the formation of tungsten oxide rich layers both on the W-DLC surface and in the transfer layers on the 319 Al counterface. The formation of WO_3 on W-DLC surface was proposed to be responsible for the low COF. Si doped DLC coatings have also shown potential for high temperature stability. Papakonstantinou et al. [74] and Zhao et al. [75] showed, using Raman spectral analyses and XPS studies, that an increase in the Si percentage promoted the sp^3 bonding in the Si-DLC film. The Si-C sp^3 bond formation intensity increased as the Si percentage was increased (from 0 to 9 at.%) as established using XPS studies [75]. Hatada et al. [76] found that for a 24 at.% Si containing H-DLC film showed no change in film structure for annealing temperatures upto 650 °C while a Si-free DLC film underwent graphitization with increasing annealing temperatures as confirmed by micro-Raman spectroscopy. The authors [76] found that for a 13 at.% Si-H-DLC annealed at 450 ˚C when tested against WC ball at room temperature and 255 RH showed a low COF of 0.03 which was attributed to the formation of

SiO2 particles during annealing. Jantschner et al. [77] tested a:C-Si coating (upto 10 at.% of Si) against Al2O3 at 450 °C and observed a low COF of <0.05. The authors attributed the low COF at elevated temperatures to Si-O or Si-OH (thermally stable oxides) on the coating surface as determined using XPS analyses. High temperature tribological performance of a-C:H/a-Si:O (Si-O-H-DLC) coatings was evaluated against performed engine grade 319 Al showed a low friction value of 0.04 at 200 ˚C [78] where conventional NH-DLC and H-DLC coatings showed high COF (Figure 1.15). The COF of a-C:H/a-Si:O was only 0.11 at 400 ˚C. It was suggested that C and Si atoms in the coating surfaces and the transfer layers were passivated by H and OH molecules leading to low friction, a mechanism that persisted until 400 ˚C whereas the low wear of the coating up to 400 ˚C was attributed to the presence of Si preventing graphitization of the bulk coating by suppressing sp^2 bond formation as shown through Raman analyses.

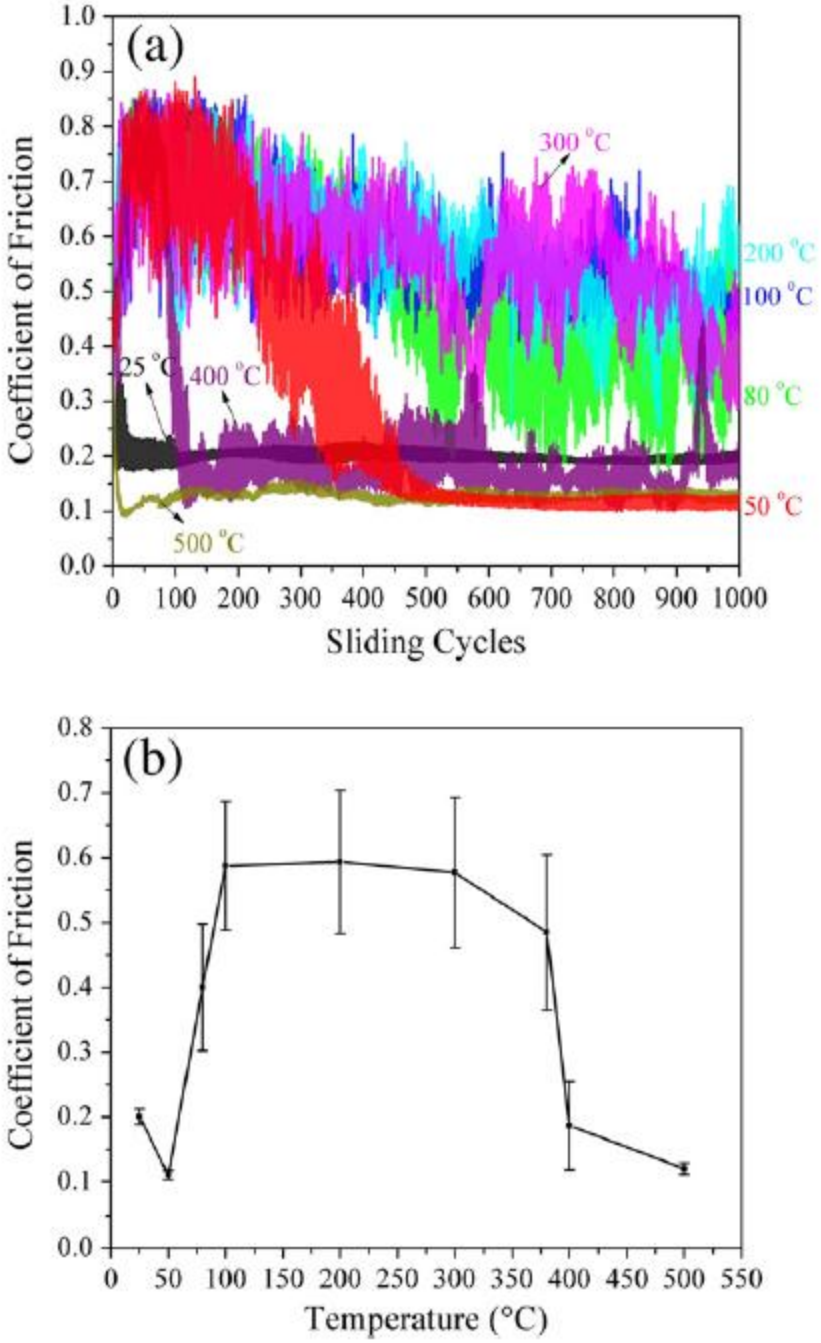

Figure 1.14. Variation of coefficient of friction of W-DLC tested against 319 Al at different temepratures [64].

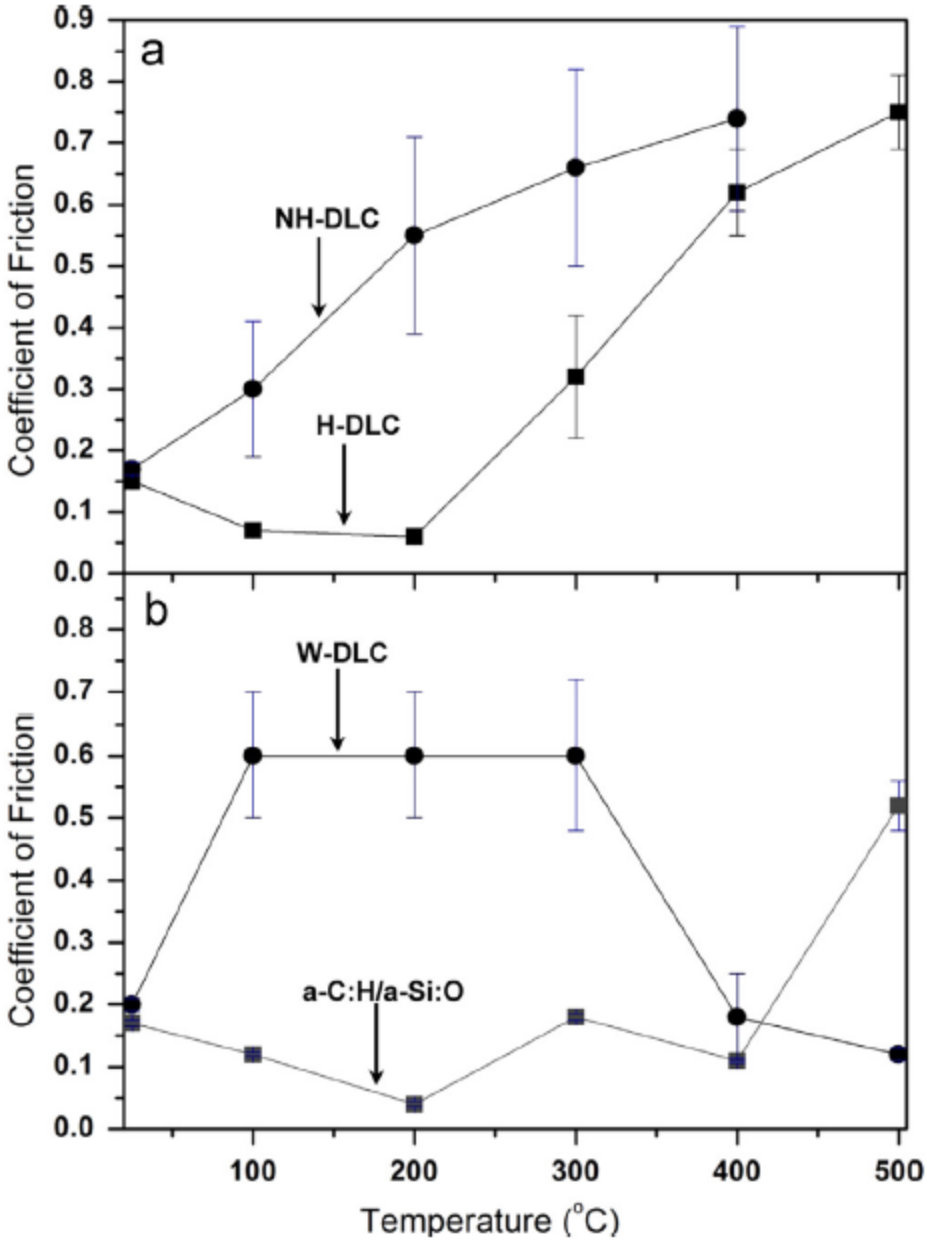

Figure 1.15. comparison of a-C:H/a-Si:O with other DLC coatings as a function of temeprature [78].

1.4.5 Tribolayers Formed During Sliding against Graphene

Solid lubricants such as graphite and MoS_2 may provide low friction due to their lamellar structure and have been studied in the literature [79–82]. Graphene, relatively new two-dimensional solid lubricant is also of interest for application involving sliding friction [83] but has a different friction reduction mechanism compared to graphite and MoS_2. Understanding friction behaviour of graphene in macro levels is essentially required in order to minimize energy losses in automotive, aerospace and micro-electromechanical industries. Graphene, a two-dimensional monolayer of sp^2 bonded carbon atoms [84], has consistently displayed low COF values when subjected to nano to micro-scale (normal applied load upto 200 nN) experiments [85–87]. It was generally observed, in case of tests using SiN, Si or diamond probes, that the friction force reduced sliding against a few-layered graphene compared to a single layer graphene. The lower friction of multi-layered graphene, MLG (≥ 4 layers), was generally attributed to an increased resistance to out-of-plane deformation or to a lower electron–phonon coupling effect. Cho et al. [88] found that substrate roughness affects the friction behaviour of MLG deposited on SiO_2 sliding against a diamond-like carbon (DLC) AFM tip under ambient conditions (25-50% RH). The authors found that ultra-flatness of both MLG and the substrate led to strong adhesion between them and resulted in low friction forces. Other studies, performed at a micro-scale, have looked into the improving the lubrication performances by adding graphene in oil or ethanol. Berman et al. [16] conducted tribological tests while the steel was sliding against steel and the tests set-up was suspended in ethanol with multilayer graphene flakes. It was shown that the COF decreased by 6 times compared to steel against steel in dry sliding conditions (Figure 1.16). The authors [89] also studied the effect of ethanol processed graphene layer on the friction behaviour of steel against steel in dry N_2 atmosphere. The authors observed

a very low COF of 0.15 when few drop of ethanol containing graphene were used during the sliding experiment compared to the COF of dry conditions. A possible explanation for the low friction behaviour was that graphene acted as a two-dimensional material, sheared easily at the sliding contact interface and, hence, provided low COF. Lin et al. [90] reported that a base oil containing 0.075 wt.% of graphene nano-sheets reduced the COF by 25% compared to the base oil without graphene sheet. Liu et al. [91] prepared composite coatings of diamond-like carbon/ionic liquid/graphene with different graphene concentrations and found that an optimum graphene concentration (0.075 mg ml^{-1}) in ionic liquid for the composite coating exhibited the lowest COF of 0.04 compared to the steel/ionic liquid/graphene (0.08).

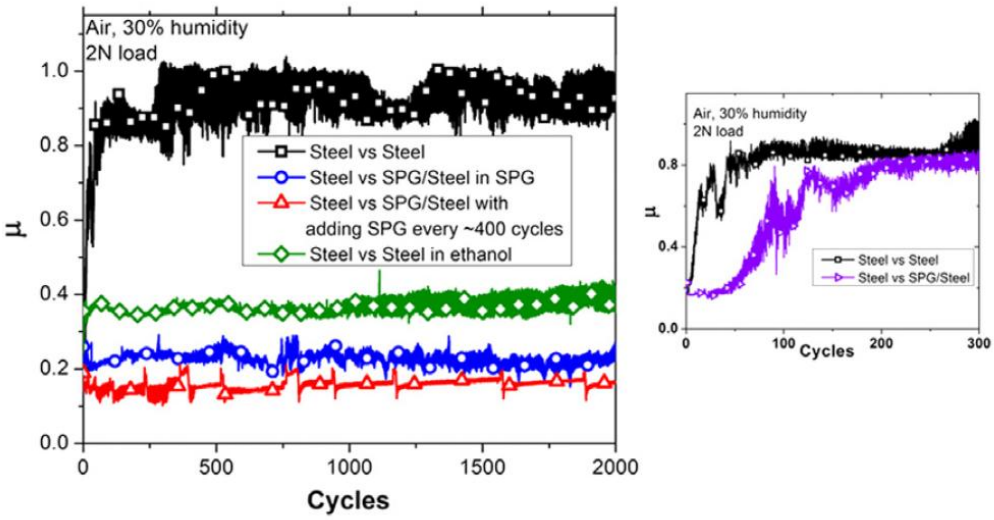

Figure 1.16. Friction of mechanically steel vs steel tests lubricated by exfoliated graphene processed in ethanol used under unlubricated sliding [16].

Study of friction behaviour of graphene dissolved in water or exposed to moisture is critical in delineating the structural changes that occur during sliding of graphene under humid

conditions. Song and Li [92] studied the friction of graphene oxide (GO) nanosheets in water based lubricants against SAE 52100 steel. It was proposed that the GO nanosheets reduced steel-on-steel friction and wear by forming a "thin tribolayer" on the counterface that prevented metallic contact. The role of atmospheric humidity as well as counterface material in determining the COF of multilayered graphene (MLG) was studied by Bhowmick et al. [93]. HR-TEM analyses was used to analyze the sliding-induced damage and interfacial material transfer processes that occur when multilayer graphene (MLG) is placed in contact with C- and N- based coatings and uncoated steel. the role of counterface materials on the friction of MLG has been elucidated. The authors found that formation of graphene transfer layers on the counterface was a necessary condition for low friction in tribosystems not involving carbonaceous counterfaces and this transfer layer formation did not occur for N- based coated counterfaces resulting in highest damage to MLG. A common feature of the worn MLG was the sliding induced defects which comprised of edge fracture, fragmented/bent graphene stacks compared to pristine graphene and disordered regions between them (Figure 1.17). When MLG was run against a C-based counterface, namely hydrogenated (40% H) diamond like carbon (H-DLC) coating low COF of 0.08 resulted without formation of transfer layers. Sliding induced defect activated H_2O (from moisture in air) dissociation and adsorption of H and OH at the defect sites were likely to be responsible for the low friction. First principles atomistic simulations have been used to delineate the passivation mechanisms of graphene. It was shown that a high activation energy barrier for H_2O dissociative adsorption on defect free graphene plane existed due to lack of preferential adsorption site, and only physisorption was possible [94,95]. In contrast, a mono-vacancy defect activated graphene provided preferential sites for adsorption resulting in a low energy barrier for H- and OH dissociation compared to that in defect free graphene [95]. Dispersion-augmented

density functional tight binding (DFTB-D) potential based studies [96,97] reported similar findings that exothermic reaction of H_2O on Stone Wales (SW) type vacancies in graphene was thermodynamically favourable and led to dissociative adsorption of water molecules. It can thus be expected that defects induced during sliding contact may facilitate passivation of the graphene layers, an effect that can be enhanced with increasing the humidity in the environment. From the above review it becomes clear that while the AFM based experiments observed that the friction of graphene would depend on the number of layers, the sliding contact experiments emphasized the importance of test atmosphere on friction and with the assistance of first-principles simulations the dissociation of water molecules in defect activated graphene layers emerged as an important mechanism of friction reduction. In this thesis, the effect of humidity on friction of graphene, run against a constant counterface will be demonstrated through sliding friction tests at varying RH levels and through subsequent microscopic and spectroscopic analyses.

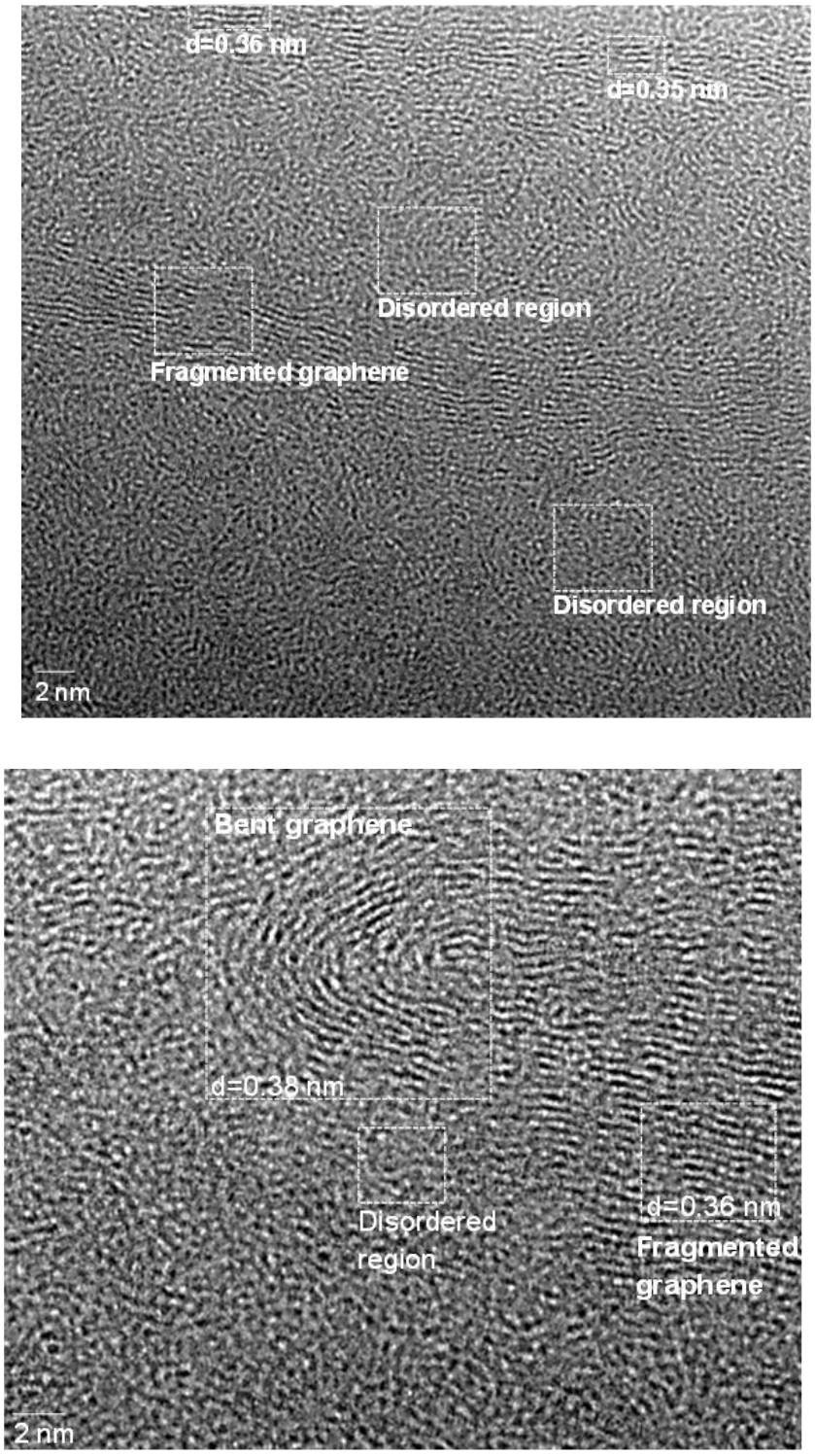

Figure 1.17. High resolution cross-sectional TEM (HR-TEM) images of worn surface of graphene run against H-DLC showing (a) fragmented graphene and (b) curved and bent graphene stacks [93].

1.5 Friction in Automotive Powertrain

A study of the tribological aspects of an IC engine powertrain involves a multi-disciplinary approach, including at the very least chemical, fluids, and mechanical engineering expertise in addition to materials science. Figure 1.18 shows the schematic representation of one cylinder from a typical overhead cam engine [65]. Components functioning within an IC engine operate under lubricated conditions with the lubricant film thickness separating the interacting component surfaces and may experience varied intensity of friction. Frictional interaction between cylinder block and the piston skirt forms a major part (25%) of the total engine friction [3]. Originally gray cast iron was used for automotive pistons but recently, due to high thermal conductivity piston materials are replaced by lightweight aluminum alloys. This has many advantages: lighter piston reduces total weight of the engine block which reduces engine vibration, high thermal conductivity of aluminum helps to prevent overheating of the piston top. The problem faced in using aluminum alloys is that owing to the higher thermal expansion coefficient than cast iron high clearance is required between the piston skirt and cylinder bore which might make the engine noisy at low temperatures. Solution to this problem lies in the use of copper and nickel based aluminum alloy (Al 336) which provides 13% lower thermal expansion coefficient than pure aluminum but still 70% more than cast iron. Another disadvantage of using Al alloys as piston skirt is the high friction between the piston skirt and the cast iron liners [98]. Solution to this problem lies in the use of polytetrafluoroethylene (PTFE) as a coating to reduce friction loss. Nickel-ceramic composite coating on aluminum alloys used as piston skirts may improve the friction behavior [99].

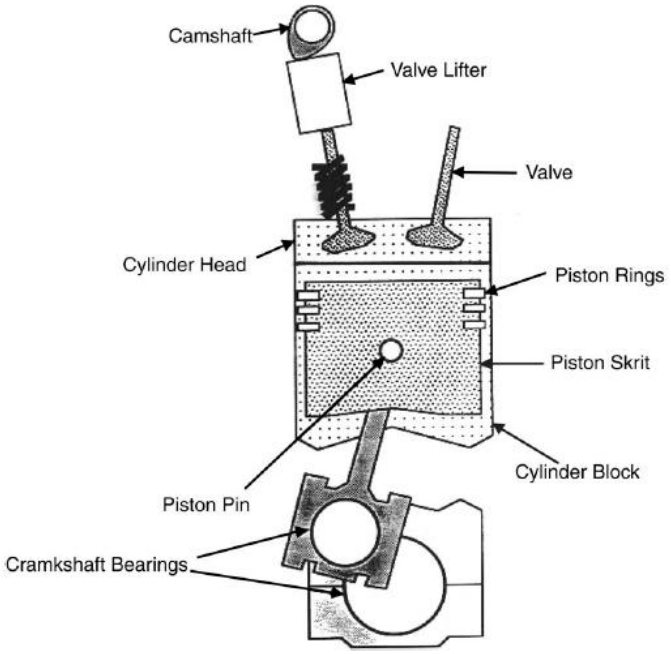

Figure 1.18. Schematic diagram of a basic overhead cam engine showing various engine parts:camshaft, valve-train, piston ring, piston skirt, cylinder block, crankshaft [65].

A piston ring fits into a groove on the outer diameter of the piston facilitating sealing of the combustion/expansion chamber and heat transfer from piston to cylinder wall. The interaction between the ring and the block accounts for almost 20% of the total engine mechanical friction [3]. For improving fuel economy efficiency cylinder blocks are being built with cast aluminum rather than the traditionally used cast iron. However, aluminum alloys do not possess sufficient wear resistance against gray cast iron rings except for Al-390 which, due to its high silicon content show sufficient wear resistance [100] and has been used as cylinder blocks. The upper compression ring is subjected to extremely high temperatures resulting in severe wear. As a remedy nitride cast iron liners coated with molybdenum by way of plasma spray process are used. More recently diamond like coatings (DLC) have become popular [56,67,101,102] as

piston ring coating providing improved engine reliability and friction properties by decreasing adhesion.

Traditionally gray cast iron and recently cast Al-Si alloys are used as cylinder bore materials. However, since hard silicon particles causes abrasion and increased wear cast iron cylinder liners are often used on aluminum alloy cylinder bores. For further reduction of weight linerless cylinders made of hypereutectic Al-Si alloys were used as cylinder bore materials [65]. Piston cylinder bore assemblies, running under lubricated conditions result in very little material removal, with the wear rate not exceeding a few nanometers per hour [103]. This feature qualifies engine wear to be classified as ultra-mild wear, since it is in every way different from the already established mild and severe wear. Extensive studies have been done on mild and severe wear of Al-Si alloys under dry conditions [43,104]. Wear of Al-Si alloys under lubricated conditions have also been studied and already discussed. The mechanisms involved in material loss in case of various wear regimes are different and hence a mechanistic approach in studying microstructural changes in case of ultra mild wear (UMW) should provide good insight into the behavior of engine wear. Ming et al. [105] investigated UMW mechanisms in eutectic Al-Si alloys (11-12% Si) tested against a 52100 hard steel counterface and observed the progression of damage. Prior to the wear tests the samples were etched (using 10% NaOH solution) so that the Si particles protrude out from the mean aluminum matrix height by 1.6-1.8 μm. The damage mechanism was studied and following sequence of events was proposed (Figure 1.19): Wear occurred under ultra mild conditions (0.5 N load, lubricated conditions) on the exposed silicon particles initially. As a result of Si particles bearing the entire load, they were embedded into the aluminum matrix (termed as sinking in). A decrease in Si particle height from initial 1.80 μm to 0.02 μm after 104 cycles in case of Al-12% Si whereas in Al-11% Si a lesser decrease in height

of Si particles was observed, from initial 1.60 μm to 0.87 μm after 10^5 cycles. Sinking in of the silicon particles leads to the plastic deformation of aluminum around the silicon particles eventually causing aluminum matrix pile up. Silicon particles adjacent to which pile up occurred were found to be fractured and fragmented into smaller fragments implying that the sinking-in and pile up process was accompanied by fragmentation of the Si particles with large aspect ratio into smaller sections. Wear of the elevated portions of aluminum plateaus by the counterface. Contact stress analysis using the Greenwood and Tripp model suggested that the applied normal pressure for Al-11% Si with higher matrix hardness (667 MPa) caused lesser surface damage (mean contact pressure 644.7 MPa less than matrix hardness) while for Al-12% Si, the mean contact pressure (665.4 MPa) being greater than the matrix hardness (392 MPa) the surface damage was greater leading to greater extent of silicon particle sinking in and aluminum matrix piling up (Figure 1.20) [103]. Thus this leads to a significant conclusion that higher matrix hardness delays the particle sinking in and consequent matrix pile up process.

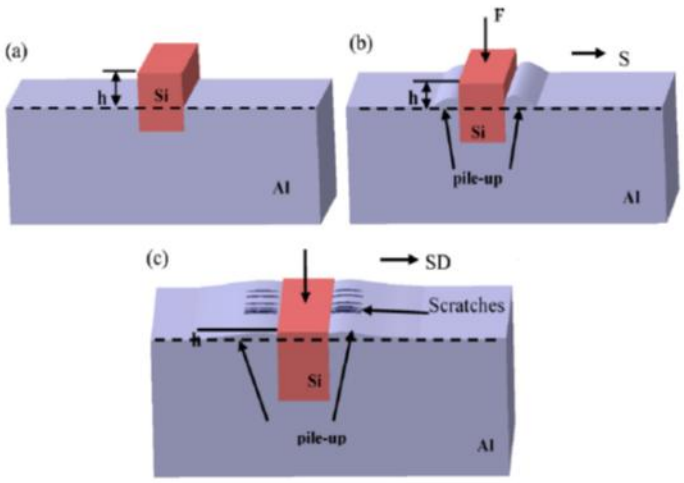

Figure 1.19. Schematic representation of UMW mechanisms in eutectic Al-Si alloy. (a)Exposure of Si particle above the Al-matrix; (b) Particle sink-in and AL-matrix pile up; (c) Micro scratch and damage on the elevated matrix [105].

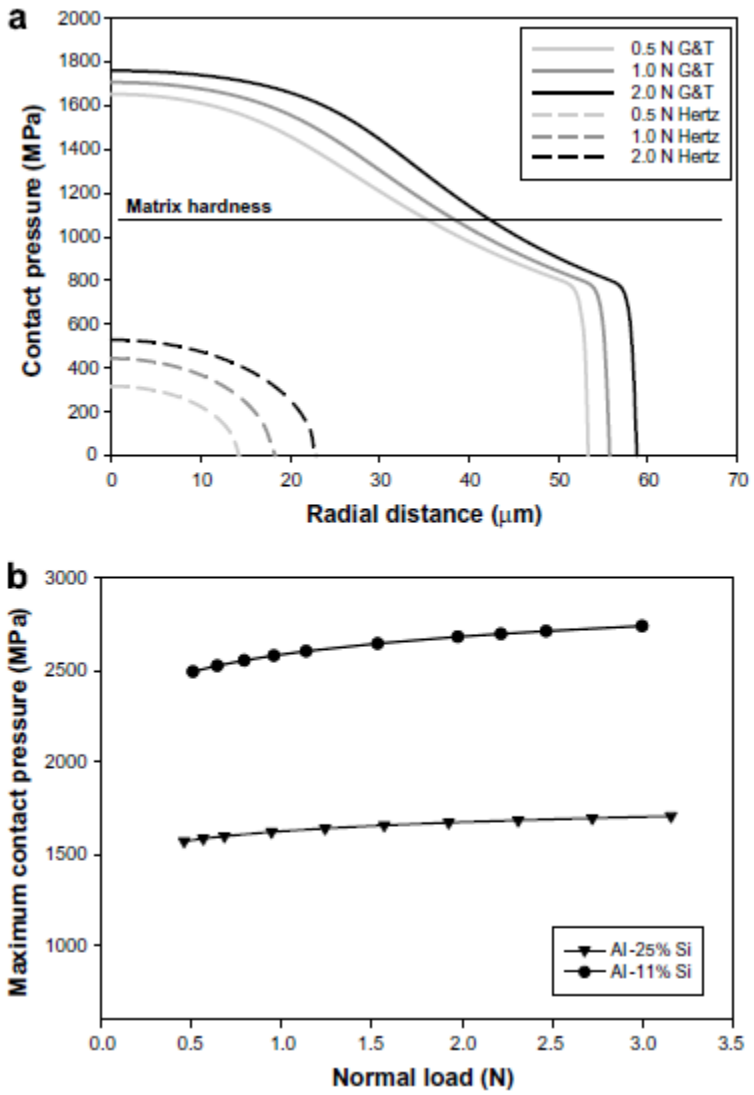

Figure 1.20. The calculated contact pressure distribution on the particles for Al–25% Si. The Hertzian contact pressure distribution is also shown; (b) variation of the maximum contact pressure applied on the particles in Al–25% Si and Al–11% Si with the applied load [103].

Ultra mild wear behavior of hypereutectic (Al-18.5% Si) was studied [100] with the objective of quantitative comparison of Al-12% Si and also to see whether the latter, with larger silicon particle size is effective in reducing wear induced damage under UMW conditions. When the etched hypereutectic alloy was subjected to UMW condition (0.5 N load and 50 mm/s sliding

velocity) it was observed that the wear damage on the exposed silicon particles was in the form of longitudinal surface scratches with virtually no effect on particle or matrix morphology. The matrix hardness (834 MPa) was sufficient to bear the maximum contact pressure of 715 MPa. The Si particle height decrease was much less than that observed in Al-12% Si. The important conclusion made from these observations is that Al-18.5% Si, owing to its microstructure, was more effective than Al-12% Si alloy, in maintaining a minimal surface damage. UMW was also observed during pin-on-disk tests performed on magnesium matrix composites designated as AM60–9% $(Al_2O_3)_f$ [106]. FIB and TEM analyses of the worn surfaces of AM60–9% $(Al_2O_3)_f$ tested at 100 °C indicated the formation of a tribolayer (oil-residue layer) that mitigated the damage to Mg matrix (Figure 1.21) tested for high sliding cycles making the AM6O-Al_2O_3 composites suitable for applications at these temperatures.

Scuffing is usually characterized by a dramatic friction increase and rapid rise in the temperature that accelerates lubricant degradation causing the scuffed surfaces to vibrate causing noise. Thus scuffing, mostly between piston ring and cylinder bore, is the most problematic type of engine damage. Scuffing in Al-Si alloys have been studied by performing wear tests on etched (with 10% NaOH) eutectic Al-Si alloys [107] at 5.0 N and 0.5 ms-1 show that scuffing resistance initially increased with etching time as the Si particles protected the matrix till a point beyond which etching lead to weakening of the particle-matrix interface. Also it was observed that the predominant mode fracture was from the root of the Si particles leading to scuffing. Larger number of second phase particle with smaller aspect ratio leads to greater scuffing resistance.

As the camshaft rotates the valve lifter reciprocates to open and close the valve. The friction loss between valve and the camshaft accounts for around 6% of the total engine mechanical friction [3]. Thus efficient selection of the cam materials and coatings can reduce

friction loss. Traditionally camshafts were made from gray cast iron because it's cheap and readily available. The use of carburized low-carbon steels has proven to be a good alternative. The failure mechanism at the cam-follower interface is greatly influenced by the regime of lubrication. The cam-follower interface is supposed to operate under continuous supply of engine oil but due to its location near the top of the engine it often operates without adequate lubrication and hence it is generally assumed that the cam-follower system operates in the boundary lubrication regime. Hence high wear rate may be expected owing to asperity contact. Thus use of iron based powder sintered metal with high chromium having good wear resistant properties for shim materials is recommended. Recently use of DLC coatings on the shims for automotive train application has shown improved frictional properties [108].

The crankshaft along with the connecting rods, converts reciprocating motion into rotating motion. The bearings used for transmission of load and sealing the crankshaft work under hydrodynamic condition where the minimum oil thickness (h_{min}) is calculated using Eqn.5. Under these conditions the shaft and the bearing is usually made of strong material to resist deformation but at the same time they must also be soft and compliant to prevent sticking of the shaft and bearing during idle periods. Usually the crankshaft is made of steel or nodular cast iron while recent engine bearings are made of aluminum-tin alloys providing strength.

From the above review it can be seen that the major energy loss due to friction occurs during the sliding interactions between the cylinder bore/liner and the piston ring at the top/bottom dead centres. In this thesis, the study undertaken would describe methods of minimizing friction by use of appropriate coatings, lubricant additives and lubricants.

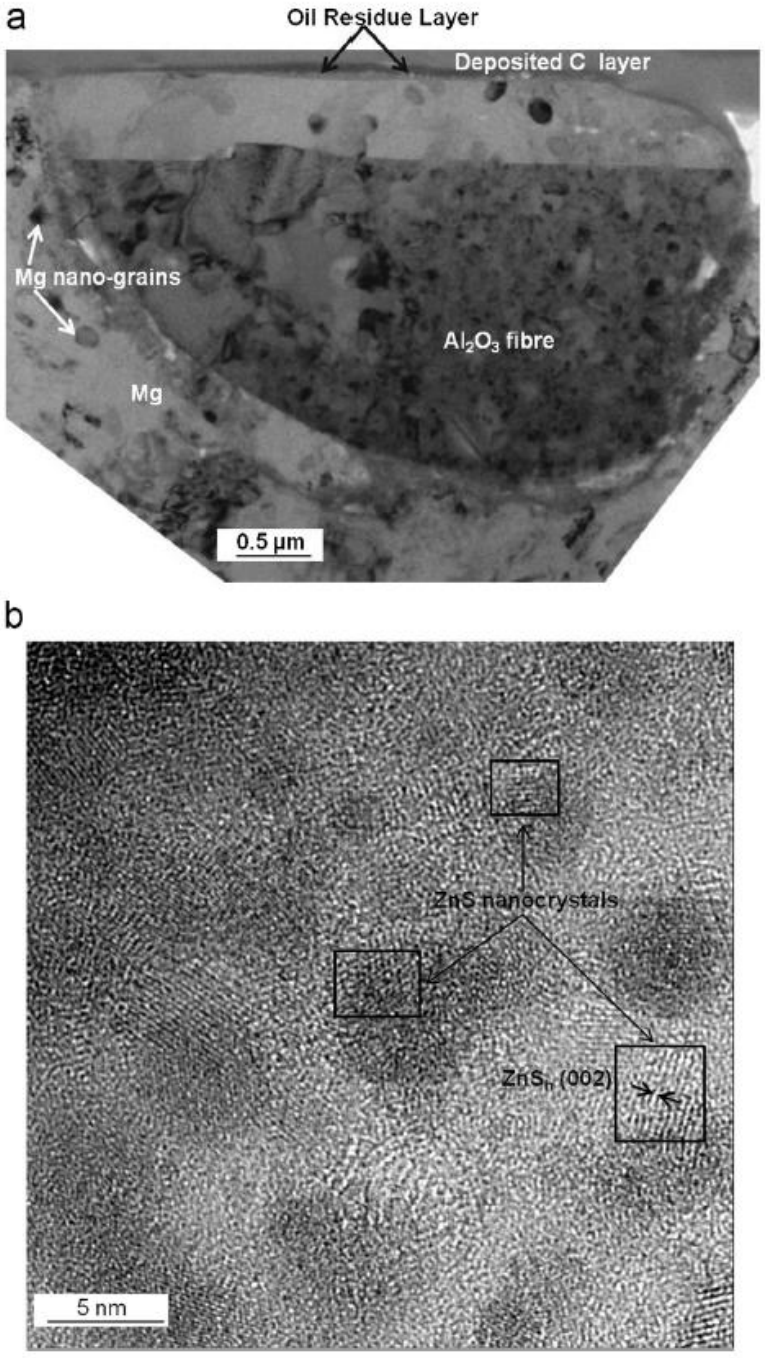

Figure 1.21. (a) Cross-sectional low magnification and (b) HR-TTEM image of the ORL formed on AM60-9%$(Al_2O_3)_f$ under the wear track tested at 1.0 N load and 100 °C [106].

Bibliography

[1] V. Karplus, S. Paltsev, Proposed vehicle fuel economy standards in the United States for 2017 to 2025: impacts on the economy, energy, and greenhouse gas emissions, Transp. Res. Rec. J. Transp. Res. Board. (2012) 132–139.

[2] T. Klier, J. Linn, New-vehicle characteristics and the cost of the Corporate Average Fuel Economy standard, RAND J. Econ. 43 (2012) 186–213.

[3] S.C. Tung, M.L. McMillan, Automotive tribology overview of current advances and challenges for the future, Tribol. Int. 37 (2004) 517–536.

[4] D.A. Green, R. Lewis, The effects of soot-contaminated engine oil on wear and friction: a review, Proc. Inst. Mech. Eng. Part D J. Automob. Eng. 222 (2008) 1669–1689.

[5] J.J. Truhan, J. Qu, P.J. Blau, A rig test to measure friction and wear of heavy duty diesel engine piston rings and cylinder liners using realistic lubricants, Tribol. Int. 38 (2005) 211–218.

[6] A.C. Hansen, Q. Zhang, P.W.L. Lyne, Ethanol–diesel fuel blends—a review, Bioresour. Technol. 96 (2005) 277–285.

[7] F. Yüksel, B. Yüksel, The use of ethanol–gasoline blend as a fuel in an SI engine, Renew. Energy. 29 (2004) 1181–1191.

[8] Y. Liu, A. Erdemir, E.I. Meletis, An investigation of the relationship between graphitization and frictional behavior of DLC coatings, Surf. Coatings Technol. 86 (1996) 564–568.

[9] C. Donnet, A. Erdemir, Tribology of diamond-like carbon films: fundamentals and applications, Springer Science & Business Media, 2007.

[10] F.G. Sen, X. Meng-Burany, M.J. Lukitsch, Y. Qi, A.T. Alpas, Low friction and environmentally stable diamond-like carbon (DLC) coatings incorporating silicon, oxygen and fluorine sliding against aluminum, Surf. Coatings Technol. 215 (2013) 340–349.

[11] D.A. Rigney, Transfer, mixing and associated chemical and mechanical processes during the sliding of ductile materials, Wear. 245 (2000) 1–9.

[12] Zinc dialkyl dithiophosphates, (1958).

[13] F.G. Rounds, Additive interactions and their effect on the performance of a zinc dialkyl dithiophosphate, Asle Trans. 21 (1978) 91–101.

[14] B. Kim, R. Mourhatch, P.B. Aswath, Properties of tribofilms formed with ashless dithiophosphate and zinc dialkyl dithiophosphate under extreme pressure conditions, Wear. 268 (2010) 579–591.

[15] D. Berman, S.A. Deshmukh, S.K.R.S. Sankaranarayanan, A. Erdemir, A. V. Sumant, Extraordinary Macroscale Wear Resistance of One Atom Thick Graphene Layer, Adv. Funct. Mater. 24 (2014) 6640–6646. doi:10.1002/adfm.201401755.

[16] D. Berman, A. Erdemir, A. V. Sumant, Few layer graphene to reduce wear and friction on sliding steel surfaces, Carbon N. Y. 54 (2013) 454–459. doi:10.1016/j.carbon.2012.11.061.

[17] P. Egberts, G.H. Han, X.Z. Liu, A.T.C. Johnson, R.W. Carpick, Frictional Behavior of Atomically Thin Islands Grown on Copper by Chemical Vapor Deposition, ACS Nano. 8 (2014) 5010–5021.

[18] K. Kim, H. Lee, C. Lee, S. Lee, H. Jang, J. Ahn, J. Kim, H. Lee, CVD – Grown Graphene : The Thinnest Solid Lubricant, Mater. Sci. (2011) 5107–5114. doi:10.1021/nn2011865.

[19] K.C. Ludema, DEFINITION OF FRICTION, CRC Handb. Lubr. Theory Pract. Tribol. Vol. II Theory Des. 2 (2010) 31.
[20] A.A. Pitenis, D. Dowson, W.G. Sawyer, Leonardo da Vinci's Friction experiments: an old story acknowledged and repeated, Tribol. Lett. 56 (2014) 509–515.
[21] E. Rabinowicz, Stick and slip, Sci. Am. 194 (1956) 109–118.
[22] J. Krim, Surface science and the atomic-scale origins of friction: what once was old is new again, Surf. Sci. 500 (2002) 741–758.
[23] M.A. Chowdhury, M.K. Khalil, D.M. Nuruzzaman, M.L. Rahaman, The effect of sliding speed and normal load on friction and wear property of aluminum, Int. J. Mech. Mechatron. Eng. 11 (2011) 53–57.
[24] H. Goto, D.H. Buckley, The influence of water vapour in air on the friction behaviour of pure metals during fretting, Tribol. Int. 18 (1985) 237–245.
[25] J.K. Lancaster, A review of the influence of environmental humidity and water on friction, lubrication and wear, Tribol. Int. 23 (1990) 371–389.
[26] W.Y.H. Liew, Effect of relative humidity on the unlubricated wear of metals, Wear. 260 (2006) 720–727.
[27] G. Bregliozzi, S.-U. Ahmed, A. Di Schino, J.M. Kenny, H. Haefke, Friction and wear behavior of austenitic stainless steel: influence of atmospheric humidity, load range, and grain size, Tribol. Lett. 17 (2004) 697–704.
[28] P. De Baets, G. Kalacska, K. Strijckmans, F. Van de Velde, A.P. Van Peteghem, Experimental study by means of thin layer activation of the humidity influence on the fretting wear of steel surfaces, Wear. 216 (1998) 131–137.
[29] A. ASTM, Standard Terminology Relating to Wear and Erosion, G40. (2013).
[30] J.F. Archard, W. Hirst, The wear of metals under unlubricated conditions, in: Proc. R. Soc. London A Math. Phys. Eng. Sci., The Royal Society, 1956: pp. 397–410.
[31] S.C. Lim, M.F. Ashby, Overview no. 55 wear-mechanism maps, Acta Metall. 35 (1987) 1–24.
[32] Y. Liu, R. Asthana, P. Rohatgi, A map for wear mechanisms in aluminium alloys, J. Mater. Sci. 26 (1991) 99–102.
[33] B.K. Yen, T. Ishihara, Effect of humidity on friction and wear of Al□ Si eutectic alloy and Al□ Si alloy-graphite composites, Wear. 198 (1996) 169–175.
[34] M. Elmadagli, A.T. Alpas, Sliding wear of an Al–18.5 wt.% Si alloy tested in an argon atmosphere and against DLC coated counterfaces, Wear. 261 (2006) 823–834.
[35] M. Roy, A. Pauschitz, J. Wernisch, F. Franek, Effect of mating surface on the high temperature wear of 253 MA alloy, Mater. Corros. 55 (2004) 259–273.
[36] M. Varga, H. Rojacz, H. Winkelmann, H. Mayer, E. Badisch, Wear reducing effects and temperature dependence of tribolayer formation in harsh environment, Tribol. Int. 65 (2013) 190–199.
[37] W. Hirst, J.K. Lancaster, Surface film formation and metallic wear, J. Appl. Phys. 27 (1956) 1057–1065.
[38] X.Y. Li, K.N. Tandon, Mechanical mixing induced by sliding wear of an Al–Si alloy against M2 steel, Wear. 225 (1999) 640–648.
[39] X.Y. Li, K.N. Tandon, Microstructural characterization of mechanically mixed layer and wear debris in sliding wear of an Al alloy and an Al based composite, Wear. 245 (2000) 148–161.
[40] A.R. Riahi, A.T. Alpas, The role of tribo-layers on the sliding wear behavior of graphitic

aluminum matrix composites, Wear. 251 (2001) 1396–1407.
[41] M. Elmadagli, A.T. Alpas, Progression of wear in the mild wear regime of an Al-18.5% Si (A390) alloy, Wear. 261 (2006) 367–381.
[42] J.A. Schey, Tribology in metalworking: friction, lubrication, and wear, (1984).
[43] I.M. Hutchings, P. Shipway, Tribology: friction and wear of engineering materials, (1992).
[44] M.A. Nicholls, T. Do, P.R. Norton, M. Kasrai, G.M. Bancroft, Review of the lubrication of metallic surfaces by zinc dialkyl-dithiophosphates, Tribol. Int. 38 (2005) 15–39.
[45] G.M. Bancroft, M. Kasrai, M. Fuller, Z. Yin, K. Fyfe, K.H. Tan, Mechanisms of tribochemical film formation: stabilityof tribo-and thermally-generated ZDDP films, Tribol. Lett. 3 (1997) 47–51.
[46] M.L. Suominen Fuller, L. Rodriguez Fernandez, G.R. Massoumi, W.N. Lennard, M. Kasrai, G.M. Bancroft, The use of X-ray absorption spectroscopy for monitoring the thickness of antiwear films from ZDDP, Tribol. Lett. 8 (2000) 187–192.
[47] Z. Yin, M. Kasrai, M. Fuller, G.M. Bancroft, K. Fyfe, K.H. Tan, Application of soft X-ray absorption spectroscopy in chemical characterization of antiwear films generated by ZDDP Part I: the effects of physical parameters, Wear. 202 (1997) 172–191.
[48] H. Spikes, The history and mechanisms of ZDDP, Tribol. Lett. 17 (2004) 469–489.
[49] Y. Wan, L. Cao, Q. Xue, Friction and wear characteristics of ZDDP in the sliding of steel against aluminum alloy, Tribol. Int. 30 (1997) 767–772.
[50] M. Fuller, M. Kasraia, J.S. Sheasby, G.M. Bancroft, K. Fyfe, K.H. Tan, X-ray absorption spectroscopy of antiwear films on aluminum alloys generated from zinc dialkyldithiophosphate, Tribol. Lett. 1 (1995) 367–378.
[51] M.A. Nicholls, P.R. Norton, G.M. Bancroft, M. Kasrai, X-ray absorption spectroscopy of tribofilms produced from zinc dialkyl dithiophosphates on Al–Si alloys, Wear. 257 (2004) 311–328.
[52] J. Robertson, Diamond-like amorphous carbon, Mater. Sci. Eng. R Reports. 37 (2002) 129–281. doi:10.1016/S0927-796X(02)00005-0.
[53] T. Yokota, T. Sawa, M. Yokouchi, K. Tozawa, M. Anzai, T. Aizawa, Frictional properties of diamond-like carbon coated tool in dry intermittent machining of aluminum alloy 5052, Precis. Eng. 38 (2014) 365–370. doi:10.1016/j.precisioneng.2013.11.007.
[54] S. Bhowmick, M.J. Lukitsch, A.T. Alpas, Tapping of Al-Si alloys with diamond-like carbon coated tools and minimum quantity lubrication, J. Mater. Process. Technol. 210 (2010) 2142–2153. doi:10.1016/j.jmatprotec.2010.07.032.
[55] S. Bhowmick, A. Banerji, A.T. Alpas, Tribological behavior of Al–6.5%,–12%,–18.5% Si alloys during machining using CVD diamond and DLC coated tools, Surf. Coatings Technol. 284 (2015) 353–364.
[56] A. Erdemir, The role of hydrogen in tribological properties of diamond-like carbon films, Surf. Coatings Technol. 146 (2001) 292–297.
[57] E. Konca, Y.-T. Cheng, A.M. Weiner, J.M. Dasch, A.T. Alpas, Vacuum tribological behavior of the non-hydrogenated diamond-like carbon coatings against aluminum: effect of running-in in ambient air, Wear. 259 (2005) 795–799.
[58] E. Konca, Y.-T. Cheng, A.T. Alpas, Sliding wear of non-hydrogenated diamond-like carbon coatings against magnesium, Surf. Coatings Technol. 201 (2006) 4352–4356.
[59] X. Meng-Burany, A.T. Alpas, FIB and TEM studies of damage mechanisms in DLC coatings sliding against aluminum, Thin Solid Films. 516 (2007) 325–335.

[60] Y. Qi, E. Konca, A.T. Alpas, Atmospheric effects on the adhesion and friction between non-hydrogenated diamond-like carbon (DLC) coating and aluminum–A first principles investigation, Surf. Sci. 600 (2006) 2955–2965.
[61] G. Zilibotti, M.C. Righi, M. Ferrario, Ab initio study on the surface chemistry and nanotribological properties of passivated diamond surfaces, Phys. Rev. B. 79 (2009) 75420.
[62] E. Konca, Y.-T. Cheng, A.M. Weiner, J.M. Dasch, A.T. Alpas, Effect of test atmosphere on the tribological behaviour of the non-hydrogenated diamond-like carbon coatings against 319 aluminum alloy and tungsten carbide, Surf. Coatings Technol. 200 (2005) 1783–1791.
[63] E. Konca, Y.-T. Cheng, A.M. Weiner, J.M. Dasch, A.T. Alpas, Elevated temperature tribological behavior of non-hydrogenated diamond-like carbon coatings against 319 aluminum alloy, Surf. Coatings Technol. 200 (2006) 3996–4005.
[64] A.A. Gharam, M.J. Lukitsch, M.P. Balogh, N. Irish, A.T. Alpas, High temperature tribological behavior of W-DLC against aluminum, Surf. Coatings Technol. 206 (2011) 1905–1912.
[65] E.P. Becker, Trends in tribological materials and engine technology, Tribol. Int. 37 (2004) 569–575.
[66] A.A. Gharam, M.J. Lukitsch, M.P. Balogh, A.T. Alpas, High temperature tribological behaviour of carbon based (B 4 C and DLC) coatings in sliding contact with aluminum, Thin Solid Films. 519 (2010) 1611–1617.
[67] A. Grill, Tribology of diamondlike carbon and related materials: an updated review, Surf. Coatings Technol. 94 (1997) 507–513.
[68] S. Bhowmick, A. Banerji, M.Z.U. Khan, M.J. Lukitsch, A.T. Alpas, High temperature tribological behavior of tetrahedral amorphous carbon (ta-C) and fluorinated ta-C coatings against aluminum alloys, Surf. Coatings Technol. 284 (2015) 14–25.
[69] M.-C. Chiu, W.-P. Hsieh, W.-Y. Ho, D.-Y. Wang, F.-S. Shieu, Thermal stability of Cr-doped diamond-like carbon films synthesized by cathodic arc evaporation, Thin Solid Films. 476 (2005) 258–263.
[70] K. Baba, R. Hatada, Deposition and characterization of Ti-and W-containing diamond-like carbon films by plasma source ion implantation, Surf. Coatings Technol. 169 (2003) 287–290.
[71] W.J. Meng, B.A. Gillispie, Mechanical properties of Ti-containing and W-containing diamond-like carbon coatings, J. Appl. Phys. 84 (1998) 4314–4321.
[72] J.C. Sánchez-López, D. Martínez-Martínez, M.D. Abad, A. Fernández, Metal carbide/amorphous C-based nanocomposite coatings for tribological applications, Surf. Coatings Technol. 204 (2009) 947–954.
[73] A.A. Voevodin, J.P. O'neill, J.S. Zabinski, Tribological performance and tribochemistry of nanocrystalline WC/amorphous diamond-like carbon composites, Thin Solid Films. 342 (1999) 194–200.
[74] P. Papakonstantinou, J.F. Zhao, P. Lemoine, E.T. McAdams, J.A. McLaughlin, The effects of Si incorporation on the electrochemical and nanomechanical properties of DLC thin films, Diam. Relat. Mater. 11 (2002) 1074–1080.
[75] J.F. Zhao, P. Lemoine, Z.H. Liu, J.P. Quinn, J.A. McLaughlin, The effects of Si incorporation on the microstructure and nanomechanical properties of DLC thin films, J. Phys. Condens. Matter. 12 (2000) 9201.

[76] R. Hatada, S. Flege, K. Baba, W. Ensinger, H.-J. Kleebe, I. Sethmann, S. Lauterbach, Temperature dependent properties of silicon containing diamondlike carbon films prepared by plasma source ion implantation, J. Appl. Phys. 107 (2010) 83307.
[77] O. Jantschner, S.K. Field, D. Music, V.L. Terziyska, J.M. Schneider, F. Munnik, K. Zorn, C. Mitterer, Sputtered Si-containing low-friction carbon coatings for elevated temperatures, Tribol. Int. 77 (2014) 15–23.
[78] S. Bhowmick, A. Banerji, M.J. Lukitsch, A.T. Alpas, The high temperature tribological behavior of Si, O containing hydrogenated diamond-like carbon (aC: H/a-Si: O) coating against an aluminum alloy, Wear. 330 (2015) 261–271.
[79] M. Dienwiebel, G.S. Verhoeven, N. Pradeep, J.W.M. Frenken, J.A. Heimberg, H.W. Zandbergen, Superlubricity of graphite, Phys. Rev. Lett. 92 (2004) 126101.
[80] B.K. Yen, B.E. Schwickert, M.F. Toney, Origin of low-friction behavior in graphite investigated by surface x-ray diffraction, Appl. Phys. Lett. 84 (2004) 4702–4704.
[81] M. Chhowalla, G.A.J. Amaratunga, Thin films of fullerene-like MoS2 nanoparticles with ultra-low friction and wear, Nature. 407 (2000) 164–167.
[82] T. Spalvins, Morphological and frictional behavior of sputtered MoS2 films, Thin Solid Films. 96 (1982) 17–24.
[83] J.S. Choi, J.-S. Kim, I.-S. Byun, D.H. Lee, M.J. Lee, B.H. Park, C. Lee, D. Yoon, H. Cheong, K.H. Lee, Friction anisotropy–driven domain imaging on exfoliated monolayer graphene, Science (80-.). 333 (2011) 607–610.
[84] A.K. Geim, K.S. Novoselov, The rise of graphene, Nat. Mater. 6 (2007) 183–191.
[85] T. Filleter, J.L. McChesney, A. Bostwick, E. Rotenberg, K. V Emtsev, T. Seyller, K. Horn, R. Bennewitz, Friction and dissipation in epitaxial graphene films, Phys. Rev. Lett. 102 (2009) 86102.
[86] C. Lee, Q. Li, W. Kalb, X.-Z. Liu, H. Berger, R.W. Carpick, J. Hone, Frictional characteristics of atomically thin sheets, Science (80-.). 328 (2010) 76–80.
[87] D. Marchetto, C. Held, F. Hausen, F. Wählisch, M. Dienwiebel, R. Bennewitz, Friction and wear on single-layer epitaxial graphene in multi-asperity contacts, Tribol. Lett. 48 (2012) 77–82.
[88] D.-H. Cho, L. Wang, J.-S. Kim, G.-H. Lee, E.S. Kim, S. Lee, S.Y. Lee, J. Hone, C. Lee, Effect of surface morphology on friction of graphene on various substrates, Nanoscale. 5 (2013) 3063–3069.
[89] D. Berman, A. Erdemir, A. V Sumant, Reduced wear and friction enabled by graphene layers on sliding steel surfaces in dry nitrogen, Carbon N. Y. 59 (2013) 167–175.
[90] J. Lin, L. Wang, G. Chen, Modification of graphene platelets and their tribological properties as a lubricant additive, Tribol. Lett. 41 (2011) 209–215.
[91] X. Liu, J. Pu, L. Wang, Q. Xue, Novel DLC/ionic liquid/graphene nanocomposite coatings towards high-vacuum related space applications, J. Mater. Chem. A. Mater. Energy Sustain. 1 (2013) 3797–3809.
[92] H.-J. Song, N. Li, Frictional behavior of oxide graphene nanosheets as water-base lubricant additive, Appl. Phys. A Mater. Sci. Process. 105 (2011) 827–832.
[93] S. Bhowmick, A. Banerji, A.T. Alpas, Friction reduction mechanisms in multilayer graphene sliding against hydrogenated diamond-like carbon, Carbon N. Y. 109 (2016) 795–804.
[94] P. Cabrera-Sanfelix, G.R. Darling, Dissociative adsorption of water at vacancy defects in graphite, J. Phys. Chem. C. 111 (2007) 18258–18263.

[95] P.C. Sanfelix, S. Holloway, K.W. Kolasinski, G.R. Darling, The structure of water on the (0001) surface of graphite, Surf. Sci. 532 (2003) 166–172.
[96] S.C. Xu, S. Irle, D.G. Musaev, M.C. Lin, Quantum chemical study of the dissociative adsorption of OH and H2O on pristine and defective graphite (0001) surfaces: reaction mechanisms and kinetics, J. Phys. Chem. C. 111 (2007) 1355–1365.
[97] M.K. Kostov, E.E. Santiso, A.M. George, K.E. Gubbins, M.B. Nardelli, Dissociation of water on defective carbon substrates, Phys. Rev. Lett. 95 (2005) 136105.
[98] A. Neville, A. Morina, T. Haque, M. Voong, Compatibility between tribological surfaces and lubricant additives—how friction and wear reduction can be controlled by surface/lube synergies, Tribol. Int. 40 (2007) 1680–1695.
[99] M. Priest, C.M. Taylor, Automobile engine tribology—approaching the surface, Wear. 241 (2000) 193–203.
[100] M. Chen, A.T. Alpas, Ultra-mild wear of a hypereutectic Al–18.5 wt.% Si alloy, Wear. 265 (2008) 186–195.
[101] S. Bhowmick, A. Banerji, A.T. Alpas, Tribological behavior and machining performance of non-hydrogenated diamond-like carbon coating tested against Ti–6Al–4V: Effect of surface passivation by ethanol, Surf. Coatings Technol. 260 (2014) 290–302.
[102] S. Bhowmick, F.G. Sen, A. Banerji, A.T. Alpas, Friction and adhesion of fluorine containing hydrophobic hydrogenated diamond-like carbon (FH-DLC) coating against magnesium alloy AZ91, Surf. Coatings Technol. 267 (2015) 21–31.
[103] M. Chen, X. Meng-Burany, T.A. Perry, A.T. Alpas, Micromechanisms and mechanics of ultra-mild wear in Al–Si alloys, Acta Mater. 56 (2008) 5605–5616.
[104] M. Elmadagli, T. Perry, A.T. Alpas, A parametric study of the relationship between microstructure and wear resistance of Al–Si alloys, Wear. 262 (2007) 79–92.
[105] M. Chen, T. Perry, A.T. Alpas, Ultra-mild wear in eutectic Al–Si alloys, Wear. 263 (2007) 552–561.
[106] A. Banerji, H. Hu, A.T. Alpas, Sliding wear mechanisms of magnesium composites AM60 reinforced with Al 2 O 3 fibres under ultra-mild wear conditions, Wear. 301 (2013) 626–635.
[107] A.R. Riahi, T. Perry, A.T. Alpas, Scuffing resistances of Al–Si alloys: effects of etching condition, surface roughness and particle morphology, Mater. Sci. Eng. A. 343 (2003) 76–81.
[108] S. V Johnston, S. V Hainsworth, Effect of DLC coatings on wear in automotive applications, Surf. Eng. 21 (2005) 67–71.

CHAPTER 2

Friction Reduction Mechanisms in Cast Iron Sliding against DLC: Effects of Biofuel (E85) Diluted Engine Oil

2.1. Introduction

Sliding friction occurring during cylinder bore (liner)-piston ring interaction is a source of energy loss in internal combustion (IC) engines [1]. Traditionally, cylinder walls or liners are made of grey cast iron (CI) [2]. Buckley [3] performed tested CI against AISI 52100 steel counterfaces at 0.5 N load to investigate their wear and friction behaviour by altering their carbon content of cast iron. A direct relationship was found between carbon content and decreasing wear. Friction values were sensitive to the relative humidity (RH) of the system. On increasing the relative humidity from 0% RH (Ar atmosphere) to 50% RH the COF reduced from 0.2 to 0.1. Unlubricated sliding in ambient conditions led to CI contact surfaces being covered with smeared graphite film and was responsible for the self-lubricating behaviour of cast [3,4]. Terheci et al [5] performed unlubricated pin-on-disk tests on self-mated grey cast iron sliding pairs and found that under ambient conditions a low coefficient of friction (COF) between 0.33-0.37 was maintained on increasing the load from 2.0 N to 10.0 N. Riahi and Alpas [6] constructed a wear map for grey cast iron for unlubricated sliding (under ambient air conditions) against AISI 52100 type steel. Three main wear regimes were identified consisting of severe, mild and ultra-mild wear, as the load and speed were reduced. In the ultra-mild wear (UMW) regime (< 1.0 N, 1.0 m/s) low wear rates (10^{-6} - 10^{-7} mm^3/m) were recorded with continuous iron oxide layers formed on both the steel counterface and the cast iron sample preventing direct metallic contact. In the UMW regime no plastic deformation at the contact surfaces was detected. At higher loads and high sliding velocities, mild wear regime was observed characterized by

discontinuous oxide layers and oxide debris formation. Another notable feature in the mild wear regime was the formation of the rosette type graphite flake morphology in the near surface region and fracture of these flakes and the matrix generating large-size debris. The transition from mild to severe wear occurred due to the local welding of the large-size cast iron debris that transferred to the counterface. The transferred material was found to be harder than the pristine cast iron which attributed to martensitic hardening. Thus, the above unlubricated sliding experiments show that friction of cast iron is sensitive to the test atmosphere whereas wear behaviour depends on the test parameters.

Normal engine operations involve boundary lubricated regime whereby transient lubrication conditions with asperity contact are experienced. Masjuki and Maleque [7] reported lower wear of cast iron pins tested against mild steel disks under boundary lubricated condition for tests in methyl ester blended with synthetic oil SAE 40 compared to tests in undiluted synthetic oil. It was suggested that the long chain esters formed a tribofilm by chemical adsorption between the polar end of the fatty acid molecules and the contact surfaces. De Silva et al. [8] tested grey cast iron cylinder liner against chromium coated piston rings under boundary lubricated conditions using ethanol+water blended synthetic oil (SAE 5W-30) and compared with tests in unmixed synthetic oil. The COF values reduced from 0.12 in synthetic oil to 0.07 in mixed oil and was attributed to changes in the additives (in oil) chemistry. Bench and dynamometer tests, performed on lightweight cylinder bore material namely Al-12% Si and Al-18.5% Si alloys, under boundary lubricated condition using synthetic oil SAE 5W-30 and analyzed using transmission electron microscopy TEM and spectroscopic methods have shown that a tribofilm is generated during sliding [9–11]. It was shown [12,13] that the tribolayers having antiwear properties could form as a result of zinc-dialkyldithiophospahte (ZDDP) degradation during

sliding contact via an ion exchange reaction between the substrate and the lubricant. In summary, during boundary lubricated tests sliding induced degradation of additives in the oil could lead to the formation of a tribolayer, which reduced wear loss and presence of ethanol or fatty acids influence the additive degradation chemistry.

The composition of piston ring coating is an important factor in determining the wear and friction behaviour of the cylinder liner-piston ring assembly. PVD deposited CrN, chromium plating film, WS_2 coating, sprayed molybdenum are few examples of wear resistant coatings deposited on piston rings [14–18]. A recent advance in piston ring surface engineering consists of the introduction of amorphous diamond-like carbon (DLC) coatings. Typically in a DLC coating sp^2 bonded graphitic clusters are embedded in a sp^3 bonded matrix of carbon atoms. Electron Energy Loss Spectroscopy (EELS) and Raman spectroscopy were instrumental in determining the C bonding states in the DLC [19–21]. The hydrogen content of the coating has direct influence on the tribological properties of DLC coatings as demonstrated in previous studies [22–29]. The hydrogen atom terminated surfaces minimize interactions between covalent σ carbon bonds. Hence, the hydrogenated DLC (40 at% H) coatings show low COF in vacuum and under inert atmospheres. Non-hydrogenated DLC (NH-DLC) coatings with < 2% H recorded low friction in humid atmosphere [25, 26]. OH groups (along with H) were dissociated from the water molecules in the surrounding atmosphere and passivated the carbon atoms on coating surfaces as well as the carbonaceous transfer layers formed on the counterface. A recent study [28] carried on NH-DLC coatings tested against Ti-6Al-4V pins in ethanol showed a near complete elimination of running-in friction and low steady state COF emphasizing the role of ethanol in passivating NH-DLC surface. It was also shown that NH-DLC coatings when used in combination with ester based oils would lead to low COF values [30]. Kano et al. [31] reported a

COF of 0.03 for NH-DLC sliding against itself when tested in ester based lubricant glycerol mono-oleate (GMO). Using time-of-flight secondary ion mass spectroscopy ToF-SIMS, formation of an OH-terminated carbon surface was detected. The occurrence of low COF was attributed to weak Van der Waals forces between the two carbon surfaces passivated by OH groups originating from the GMO lubricant. Matta et al. [32] performed similar sliding experiments in which NH-DLC sliding against itself was lubricated with glycerol blended with hydrogen peroxide resulted in a COF of 0.03. X-ray photoelectron spectroscopy (XPS) and ToF-SIMS observations supported the earlier view that carbon surfaces were terminated by OH. This shows that lubricants such as GMO or glycerol/H_2O_2 that can provide OH groups are effective in reducing the friction. The effect of alcohol blended lubricants was explored by Hu et al. [33] where 2-ethylhexanol mixed with ZDDP additives in the engine oil was shown to increase its load-carrying capacity. The improved antiwear behaviour of 2-ethylhexanol (up to 8 wt%) and ZDDP (in base oil) mix tested against 52100 steel was attributed to the adhesion of polar hydroxyl groups to the metal surface and formation a protective film although no spectroscopic evidence was provided for the same. ToF-SIMS studies performed on DLC/DLC (both hydrogenated and non-hydrogenated) and DLC/steel tested in zinc dialkyldithiophosphate (ZDDP) containing oil led to formation of ZDDP derived tribofilms on the DLC surfaces [34] in agreement with other studies [35,36]. In case of tests conducted on WC doped H-DLC against steel no tribofilm formation was found on the coating surface when tested in polyalpha-olefin (PAO) oil with extreme pressure additives [37,38]. The low friction ranging between 0.06-0.09 was attributed to the formation of a tribofilm on the steel counterface and steel substrate once the coating was worn. This tribofilm incorporated W and C from the coating and also S from the additive in the lubricating oil.

From the above review it becomes clear that during cylinder liner-piston ring interactions two factors are important for maintaining low friction and to reduce wear losses. These are i) formation of a tribolayer during boundary lubricated sliding comprising of ZDDP degraded antiwear components, and ii) in case of DLC coated counterfaces passivation of the carbonaceous surfaces by dissociated water molecules, or OH molecules from ethanol or similar additives in engine oil. Accordingly, the aim of this paper is to study the micromechanisms of tribolayer formation and surface passivation during sliding contact of a typical engine block material, type A cast iron, tested against a NH-DLC coated steel counterfaces. Tests were conducted under boundary lubrication sliding contact using synthetic oil and oil diluted by ethanol containing biofuel E85. Comparisons were made with cast iron and uncoated 52100 steels. Surface characterization by electron microscopy and spectroscopic methods helped to delineate the mechanisms that control friction and wear.

2.2. Experimental

2.2.1 Materials and Coatings

A typical engine block material, grey cast iron (CI) consisting of ASM type A graphite flakes [39] was used in the tribological tests. The graphite flakes with an average length of 35.18±8.2 μm were embedded in a pearlite matrix (Figure 2.1a, b). The bright-field TEM image of the pearlite with well-known lamellar microstructure consisting of alternate layers of ferrite and cementite is shown in Figure 2.1c. The average width of the cementite lamellae was 53.7±6.4 nm, while ferrite had an average width of 194.2±28.6 nm. The Vickers hardness of the CI was determined as 202.9±12 HV_{100}.

NH-DLC coatings were deposited on AISI 52100 steel balls of 6.0 mm diameter using an unbalanced magnetron sputtering system equipped with one chromium and two graphite targets.

A 1.50 μm thick NH-DLC coating was deposited on a Cr interlayer to promote adhesion to the steel substrate. The hydrogen content, measured using elastic recoil detection (ERD) technique, was < 2.00 at.%. The as-deposited DLC coating exhibited a broad Raman peak around 1500 cm^{-1}, commonly termed as the G-band, indicating an amorphous structure with primarily sp^2 type bonding. The hardness and the elastic modulus of the coatings were calculated from the loading–unloading curves obtained by a Berkovich type nano-indenter that penetrated to a maximum depth of 200 nm below the surface. Average hardness and elastic modulus values of NH-DLC were 13.00 ± 1.10 GPa and 158.55 ± 6.82 GPa, respectively. The average surface roughness (R_a) of the DLC coatings was measured as 15.5±6.2 nm using an optical surface profilometer.

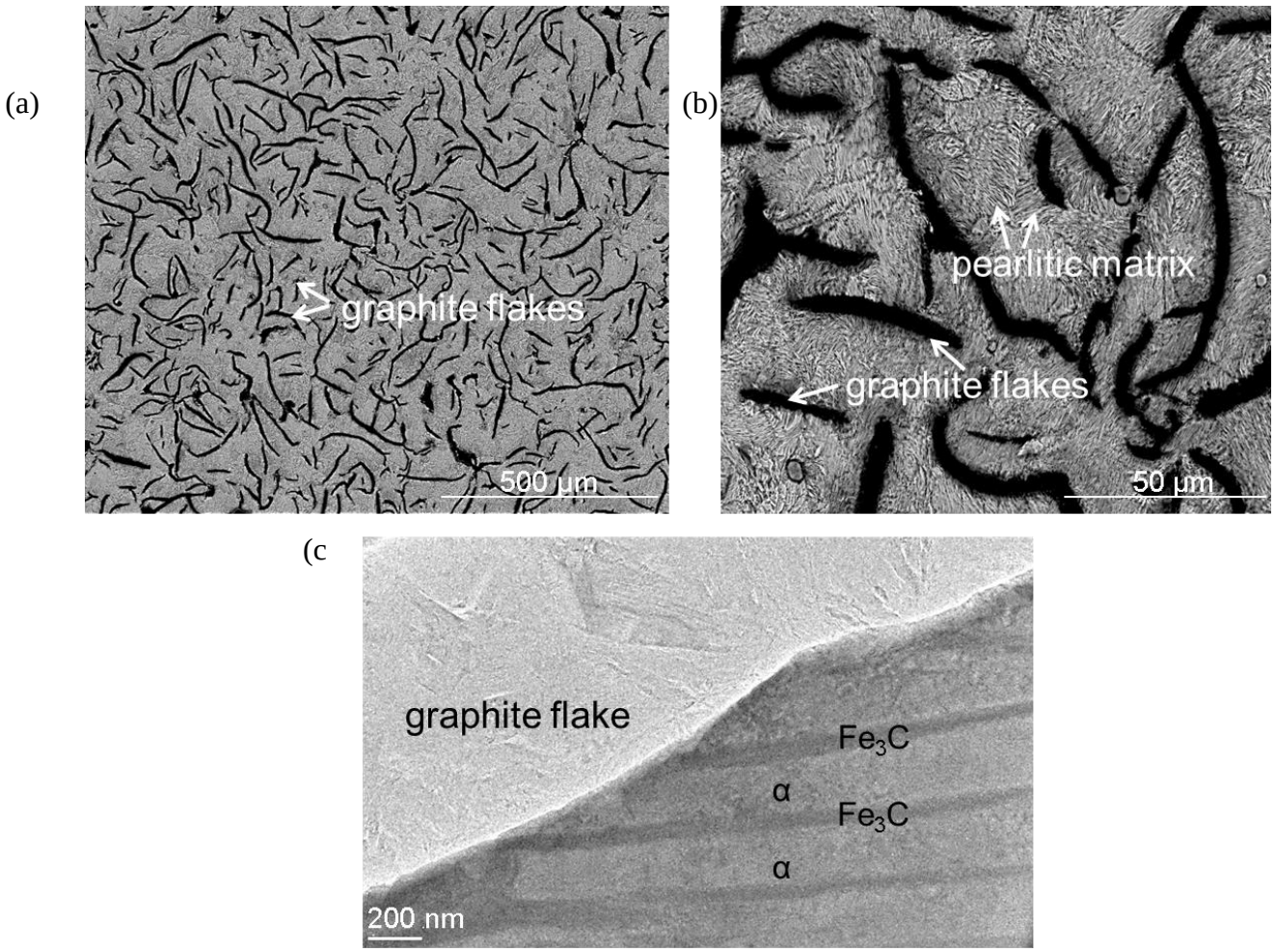

Figure 2.1. (a) Low and (b) high magnification cross-sectional secondary electron images of cast iron with graphite flakes embedded in a pearlitic matrix; (c) Bright-field TEM image of the α-Ferrite and the Fe_3C lamellae adjacent to a graphite flake.

2.2.2 Tribological Tests

Sliding wear tests were conducted using a unidirectional rotating ball-on-disk tribometer (CSM) using 6.0 mm diameter NH-DLC coated 52100 steel balls against CI disks (25.0 mm diameter) under 5.0 N load and at 0.05 m/s sliding velocity in ambient air with relative humidity

(RH) range between 34%-40% and in nitrogen atmosphere with (0.2% RH). The sliding wear tests were performed at room temperature (25 °C). The CI disks were also tested against uncoated SAE 52100 steel balls as well as ASM type A CI using the same tribometer and under the same test conditions. The lubricated tests used synthetic engine oil SAE 5W-30 (ILSAC GF-5) under the same conditions of load and speed as for the unlubricated tests. The load and sliding velocity were selected to simulate ultra-mild wear according to previous laboratory tests [10, 40]. A mixture of synthetic oil blended with E85 (85% ethanol and 15% gasoline) in 1:1 ratio (by volume)—designated as diluted oil—was also used to study the role of E85 on COF and wear. The COF for each test was recorded. The volumetric wear loss measurements were taken from different regions of the cast iron wear tracks after sliding for different sliding cycles using a white light non-contact profilometry method as described in [12,41]. At least three sliding tests were performed under each test condition and a new counterface was used for each test. For each friction curve, the average value of steady state friction (μ_S) was calculated from the arithmetic mean of the COF signals obtained as a function of number of sliding cycles. The mean values μ_S obtained from three tests for each loading condition and their standard deviations were reported. The lubrication regime, was determined from the ratio (λ) of minimum film thickness (h_{min}) to the r.m.s roughness (r*) of the contacting surfaces [42]. The parameters used for calculation of lubrication regime are listed in Table 2.1. As $\lambda = 0.008$ initially for tests conducted in engine oil and 0.001 in case of tests in E85/oil (1:1) blend boundary lubrication condition prevailed [42].

2.2.3 Examination of Worn Surfaces

The details of surface damage features were studied using FEI Quanta 200 FEG scanning electron microscope (SEM) equipped with an energy-dispersive X-ray (SiLi Detector) spectrometer (EDS). Samples for Transmission Electron Microscopic (TEM) studies were

prepared by focused ion beam (FIB) lift-out technique [43] using Carl Zeiss NVision 40 CrossBeam. Prior to the ion milling process using gallium ion source at 30 kV, the surfaces were protected from damage by sputtering them with a layer of carbon. The cross-sectional TEM samples were ion-milled from both sides to a thickness of about 100 nm. The TEM observations were made using a FEI Titan 80-300 HR-TEM. The high-resolution TEM images and diffraction patterns of the ORL on the CI surface and the NH-DLC coating were obtained. Energy Electron Loss Spectra (EELS) analyses were also performed on the TEM cross-sections after they were further nano-milled to about 25 nm. For O-K edge analyses, the TEM samples were cooled cryogenically in liquid N_2. The spectra were obtained by cumulative acquisition (10-15 spectra) with an acquisition time of up to 1 second per spectrum. Semi-quantitative chemical analyses of the worn surfaces were conducted by X-ray photoelectron spectroscopy (XPS) using a Kratos Axis Ultra X-ray photoelectron spectrometer. The survey scans were carried out with pass energy of 160 eV. The high-resolution analyses were carried out with pass energy of 40 eV. The XPS analyses were carried out on the NH-DLC coating contact surface and the tribolayers formed on the CI pin surface. Micro-Raman spectra of the as deposited and worn NH-DLC surfaces were obtained using a Horiba Raman micro-spectrometer with 50 mW Nd–YAG laser (532 nm excitation line) through the 50× objective lens. The laser spot on the specimen surface was 1 μm diameter.

Table 2.1. Parameters used to calculate the lubrication conditions (λ=hmin/r*) values for tests of CI in contact with NH-DLC in SAE 5W-30 engine oil and diluted oil. R is the radius of the counterface ball in m, V is the sliding velocity in m/s, P is the normal load in N, E* is the composite elastic modulus (in GPa) could be calculated by equation 1, η0 is the viscosity constant of lubricants, α is the lubricant pressure viscosity coefficient, and r* is the r.m.s. surface roughness of the contacting surfaces. The minimum lubrication thickness hmin and r* of CI in contact with NH-DLC coating were calculated using equations 2 and 3, respectively:

$$\frac{1}{E^*} = \frac{1-\nu_{CI}^2}{E_{CI}} + \frac{1-\nu_{DLC}^2}{E_{DLC}} \quad [2\text{-}1]$$

where E_{CI} is 118 GPa, E_{DLC} is 158 GPa, Poisson's ratio of 1010 coating ν_{1010} is 0.32 and Poisson's ratio of DLC coating ν_{DLC} is 0.22.

$$h_{min} = 1.79R^{0.47}\alpha^{0.49}{\eta_o}^{0.68}V^{0.68}(E^*)^{-0.12}P^{-0.07} \quad [2\text{-}2]$$

$$r^* = \sqrt{{r_{CI}}^2 + {r_{NH-DLC}}^2} \quad [2\text{-}3]$$

R (m)	V (m/s)	P (N)	E* (GPa)	r* (μm)	η_0 (Pa.s)		α ($\times 10^{-8}$)		h_{min} (μm)	
					Diluted Oil	Oil	Diluted Oil	Oil	Diluted Oil	Oil
0.03	0.05	5.0	73.57	1.92	0.005	0.052	1.62	2.25	0.002	0.016

2.3. Results

2.3.1 Effect of Moisture on Unlubricated Sliding during Tests with Varying RH

Exploratory tests were designed to investigate the effect of humidity on the COF of CI samples when tested against NH-DLC coated steel, uncoated CI and steel. The sliding friction tests were carried out in a nitrogen atmosphere with a 0.2% RH for the first 3×10^3 cycles. Then the test was continued for the next 4×10^3 cycles in ambient air with 34% RH. Following this, dry nitrogen was re-introduced into the environmental chamber reducing the humidity again to 0.2% RH for the last stage of the friction test that lasted for 2×10^3 cycles.

Figure 2.2 shows the COF values CI disks tested against NH-DLC coated counterfaces, uncoated steel as well as against CI counterfaces. The variations of COF values were continuously recorded while the humidity in the test chamber altered from 0.2 % RH to 34%RH and back to 0.2 % RH as explained above. Uncoated CI samples were tested against themselves for comparison and results are reported in Figure 2.2. Additionally, the steel samples were tested against themselves under the same environmental and loading conditions to investigate the effect of moisture on COF for a tribocouple without carbon containing interfaces (of CI and DLC). Figure 2.2 shows that the lowest COF values were observed when CI pins were tested against NH-DLC coated disks; an initial (running in) COF peak of 0.62 was observed for the first 2×10^3 cycles for tests in 0.2% RH and a drop to a COF of 0.39±0.03 followed for another 1×10^3 cycles under the same dry atmosphere. When the humidity was increased to 34% RH during the test the COF was reduced to 0.31±0.02. This was followed by an increase to 0.39±0.03 when the dry (0.2% RH) air was re-introduced into the system. When the tests were started at 34% RH and then the RH was reduced to 0.2%, it was found that the friction values were reproducible and the friction trend was similar to that shown in Figure 2.2. NH-DLC coated counterfaces have been

shown to reduce the COF values of Al [25], Ti-6Al-4V [28] and steel [22] in test environments with high humidity. However unlubricated friction tests performed on NH-DLC at 34% RH against Al (0.18) [25] and Ti-6Al-4V (0.12) [28] showed lower COF values: a notable difference was the formation of carbonaceous transfer layers on the Al and Ti surfaces which was not observed for CI contact surfaces. CI vs. CI and CI vs. steel tribosystems showed similar behaviour exhibiting high COF values of 0.72±0.06 in 0.2% RH which were reduced to 0.52±0.04 in 34% RH. The steel counterfaces when tested against itself showed a high COF value of 0.90±0.02 in 0.2% RH which was only reduced to 0.79±0.02 in 34% RH revealing that the presence of graphite was responsible for the lower COF values.

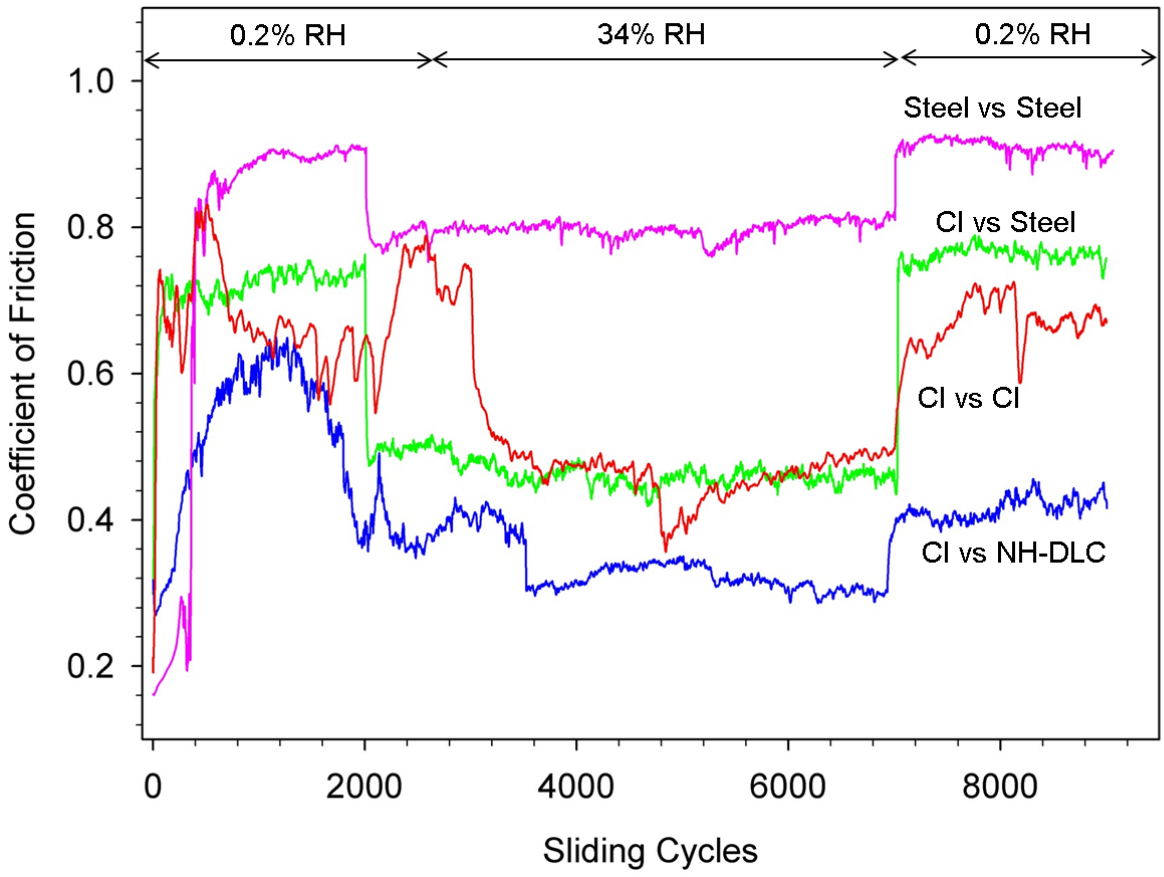

Figure 2.2. Variations of COF values with the relative humidity (% RH) for unlubricated sliding tests performed on CI against NH-DLC, CI and uncoated steel. COF of steel sliding against itself is shown for comparison. Load = 5.0 N and sliding velocity = 0.05 m/s for all tests.

2.3.2. Continuous Sliding Tests at constant RH: COF vs. Volumetric Wear Loss Diagram

Unlubricated tests of CI disks against NH-DLC, CI and steel counetrfaces were performed at constant humidity of 34% to assess the friction and wear of different tribocouples (Figure 2.3). Figure 2.3a shows that CI tested against NH-DLC counterfaces had lower COF of 0.26±0.01 compared to CI run against CI counterfaces (COF = 0.28±0.01). Under constant RH tests, lower COF values were observed for CI tested against itself than that observed in varying RH tests (Figure 2.2). Previous findings [44] suggested that presence of moisture is required to saturate the dangling bonds in graphite surfaces resulting in low friction of graphite. Accordingly, in absence of moisture as shown in Figure 2.2, high and fluctuating friction values of >0.7 which decreased only to 0.39 in ambient air, yet even lower COF values of 0.28 were observed for tests performed in constant humid environment (Figure 2.3a).

The unlubricated sliding tests results, for experiments performed at constant 34% RH, are summarized in a COF vs volumetric wear loss diagram as shown in Figure 2.3b. The volumetric wear of CI/NH-DLC (0.57×10^{-4} mm^3) and CI/CI (2.05×10^{-4} mm^3) pairs were lower compared to those of CI/steel (65.08×10^{-4} mm^3) and steel/steel (97.5×10^{-4} mm^3) pairs. At the same time the COF of CI/CI (0.22) and CI/NH-DLC (0.26) were lower compared to that of CI/steel (0.45) and steel/steel (0.82). The white light optical profilometer images (in the inset of Figure 2.3b) of the CI wear track tested against NH-DLC shows the less damage when compared to steel/steel wear tracks. It is clear that presence of graphitic or amorphous carbon in both the mating surfaces is critical in maintaining low wear as well as low friction under unlubricated sliding conditions. The unlubricated tests provide an insight into the scuffing resistance of different tribocouples during engine cold start (oil starvation) conditions so that the CI sliding against NH-DLC and CI

tribosystems are the best cylinder bore-piston ring combinations and in the rest of the paper only these systems will be considered.

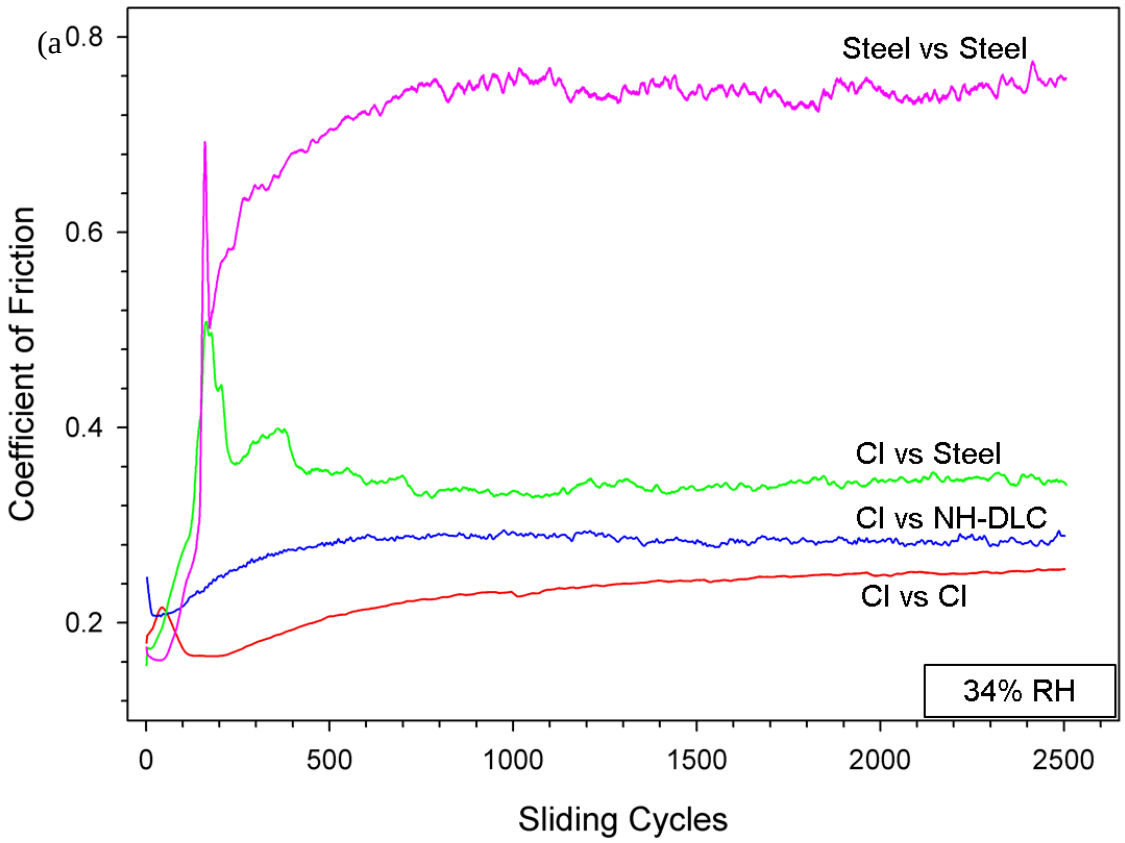

Figure 2.3.(a) Typical COF vs sliding cycles plots of CI tested against NH-DLC, CI and steel. COF plot of steel run against steel is COF plot is also shown; (b) COF vs volumetric wear plot for CI tested against NH-DLC, CI and steel as well as steel vs steel in 34% RH for 5×10^3 cycles. The 3-D optical profilometer images in the inset show wear surfaces of CI/NH-DLC, CI/CI and steel/steel tribo-couples.

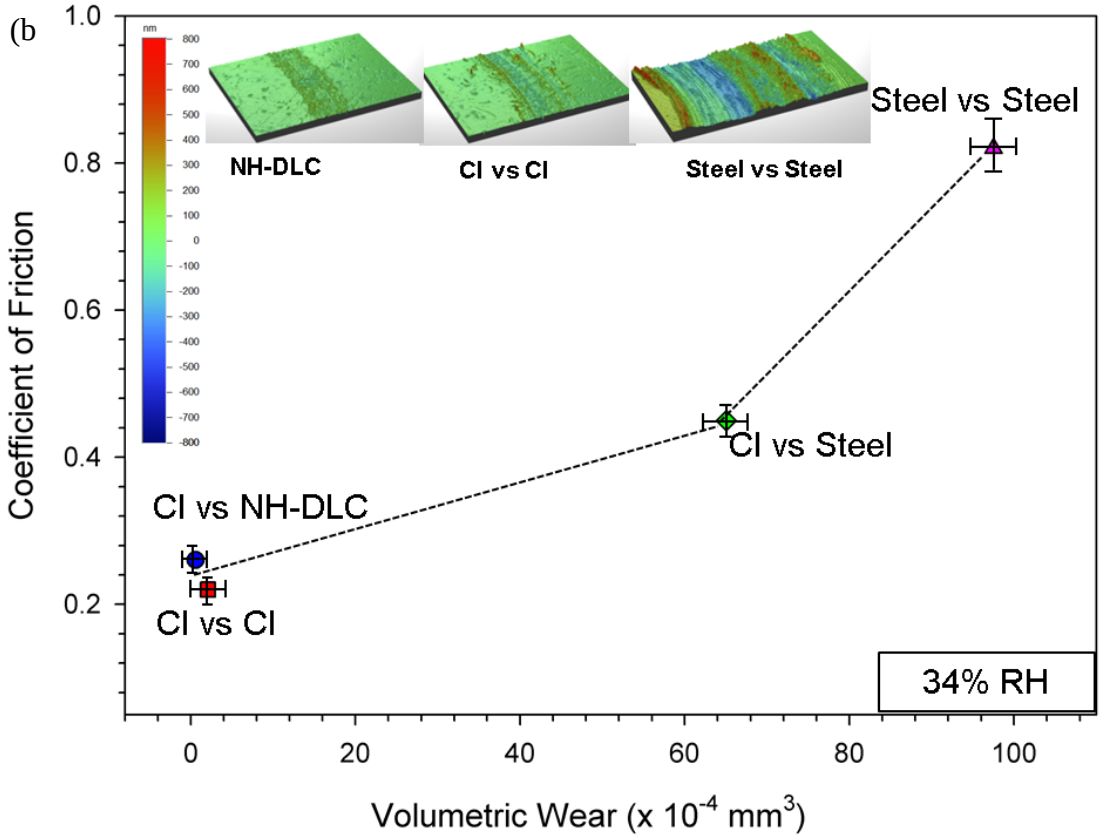

Figure 2.3. contd.

2.3.3. Lubricated Tests Using Engine Oil and Diluted Oil

Lubricated tests were conducted using engine oil SAE 5W-30 and oil diluted at 1:1 ratio with ethanol containing E85 under boundary lubricated conditions. Figure 2.4 shows that diluted oil reduced the steady state COF of both CI/NH-DLC and CI/CI systems. The CI/NH-DLC test showed the lowest μ_S of 0.07±0.01 in diluted oil after sliding for 5×10^3 cycles compared to μ_S of 0.09±0.01 for CI/NH-DLC tests in unmixed engine oil. CI/CI tests also showed a reduction of COF from 0.13±0.01 in oil to 0.12±0.01 in diluted oil. Increasing the proportion of E85 in oil mixing ratio to a mixing ratio of 3:1 did not have an effect on COF as average μ_S value remained almost the same at about 0.07 for CI/NH-DLC and about 0.12 for CI/CI. Tests conducted in an unmixed E85 (100%) resulted in a high COF value of 0.18±0.02.

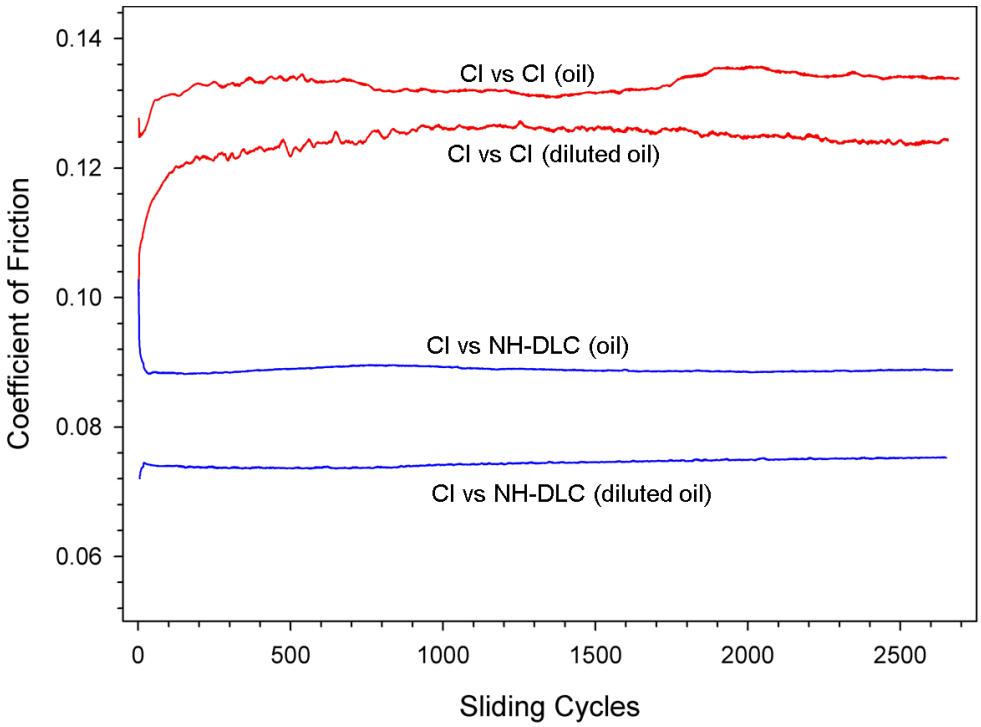

Figure 2.4. Typical COF vs. sliding cycles plots for CI / CI and CI / NH-DLC in engine oil (SAE 5W-30) and in diluted oil. Load = 5.0 N and sliding velocity = 0.05 m/s for all tests.

Sliding tests were performed for higher sliding cycles to measure the COF and volumetric wear at specific sliding cycle intervals. Figure 2.5a shows the average steady state COF values plotted against the sliding cycles for CI/NH-DLC and CI/CI in undiluted oil and diluted oil (1:1) where each data point represents result from a fresh sample. CI/NH-DLC in diluted oil consistently maintained low μ_S between 0.07-0.08 compared to tests in unmixed oil for which the COF values varied between 0.09 and 0.11. The addition of ethanol to the oil reduced the COF values of CI/CI as well but the μ_S did not drop as much as that of the CI/NH-DLC.

Figure 2.5b where volumetric wear loss vs sliding cycles test results for CI/NH-DLC and CI/CI in oil and diluted oil are shown indicate that CI/NH-DLC system showed lower volumetric wear compared to CI/CI. It is noted that although the effect of ethanol addition on the wear of the CI/NH-DLC system was not prominent CI/NH-DLC exhibited a low and constant wear rate up to 10^6 cycles in the range 0.2×10^{-4}-0.5×10^{-4} mm^3 in both unmixed oil and diluted oil tests. On the contrary the wear of CI/CI system increased after sliding for 10^5 cycles and showed high volumetric wear of 11×10^{-4} mm^3 in unmixed oil and 5.0×10^{-4} mm^3 in diluted oil at the end of 10^6cycles. In summary, the wear rates at 10^6 cycles were 4.38×10^{-9} mm^3/m and 10.9×10^{-9} mm^3/m for CI/NH-DLC tests in dilute oil and oil while for CI/CI wear rates were 1.09×10^{-7} mm^3/m and 2.43×10^{-7} mm^3/m in dilute oil and oil.

The boundary lubricated tests reported in this section indicate that regardless of the lubricant type, the tribological performance was improved when CI/NH-DLC system was compared with CI/CI. Dilution of engine oil with ethanol reduced the steady state friction by 20-25% for both CI/CI and CI/NH-DLC tribocouples. Following the tribological tests FIB/SEM, TEM, micro-Raman and XPS analyses were performed on the contact surfaces of NH-DLC and CI to delineate the wear and friction results and are described in Section 3.4.

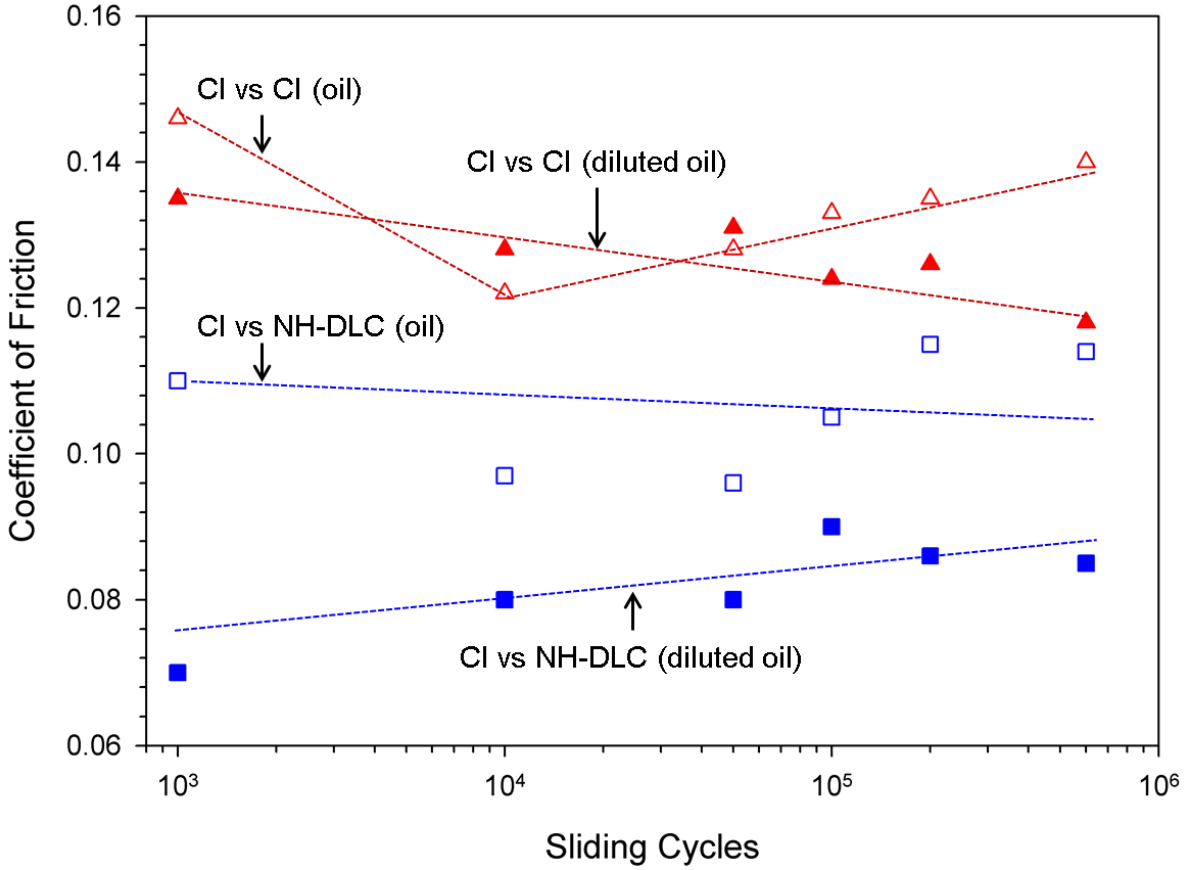

Figure 2.5. (a) Average steady state COF values obtained from CI vs CI and CI vs NH-DLC tests in oil (SAE 5W-30) and in diluted oil at different sliding cycles. Each point on this plot represents average COF value obtained from tests on fresh samples performed for that sliding cycle. The error for an average COF data point for each sliding cycle is about 10%; (b) Volumetric wear loss of CI samples plotted against sliding cycles for tests against CI and NH-DLC in oil (SAE 5W-30) and in diluted oil. Each point on this plot represents average volumetric wear loss value obtained from tests on fresh samples performed for that sliding cycle.

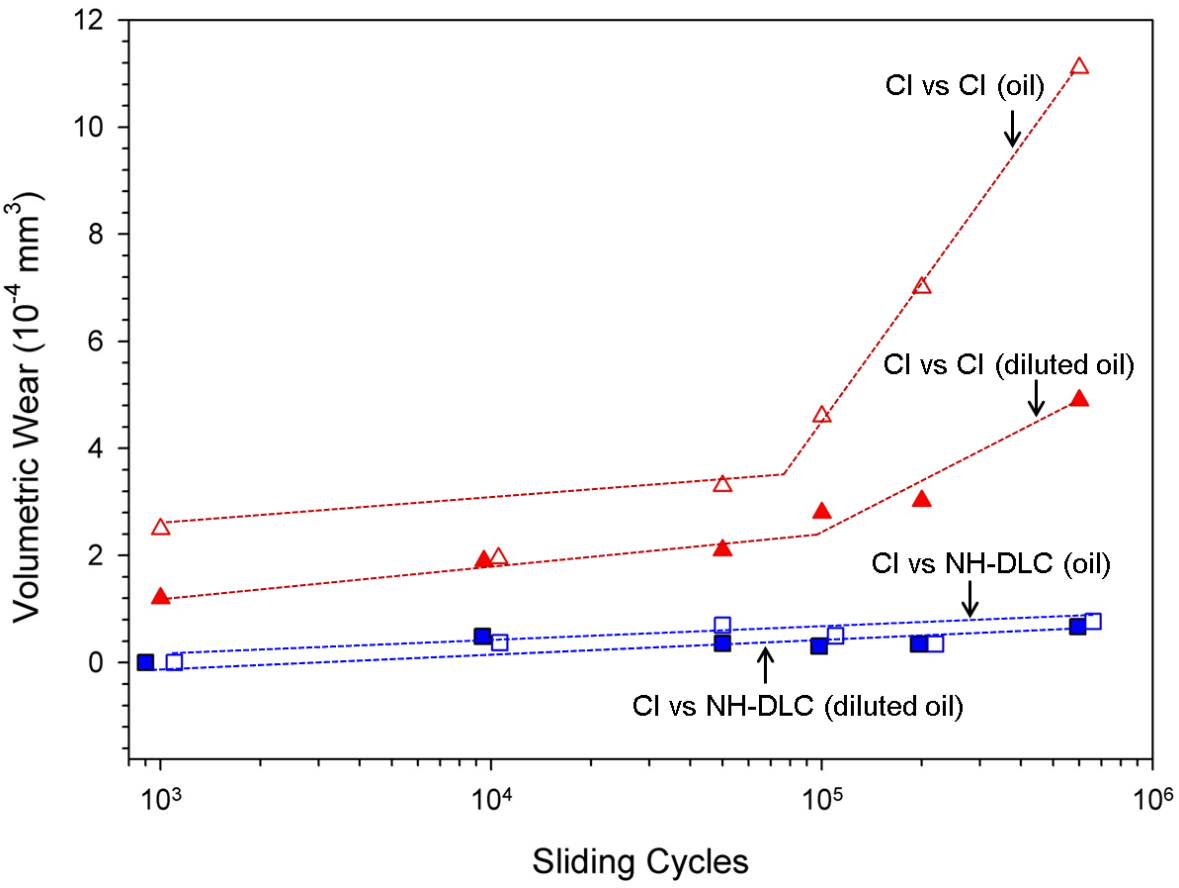

Figure 2.5. contd.

2.3.4 Microscopic and Spectroscopic Analyses of Contact Surfaces

2.3.4.1 Cross-sectional TEM and micro-Raman examinations of NH-DLC coating

SEM observations of the wear tracks formed on the NH-DLC coating surface after the unlubricated tests against CI under an atmosphere with 34% RH indicated that the coating was mostly intact and damage free after the dry sliding test. FIB/TEM cross-sectional studies that were conducted across the worn surfaces of NH-DLC counterfaces however revealed that in some locations debris particles comprising of iron oxide was adhered to the contact surface. Site specific cross-sectional studies of the regions of the wear track covered with adhered debris were further investigated by FIB/SEM (Figure 2.6a). Through thickness cracks extending across the coating were also observed. Interfacial cracks running between the coating and the substrate could also be identified in Figure 2.6a. Sinking in of the edges of the fractured segments of the coatings into the substrate was another notable damage feature. Micro-Raman spectrum of the as-deposited NH-DLC coating is shown in Figure 2.6b and displays a broad peak between 1300 and 1600 cm^{-1} which is typical of hydrogen free amorphous carbon structure [21]. Raman spectra of the worn surface of NH-DLC, also shown in Figure 2.6b, are characterized by a high intensity D-peak at 1345 cm^{-1} indicating possible sliding induced graphitization of the amorphous carbon structure [21]. The Raman spectrum taken from another location of the worn NH-DLC contact surface shows Raman peaks between 215 and 660 cm^{-1} which are typically attributed to iron oxide (Fe_2O_3) [45] as observed in the FIB/SEM image as well (Figure 2.6a). Figure 2.6c shows a typical FIB/SEM cross-section image of the NH-DLC coating surface when tested against CI in diluted oil after 2×10^5 cycles. The image is typical and shows that none of the localized damage features that characterized the cross-sections of the same coating under the unlubricated tests occurred. Micro-Raman spectrum of the NH-DLC coating subjected to wear in dilute oil is

shown in Figure 2.6d. A slight increase in the D-peak intensity compared to the as deposited coating is the only effect that sliding contact caused on the coating structure and no oxide adhesion could be observed.

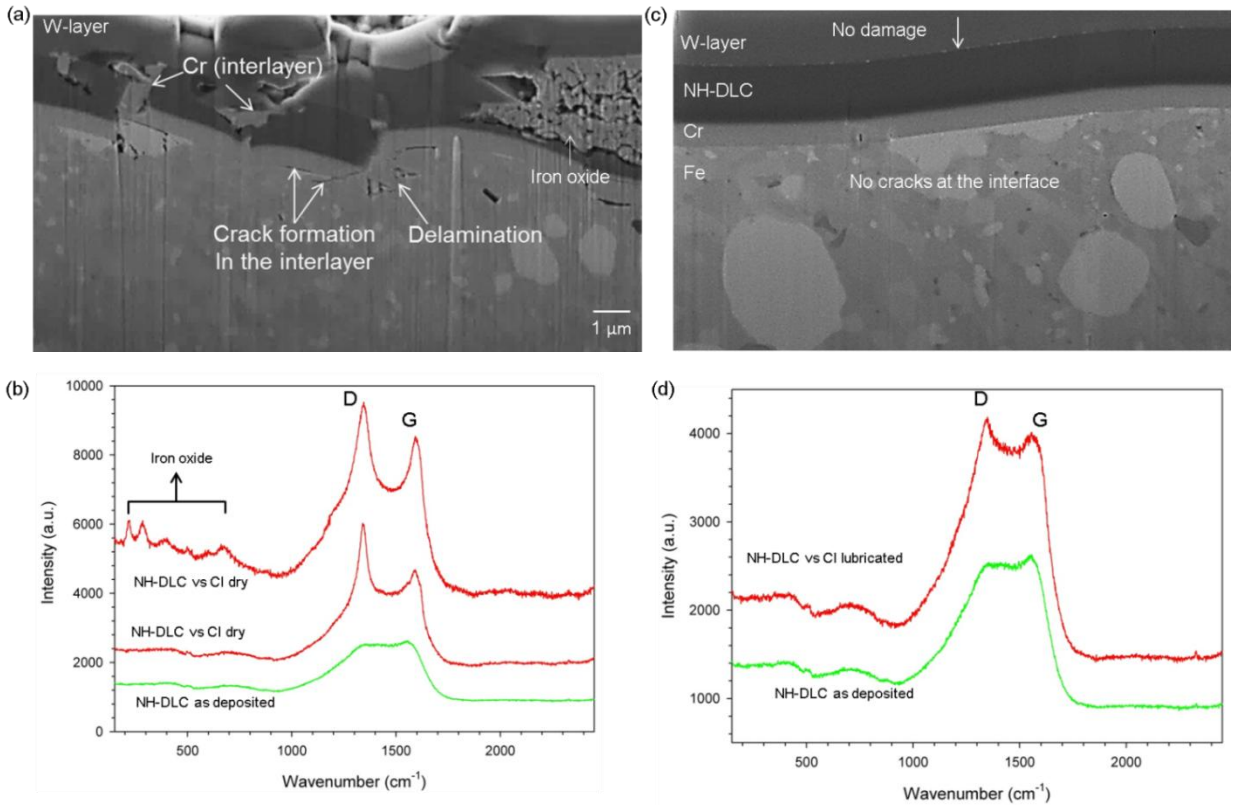

Figure 2.6. (a) Cross-sectional FIB/SEM image of the NH-DLC used as counterface against CI in unlubricated sliding test for 5×10^3 cycles (34 % RH) showing adhered material (iron oxide) as well as through thickness and interface fracture at a section subjected to significant wear damage and (b) micro-Raman spectra of worn NH-DLC after unlubricated tests for 5×10^3 cycles against CI; (c) Cross-sectional FIB/SEM image of the NH-DLC tested against CI under the boundary sliding condition for 2×10^5 cycles showing no coating damage and (d) micro-Raman spectra worn NH-DLC after boundary lubricated sliding for 2×10^5. (Raman spectra of as-deposited NH-DLC are given in figure b and d as reference).

2.3.4.2 SEM and XPS Examinations of CI contact Surfaces

The contact surfaces of CI samples subjected to lubricated tests were studied in detail to understand the compositional changes during sliding wear. A tribolayer formed on the CI surfaces tested against uncoated CI and NH-DLC coatings, as a result of sliding induced degradation of ZDDP additive as well as detergents in the engine oil and is referred as the oil residue layer or ORL.

Figure 2.7a shows a typical backscattered SEM image taken from the worn surface of CI tested against NH-DLC in diluted oil. The ORL was not continuous but formed isolated pockets on the contact surface. On the CI contact surface ORL pockets of different chemical compositions were detected. Compositions of elements detected by EDS on the surface contact shown in Figure 2.7a are displayed in Figures 2.7 (b-h). Accordingly, the main constituents of the ORL were Zn, S, P, Ca, O, Fe and C. The presence of Zn, S, P, and Ca are from degradation of additive components in the oil. The bright grey ORL pockets marked in Figure 2.7a is rich in Zn and S (Figures 2.7 b and c) and likely consisted of ZnS. The larger ORL pocket (dark area) was rich in P, Ca, O (Figures 2.7 d-f) and thus could be identified as a phosphate layer. More detailed compositional analysis of the ORL pockets was given by the analyses of XPS results.

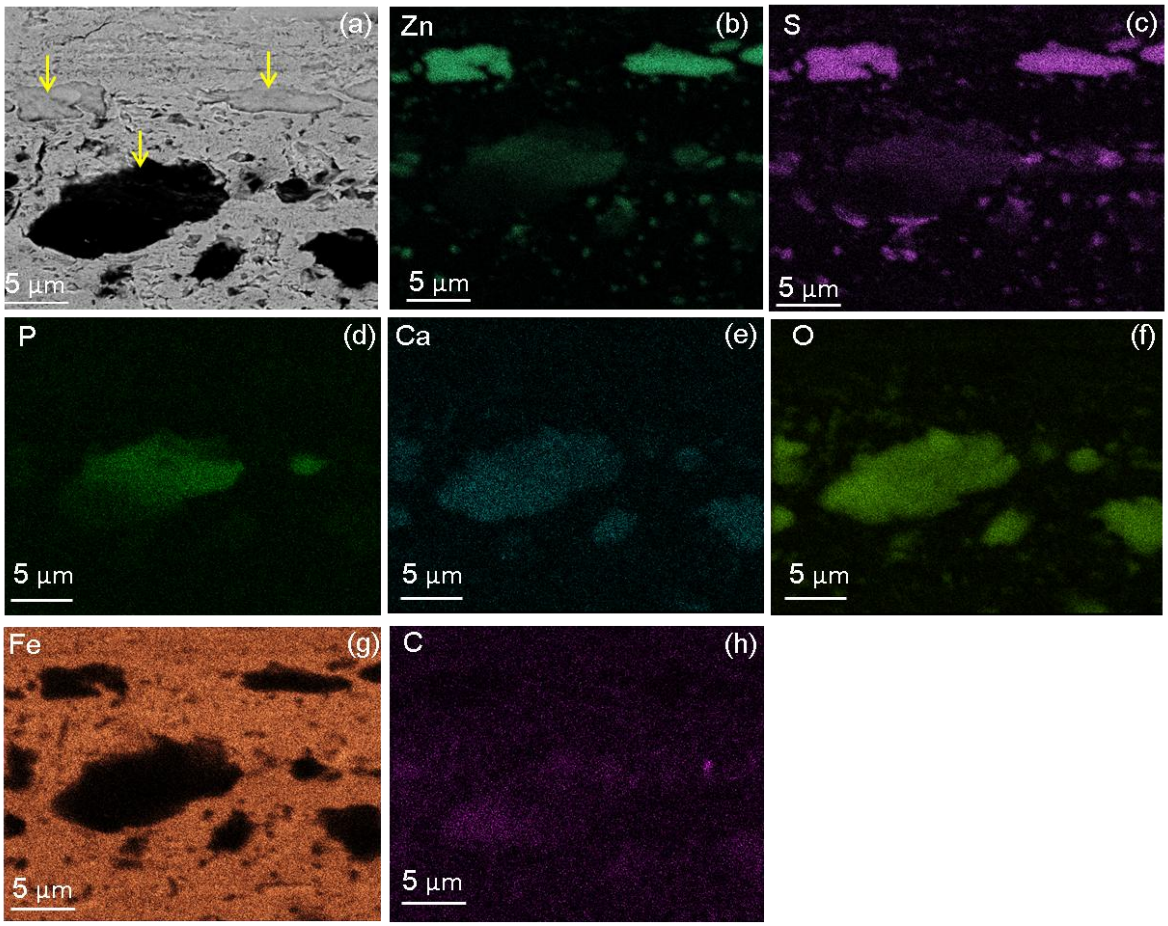

Figure 2.7. (a) Backscattered SEM image of CI worn surface after sliding against NH-DLC coating in diluted oil for 2×10^5 cycles; (b) Elemental EDS maps taken from (a) showing the distributions of (b) Zn, (c) S, (d) P, (e) Ca, (f) O (g) Fe and (h) C. Arrows in figure a show different pockets of the ORL.

High-resolution XPS spectra acquired from the ORL formed on the freshly tested CI contact surfaces placed in sliding contact against NH-DLC after 2×10^5 cycles (long term tests) are shown in Figures 2.8a-f. Figure 2.8a indicates a Zn $2p_{3/2}$ peak at 1022.2 eV, which corresponds to either a zinc phosphate or/and sulphide—both of which are likely to originate from the degradation of ZDDP molecules [46]. In Figure 2.8b the S 2p peak is de-convoluted into S $2p_{3/2}$ and $2p_{1/2}$ peaks. The S $2p_{3/2}$ peak at 161.8 eV and the S $2p_{1/2}$ peak at 163.2 eV are possibly due to metal–sulphide (M–S) and organic sulphide (C-S) bonds respectively. The S $2p_{3/2}$ and S $2p_{1/2}$ peaks at 168.5 eV

and at 168.9 eV could be attributed to sulphates (SO_2^{-4}) [47]. The Zn 2p and S 2p peaks when considered together suggest the formation of ZnS and $ZnSO_4$ observed in Zn and S rich ORL pockets shown in Figure 2.7a. Figure 2.8c shows the P 2p peak which is deconvoluted into two peaks, namely the P $2p_{3/2}$ and P $2p_{1/2}$ peaks. It can be suggested that both the P $2p_{3/2}$ peak at 133.5 eV and the P $2p_{1/2}$ peak at 134.2 eV would correspond to phosphate [48,49] formation possibly incorporating Zn, Ca or Fe cations. The Ca 2p peak (Figure 2.8d), deconvoluted into a Ca $2p_{3/2}$ peak at 347.8 eV and a Ca $2p_{1/2}$ peak at 351.2 eV, suggest formation of a Ca phosphate compound [50]. Integral area calculations of the decomposed C peaks in Figure 2.8e revealed that about 85 at.% of the C was aliphatic (C–C/C–H bonds) [46], assigned to peak at 284.9 eV. The binding energies of 286.4 eV could be assigned to C–OH/C–O–C bonds whereas the small intensity peaks at 288.9 and 287.9 were assigned to O-C=O and C=O respectively [46]. Deconvolution of O 1s spectra in Figure 2.8f resulted in two peaks one at 531.8 and the other at 530.1 eV that are assigned to hydroxide and oxide groups respectively [47]. Thus, the XPS analyses identified the constituents of ORL, formed via degradation of engine oil additives, as i) zinc sulphide and sulphate, ii) phosphates of zinc, iron or calcium and iii) carbon and oxygen corresponding to C-H, C-OH and O^{2-}.

In summary, the salient results arising from Section 3 are that under both lubricated and unlubricated conditions the use of NH-DLC coatings could reduce COF of CI. Boundary lubricated tests conducted on CI vs NH-DLC in engine oil showed lower friction and wear losses compared to CI sliding against uncoated CI. A protective tribolayer, ORL, formed on the CI surface. The role of the ORL (composition and formation mechanisms) in reducing the wear are discussed in Section 4 starting from sliding induced sub-surface damage features of CI. The friction reducing mechanisms and the benefits of the ethanol addition in oil are also discussed.

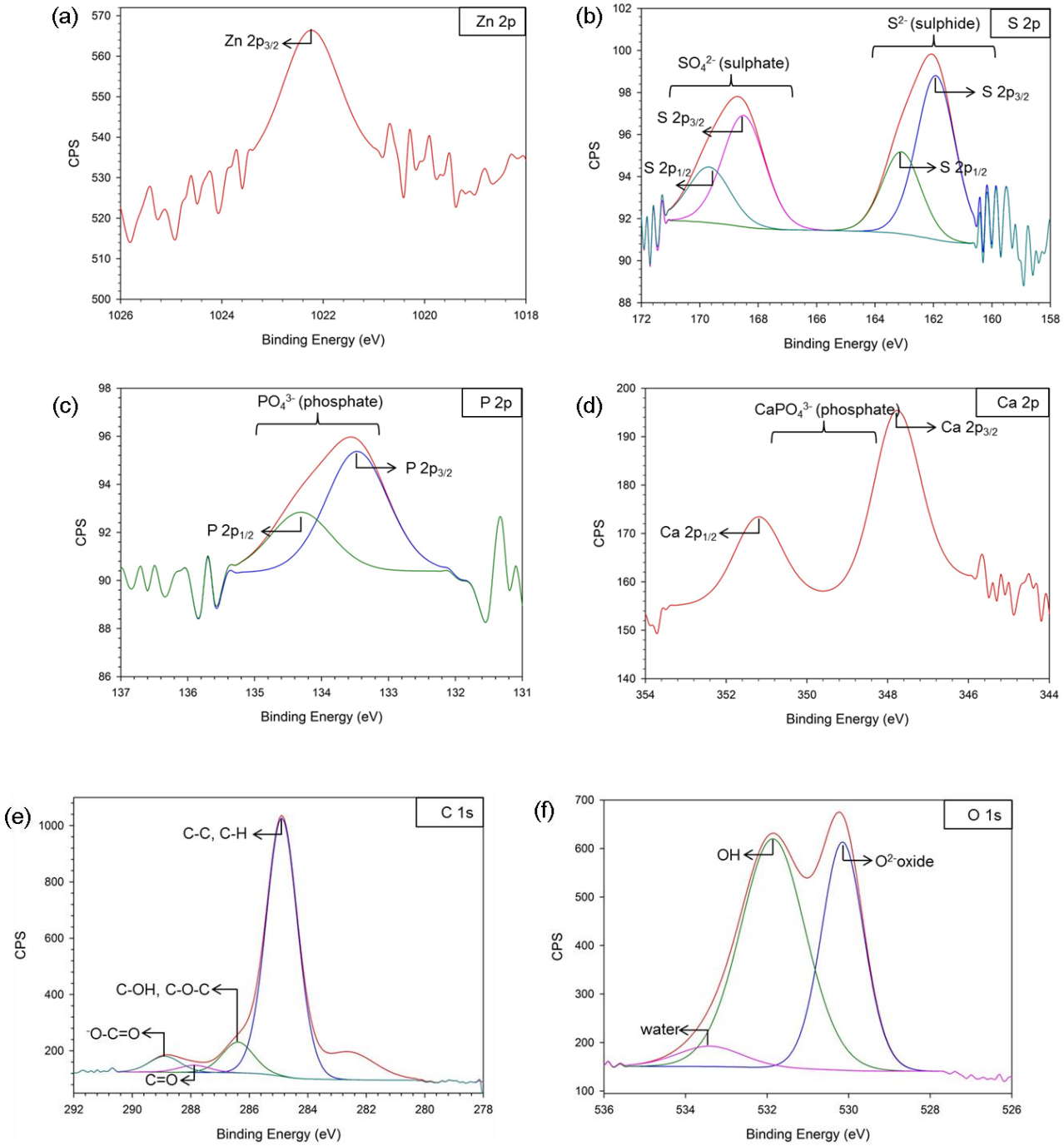

Figure 2.8. High-resolution XPS spectra showing deconvoluted peaks of (a) Zn 2p, (b) S 2p, (c) P 2p, (d) Ca 2p, (e) C 1s and (f) O 1s obtained of ORL formed on CI subjected to sliding tests using diluted oil for 2×10^5 cycles.

2.4. Discussion

The ORL formed during lubricated sliding on CI surfaces was responsible for maintaining low wear during boundary sliding tests. The composition of ORL was affected by the degradation of ZDDP additives in the synthetic oil. The lower volumetric wear of CI when tested in diluted oil compared to tests in unmixed oil (Figure 2.5b), could be attributed to the facilitation of the ZDDP degradation process by ethanol resulting in formation of an ORL richer in antiwear components [51]. It is also conceivable that the ORL would form more readily when ethanol is present in the oil, as demonstrated in a study of Al-11.5% Si tested against 52100 grade steel [51]. The compositional and morphological features of the ORL are discussed by providing additional HR-TEM and selected area electron diffraction (SAED) evidence in Section 4.1. On the other hand, differences in ORL layers' composition and microstructure cannot account for the differences in the COF. The COF of CI running against NH-DLC reduced with atmospheric humidity in unlubricated tests. Similarly CI running against itself had low COF when tested in a high humidity atmosphere (Figure 2.3). In addition during the lubricated sliding tests friction values of both systems were reduced when tested in diluted oil compared to unmixed oil (Figure 2.4). Surface passivation of the NH-DLC coating was a possible reason for the low friction due to dissociation of atmospheric moisture to H and OH groups [27] and passivation of carbon bonds. It can be postulated that during lubricated wear the dissociation of OH from ethanol would assist with passivation of carbon atoms on DLC surfaces and thus low COF could be expected. Evidence for the OH- passivation of carbon atoms on DLC surfaces has been provided using TEM/EELS analyses of the worn coating surface and used in the interpretation of the friction reduction mechanisms in Section 4.2.

2.4.1 Micromechanisms of Wear

It is pertinent to start the discussion by considering the changes that occurred in the subsurface layers of CI during wear and then consider the role of ORL in reducing wear. Sliding wear of CI led to accumulation of large plastic strains in the subsurface layers. A damaged subsurface microstructure exhibiting high localized plastic strain gradients was observed after the lubricated wear tests in diluted oil (Figure 2.9). Cross-sectional TEM of the CI subsurface microstructure, revealed a band of elongated grains, comprising of fragmented cementite lamellae re-orientated parallel to the sliding direction, formed below equiaxed ultrafine grains of average grain size 200-700 μm (Figure 9 a, b). The characteristic features of sliding wear induced subsurface damage are shown schematically in Figure 2.9c. Accordingly, at depths >2.5 μm, the pearlite lamellae was strain free—similar to the initial microstructure shown in Figure 2.1c. At a depth of ~1.5 μm from the contact surface parallel bands of elongated grains divided into smaller subgrains were observed as the strain increased to ε~0.7-1.0, as estimated from the orientation of ferrite plates to the sliding direction. As a result the cementite lamellae started to break up due to the dissolution of the carbon atoms in the carbide by crossing dislocations [52]. At higher strains nearer to the contact surface dense dislocation walls (DDW) in the ferrite lamellae subjected to high strains led to the formation of ultrafine grains with equiaxed cell blocks of high misorientation angles [53,54]. An important feature revealed by the cross-sectional TEM, as shown in Figure 2.9, is the presence of a tribolayer—an ORL on top of the damaged microstructure. It has been suggested that the formation of ultrafine grains immediately underneath the contact surface, such as those observed in Figure 2.9, would increase the hardness of material layers immediately under the ORL [55–57] and as such would serve to support the ORL.

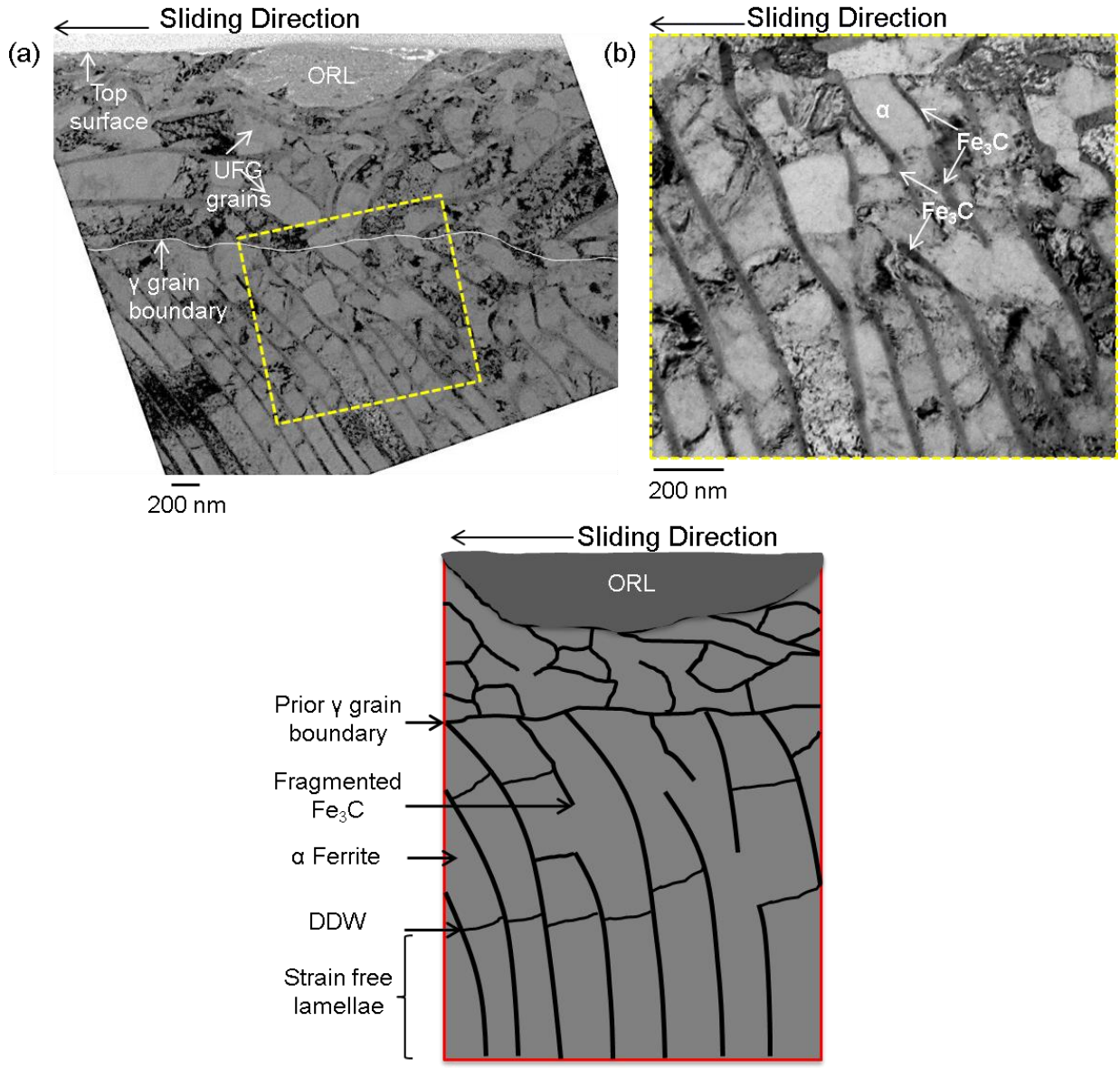

Figure 2.9. (a) Cross-sectional TEM image showing the microstructure of subsurface of CI under the worn surfaces with pockets of ORL when tested against NH-DLC for 1×10^4 cycles in diluted oil; (b) Higher magnification image of the region indicated by a dotted rectangle shown in (a). Dark strips represent Fe_3C (cementite) phase (~54 nm wide) between the lighter and thicker (~200 nm) bands of α (Ferrite) phase. The pearlite (cementite and ferrite) colonies, with two distinct orientations one nearly parallel to the sliding direction and the other nearly perpendicular, were allocated at each side of a prior γ (austenite) grain boundary; (c) schematic representation of the subsurface deformation features.

The different components of the ORL, responsible for maintaining low steady state wear, has been investigated in details using TEM/SAED analyses. Figure 2.10a shows a cross-sectional

TEM image of the ORL formed on CI after sliding for 1×10^4 cycles. A HR-TEM image (Figure 2.10b) of the ORL formed on the CI pin revealed crystalline regions with a planar d-spacing of 0.31 nm corresponding to ZnS crystals. Electron diffraction patterns (Figure 2.10c) obtained from the ORL showed in addition to crystallographic planes with d-spacings of 0.31 nm those with 0.19 nm and 0.16 nm corresponding to {111}, {220} and {311} planes confirming the presence of cubic ZnS (sphalerite) [58,59] with space group F43m. It is conceivable that the ZDDP molecules in the oil dissociated during sliding to form these ZnS crystals. Cubic ZnS (sphalerite) structure was found in the ORL formed for CI tested in unmixed oil as well. TEM analyses of the CI worn surface tested against NH-DLC in diluted oil blend for 2×10^5 cycles revealed that the discontinuous morphology of ORL persisted during the high cycle tests, as shown in Figure 2.11a. Some portions of the ORL had thickness reaching 800±50 nm (Figure 2.11b) and thus would keep the two surfaces from becoming in direct contact preventing the progression of wear. The ORL pockets had different chemical composition of the antiwear components (Figure 2.11a)—ORL made of zinc sulphide and ORL made of zinc pyrophosphate. The HR-TEM image (Figure 2.11c) of the ORL made of zinc pyrophosphate revealed randomly distributed nano-crystals in an amorphous carbon matrix [11]. A FFT-derived diffraction pattern of the HR-TEM image in Figure 11c, shows ring formations (Figure 2.11d) that correspond to d-spacing values of 0.30 nm, 0.25 nm and 0.20 nm belonging to zinc pyrophosphate nanocrystals [60]. Chains of zinc pyrophosphate in the ORL act as antiwear components and maintain steady state wear by undergoing pressure induced cross-linking [61].

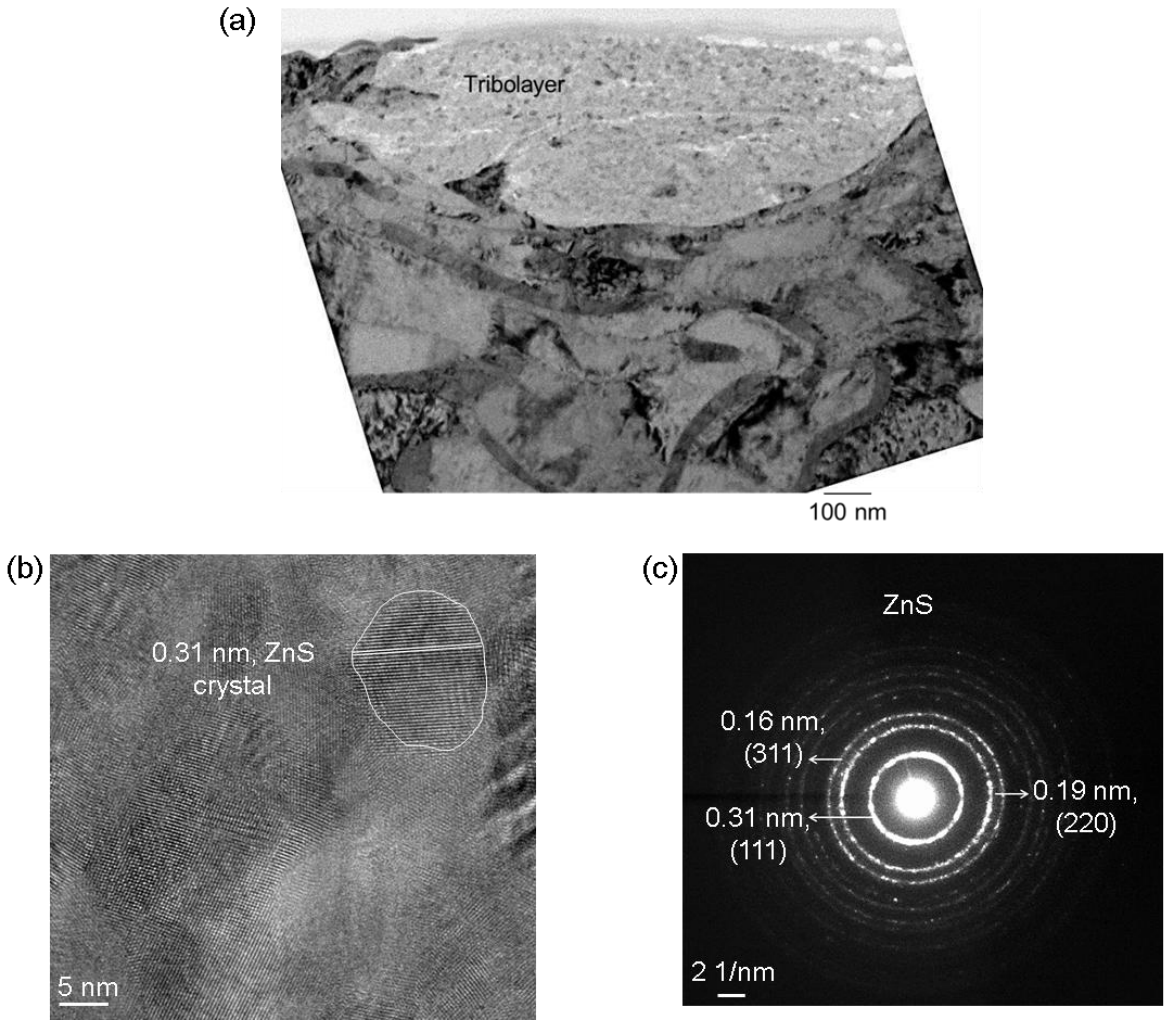

Figure 2.10. (a) Cross-sectional TEM image showing ORL on CI surface tested against NH-DLC for 1×10^4 cycles in diluted oil; (b) High resolution TEM image of the crystalline ZnS region from the ORL with interplanar spacing measured as 0.31 nm; (c) selected Area diffraction pattern of the HR-TEM area shown in (b).

The slight increase in wear loss of CI/CI lubricated systems (Figure 2.5b) at higher cycles maybe attributed to the discontinuous nature of the ORL. On the other hand, the CI/NH-DLC system does not show signs of enhanced localized wear as the amorphous carbon coating prevented metallic contact and inflicted minimal damage to the CI surface. This is evident in Figure 2.5b that shows a near zero wear loss for tests conducted on CI against NH-DLC. Ethanol additions to oil led to significant decrease in the COF of both CI/NH-DLC and CI/CI compared

to tests in unmixed oil (Figure 2.4). It is conceivable that compatibility of the coating chemistry with the lubricant composition plays a prominent role. This will be considered in Section 4.2.

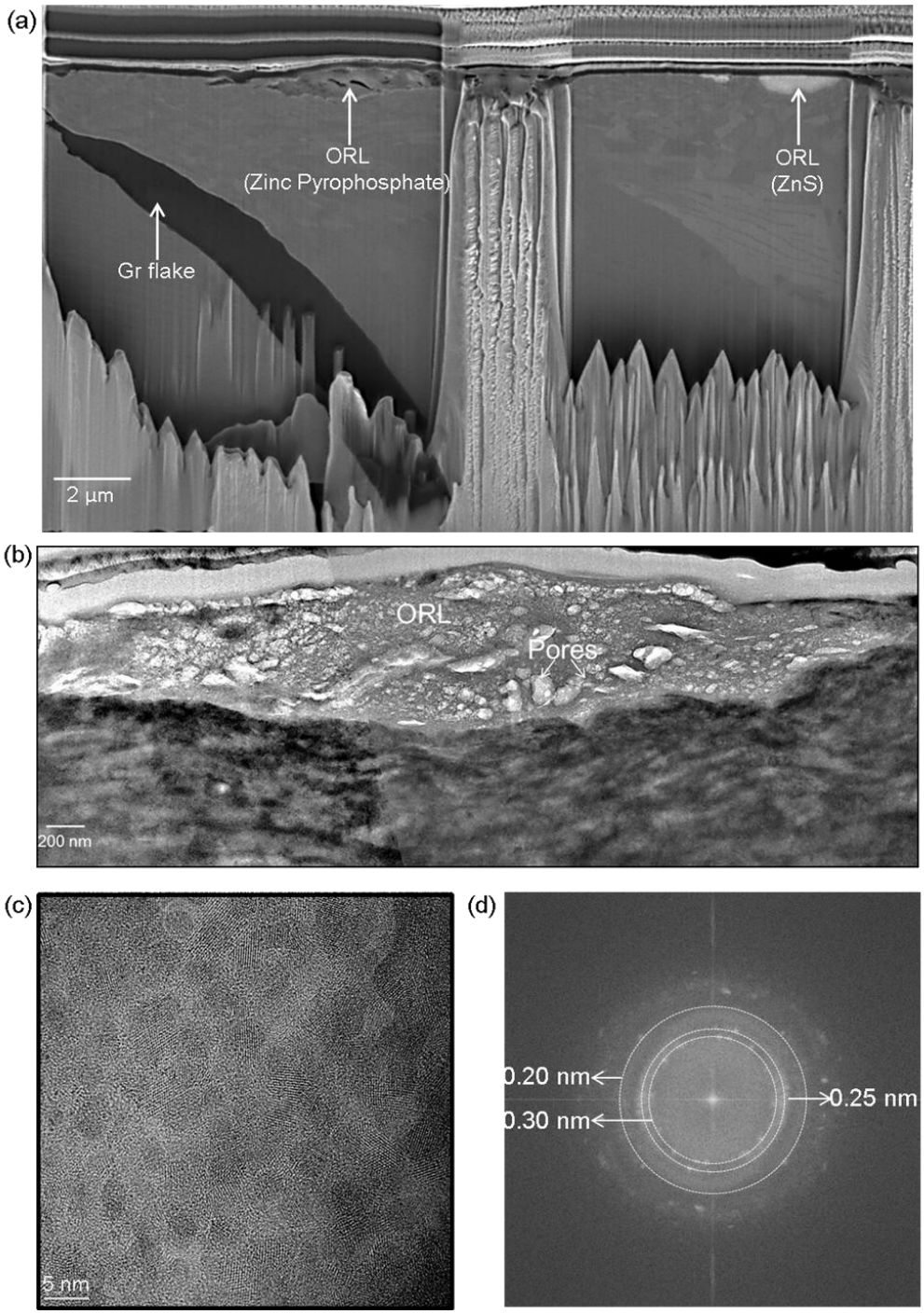

Figure 2.11. (a) Cross-sectional FIB/SEM image showing different antiwear components of the ORL two regions of ORL formed on CI surface tested against NH-DLC for 2×10^5 cycles in diluted oil; (b) brightfield TEM, (c) HR-TEM image and (d) FFT-derived diffraction pattern of the of the region marked as zinc pyrophosphate in (a) showing nano-crystalline structure with interplanar spacing 0.30 nm.

2.4.2 Micromechanisms of Friction

Figure 2.4 shows that addition of ethanol reduced the COF of CI running against NH-DLC which could be attributed to the passivation of the surface carbon atoms. Passivation of amorphous [24–27,62] and crystalline carbon materials [63,64] by OH and H groups [27, 28] has been previously suggested. Carbon atoms on both DLC and graphite flakes could be subjected to passivation and hence the effect of ethanol is to reduce the COF of CI running against both NH-DLC and against itself while the effect is more pronounced in the former tribo system, Figure 2.4. The interactions between carbon atoms and OH molecules were studied using molecular dynamics simulations [27,65]. A methanol molecule sandwiched between two H-DLC surfaces was shown [65] to dissociate and produce OH molecules that terminate the C atoms under the sliding conditions. In this work we provide experimental evidence for the OH passivation of carbon surfaces. Electron energy loss spectroscopy (EELS) conducted on the NH-DLC surfaces sliding in diluted oil provided evidence for this effect (Figure 2.12) where the distinct peak detected at 528 eV is the fingerprint of the OH group [66]. The O-K 1s core loss peak is a typical broad peak appearing in the range 534-538 eV—the presence of H 1s electron (in O-H) is responsible for the additional peak at 528 eV [66,67]. This peak did not appear at depths greater than 20 nm from the surface implying that OH passivation on NH-DLC coating is restricted to surface C atoms. Also, the OH peak (at 528 eV) had a random distribution on the surface and was not as a continuous passivated layer. Accordingly the TEM/EELS analyses provide evidence for the OH passivation mechanism and confirm that only surface carbon atoms of the NH-DLC coating are passivated.

In summary, during boundary lubricated tests carried on CI sliding against NH-DLC the COF was reduced as a result of tribochemical interactions between the NH-DLC coating and the

–OH groups from ethanol mixed with the engine oil. Passivation of the carbon bonds at the surface of NH-DLC coating in contact with CI assisted in reducing the friction. An equally important tribochemical reaction occurred between engine oil containing ZDDP and the CI surface. The formation of an ORL, comprising of an amorphous carbon matrix mixed with the ZDDP decomposition products of zinc sulphides and iron phosphate that act as anti-wear components, was responsible for maintaining low wear of CI surface.

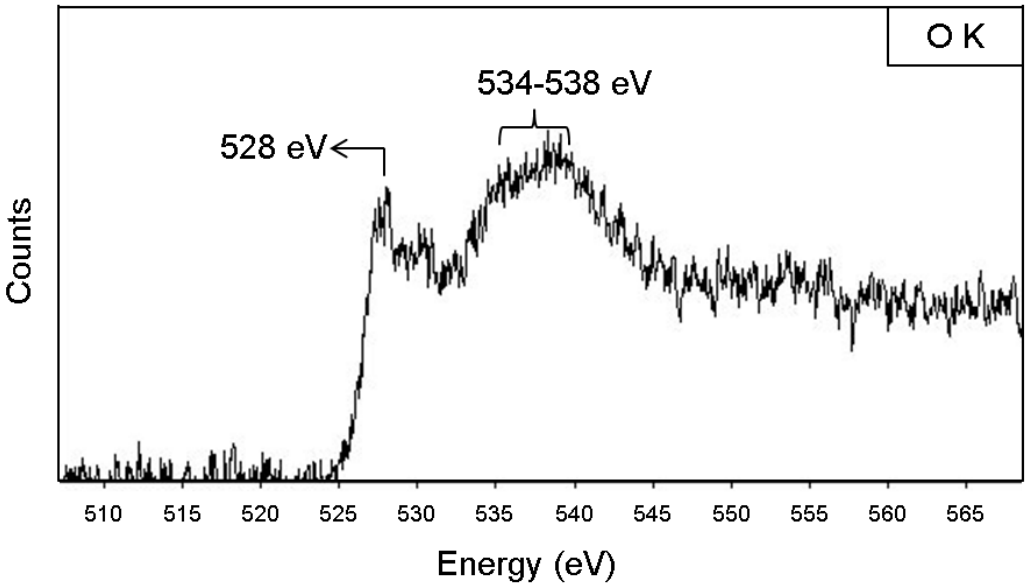

Figure 2.12. EELS O-K edge spectra obtained from the top surface of the NH-DLC coating after testing against CI for 2×10^5 cycles in diluted oil showing peaks at 528 eV, attributed to OH adsorption on NH-DLC, and in the oxygen K edge peaks in the range 534-538 eV.

Summary and Conclusions

The main results from the study of type A cast iron (CI) tested against a non-hydrogenated DLC (NH-DLC) coatings are summarized below:

1. Unlubricated tests of CI against NH-DLC and CI counterface showed lower COF in air with 34% RH compared to tests in nitrogen atmosphere with 0.2% RH indicating passivating effect of moisture on carbon containing sliding components. Results of unlubricated sliding tests performed on CI in constant RH summarized in the form of a COF vs. volumetric wear loss diagram showed that use of NH-DLC counterface resulted in lowest volumetric wear loss and a low COF of 0.28.

2. Boundary lubricated sliding of CI in engine oil tested against NH-DLC showed a lower COF (0.10) and volumetric wear loss (0.5×10^{-4} mm^3) compared to tests against CI counterfaces. The use of oil diluted with ethanol further reduced the COF to 0.08 for CI tested against NH-DLC accompanied by lowest wear loss of at 0.2×10^{-4} mm^3.

3. The wear reduction mechanism consisted of the formation an oil residue layer (ORL) which is a protective tribolayer comprised of anti-wear components including zinc sulphide and zinc pyrophosphate formed by degradation of ZDDP additive in the oil. A further reduction in wear was observed when the oil was diluted using ethanol as the latter facilitated ZDDP degradation. The friction reduction mechanism was identified as OH passivation of the NH-DLC coatings' dangling carbon bonds both in air and in oil diluted with ethanol. Thus, NH-DLC can be used to achieve low friction and wear against CI run in oil mixed with ethanol-based additives.

In conclusion, this manuscript shows that the use of NH DLC counterface against CI system was beneficial to reduce friction and wear. Ethanol dilution of engine oil facilitated ORL

formation and promoted decomposition of anti-wear components. As the COF of CI was the lowest when OH passivation of NH-DLC coating occurred it can be recommended that piston rings coated with NH-DLC run against cast iron liners would be advantageous. Another important implication of this work is that delineating the micromechanisms that are responsible for reduction in friction and wear, is critical for development of appropriate materials and coatings for powertrain components.

Bibliography

[1] S.C. Tung, M.L. McMillan, Automotive tribology overview of current advances and challenges for the future, Tribol. Int. 37 (2004) 517–536.

[2]M. Priest, C.M. Taylor, Automobile engine tribology—approaching the surface, Wear. 241 (2000) 193–203.

[3]D.H. Buckley, Effect of carbon content on friction and wear of cast irons, (1977).

[4]J. Sugishita, S. Fujiyoshi, The effect of cast iron graphites on friction and wear performance I: Graphite film formation on grey cast iron surfaces, Wear. 66 (1981) 209–221.

[5]M. Terheci, R.R. Manory, J.H. Hensler, The friction and wear of automotive grey cast iron under dry sliding conditions Part 1-relationships between wear loss and testing parameters, Wear. 180 (1995) 73–78.

[6]A.R. Riahi, A.T. Alpas, Wear map for grey cast iron, Wear. 255 (2003) 401–409.

[7]H.H. Masjuki, M.A. Maleque, The effect of palm oil diesel fuel contaminated lubricant on sliding wear of cast irons against mild steel, Wear. 198 (1996) 293–299.

[8]P.R. De Silva, M. Priest, P.M. Lee, R.C. Coy, R.I. Taylor, Tribometer investigation of the frictional response of piston rings when lubricated with the separated phases of lubricant contaminated with the gasoline engine biofuel ethanol and water, Tribol. Lett. 43 (2011) 107–120.

[9]M. Chen, A.T. Alpas, Ultra-mild wear of a hypereutectic Al–18.5 wt.% Si alloy, Wear. 265 (2008) 186–195.

[10] M. Chen, X. Meng-Burany, T.A. Perry, A.T. Alpas, Micromechanisms and mechanics of ultra-mild wear in Al–Si alloys, Acta Mater. 56 (2008) 5605–5616.

[11] S.K. Dey, T.A. Perry, A.T. Alpas, Micromechanisms of low load wear in an Al–18.5% Si alloy, Wear. 267 (2009) 515–524.

[12] H. Fujita, H.A. Spikes, The formation of zinc dithiophosphate antiwear films, Proc. Inst. Mech. Eng. Part J J. Eng. Tribol. 218 (2004) 265–278.

[13] H. Spikes, The history and mechanisms of ZDDP, Tribol. Lett. 17 (2004) 469–489.

[14] M. Ooya, Coating of chromium and nitrogen having good wear resistance properties, (1996).

[15] R.D. Anderson, Coated piston ring, (1959).

[16] T.J. Smith, S.J. Sytsma, Piston ring coating, (2006).

[17] C. Friedrich, G. Berg, E. Broszeit, F. Rick, J. Holland, PVD Cr x N coatings for tribological application on piston rings, Surf. Coatings Technol. 97 (1997) 661–668.

[18] G. Ryk, I. Etsion, Testing piston rings with partial laser surface texturing for friction reduction, Wear. 261 (2006) 792–796.

[19] D. Galvan, Y.T. Pei, J.T.M. De Hosson, A. Cavaleiro, Determination of the sp 3 C content of aC films through EELS analysis in the TEM, Surf. Coatings Technol. 200 (2005) 739–743.

[20] L. Ponsonnet, C. Donnet, K. Varlot, J.M. Martin, A. Grill, V. Patel, EELS analysis of hydrogenated diamond-like carbon films, Thin Solid Films. 319 (1998) 97–100.

[21] A.C. Ferrari, J. Robertson, Interpretation of Raman spectra of disordered and amorphous carbon, Phys. Rev. B. 61 (2000) 14095.

[22] C. Donnet, J. Fontaine, A. Grill, T. Le Mogne, The role of hydrogen on the friction mechanism of diamond-like carbon films, Tribol. Lett. 9 (2001) 137–142.

[23] A. Banerji, S. Bhowmick, A.T. Alpas, High temperature tribological behavior of W containing diamond-like carbon (DLC) coating against titanium alloys, Surf. Coatings Technol. 241 (2014) 93–104.

[24] J. Andersson, R.A. Erck, A. Erdemir, Friction of diamond-like carbon films in different atmospheres, Wear. 254 (2003) 1070–1075.

[25] E. Konca, Y.-T. Cheng, A.T. Alpas, Dry sliding behaviour of non-hydrogenated DLC coatings against Al, Cu and Ti in ambient air and argon, Diam. Relat. Mater. 15 (2006) 939–943.

[26] E. Konca, Y.-T. Cheng, A.T. Alpas, Sliding wear of non-hydrogenated diamond-like carbon coatings against magnesium, Surf. Coatings Technol. 201 (2006) 4352–4356.

[27] Y. Qi, E. Konca, A.T. Alpas, Atmospheric effects on the adhesion and friction between non-hydrogenated diamond-like carbon (DLC) coating and aluminum–A first principles investigation, Surf. Sci. 600 (2006) 2955–2965.

[28] S. Bhowmick, A. Banerji, A.T. Alpas, Tribological behavior and machining performance of non-hydrogenated diamond-like carbon coating tested against Ti–6Al–4V: Effect of surface passivation by ethanol, Surf. Coatings Technol. 260 (2014) 290–302.

[29] S. Bhowmick, A. Banerji, M.J. Lukitsch, A.T. Alpas, The high temperature tribological behavior of Si, O containing hydrogenated diamond-like carbon (aC: H/a-Si: O) coating against an aluminum alloy, Wear. 330 (2015) 261–271.

[30] S. Konishi, M. Kano, Y. Yasuda, Y. Mabuchi, T. Hamada, S. Takeshima, K. Tsushima, Low-friction sliding mechanism, (2005).

[31] M. Kano, Y. Yasuda, Y. Okamoto, Y. Mabuchi, T. Hamada, T. Ueno, J. Ye, S. Konishi, S. Takeshima, J.M. Martin, Ultralow friction of DLC in presence of glycerol mono-oleate (GNO), Tribol. Lett. 18 (2005) 245–251.

[32] C. Matta, M.I. De Barros Bouchet, T. Le-Mogne, B. Vachet, J.M. Martin, T. Sagawa, Tribochemistry of tetrahedral hydrogen-free amorphous carbon coatings in the presence of OH-containing lubricants, Lubr. Sci. 20 (2008) 137–149.

[33] X. Hu, H. Wo, G. Han, Y. Lu, Tribochemical effect of impurities in zinc dialkyldithiophosphate in engine oil, Lubr. Sci. 15 (2003) 351–360. https://www.scopus.com/inward/record.uri?eid=2-s2.0-0141563400&partnerID=40&md5=4b51be8ba97c0a66c34dc6042435d5e1.

[34] B. Vengudusamy, J.H. Green, G.D. Lamb, H.A. Spikes, Tribological properties of tribofilms formed from ZDDP in DLC/DLC and DLC/steel contacts, Tribol. Int. 44 (2011) 165–174.

[35] S. Equey, S. Roos, U. Mueller, R. Hauert, N.D. Spencer, R. Crockett, Tribofilm formation from ZnDTP on diamond-like carbon, Wear. 264 (2008) 316–321.

[36] K. Topolovec-Miklozic, F. Lockwood, H. Spikes, Behaviour of boundary lubricating additives on DLC coatings, Wear. 265 (2008) 1893–1901.

[37] B. Podgornik, S. Jacobson, S. Hogmark, Influence of EP additive concentration on the tribological behaviour of DLC-coated steel surfaces, Surf. Coatings Technol. 191 (2005) 357–366.

[38] B. Podgornik, S. Jacobson, S. Hogmark, DLC coating of boundary lubricated components—advantages of coating one of the contact surfaces rather than both or none, Tribol. Int. 36 (2003) 843–849.

[39] H.-S.L.-A. Steels, Properties and Selection: Irons, Steels, and High-Performance Alloys, Vol 1, ASM Handbook, (1990).

[40] A. Banerji, H. Hu, A.T. Alpas, Sliding wear mechanisms of magnesium composites AM60 reinforced with Al 2 O 3 fibres under ultra-mild wear conditions, Wear. 301 (2013) 626–635.

[41] A. Banerji, H. Hu, A.T. Alpas, Ultra-Mild Wear of Al2O3 Fibre and Particle Reinforced Magnesium Matrix Composites, in: Adv. Mater. Res., Trans Tech Publ, 2012: pp. 503–508.

[42] I.M. Hutchings, P. Shipway, Tribology: friction and wear of engineering materials, (1992).

[43] X. Meng-Burany, T.A. Perry, A.K. Sachdev, A.T. Alpas, Subsurface sliding wear damage characterization in Al–Si alloys using focused ion beam and cross-sectional TEM techniques, Wear. 270 (2011) 152–162.

[44] B.K. Yen, B.E. Schwickert, M.F. Toney, Origin of low-friction behavior in graphite investigated by surface x-ray diffraction, Appl. Phys. Lett. 84 (2004) 4702–4704.

[45] D.L.A. De Faria, S. Venâncio Silva, M.T. De Oliveira, Raman microspectroscopy of some iron oxides and oxyhydroxides, J. Raman Spectrosc. 28 (1997) 873–878.

[46] M. Crobu, A. Rossi, F. Mangolini, N.D. Spencer, Chain-length-identification strategy in zinc polyphosphate glasses by means of XPS and ToF-SIMS, Anal. Bioanal. Chem. 403 (2012) 1415–1432.

[47] K. Varlot, J.M. Martin, C. Grossiord, R. Vargiolu, B. Vacher, K. Inoue, A dual-analysis approach in tribochemistry: application to ZDDP/calcium borate additive interactions, Tribol. Lett. 6 (1999) 181–189.

[48] C.C. Chusuei, D.W. Goodman, M.J. Van Stipdonk, D.R. Justes, E.A. Schweikert, Calcium phosphate phase identification using XPS and time-of-flight cluster SIMS, Anal. Chem. 71 (1999) 149–153.

[49] C. Chen, H. Bosse, L. Deters, Effects of various base oils and additives on the tribological behaviour of lubricated aluminium-on-aluminium and steel-on-aluminium contacts, Proc. Inst. Mech. Eng. Part J J. Eng. Tribol. 223 (2009) 571–580.

[50] L. Cizaire, J.M. Martin, T. Le Mogne, E. Gresser, Chemical analysis of overbased calcium sulfonate detergents by coupling XPS, ToF-SIMS, XANES, and EFTEM, Colloids Surfaces A Physicochem. Eng. Asp. 238 (2004) 151–158.

[51] A. Banerji, A. Edrisy, V. Francis, A.T. Alpas, Effect of bio-fuel (E85) addition on lubricated sliding wear mechanisms of a eutectic Al–Si alloy, Wear. 311 (2014) 1–13.

[52] F. Wetscher, R. Pippan, S. Sturm, F. Kauffmann, C. Scheu, G. Dehm, TEM investigations of the structural evolution in a pearlitic steel deformed by high-pressure torsion, Metall. Mater. Trans. A. 37 (2006) 1963–1968.

[53] D.A. Hughes, N. Hansen, High angle boundaries formed by grain subdivision mechanisms, Acta Mater. 45 (1997) 3871–3886.

[54] N.R. Tao, Z.B. Wang, W.P. Tong, M.L. Sui, J. Lu, K. Lu, An investigation of surface nanocrystallization mechanism in Fe induced by surface mechanical attrition treatment, Acta Mater. 50 (2002) 4603–4616.

[55] V.M. Segal, Materials processing by simple shear, Mater. Sci. Eng. A. 197 (1995) 157–164.

[56] D.A. Rigney, Sliding wear of metals, Annu. Rev. Mater. Sci. 18 (1988) 141–163.

[57] A.L. de M. Costa, A.C. da C. Reis, L. Kestens, M.S. Andrade, Ultra grain refinement and hardening of IF-steel during accumulative roll-bonding, Mater. Sci. Eng. A. 406 (2005) 279–285.

[58] P.D. File, Joint committee on powder diffraction standards, ASTM, Philadelphia, Pa. (1967) 9–185.

[59] Y. Wang, Q. Guo, S. Lin, B. Chen, D. Zheng, Growth and properties of ZnO/ZnS core/shell nanostructures, in: J. Phys. Conf. Ser., IOP Publishing, 2009: p. 12018.

[60] H.L. Rittler, Nanocrystalline materials, (1994).

[61] N.J. Mosey, M.H. Müser, T.K. Woo, Molecular mechanisms for the functionality of lubricant additives, Science (80-.). 307 (2005) 1612–1615.

[62] S. Bhowmick, F.G. Sen, A. Banerji, A.T. Alpas, Friction and adhesion of fluorine containing hydrophobic hydrogenated diamond-like carbon (FH-DLC) coating against magnesium alloy AZ91, Surf. Coatings Technol. 267 (2015) 21–31.

[63] S. Bhowmick, A. Banerji, A.T. Alpas, Role of humidity in reducing sliding friction of multilayered graphene, Carbon N. Y. 87 (2015) 374–384.

[64] A. Banerji, S. Bhowmick, M.J. Lukitsch, A.T. Alpas, Friction Behaviour of Multilayered Graphene against Steel, in: MRS Proc., Cambridge Univ Press, 2016: p. imrc2015s6b-o001.

[65] K. Hayashi, S. Sato, S. Bai, Y. Higuchi, N. Ozawa, T. Shimazaki, K. Adachi, J.-M. Martin, M. Kubo, Fate of methanol molecule sandwiched between hydrogen-terminated diamond-like carbon films by tribochemical reactions: tight-binding quantum chemical molecular dynamics study, Faraday Discuss. 156 (2012) 137–146.

[66] R. Wirth, Water in minerals detectable by electron energy-loss spectroscopy EELS, Phys. Chem. Miner. 24 (1997) 561–568.

[67] T. Kendelewicz, P. Liu, C.S. Doyle, G.E. Brown, Spectroscopic study of the reaction of aqueous Cr (VI) with Fe 3 O 4 (111) surfaces, Surf. Sci. 469 (2000) 144–163.

CHAPTER 3

Effect of Biofuel (E85) Addition on Lubricated Sliding Wear Mechanisms of a Eutectic Al-Si Alloy

3.1. Introduction

Reduction of vehicle mass by increasing the use of lightweight Al–Si alloys in engine components has been a key area of focus for the automotive industry over the past decade [1,2]. This has stimulated research on tribological behaviour of cylinder bores made of Al-Si alloys during piston ring contact. The wear resistance provided by Al-Si alloys arise from the specific surface preparation techniques and near-surface microstructural evolution during sliding contact [3–11]. Slattery et al. [3, 4] investigated the micro-mechanisms of wear in linerless engine block made of a near eutectic Al-Si alloy (with Ni and Cu as alloying elements) subjected to dynamometer testing. After nearly 300 hours of testing, the engine showed negligible wear, which was attributed to the combined effects of Si particle exposure (by honing [4]), formation of oil deposits on the contact surface during sliding and generation of a near-surface zone with ultra-fine aluminium grains [3-5, 11]. The very low wear rates (few nanometers of material removal per hour) corresponded to a wear regime described as ultra-mild wear (UMW) [5-7]. The mechanisms responsible for very low wear rates that occur under UMW conditions have been simulated under the laboratory testing conditions for both hypereutectic alloys [8, 9] and near-eutectic Al-Si alloys [10, 11].

3.1.1. Micromechanisms of UMW in Al-Si Alloys

In an engine grade hypereutectic Al-18.5% Si alloy [8], UMW damage was found to be restricted to the top surfaces of large Si particles that acted as load bearing 'asperities' on which a contact pressures as large as 1080 MPa were applied (at 2.0 N) [9]. For alloys with smaller Si

particles like a spray deposited Al-25% Si alloy [5], the Si particles experienced higher contact pressure of 1680 MPa resulting in sinking-in of particles into the Al matrix. An Al-11% Si alloy [5, 10] with a similarly low aspect ratio (~1.5) but lower particle volume fraction experienced 60% higher contact pressure [5]. Consequently an earlier transition occurred, from the first stage of UMW where the protruded particles mitigated the matrix wear, to the UMW II stage where the Si particles were sunken in the matrix and hence UMW II stage defined a running-in period where high volumetric wear occurred. For high sliding cycles a reduction in wear rate was observed (UMW III stage). This was attributed to the formation of a tribolayer called as an oil residue layer (ORL) that covered wear tracks [5, 11]. Underneath the ORL evidence was found for localized severe plastic deformation [12] that manifested itself by the formation of a nanocrystalline Al grain structure [5, 11] which was harder than the initial surface and thought to support the ORL. Thus, once the ORL was established, it acted as an antiwear layer allowing the near-eutectic Al-Si alloys to operate at near zero wear rates similar to the hypereutectic grades.

Details of chemical composition of the ORL formed under boundary lubricating conditions when using synthetic engine oil (containing zinc dialkyldithiophospahte, ZDDP, additives) are not yet to be clarified. The ORL on Al-Si alloys tested at 25 °C consisted of amorphous carbon (detected using EELS) as well as Zn, S, P and Ca [5, 11] compounds which was consistent with tribolayer composition detected on a hypereutectic Al-Si alloy sliding against 34CrNiMo6 steel lubricated by ZDDP (1.5 wt%) in base oil [13]. For the ferrous alloys (AISI 52100 grade), Fujita and Spikes [14] provided evidence that the tribolayers having antiwear properties could form as a result of ZDDP degradation during sliding contact at room temperature. Tribolayers formed on A2 grade steel [15] during sliding at 100 °C were shown to consist of polyphosphate chains with shorter length compared to the antiwear films formed thermally at 200 °C and had lower sulphur

content. Pereira et al. [16] found that the antiwear layer formed on Al-25% Si alloy tested with ZDDP (in base oil) heated at 100 °C had similar chemical composition and Young's modulus to those formed on steel surfaces tested at similar temperature. In ORL formed on tops of Si particles in an Al-12.6% Si alloy tested at 100 °C, using fully formulated synthetic oil (containing ZDDP), nano-crystals of zinc sulphide [17] and zinc polyphosphates with short chain lengths were identified [18]. It was also noted that the tribolayers may act as an energy-absorbing entity and possibly delay Si fracture [19]. The ZDDP degradation mechanism is complex and involves several steps [20,21]. Willermet et al. [20] proposed that ZDDP degradation would start with a ZDDP adsorption process and a reaction with the metal substrate that would lead to the formation of Zn terminated phosphate compounds. Nicholls et al. [21] suggested that antiwear layers produced on Al 319 (Al-7% Si) alloys placed in sliding contact with steel at 60 °C involved formation of a linkage isomer that was absorbed on the metal surface leading to the formation of zinc polyphosphates as well as sulphur species in their reduced form (sulphides).

3.1.2. Effect of E85 Mixed Fuel on Wear

The motivation for using ethanol based bio-fuels in modern powertrains is to provide a clean energy source with reduced carbon and sulphur content and consequently decreasing atmospheric emissions [22]. A common ethanol-gasoline blend that consists of 85% ethanol and 15% gasoline, E85, is known to improve fuel quality by increasing its octane value [23]. Combustion properties of ethanol-gasoline blends have been studied [23–25]. As ethanol has a high latent heat of vaporization and moderately high boiling point (78 °C) it can easily reach the cylinder walls (as well as the crankcase lubrication reservoir) [25]. Ethanol is corrosive to Al due to the presence of azeotropic water. Thus, freshly formulated ethanol fuel blends should contain neutral dry-ethanol having little corrosive effect on Al. A stagnant ethanol-fuel blend would

absorb moisture from the atmosphere posing corrosion related problems that may contribute to surface degradation [22]. There are only few studies in the literature detailing the effect of ethanol on the friction and wear in a piston-cylinder (cast iron) assembly. De Silva et al. [25] reported around 20% reduction in friction of grey cast iron cylinder liner tested against chromium coated piston rings lubricated by a mixture of engine oil and ethanol (5wt%)-water (8 wt%) blend. The authors observed scuffing under under starved lubrication condition when the fuel (ethanol–water mixture)-oil blend was used for grey cast iron top compression ring sliding against chrome coated stainless steel rings [25]. Tung and Gao [26] studied boundary lubricated wear of cast iron cylinder liners using a mixture 2% engine oil and 98% E85 fuel and found that the fuel with higher acidity (pH=4) inflicted more severe wear to the piston rings as well as the liners. Hu et al. [27] explored the effects of alcohol on the ZDDP additives and reported that incorporation of 2-ethylhexanol in the engine oil increased its load-carrying capacity. The authors explained the improved antiwear behaviour of 2-ethylhexanol (upto 8wt%) and ZDDP (in base oil) mix by attributing to the adhesion of polar hydroxyl groups to the metal surface and formation a protective film although no evidence was provided for the same. This warrants for further study into the possible antiwear mechanisms when alcohol is blended with oil containing ZDDP.

The possible expansion of the use of ethanol based fuels in near future prompts the need for a systematic study of the role of ethanol/ gasoline blends (with engine oil) on wear of the Al-Si alloys intended for powertrain applications. Accordingly, this study examines the effect of E85fuel-oil blends on the wear behaviour of an Al-12.6% Si alloy, with a particular focus on the evolution of microstructural and morphological features of the contact surface during sliding. As the UMW regime is of the greatest interest for durability requirements of near eutectic Al-Si

alloys, the sliding experiments conducted here employed testing conditions that simulated the very low wear rates encountered in piston ring cylinder bore contact using an E85-fuel blend mixed with synthetic engine oil at 1:1 ratio (E85/oil (1:1) blend). The wear mechanisms and formation of tribolayers on contact surfaces were studied using a wide range of surface characterization techniques including white light profilometry, cross-sectional FIB/SEM, TEM and XPS. In this way the critical role of the tribolayers formed in presence of E85-oil blends on Al-Si surfaces on controlling wear rates was rationalized.

3.2. Experimental

3.2.1 Description of the Alloy's Microstructure

Samples used for sliding wear tests were taken from sand-cast eutectic Al–Si alloy with a composition, in weight percentage, consisting of 12.6% Si, 0.87% Cu, 0.37% Fe, 0.79% Mn, 0.26% Mg, 1.0% Ni, 0.02% Sr, 0.11% Ti, and the balance Al. This alloy is designated Al–12.6 wt% Si. Fig. 1(a) shows an optical micrograph of the alloy0 s microstructure. The backscattered electron image (BSI) in Fig. 3.1 (b) illustrates the morphology and distribution of the eutectic Si particles along with the intermetallic phases. Figure 3.1(c) shows an EDS elemental map of the BSI image shown in 3.1(b). The Si particles in the alloy had either a needle-like morphology with an aspect ratio of 10.0–15.0 and/or dense Si colonies of fine spherical particles with an aspect ratio of 1.0-2.0, depending on the particles0 locations with respect to the dendritic and interdendritic regions, similar to that observed in [11]. The prominent intermetallic phases in the Al–12.6% Si were Al15(Fe, Mn)3Si2 and AlNi3. The alloy was heat-treated to T7 condition resulting in a bulk hardness of 93.0±1.0 HB (~97 HV) measured using a tungsten carbide indenter at 500 kg load [17]. Six-millimeters-diameter AISI 52100 grade steel balls were used as counterface. The hardness of the AISI 52100 was as 700 HV using a diamond indenter at 25 g

load. The initial average surface roughness of polished AISI 52100 steel balls was determined as 95740 nm using an optical surface profilometer.

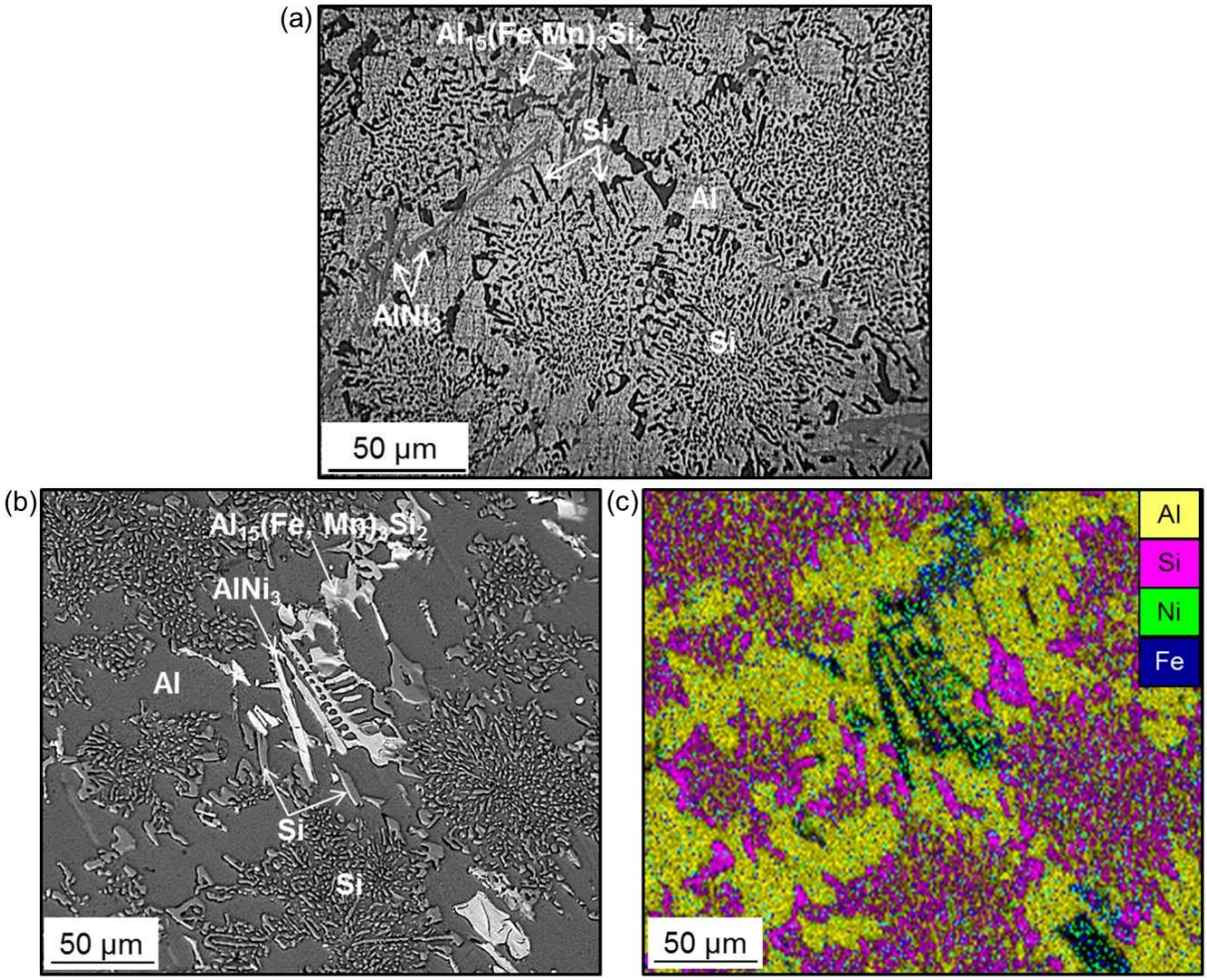

Figure 3.1. (a) Optical micrograph showing the microstructure of Al–12.6% Si alloy etched with 10% NaOH solution. (b) Backscattered electron image (tilted at 45o to the beam) of etched Al–12.6% Si alloy. (c) EDS map of image (b) showing the distribution of Si and Ni, Fe in intermetallic phases.

3.2.2 Wear Test Procedure

Test coupons were in the form of 12.5×12.5 mm square blocks mechanically polished upto 1.0 μm diamond suspension. The Al matrix was etched with 10% NaOH solution as described in [28]. This procedure generated a surface topography where the Si particles became protruded above the Al matrix by 1.66 ± 0.05 μm. The samples were cleaned ultrasonically in ethanol for 20 seconds before each test.

Sliding wear tests were conducted using a unidirectional rotating pin-on-disk tribometer (CSM) at a normal load of 2.0 N and linear sliding speed of 0.05 m/s typically for 2×10^6 cycles. These parameters were selected according to previous laboratory tests that reproduced the wear mechanisms [5, 11] that were observed for eutectic and near-eutectic Al-Si linerless engines [3, 4, 11]. The contact surfaces were lubricated using synthetic engine oil (Mobil 5W30) mixed with E85 fuel blend (85% ethanol and 15% gasoline) at 1:1 ratio; The E85/oil (1:1) blend was continuously stirred and introduced to the surface using a peristaltic pump at a constant flow rate of 0.04 ml/min. In addition, tests were conducted using pure ethanol and also using synthetic engine oil without E85 for comparison of wear rates and mechanisms. The minimum lubricant thickness (h_{min}) and the r.m.s. roughness (r*) between the surfaces in contact were determined. The h_{min}/ r* ratio (λ) [29] was 0.012 for tests that used ethanol, 0.270 for tests with engine oil, and 0.043 for tests with E85/oil (1:1), indicating that boundary lubrication ($\lambda < 1$) condition prevailed at the beginning of all tests.

3.2.3 Volumetric Wear Loss

Conventional mass-loss based wear measurement techniques [30] were not suitable for quantifying the material loss that occurred during in the UMW regime, because of the very small quantities of material that were removed. Wear measurements were made using a white light

optical surface profilometer (WYKO NT-1100), as described in [5]. The amount of material removed was calculated from the cross-sectional areas of the wear tracks by taking the initial matrix elevation as the reference. Measurements were made from six different regions across the wear track and four line profiles were taken from each region, for a total of 24 measurements on each surface. Figure 3.2(a) shows the 3-D profilometer image of worn Al-12.6% Si alloy surface. The locations of Si particles and Al ridges (R) and grooves formed during wear were marked along the line A-A'. Figure 3.2(b) shows the 2-D surface profile of the wear track along the line A-A'.

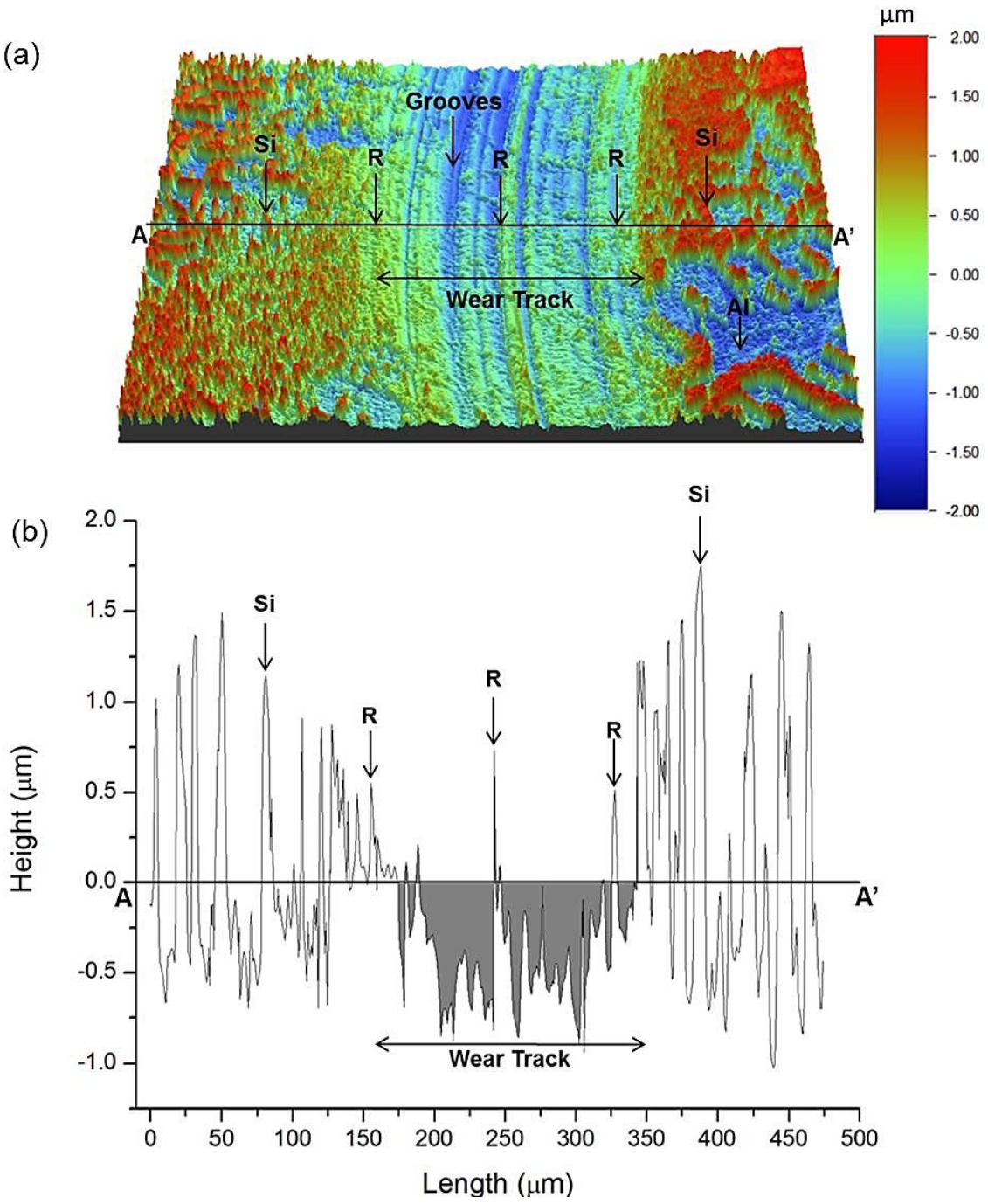

Figure 3.2. (a) 3-D surface profilometer image of Al-12.6% Si alloy showing surface damage after sliding for 1×10^5 cycles. The line profile indicated by A-A' shows the location of Si particles and Al ridges (R) inside the wear track. Si particles and Al matrix in the unworn region are also marked. (b) Cross-sectional profile along A-A' showing matching locations of Si particles and Al ridges (R) corresponding to their locations labelled in Figure 3.2(a).

3.2.4 Examination of Worn Surfaces

The details of surface damage were studied using JEOL 6400 and FEI Quanta 200 FEG scanning electron microscopes equipped with an energy-dispersive X-ray EDAX SiLi Detector spectrometer, having a super ultra thin window (SUTW). Chemical analyses of the worn surface were conducted by X-ray photoelectron spectroscopy (XPS) using a Kratos Axis Ultra X-ray photoelectron spectrometer. The survey scan analyses were carried out with a pass energy of 160 eV, while the high-resolution analyses were carried out with a pass energy of 40 eV. Subsurface damage was examined by transmission electron microscopy (JEOL JEM-2100F). The TEM samples were prepared by the lift-out technique using a gallium ion source (30kV) [11]. Prior to the ion milling process, the surfaces were protected by sputtering them with a layer of carbon.

3.3. Results

The wear test results are presented in the next section, followed by the results of electron microscopic investigation and spectroscopic analyses of the ORL formed on the worn surfaces. These investigations helped to identify micromechanisms of wear operating during each stages of UMW when an E85/oil (1:1) blend was used. It is to be noted that the coefficient of friction recorded for each test was 0.12±0.1, regardless of whether the lubricant mixture was the E85/oil (1:1) blend or engine oil alone.

3.3.1 Volumetric Wear Loss

The volumetric wear loss of Al-12.6% Si tested using E85/oil (1:1) blend is plotted in Figure 3.3 (solid line) as a function of sliding cycles. The highest volumetric wear calculated was 2.0×10^{-9} mm^3/cycle (for UMW II stage), confirming that UMW conditions were maintained throughout the tests. Figure 3.3 identifies the three distinct stages of UMW regime. The initial stage, UMW I, corresponds to short sliding cycles ($\leq10^4$ cycles), where no material loss could be

measured, and thus, a near zero wear rate was recorded. This was followed by a stage characterized by rapid material removal (UMW II) or the running-in stage. However, the wear in UMW II stage did not endure at high sliding cycles. At sliding cycles $\geq 10^5$, the volumetric wear loss decreased, and a steady-state wear stage with near zero wear rate was noted again, UMW III that persisted for the remainder of the test (up to 2×10^6 cycles).

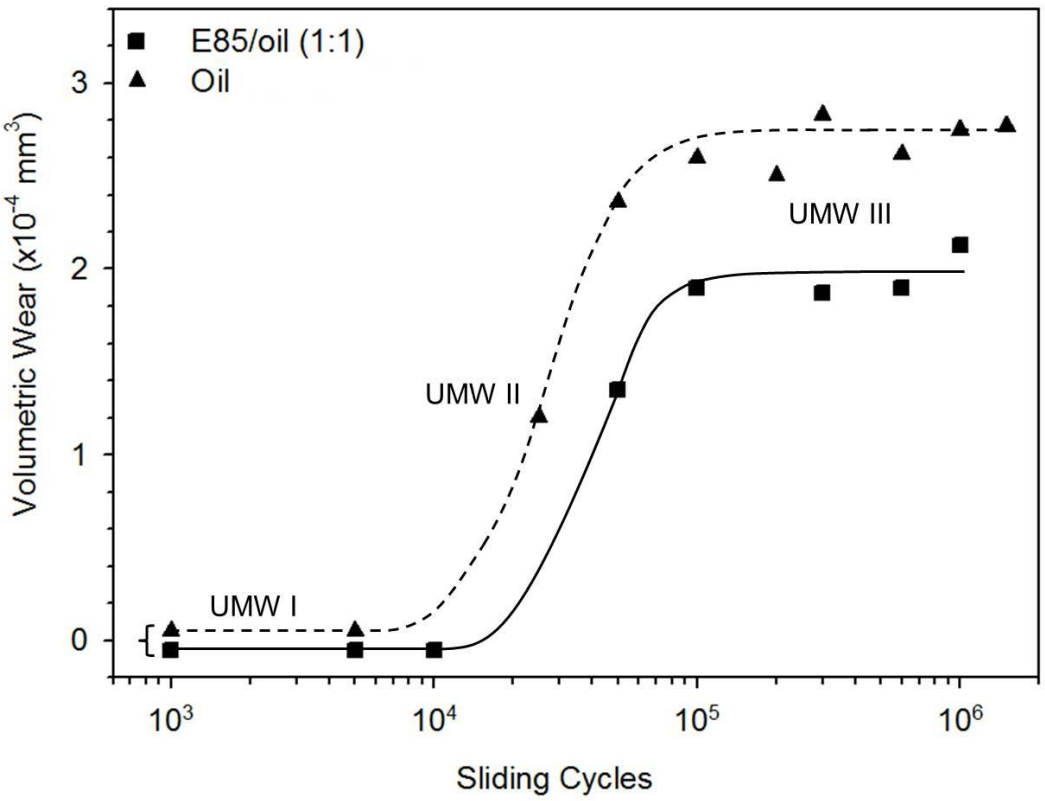

Figure 3.3. Variation of volumetric wear of Al-12.6% Si with sliding cycles tested using E85/oil (1:1) blend (solid lines) and unmixed oil (dashed lines) at a constant load of 2.0 N and sliding speed of 5.0 cm/s. The three stages of UMW are identified for both conditions.

Figure 3.3 also shows the variation in the volumetric wear of Al-12.6% Si tested under the identical loading conditions, but using the synthetic motor oil, without the addition of E85, for comparison. Therefore, addition of E85 to the synthetic motor oil did not change the wear

behaviour, as the same three UMW stages were identified. However, a slightly higher total wear was note in the case of synthetic oil without E85 addition, a point that will be discussed in Section 3.4.

Comparisons were also made with a series of wear tests conducted using ethanol unblended with oil. The UMW behaviour was not observed in this case; as Figure 4(a) shows, the rate of material loss for tests conducted with unmixed ethanol was at least one order of magnitude higher than the rates generated in tests with the E85/oil (1:1) blend. For example, after 10^5 cycles, the volumetric wear loss was 1.9×10^{-3} mm^3 for tests with unmixed ethanol, whereas for tests with the E85/oil (1:1) blend the volumetric wear loss was 2.0×10^{-4} mm^3. Figure 3.4(b) is a secondary electron image of the wear track at the surface of Al-12.6% Si after sliding for 10^4 sliding cycles that shows significant damage and formation of layers at the surface. Figure 3.4(c) shows a 3D optical profilometry image of the wear track that was taken after sliding for 10^5 sliding cycles. The wear track measured 2.2 μm in depth and 350 μm in width. A high concentration of oxygen was detected using semi-quantitative EDS on the surface of the wear track, suggesting the formation of aluminum oxide and iron oxide. Oxide layers can detach from the surface and act as third-body abrasives during sliding wear resulting in high wear rates shown in Figure 3.4(a).

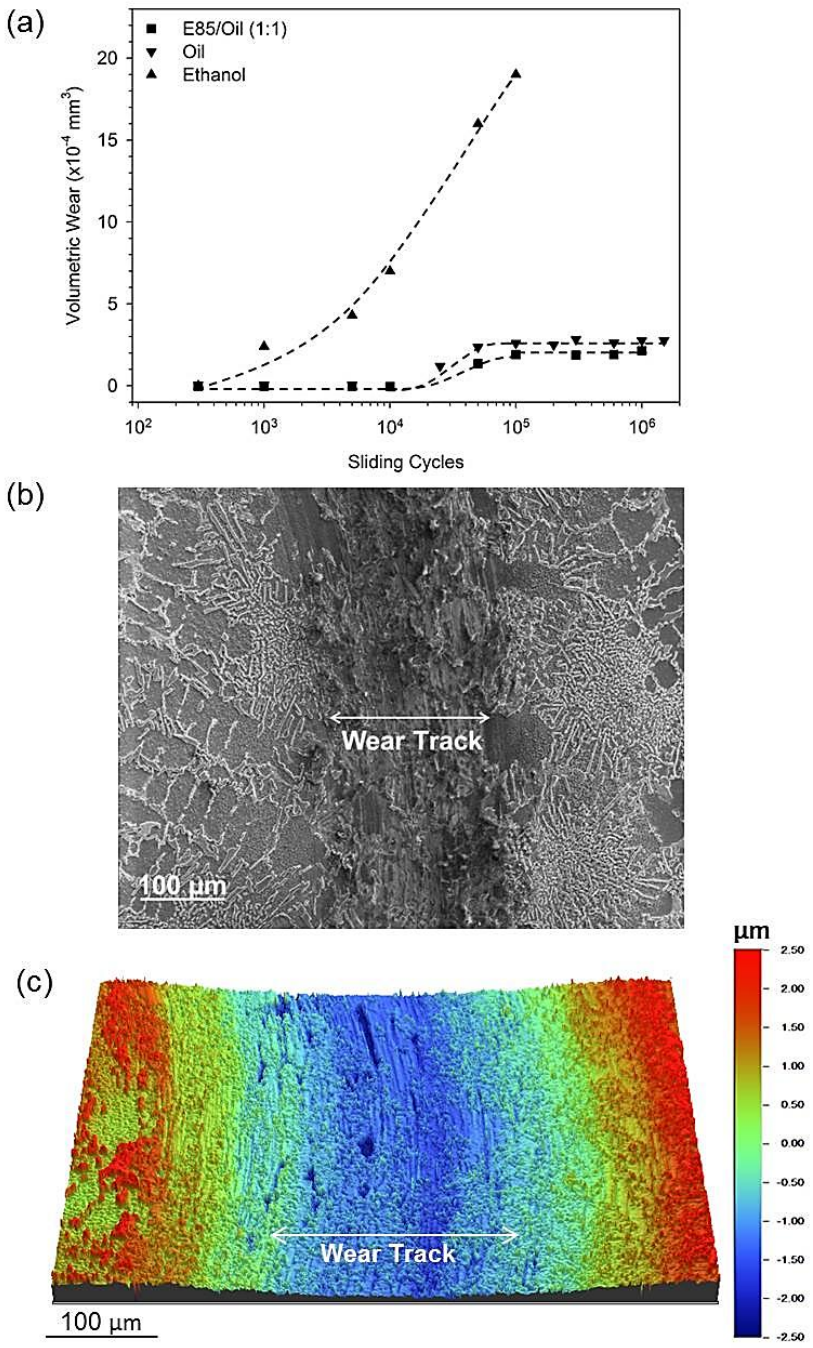

Figure 3.4. (a) Variation of volumetric wear of Al-12.6% Si with sliding cycles using unmixed ethanol at 2.0 N load and a sliding speed of 5 cm/s. Wear of the alloy tested using E85/oil (1:1) blend and unmixed oil are shown for comparison. (b) Secondary electron image (SEI) of the wear track after sliding for 10^4 cycles and (c) 3-D surface profilometry image of the wear track after sliding for 10^5 cycles for tests with ethanol.

The oxide formation observed in tests that used unmixed ethanol was not observed in the tests with either E85/oil (1:1) blend or synthetic motor oil alone. The two curves obtained for the latter conditions were similar and typical of the wear behaviour of the UMW regime of the near-eutectic and eutectic Al–Si alloys previously investigated [5, 16]. The wear mechanisms that occurred in each of three stages of UMW are described in detail in the Sections 3.2-3.4, following which the effect of E85 addition on these mechanisms is discussed in detail.

3.3.2 Ultra-Mild Wear Stage I

In UMW I stage the wear damage on the surface of the Al-12.6% Si alloy tested in E85/oil (1:1) blend manifested itself in the form of scratches on the tops of the Si particles. Meanwhile, the Al matrix remained unscathed during sliding contact, with the exception of regions near the Si particles. Other typical features of damage included Si particle fracture, and equally important, sinking of the particles into the Al matrix. These damage features are depicted in the secondary electron image (SEI) in Figure 3.5(a) and backscattered electron image (BEI) in Figure 3.5(b) of the same area of the wear track, each emphasizing different aspects of damage due to wear in UMW I stage. The wear marks on the surfaces of the Si particles can be seen clearly in Figure 5(a). Fractured Si particles are shown in both Figures 3.5(a) and (b). Other particles with wear scars were intact, but appeared to be embedded in the Al matrix. The matrix material formed pile-ups adjacent to the sunken particles, as shown in these images. The pile-ups were exposed to sliding contact damage, as revealed by the wear marks observed on these elevated portions of the matrix. Clearly, the rest of the matrix, away from the pile-ups around the sunken particles, displayed the original, undamaged surface (etched) morphology. These features were typical of

damage during the initial cycles (i.e., up to 10^4 sliding cycles), when only UMW I stage was observed.

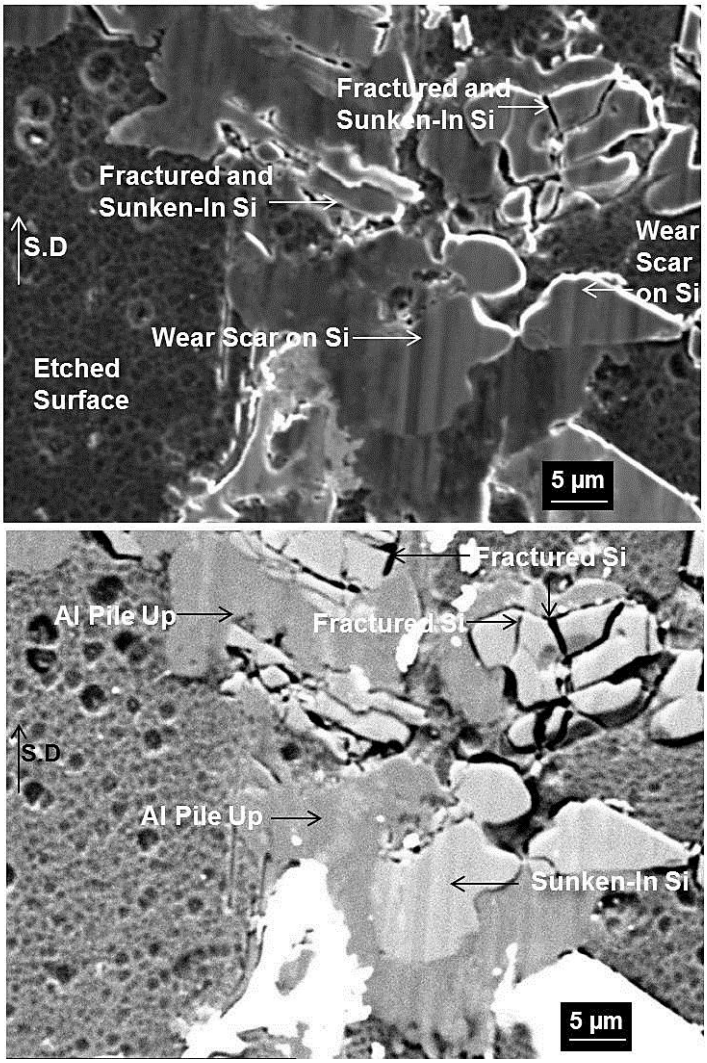

Figure 3.5. . Typical surface damage features of Al–12.6% Si after sliding for 5 103 cycles (UMW I) tested using E85/oil (1:1) blend. (a) SEI image showing wear scar on a Si particle (in the middle) without fracture and also sunken-in fractured Si particles (middle–top and top-right). (b) BSI of the same area showing sunken-in Si particles and adjacent Al pile-ups. Fractured Si particles are marked on both images.

3.3.3 Ultra-Mild Wear Stages II and III

The transition from UMW I to UMW II coincided with rapid removal of material from the Al–Si surface, as the Al matrix was no longer protected effectively by the Si particles, as most of them were either fractured and/or sunken into the matrix. Figure 3.3 shows that after 5×10^{4} cycles, the volumetric wear of Al–12% Si tested in E85/oil (1:1) blend was 1.4×10^{-4} mm^3—a considerable increase from the near zero wear in UMW I. The wear rates in UMW II (the slopes of volumetric wear vs. sliding cycle curve for Al–12% Si) were similar namely, 5.7×10^{-9} mm^3/cycles for tests carried out in presence of unmixed synthetic oil and 3.5×10^{-9} mm^3/cycles for E85/oil (1:1) blend. An important distinction however was that the total wear at the end of UMW II (10^5 cycles) in tests with the E85/oil (1:1) blend was less than that that observed for tests conducted in unmixed sythetic oil. At the onset of UMW III, the volumetric wear loss for tests with the E85/oil (1:1) blend was 1.8×10^{-4} mm^3 while for the unmixed oil a volumetric wear loss of 2.6×10^{-4} $mm^3$was recorded.

The UMW III stage initiated after approximately 10^5 cycles, when the wear rates were reduced once more to near zero. Once UMW III stage was established, steady-state conditions were maintained, regardless of the amount of prior wear. The microstructural features and steady-state wear observed in the UMW III stage using E85/oil (1:1) blend were similar to those observed in linerless IC engines made of near-eutectic Al–Si alloy subjected to dynamometer tests [3, 4, 11].

The above observations can be better construed by considering the changes in the wear-induced surface morphologies. As indicated previously, the rapid increase in wear during UMW II was due to the soft Al matrix coming into contact with the counterface. The Si particles that

became embedded in the Al at the end of UMW I was no longer effective as load-bearing elements. As a result, the matrix began to exhibit signs of sliding damage in the form of formation of longitudinal grooves extending along the sliding direction. The progression of wear can be seen in Figures 3.6(a)–(c), which provides 3-D surface profilometry images at selected sliding distances, illustrating the typical changes in wear track morphologies in each of the UMW stages. Si particles inside the wear track that stood above the Al in the UMW I stage can be seen in Figure 3.6(a). Most of these Si particles had elevations lower than their initial height, thus already partially embedded in the matrix and formed the pile ups described previously. On average, the particle heights within the wear track were 0.6± 0.2 μm lower than those outside the wear track, for which the (unworn) Si elevation was 1.6±0.2 μm. Overall, the wear track was only faintly detectable. In contrast, Figure 3.6(b) shows a representative surface profilometry image taken after sliding for 1×10^5 cycles, which corresponds to the later period of UMW II and indicates that the damage was more conspicuous across the wear track. Sliding wear induced damage to the contact surface of the Al-12.6% Si alloy in the form of narrow, long grooves that can be seen clearly in this image. The Si particles within the wear track were embedded in the matrix as no elevation difference could be discerned between the matrix and the particles. Figure 3.6(c) shows that in UMW III, there is no further damage to the contact surface and, in fact, the wear track appeared to be smoother than for UMW II, as the grooves that formed during the latter were no longer identifiable.

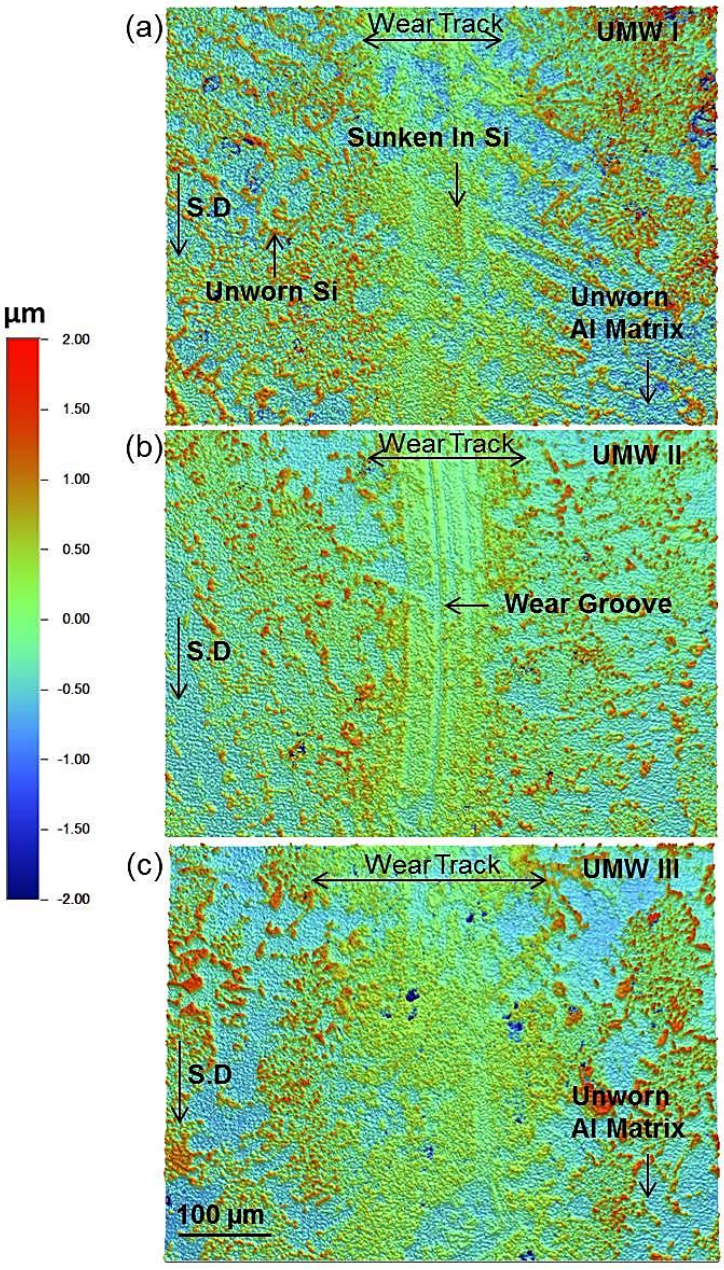

Figure 3.6. 3-D surface profilometry images of Al-12.6% Si tested in E85/oil (1:1) blend showing surface evolution after sliding for characteristic cycles representing each UMW regime (WT shows the width of wear track). (a) 10^4 cycles showing the protruded Si particles (in red) outside the wear track become embedded in the Al matrix within the wear track. (b) 10^5 cycles showing that wear marks on the Al and sunken-in Si particles. (c) 6×10^5 cycles showing the wear track with smoother appearance compared to (b). The micron bar shown in (c) and the height bar shown on the right apply to all figures.

The reduction in wear rates and smoothing of the morphology of the wear tracks observed in UMW III was due to the formation of a tribolayer during sliding contact. This tribolayer can be called an oil residue layer, ORL, in reference to the information provided in Fig. 3.7 and in subsequent figures. The morphology of the ORL generated on the surface of Al–12.6% Si during tests conducted with the E85/oil (1:1) blend is shown in Fig. 3.7(a). A similar ORL morphology was detected on the surface of Al–12.6% Si alloy tested using synthetic engine oil without E85 addition. A characteristic surface morphology generated during UMW III, with polished, glaze-like appearance is shown in Fig. 3.7(b) after sliding for 3×10^5 cycles. Fig. 3.7(c) shows a higher magnification BSI of Al–12.6% Si surface morphology generated when the alloy was tested using E85/oil (1:1) blend and indicated again that the worn surface was covered by an ORL. EDS spectrum obtained from region (d), shown in Fig. 7(d) was representative as it depicts ORL constituents namely, Zn, S, P, Ca, C, O—most of which may have originated from the oil and ZDDP additive—along with Al, Si, and Mg, which were part of the base alloy. The composition of the ORL is consistent with the analyses performed in previous studies [5,11]. Fe (oxide) that was observed in certain regions of the wear track (Fig. 3.7(c)) and identified by EDS (Fig. 3.7(e)) was likely formed at an earlier stage of sliding as a result of abrasion of steel counterface by the protruded Si particles. The origin of the ORL can be traced to UMW II, as small patches of this layer started forming on both Al and Si particles during the high wear that occurred at this stage. Once the ORL became established and covered the contact surface, the high wear in UMW II stopped, and the surfaces were protected from additional wear, establishing the near zero wear rates of the UMW III stage.

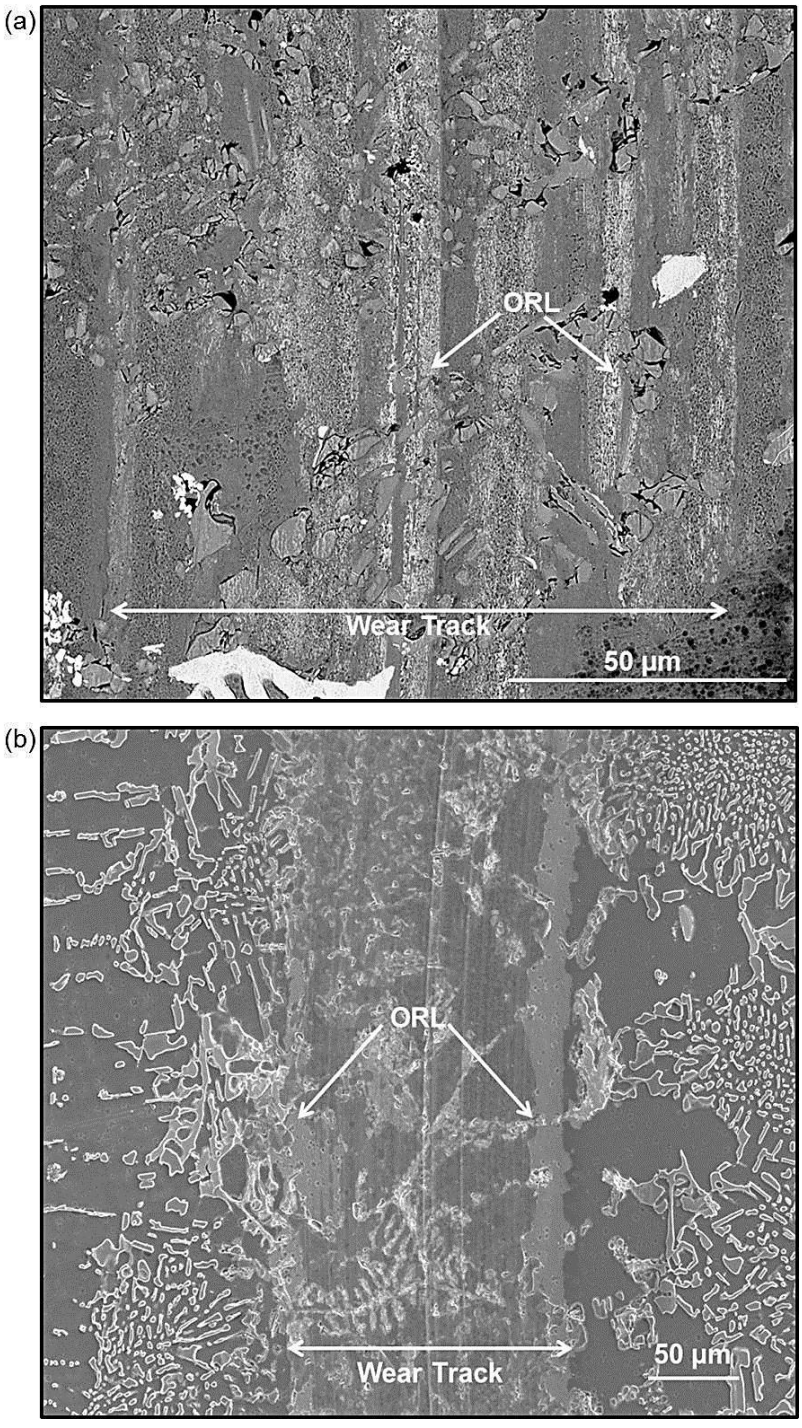
(a)
ORL
Wear Track
50 µm
(b)
ORL
Wear Track
50 µm

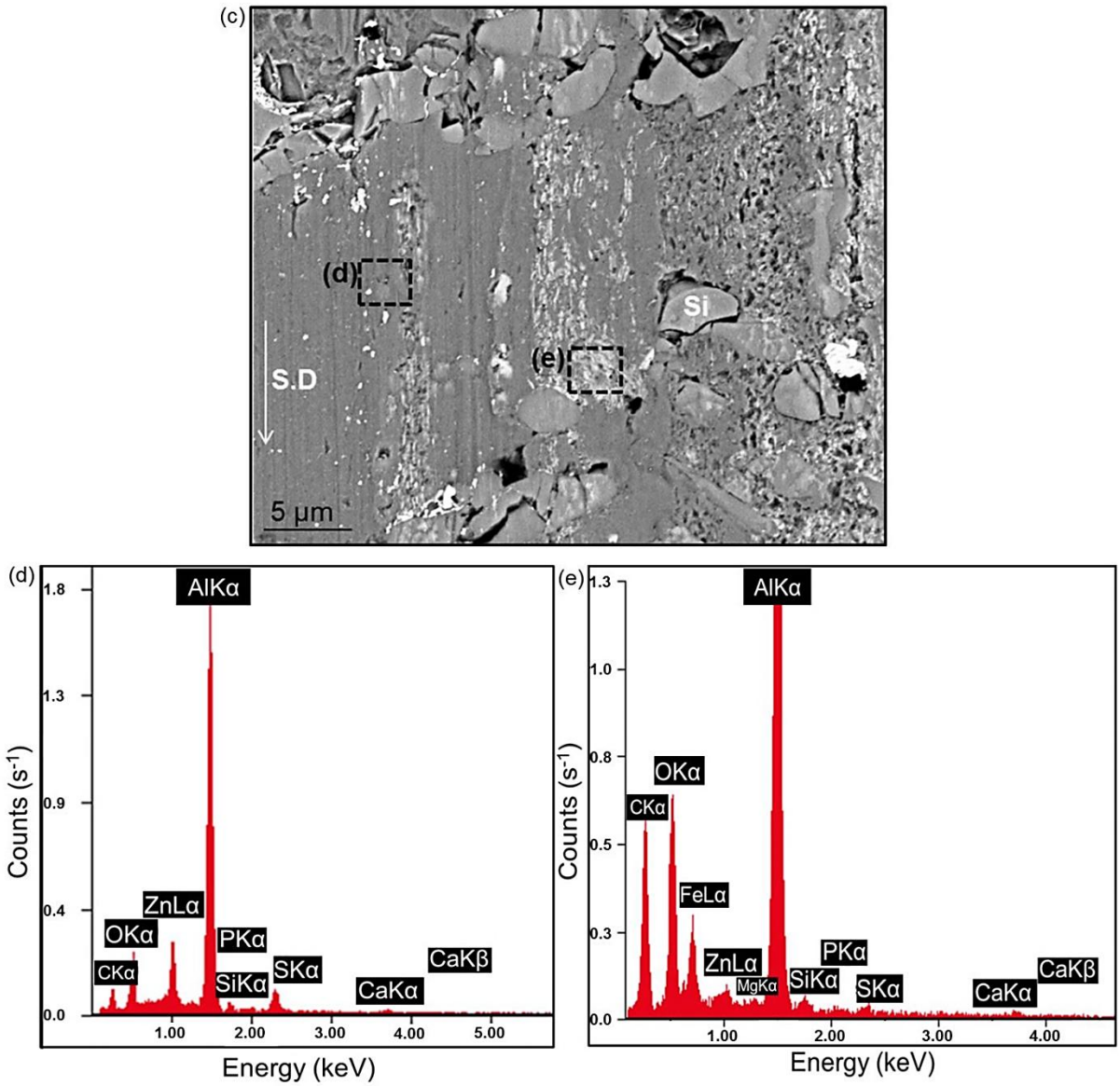

Figure 3.7. (a) BSI image of wear surface morphology of Al–12.6% Si tested using E85/oil (1:1) blend after sliding for 3 105 cycles showing formation of ORL on the wear track. (b) SEI image of wear surface morphology of Al–12.6% Si tested in unmixed oil after sliding for 3 105 cycles also showing ORL. (c) Higher magnification BSI image of wear surface morphology of Al–12.6% Si tested in E85/oil (1:1) blend. (d) EDS spectrum of the ORL taken from region marked (d) in (c). (e) EDS spectrum of the ORL taken from region marked (e) in (c) which additionally shows the presence of Fe, possibly due to abrasion of counterface by Si particles.

3.3.4. TEM Analyses of ORL and Subsurface Microstructure

The wear track generated on the surface of the Al-12.6% Si alloy tested using E85/oil (1:1) blend after sliding for 3×10^5 cycles, was sectioned by means of FIB milling, to expose the cross-sectional view of the ORL and the near-surface Al and Si microstructures underneath this layer. The location of the FIB cross-section taken from the mid-section of the wear track in a direction parallel to the sliding direction (a longitudinal cross-section) is marked in Figure 3.8(a). Figure 3.8(b) shows the cross-sectional TEM micrograph of the ORL and the underlying microstructure. In this section, the thickness of the ORL varied between 50 and 120 nm, and the layer spread over both the Si particles and the Al matrix surface. Oil residues could also be detected in the crack that formed between the sunken silicon and the matrix. Immediately under the ORL, a zone that exhibited nanocrystalline Al, with an average size of 50–300 nm, was detected. This observation is consistent with the previous observations with tests conducted under the same loading and synthetic oil lubrication conditions, but without the E85 addition [5, 11]. The formation of the small, equiaxed grains was attributed to the generation of large subsurface strains during sliding contact and the existence of a hydrostatic stress field [5]. As indicated in Figure 3.8(b), the nanocrystalline grains were formed within a narrow subsurface zone of 500 nm. The undeformed bulk Al alloy microstructure can be seen at approximately 700 nm below the ORL. It is suggested that the sliding-induced microstructure that evolved in UMW II was responsible for supporting the ORL, and hence, maintaining the steady–state wear, with near zero rates in UMW III. In the UMW II stage, large strains responsible for grain subdivision [12] and nanocrystalline grain formation were developed upon counterface to matrix contact, and the formation of this zone (which should be harder than the bulk [5]) may play an important part in the subsequent stabilization of UMW.

Fig. 3.8(c) shows a high resolution TEM (HR-TEM) image of the interface between the ORL and the nanocrystalline Al grains of the deformed matrix. Lattice images of {111} Al crystal planes, with an interplanar spacing (d-spacing) of 0.23 nm are marked. Inside the region marked by the dashed line, multiple crystal lattice images of arising from different components of the ORL were observed. The thorough indexing of this region was not straightforward. Using fast Fourier transform (FFT) derived diffraction patterns in Fig. 3.8(d) obtained from the regions marked as (d), the d-spacing values that corresponded to 0.23 nm were identified and assigned to {111} planes of Al [31]. This indicated that Al debris detached from the matrix were mixed with ORL. In addition, an interplanar distance of 0.31 nm was recorded, which corresponded to the dspacing between the {111} planes of Si [32]. Hence some nanocrystalline Si fragments were also mixed with ORL. The d-spacing of 0.32 nm in Fig. 3.8(d) could be assigned to the {111} planes of ZnO with the zinc blende structure [33] whereas the d-spacing of 0.33 nm provided a good match with the {100} planes of wurtzite structure of ZnS [34]. On the other hand, the HR-TEM image obtained from the region marked (e) in Fig. 3.8(c) provided evidence for amorphous regions in the ORL as shown in Fig. 3.8(e). The amorphous region is marked on the top left corner of Fig. 8(e) and the corresponding FFT image is given in Fig. 3.8(f). Previous EELS analyses [11] found amorphous carbon in ORL. It is conceivable that phosphates (of Zn or Ca) formed by degradation of ZDDP may also be part of the amorphous part of ORL [35–37]. FFT derived diffraction pattern taken from the crystalline region marked (g) in Fig. 3.8(e) suggests d-spacing values of 0.33 nm and 0.19 nm (Fig. 3.8 (g)) that corresponded to (111) and (110) planes of ZnS. In summary, FFT analyses of the ORL suggested that ORL had a complex structure consisting of nano-fragments of Al, Si mixed with crystalline ZnO and ZnS in an amorphous matrix with C and possibly phosphates. EELS analyses on the ORL are needed to clarify the

composition of the amorphous regions. Evidence for phosphates is given in Figs. 3.9 and 3.10 (see Section 3.5).

(a)

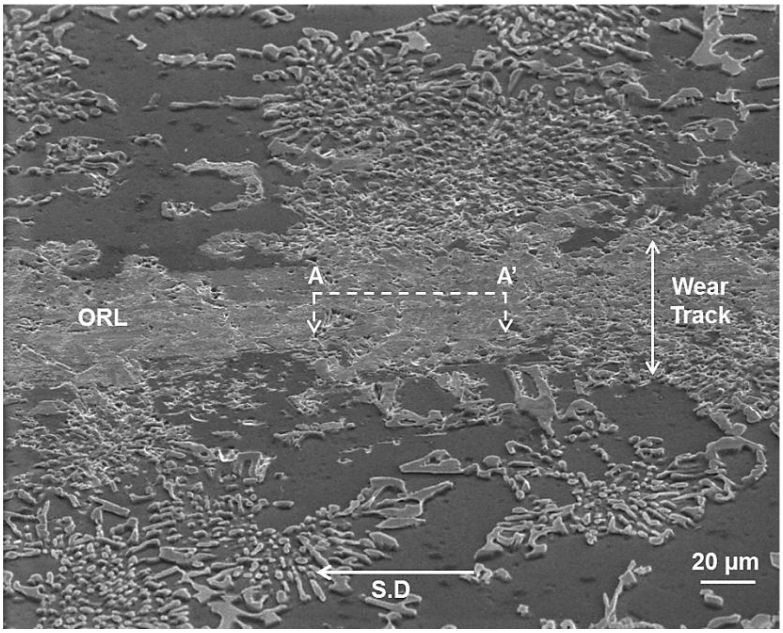

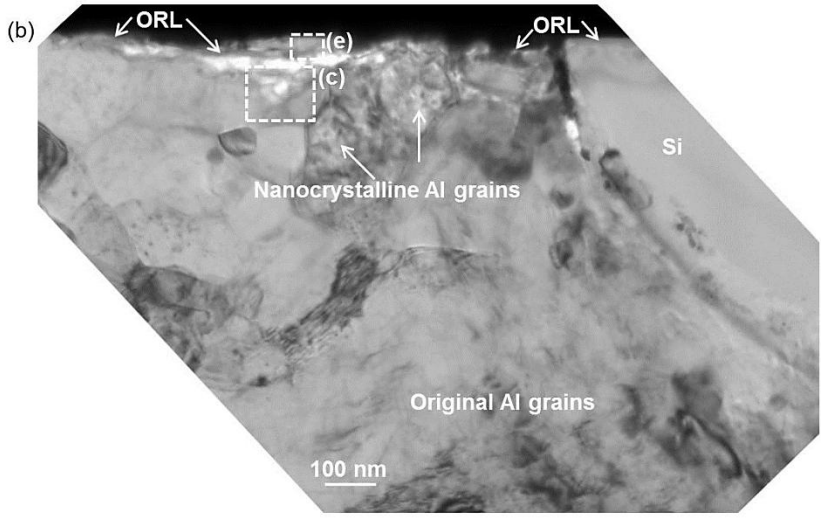
(b)
ORL
ORL
(e)
(c)
Si
Nanocrystalline Al grains
Original Al grains
100 nm

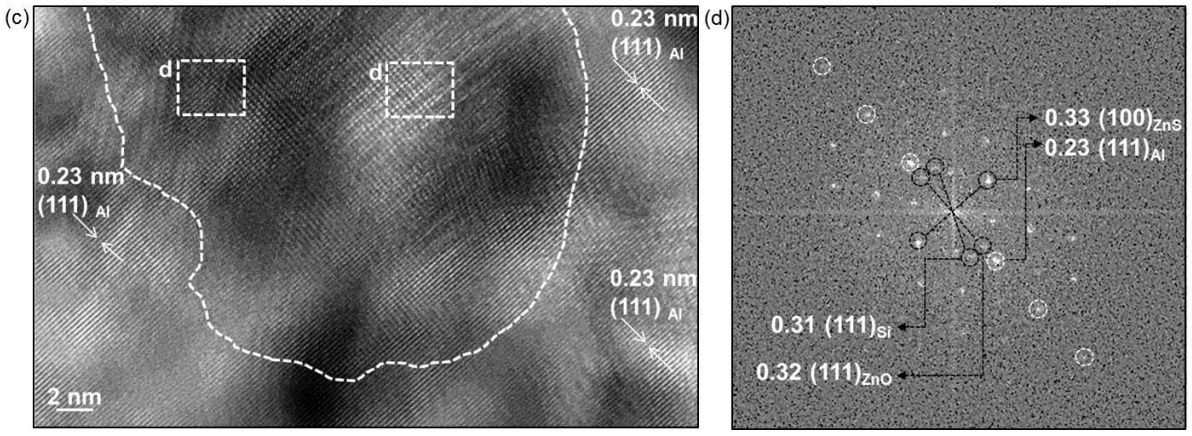
(c)
d
d
0.23 nm
(111) Al
0.23 nm
(111) Al
0.23 nm
(111) Al
2 nm
(d)
0.33 (100)ZnS
0.23 (111)Al
0.31 (111)Si
0.32 (111)ZnO

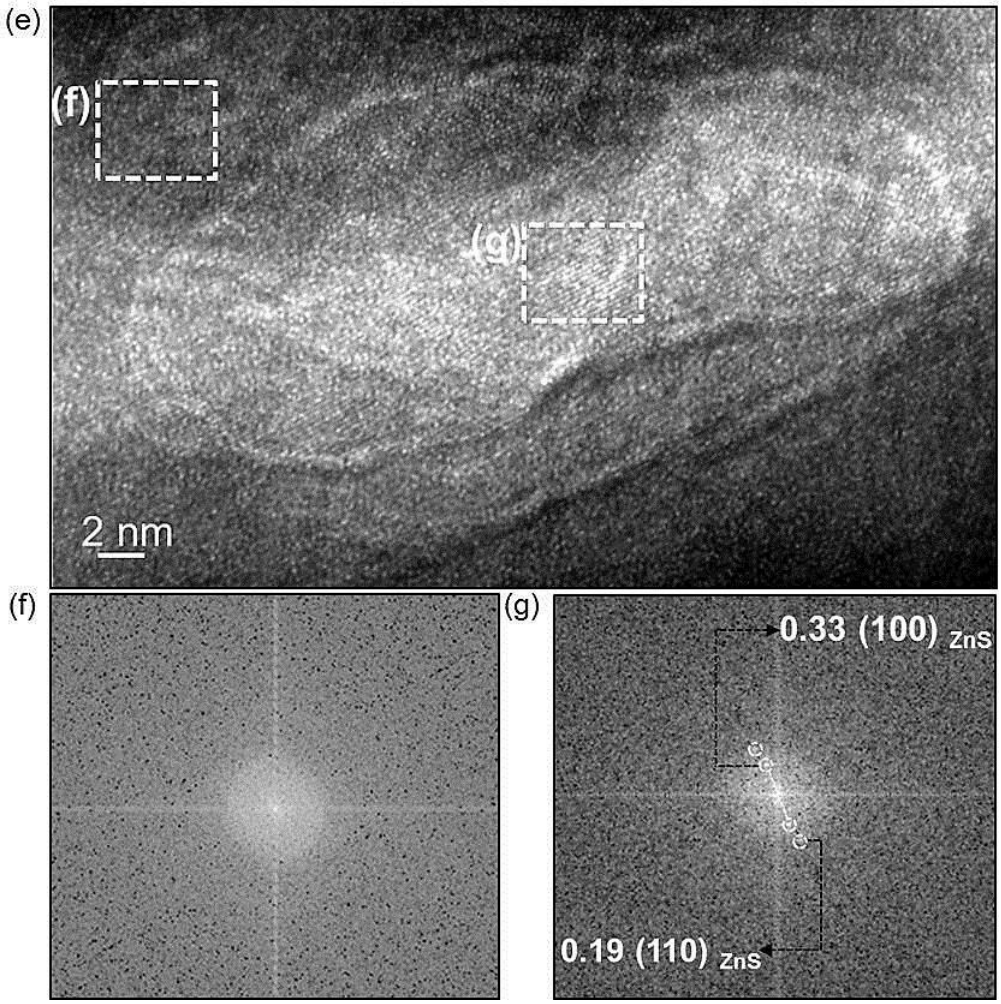

Figure 3.8. (a) SEI of the wear track (tilted at 54o to the beam) of a sample tested for 3 105 sliding cycles using E85/oil (1:1) blend. (b) Cross-sectional TEM micrograph taken from A–A0 in (a) showing the ORL that covered Si surfaces and the nanocrystalline Al grains. (c) HR-TEM image obtained from the interface region indicated in plate (b). The dashed line demarcates the approximate boundary between nanocrystalline Al and ORL. (d) FFT derived diffraction patterns of the regions marked as (d) in plate (c) revealing some components of ORL. (e) HR-TEM image obtained from ORL showing an amorphous region (from (e) in plate b) on top left marked as (f) and crystalline region marked as (g). (f) FFT derived diffraction patterns of the regions marked as (f) in plate (e) showing a diffuse halo indicative of amorphous regions in ORL. (g) FFT derived diffraction patterns of the regions marked as (g) in plate (e). Interplanar distances in the plates (c), (d) and (g) are in nanometers.

3.3.5 XPS Analyses of ORL

High-resolution XPS spectra acquired from the wear track of the Al-12.6% Si samples tested both using E85/oil (1:1) blend, and synthetic oil without E85 is shown in Figures 9(a–c). The XPS spectra provided detailed semi-quantitative compositional analyses (in atomic percentages) of the ORL. Figures 9(a–c) show the P, S, and O spectra obtained from ORL in tests carried out using the E85/oil (1:1) blend. By analyzing the XPS spectra of Zn, Ca, and C (Figures 10 [a–d]), the chemical compounds that may have formed could be elucidated.

3.3.5.1 XPS Spectra of Negatively Charged Radicals

XPS Spectra of Phosphorus: Figure 3.9(a) shows the P $2p_{3/2}$ and $2p_{1/2}$ peaks at 133.0 eV and 133.8 eV, respectively, which were attributed to formation of phosphates (PO_4^{3-}) [38,39] belonging to different compounds (Zn, Ca or Al) as will be discussed in section 3.5.2.

XPS Spectra of Sulphur: Figure 3.9(b) shows the S $2p_{3/2}$peaks at 161.8 eV corresponding to the metal–sulphide (M–S) bond and S $2p_{1/2}$ at 163.0 eV corresponding to the organic sulphide (C-S) bond [40]. The S $2p_{3/2}$ peaks, at 167.8 eV and at 168.9 eV, were attributed to the formation of sulphates (SO_4^{2-}) [40].

XPS Spectra of Oxygen: The O peaks observed at 529.8 eV, 531.4 eV, and 532.5 eV are shown in Figure 3.9(c). The O 1s peak at 529.8 eV indicates metal oxide formation [40]. Several compounds may be associated with the O 1s peaks detected at 531.4 eV and 532.5 eV including phosphates, sulphates, and carbonates [39]. It was suggested that the O 1s peak at 531.4 eV might belong to hydroxides [41]. Further analyses, involving Raman and Fourier Transform Infrared Spectroscopy (FTIR), are required to determine in which form the hydroxides are present in the ORL. The role of hydroxide ions in ZDDP degradation will be discussed in Section 4.2.

The phosphates, sulphide, oxides, sulphates identified in Figures 3.9(a-c), can form compounds with Zn, Ca, and C, as described in Section 3.5.2.

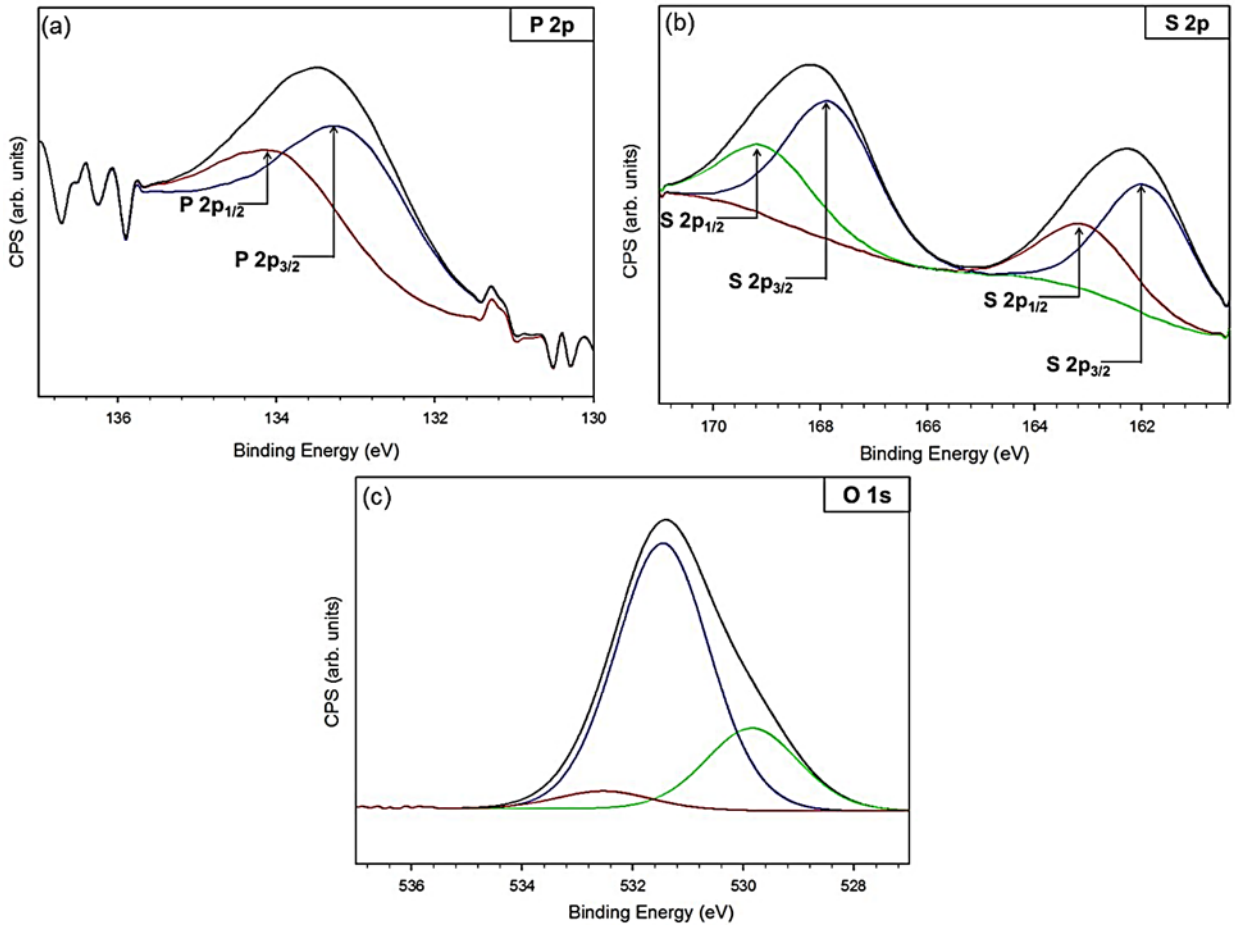

Figure 3.9. High-resolution XPS spectra and deconvoluted peaks of (a) P 2p, (b) S 2p (c) O 1s, from analyses conducted on ORL formed during sliding tests using E85/oil (1:1) blend.

3.3.5.2 XPS Spectra of Compounds Formed by Zn, Ca and C

Zn Compounds: Figure 10(a) shows the Auger Zn LMM signal at 498.6 eV. The Zn $2p_{3/2}$ peak appeared at 1022.0 eV as shown in Figure 10(b). Previous XPS peak analyses [38,39,42–44] attributed the two peaks shown in Figures 10 (a) and (b) to zinc phosphate ($Zn_3(PO_4)_2$), zinc sulphate ($ZnSO_4$),or zinc oxide (ZnO). However, based on the high-resolution XPS spectra of sulphur, in Figure 9(b) zinc sulphide (ZnS) may likely be the reaction product corresponding to the Zn $2p_{3/2}$ peak, consistent with the XPS results of the ZnS nanoparticles and the ZnS single-crystal [45]. Presence of ZnS nanoparticles have been previously suggested by FFT analyses of TEM images of ORL as shown in Figure 8(c, d). The HR-TEM of the tribolayers formed on Al–Si [16], and Mg–Al_2O_3 composites [46] interpreted some nanocrystalline structures observed within these layers as ZnS. $Zn_3(PO_4)_2$ is another likely reaction product, formed as a result of degradation of the ZDDP molecule as will be discussed in Section 4.2.

Calcium compounds: Figure 10(c) shows that two distinct calcium peaks appeared, the peak at 347.1 eV, corresponded to Ca $2p_{3/2}$, and the one at 350.7 eV, corresponded to Ca $2p_{3/2}$. These peaks may be ascribed to amorphous calcium phosphates ($Ca_3(PO_4)_2$)), as discussed in [47,48]. Calcium phosphate shows calcium-based detergents in the composition of ORL. The Ca $2p_{3/2}$ peak also indicates the possibility of calcium carbonate, as per [41, 48], originating from overbased calcium detergents.

Carbon compounds: Deconvolution of C spectra (Figure 10(d)) and integral area calculations of the decomposed peaks revealed that 81.7% of the C was present in the form of aliphatic carbon groups, C-C/C-H bonds corresponding to the peak at 284.7 eV, whose source might be the thiols, base oil or aliphatic compounds in ZDDP [40]. The binding energies of 289.4, 287.7, 286.2 eV can be assigned to CO_3^{2-}, C=O, and C-OH/C-O-C, respectively [47].

It is to be noted that the XPS spectra of Al 2p (not shown), recorded at binding energy of 75 eV, probably corresponded to aluminium phosphates ($AlPO_4$) [40,49]. The formation of this compound implies occurrence of a reaction between metal substrate Al and the Zn or Ca phosphates leading to $AlPO_4$. Also, a binding energy peak for Fe 2p was recorded at 710.65 eV (not shown), which may correspond to formation of iron oxide [40]. The evidence of iron oxide formation, as a result of abrasion, has been previously presented in Section 3.3 (Figure 7(e)). The reactions leading to phosphates will be elaborated in Section 4.2 where the ZDDP degradation mechanisms are discussed.

The XPS spectra acquired from the wear tracks of the Al-12.6% Si tested using the E85/oil (1:1) blend and using synthetic oil without E85 addition determined the atomic percentages of the elements detected in ORL, as shown in Table 1. The atomic percentage of Zn was 50% higher in tests with E85/oil (1:1) blend compared to tests with unmixed oil. Similarly, while P and S elements were present in negligible amounts in the tests with oil alone for ORL formed when E85/oil (1:1) blend was used at % of P and S were 0.4% and 0.5% respectively. The higher amounts of Zn, P, and S found in ORL in tests with E85/oil (1:1) blend are significant as they imply and increase in the amount of corresponding compounds—zinc(poly/ortho)phosphates, zinc sulphates and sulphides in the ORL when E85 was added. The mechanisms of ORL layer formation will be discussed in Section 4.2.

Table 3.1. Atomic percentages of the elements detected by XPS in the ORL formed on Al-12.6% Si when using E85/oil (1:1) blend and unmixed (without E85) synthetic oil.

	Zn	P	S	Ca	C	O
E85/oil (1:1)	1.0	0.4	0.5	3.7	50.5	33.0
oil	0.5	<0.1	<0.1	3.8	45.6	33.6

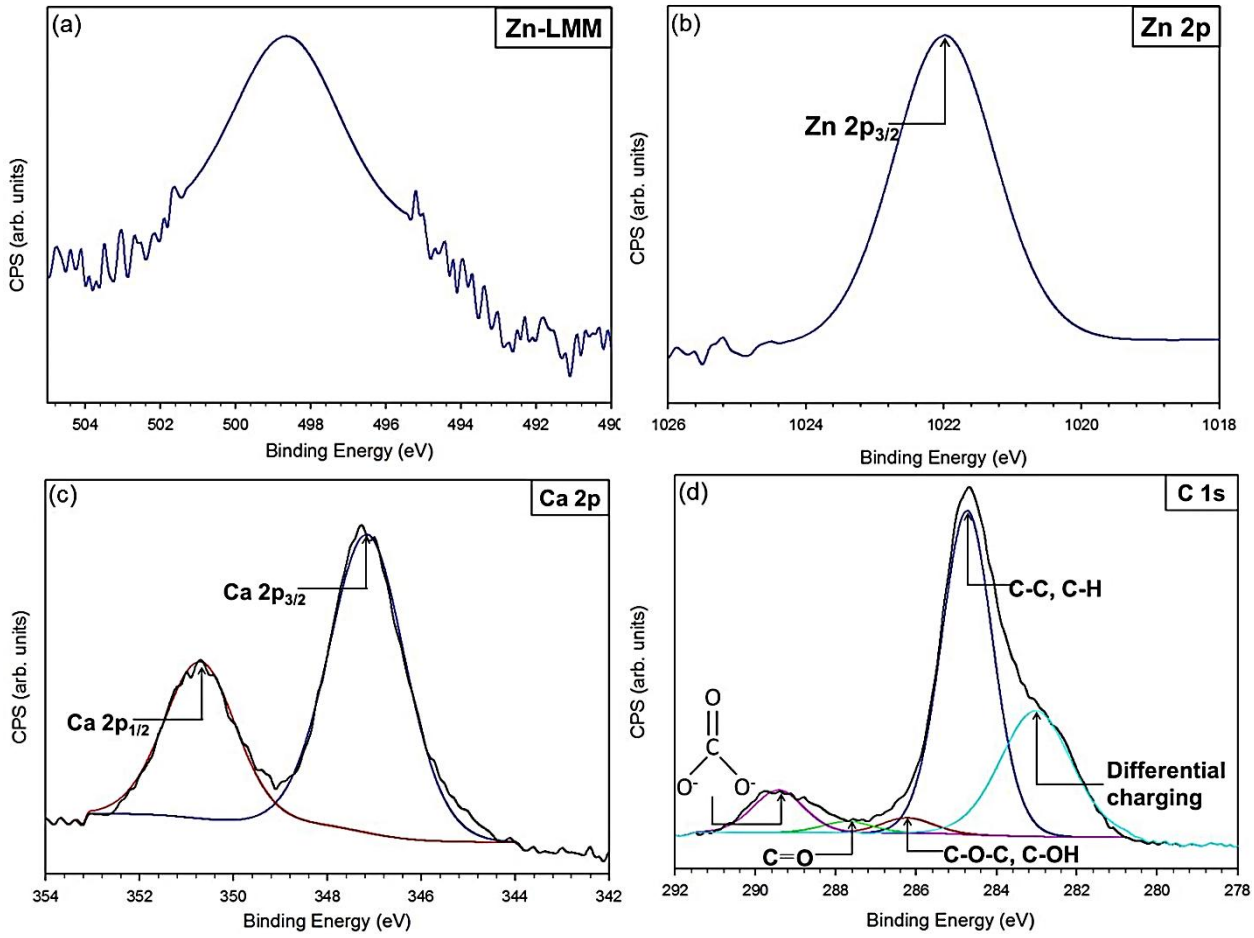

Figure 3.10. High-resolution XPS spectra and deconvoluted peaks showing the ORL components formed for tests with E85/oil (1:1) blend (a) Zn LMM, (b) Zn $2p_{3/2}$ (c) Ca $2p_{3/2}$, (d) C 1s peaks.

3.4. Discussion

The results presented in Section 3 revealed that the wear behaviour of Al-12.6% Si alloy was not significantly altered when using the E85/oil (1:1) blend rather than unmixed synthetic oil. The mechanisms of UWM were similar in both cases. The three stages of UMW were observed during boundary lubricated sliding under low loads, for both the unmixed synthetic oil and the oil blended with E85. Meanwhile, it was noted that the in the UMW II stage (the running-in stage) the volumetric wear of Al-12.6 % Si was slightly lower when the E85/oil (1:1) blend was used. It was also observed that the transition from UMW II to UMW III occurred earlier when the tests were conducted using an E85/oil (1:1) blend. Although rather subtle, the use of E85/oil (1:1) blend had therefore a positive effect on the wear of Al-12.6% Si alloy. The results also suggested that the formation of the ORL was a critical aspect of the lubricated wear of Al-12.6% Si alloy. In this section, the effects of blending E85 with engine oil on the sliding wear of Al-12.6% Si alloy are discussed by considering the microstructural and compositional changes that led to formation of the ORL.

3.4.1 Role of Microstructure on ORL Formation

The origin of the ORL can be traced back to the UMW I stage. During this stage the volumetric wear loss was negligibly low (Figures 3.3 and 3.6(a)). The damage was limited to the Si particles and occurred in several forms; wear marks formed on their top surfaces and particles were pushed into the softer Al matrix. There was also evidence for Si particle fracture (Figures 3.5(a) and (b)). As a result of plastic deformation of Al adjacent to sinking silicon particles Al pileups were formed around these particles. Si particles shielded the matrix from wear despite particle fracture and sinking in. In fact, if the first contact with a hard counterface was established with the Al matrix that was not protected by Si particles (such as in a 6061 alloy

[29]), the UMW regime would not be attained, and a high wear regime would be established. Thus, the initial protection provided by the Si particles is an essential step in the evolution of a wear-resistant surface and for the formation of ORL. The transition to the UMW II stage was characterized by an increase in the volumetric wear (Figure 3.3 and 3.4(b)). At the end of UMW I, as the piled-up Al and the embedded Si particles attained approximately the same elevation, the Al became exposed to sliding damage by the counterface. The matrix wear occurred in the form of long wear grooves and scratches across the matrix and particles. Consequently, both Al and Si nano-fragments were found in the TEM cross-sections of ORL [11]. ORL may also involve mixing of Fe fragments abraded from the counterface possibly by Si particles, as suggested by Figures 3.7(c) and (e). However there is no direct evidence for Fe in the composition of ORL. Once the UMW III stage was attained, the formation of ORL was complete and the steady state with near zero rate wear occurred at high sliding cycles.

As noted in the introduction, in an Al-12.6% Si alloy lubricated with synthetic engine oil, the ORL reached a maximum thickness of 109±6 nm after 2×10^6 cycles [11] and maintained it for the remainder of test cycles. The ORL formed on the sliding surface of Al-12.6% Si alloy using the E85/oil (1:1) blend had similar composition and morphology. In tests conducted using the E85/oil (1:1) blend examination of several sections including the one shown in Figure 3.8(b) indicated that after sliding for 3×10^5 cycles, the thickness of the ORL was 112±5 nm. Figure 8(b) indicates the formation of a near surface zone consisting of nanocrystalline Al grains underneath the ORL that may have served to support the ORL similar to the hardened nanocrystalline zones found in near eutectic Al-Si alloys tested in unmixed engine oil [5, 11].

As the onset of UMW III was reached faster in the tests conducted using E85/oil (1:1) blend and the total wear was less, it can be suggested that the ORL started to form earlier in the

presence of E85 and acted as an effective protective layer. It is conceivable that the addition of E85 modified the composition of the ORL by enriching it with antiwear agents and led to lower total wear. Semi-quantitative XPS analyses supports this view as higher atomic percentages of the Zn, P and S are detected in ORL (Table I) in case of E85/oil (1:1) blend compared to unmixed oil, which indicates the presence of higher amounts of anitwear agents like zinc phosphates and sulphides as derived from XPS investigations (Figures 3.9(a, b) and 10(a, b)) and HR-TEM studies (Figure 3.8 (d,e)). The formation of the antiwear agents in the ORL formed from E85/oil (1:1) blend can be attributed to the role that OH^- functional groups that was provided by ethanol. This will be considered in Section 4.2.

3.4.2 Role of E85 Addition on ORL Formation Mechanisms

The hydroxyl (OH^-) functional group could serve as a nucleophile (chemical species capable of donating electron pair) that initiates a reaction pathway [50] once the ZDDP molecule degrades as a result of sliding. The dithiophosphate molecule ($[(RO)_2PS_2]^-$), generated as a result of ZDDP degradation, would form polyphosphates and/or poly(thio)phosphates, via a ligand exchange mechanism [51–55] in presence of the OH^- groups. The formation of $[(RO)_2PS_2]^-$ during ZDDP degradation was shown previously [51] using Raman and ^{31}P-NMR spectropscopy. Coy and Jones [53] additionally used ^{1}H-NMR technique to show that the exchange between O and S in dithiophosphate $[(RO)_2PS_2]^-$ was possible during thermal degradation of ZDDP. It is thus reasonable that an adequate supply of OH^- (nucleophile) might have led to an interchange of alkyl groups between O and S in a dithiophosphate molecule under sliding contact conditions, as shown in Figure 3.11(a). The OH^- group may initiate the swapping of alkyl groups (R) between O and S, changing the P-O-R bond to the P-S-R bond in a tribolayer, the evidence of which was

given by Coy and Jones [53], and later by Fuller et al. [55], for A2 steel sliding pairs examined using P L-edge and P K-edge XANES spectroscopy.

A hydroxyl ion induced ZDDP degradation mechanism is proposed in Figure 3.11(b) based on the XPS and TEM results. A possible initial step for the proposed ORL formation route is the dissociation of ZDDP molecule and formation of zinc ions and dithiophosphates, induced by boundary lubricated tribological sliding contact between the Al-12.6% Si alloy and the counterface. At this stage, the nucleophilic hydroxyl ions (OH^-) present in ethanol (E85) may play a critical role as they are likely to catalyse the ligand exchange between O and S and formation of the dithionylphosphate $[(RO)_2PS_2]^-$ in the next step. This would lend itself to the formation of zinc (ortho)phosphates possibly through polymerisation and disproportionation reactions. The evidence for formation of $Zn(PO_3)_2$ or $Zn_3(PO_4)_2$ can be found when Figure 3.9(a) and 3.10(a, b) are considered together in addition to the HR-TEM and corresponding diffraction pattern analyses.. It is also conceivable that the zinc (ortho)phosphates would react with the Al substrate, where the Al ions were likely to replace the zinc ions and form aluminum phosphate ($AlPO_4$).

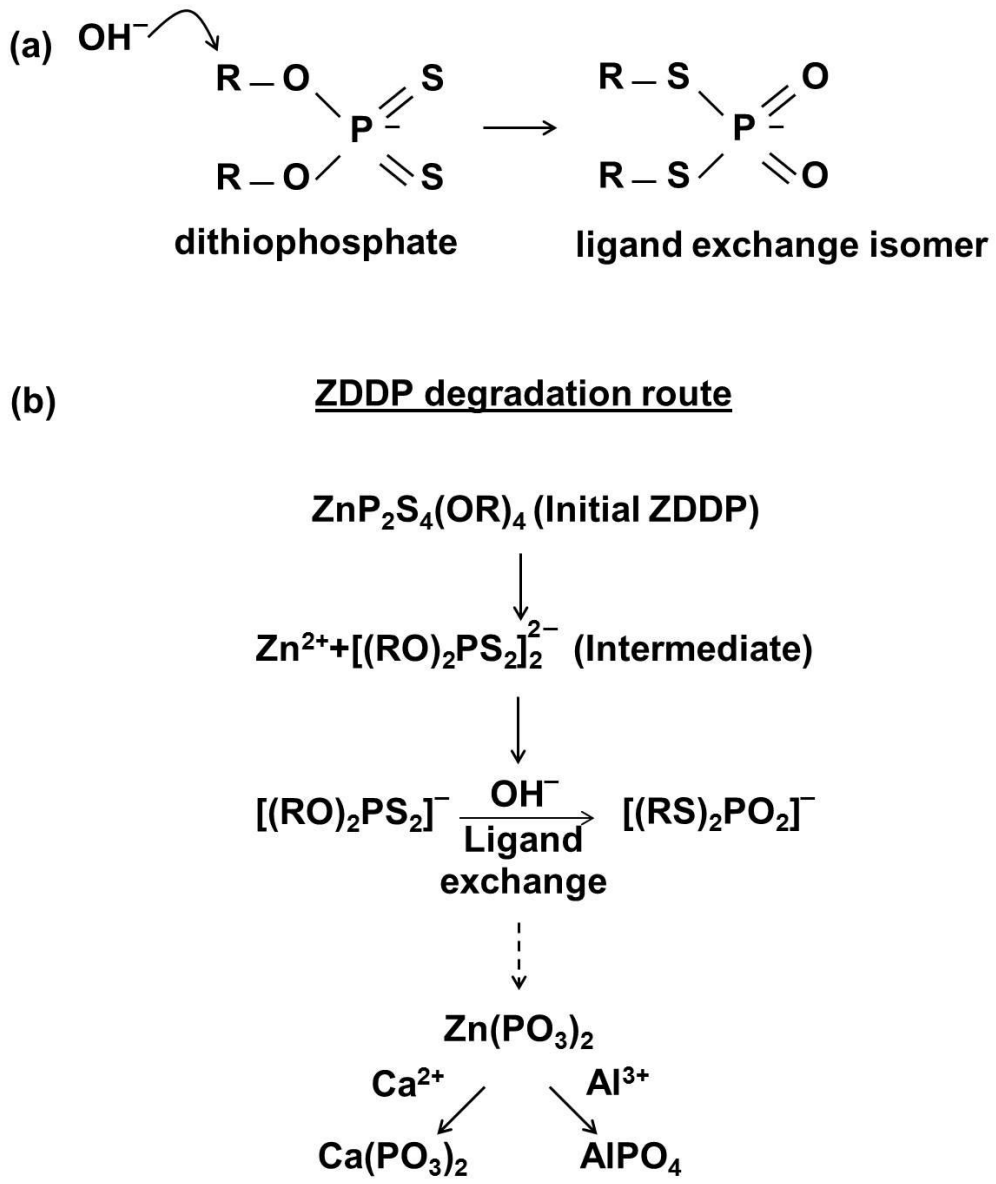

Figure 3.11. (a) OH^- induced ligand exchange of dithiophsophate. (b) Proposed reaction route for ZDDP degradation and possible reaction products leading to antiwear compounds.

Fuller et al. [55] examined sliding of self-mated of A2 steel pins and coupons using ZDDP (1.2 wt%) in base oil as lubricant forming at 100 °C antiwear layer. The mechanisms of antiwear layer formation, involving triblogical sliding process, were comparable to the thermally formed

antiwear films [52, 53]. The authors found evidence for the O/S exchange isomer ($(RS)_2PO_2$), using P L-edge and P K-edge XANES spectroscopy, termed linkage isomer (LI-ZDDP), as an important precursor leading to tribofilm formation. It was suggested that the O/S exchange isomer could form due to tribological contact and would be eventually converted to a polyphosphate film. This supports the proposed mechanism of polyphosphate film formation when using the E85/oil (1:1) blend. Catalysed by the nucleophilic OH^- groups (Figure 3.11(a)) that originated from ethanol in E85 the O/S exchange isomer eventually led to the formation of anti-wear compounds. The increased concentrations of Zn, P, S (Table I) in tests with E85/oil (1:1) blend provide support for the enhancement of the above described mechanism in presence of ethanol. It is well known that of the zinc phosphates—zinc orthophosphate, pyrophosphate, or metaphosphate—can act as thermal antiwear layers. The chain lengths of these compounds can be accurately determined by XANES analyses [14, 19, 20] as well as by calculating the atomic concentration ratios of P and Zn obtained from XPS studies on zinc polyphosphates [56]. In tests with E85/oil (1:1) blend the XPS analyses (Table I) resulted in a P/ Zn ratio of 2/5, which may be interpreted as evidence for zinc orthophosphate ($Zn_3(PO_4)_2$) formation. However more work, using XANES and EELS analyses, is required to determine the chain length which would shed light on cross-linking theory of the antiwear compounds as will be discussed at the end of this section.

Sulphur compounds (ZnS, $ZnSO_4$, and organo-sulphur compounds) may have also formed, as a result of degradation of reaction intermediates (thiophosphates) and react with Zn ions and/or the C of the alkyl groups from the initial ZDDP molecule. It is proposed that this would account for the higher concentrations of C and S in the ORL that formed when E85/oil (1:1) blend was used. It should be noted that the base oil is likely to play a role in forming the carbon-

based amorphous matrix [5, 11]. The presence of Ca-based detergents also requires attention; the Ca^{2+} ion tends to substitute for the Zn^{2+} ions to form $CaSO_4$ and $Ca(PO_3)_2$—as evidenced in Figure 3.9(a, b) and Figure 3.10(c)—consistent with observations made in the literature [57].

A schematic representation of the suggested mechanisms of ORL formation is provided in Figure 3.12. As discussed above, important aspect of the ORL formed on the contact surfaces of Al-12.6% Si was that this layer was supported by a highly deformed subsurface zone comprised of nanocrystalline Al grains (Figure 3.12(b)). The polyphosphates terminated by Zn, Al, or Ca, (Figure 3.12(a)) are known to enhance the anti-wear properties of ORL, due to the pressure-induced cross-linking of the phosphate chains [58] and/or amorphization of zinc phosphates [59]. In summary, the positive effect of E85 was to improve the antiwear properties of ORL whose performance as a protective layer is critical for long-term engine durability of Al-Si engine bore surfaces.

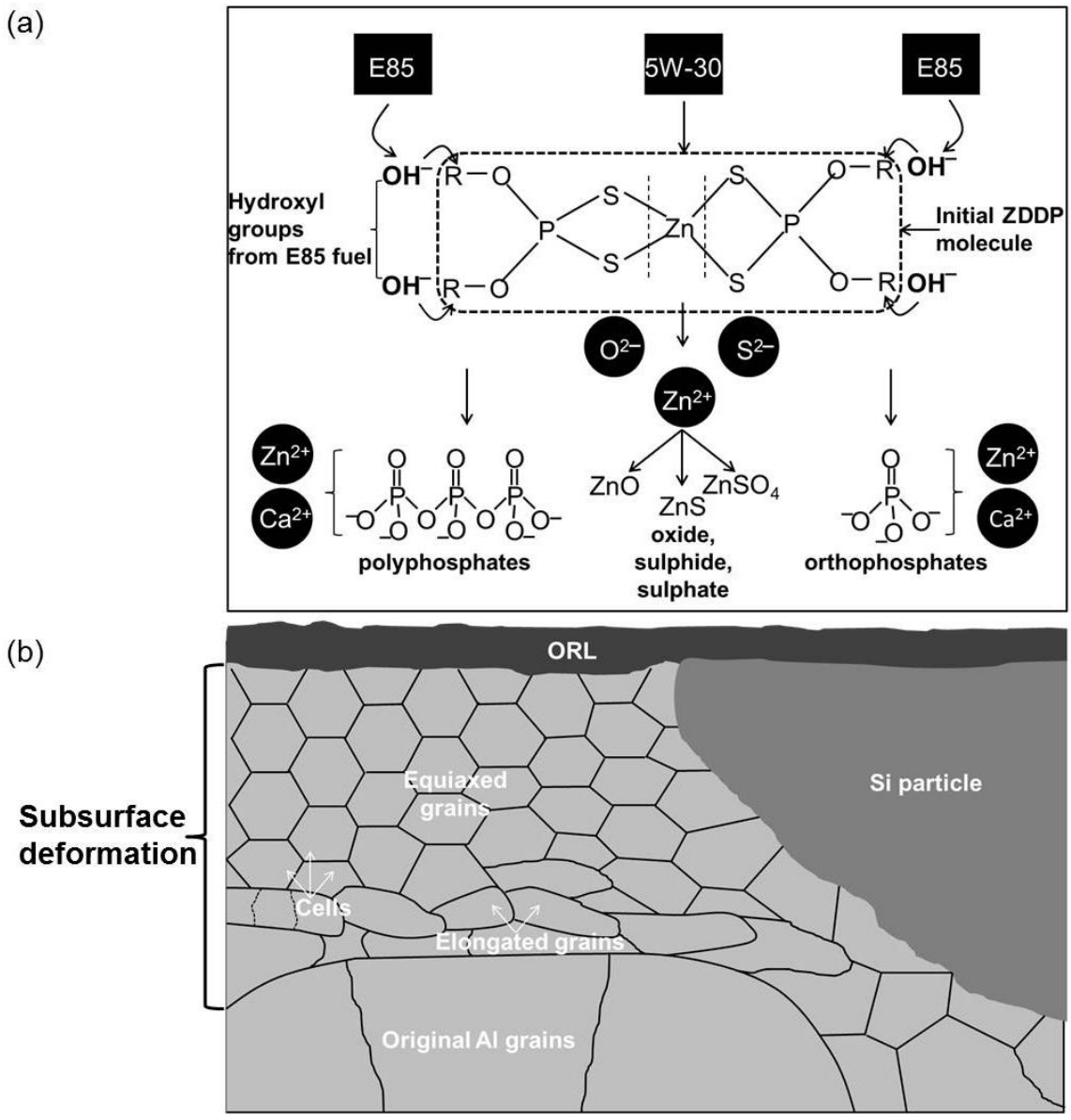

Figure 3.12. (a) Schematic representation of the ethanol induced ZDDP degradation mechanism leading to the formation of zinc, calcium and Al phosphates, sulphides, sulphates and oxides in ORL. It is to be noted that the ORL also comprises of amorphous carbon. (b) Schematic representation of the ORL formed on a sunken Si particle and Al matrix supported by a highly deformed subsurface zone comprised of nanocrystalline Al grains. . Elongated grains became divided into cells as a result of high strains, leading to the formation of equiaxed grains in the subsurface proximal to the ORL.

Summary and Conclusions

The role of biofuel (E85) addition to synthetic engine oil the wear of an Al-12.6% Si alloy was investigated by applying an E85-synthetic oil mixture—E85/oil (1:1) blend. Sliding tests were conducted under ultra-mild wear conditions, akin to very low wear that should be maintained in linerless eutectic Al–Si powertrain components. The micromechanisms of wear in the presence of E85 were determined. The main conclusions are as follows:

1. Wear mechanisms of Al-12.6% Si that tested using E85/oil (1:1) blend were similar to those of observed when using synthetic oil without E85 addition, with the three stages of ultra-mild wear regime clearly distinguishable. Addition of E85 did not modify the desirable near zero wear rates obtained for long sliding cycles of Al-12.6% Si. In addition, a positive behaviour—namely, lower cumulative volumetric wear—was obtained in tests that used the E85/oil (1:1) blend.

2. Protection of alloy surfaces with an oil residue layer (tribolayer) was instrumental in maintaining steady-state low wear rates. Sliding tests conducted with the E85/oil (1:1) blend led to formation of a modified oil residue layer enriched with Zn, P, and S—suggesting the higher amounts of antiwear compound like zinc phosphates and sulphides in the oil residue layer.

3. A model explaining the ZDDP degradation, in presence of the E85/oil (1:1) blend, was suggested based on the spectroscopic and microscopic evidence. The hydroxyl groups present in the ethanol molecule in the E85 biofuel were suggested to facilitate the ligand exchange of the degraded ZDDP molecule, leading to the formation of antiwear polyphosphates.

Bibliography

[1] E.P. Becker, Trends in tribological materials and engine technology, Tribol. Int. 37 (2004) 569–575.

[2] S.C. Tung, M.L. McMillan, Automotive tribology overview of current advances and challenges for the future, Tribol. Int. 37 (2004) 517–536.

[3] B.E. Slattery, A. Edrisy, T. Perry, Investigation of wear induced surface and subsurface deformation in a linerless Al–Si engine, Wear. 269 (2010) 298–309.

[4] B.E. Slattery, T. Perry, A. Edrisy, Microstructural evolution of a eutectic Al–Si engine subjected to severe running conditions, Mater. Sci. Eng. A. 512 (2009) 76–81.

[5] M. Chen, X. Meng-Burany, T.A. Perry, A.T. Alpas, Micromechanisms and mechanics of ultra-mild wear in Al–Si alloys, Acta Mater. 56 (2008) 5605–5616.

[6] M. Scherge, K. Pöhlmann, A. Gervé, Wear measurement using radionuclide-technique (RNT), Wear. 254 (2003) 801–817.

[7] E.W. Schneider, D.H. Blossfeld, Effect of break-in and operating conditions on piston ring and cylinder bore wear in spark-ignition engines, SAE Technical Paper, 2004.

[8] M. Chen, A.T. Alpas, Ultra-mild wear of a hypereutectic Al–18.5 wt.% Si alloy, Wear. 265 (2008) 186–195.

[9] S.K. Dey, T.A. Perry, A.T. Alpas, Micromechanisms of low load wear in an Al–18.5% Si alloy, Wear. 267 (2009) 515–524.

[10] M. Chen, T. Perry, A.T. Alpas, Ultra-mild wear in eutectic Al–Si alloys, Wear. 263 (2007) 552–561.

[11] X. Meng-Burany, T.A. Perry, A.K. Sachdev, A.T. Alpas, Subsurface sliding wear damage characterization in Al–Si alloys using focused ion beam and cross-sectional TEM techniques, Wear. 270 (2011) 152–162.

[12] D.A. Hughes, N. Hansen, High angle boundaries formed by grain subdivision mechanisms, Acta Mater. 45 (1997) 3871–3886.

[13] F. Grün, F. Summer, K.S. Pondicherry, I. Gódor, M. Offenbecher, E. Lainé, Tribological functionality of aluminium sliding materials with hard phases under lubricated conditions, Wear. 298 (2013) 127–134.

[14] H. Fujita, H.A. Spikes, The formation of zinc dithiophosphate antiwear films, Proc. Inst. Mech. Eng. Part J J. Eng. Tribol. 218 (2004) 265–278.

[15] M. Fuller, Z. Yin, M. Kasrai, G.M. Bancroft, E.S. Yamaguchi, P.R. Ryason, P.A. Willermet, K.H. Tan, Chemical characterization of tribochemical and thermal films generated from neutral and basic ZDDPs using X-ray absorption spectroscopy, Tribol. Int. 30 (1997) 305–315.

[16] G. Pereira, A. Lachenwitzer, M.A. Nicholls, M. Kasrai, P.R. Norton, G. De Stasio, Chemical characterization and nanomechanical properties of antiwear films fabricated from ZDDP on a near hypereutectic Al–Si alloy, Tribol. Lett. 18 (2005) 411–427.

[17] S.K. Dey, M.J. Lukitsch, M.P. Balogh, X. Meng-Burany, A.T. Alpas, Ultra-mild wear mechanisms of Al–12.6 wt.% Si alloys at elevated temperature, Wear. 271 (2011) 1842–1853.

[18] S. Dey, ELEVATED TEMPERATURE LUBRICATED WEAR OF Al-Si ALLOYS, (2012).

[19] S. Bhattacharya, A.T. Alpas, Role of sliding-induced tribofilms on fracture of particles in aluminium–silicon alloys, Wear. 301 (2013) 707–716.
[20] M.A. Nicholls, P.R. Norton, G.M. Bancroft, M. Kasrai, X-ray absorption spectroscopy of tribofilms produced from zinc dialkyl dithiophosphates on Al–Si alloys, Wear. 257 (2004) 311–328.
[21] P.A. Willermet, D.P. Dailey, R.O. Carter, P.J. Schmitz, W. Zhu, Mechanism of formation of antiwear films from zinc dialkyldithiophosphates, Tribol. Int. 28 (1995) 177–187.
[22] A.C. Hansen, Q. Zhang, P.W.L. Lyne, Ethanol–diesel fuel blends—a review, Bioresour. Technol. 96 (2005) 277–285.
[23] F. Yüksel, B. Yüksel, The use of ethanol–gasoline blend as a fuel in an SI engine, Renew. Energy. 29 (2004) 1181–1191.
[24] R.K. Niven, Ethanol in gasoline: environmental impacts and sustainability review article, Renew. Sustain. Energy Rev. 9 (2005) 535–555.
[25] P.R. De Silva, M. Priest, P.M. Lee, R.C. Coy, R.I. Taylor, Tribometer investigation of the frictional response of piston rings when lubricated with the separated phases of lubricant contaminated with the gasoline engine biofuel ethanol and water, Tribol. Lett. 43 (2011) 107–120.
[26] S.C. Tung, H. Gao, Tribological characteristics and surface interaction between piston ring coatings and a blend of energy-conserving oils and ethanol fuels, Wear. 255 (2003) 1276–1285.
[27] L. Coppin, Engine Oil, (2003).
[28] A.R. Riahi, T. Perry, A.T. Alpas, Scuffing resistances of Al–Si alloys: effects of etching condition, surface roughness and particle morphology, Mater. Sci. Eng. A. 343 (2003) 76–81.
[29] I.M. Hutchings, P. Shipway, Tribology: friction and wear of engineering materials, (1992).
[30] J. Zhang, A.T. Alpas, Transition between mild and severe wear in aluminium alloys, Acta Mater. 45 (1997) 513–528.
[31] S. Popović, B. Gržeta, V. Ilakovac, R. Kroggel, G. Wendrock, H. Löffler, Lattice constant of the FCC Al-rich α-Phase of Al-Zn alloys in equilibrium with GP zones and the β (Zn)-Phase, Phys. Status Solidi. 130 (1992) 273–292.
[32] Y. Okada, Y. Tokumaru, Precise determination of lattice parameter and thermal expansion coefficient of silicon between 300 and 1500 K, J. Appl. Phys. 56 (1984) 314–320.
[33] J.E. Jaffe, R. Pandey, A.B. Kunz, Electronic structure of the rocksalt-structure semiconductors ZnO and CdO, Phys. Rev. B. 43 (1991) 14030.
[34] H. Zhang, L. Qi, Low-temperature, template-free synthesis of wurtzite ZnS nanostructures with hierarchical architectures, Nanotechnology. 17 (2006) 3984.
[35] D. Shakhvorostov, M.H. Müser, N.J. Mosey, D.J. Munoz–Paniagua, G. Pereira, Y. Song, M. Kasrai, P.R. Norton, On the pressure-induced loss of crystallinity in orthophosphates of zinc and calcium, J. Chem. Phys. 128 (2008) 74706.
[36] M. Gauvin, F. Dassenoy, M. Belin, C. Minfray, C. Guerret-Piecourt, S. Bec, J.M. Martin, G. Montagnac, B. Reynard, Boundary lubrication by pure crystalline zinc orthophosphate powder in oil, Tribol. Lett. 31 (2008) 139.
[37] M. Gauvin, F. Dassenoy, C. Minfray, J.M. Martin, G. Montagnac, B. Reynard, Zinc phosphate chain length study under high hydrostatic pressure by Raman spectroscopy, J. Appl. Phys. 101 (2007) 63505.

[38] K. Varlot, J.M. Martin, C. Grossiord, R. Vargiolu, B. Vacher, K. Inoue, A dual-analysis approach in tribochemistry: application to ZDDP/calcium borate additive interactions, Tribol. Lett. 6 (1999) 181–189.
[39] M. Crobu, A. Rossi, F. Mangolini, N.D. Spencer, Chain-length-identification strategy in zinc polyphosphate glasses by means of XPS and ToF-SIMS, Anal. Bioanal. Chem. 403 (2012) 1415–1432.
[40] C. Chen, H. Bosse, L. Deters, Effects of various base oils and additives on the tribological behaviour of lubricated aluminium-on-aluminium and steel-on-aluminium contacts, Proc. Inst. Mech. Eng. Part J J. Eng. Tribol. 223 (2009) 571–580.
[41] L. Cizaire, J.M. Martin, T. Le Mogne, E. Gresser, Chemical analysis of overbased calcium sulfonate detergents by coupling XPS, ToF-SIMS, XANES, and EFTEM, Colloids Surfaces A Physicochem. Eng. Asp. 238 (2004) 151–158.
[42] R. Heuberger, A. Rossi, N.D. Spencer, XPS study of the influence of temperature on ZnDTP tribofilm composition, Tribol. Lett. 25 (2007) 185–196.
[43] P. Njiwa, C. Minfray, T. Le Mogne, B. Vacher, J.-M. Martin, S. Matsui, M. Mishina, Zinc dialkyl phosphate (ZP) as an anti-wear additive: comparison with ZDDP, Tribol. Lett. 44 (2011) 19.
[44] G.M. Bancroft, M. Kasrai, M. Fuller, Z. Yin, K. Fyfe, K.H. Tan, Mechanisms of tribochemical film formation: stabilityof tribo-and thermally-generated ZDDP films, Tribol. Lett. 3 (1997) 47–51.
[45] J.F. Xu, W. Ji, J.Y. Lin, S.H. Tang, Y.W. Du, Preparation of ZnS nanoparticles by ultrasonic radiation method, Appl. Phys. A Mater. Sci. Process. 66 (1998) 639–641.
[46] A. Banerji, H. Hu, A.T. Alpas, Sliding wear mechanisms of magnesium composites AM60 reinforced with Al 2 O 3 fibres under ultra-mild wear conditions, Wear. 301 (2013) 626–635.
[47] C.C. Chusuei, D.W. Goodman, M.J. Van Stipdonk, D.R. Justes, E.A. Schweikert, Calcium phosphate phase identification using XPS and time-of-flight cluster SIMS, Anal. Chem. 71 (1999) 149–153.
[48] N. Han, L. Shui, W. Liu, Q. Xue, Y. Sun, Study of the lubrication mechanism of overbased Ca sulfonate on additives containing S or P, Tribol. Lett. 14 (2003) 269–274.
[49] A.T. Appapillai, A.N. Mansour, J. Cho, Y. Shao-Horn, Microstructure of LiCoO2 with and without “AlPO4” nanoparticle coating: Combined STEM and XPS studies, Chem. Mater. 19 (2007) 5748–5757.
[50] H. Spikes, The history and mechanisms of ZDDP, Tribol. Lett. 17 (2004) 469–489.
[51] J.L. Paddy, N.C.J. Lee, D.N. Waters, W. Trott, Zinc dialkyldithiophosphate oxidation by cumene hydroperoxide: kinetic studies by Raman and 31P NMR spectroscopy, Tribol. Trans. 33 (1990) 15–20.
[52] R.C. Coy, R.B. Jones, The thermal degradation and EP performance of zinc dialkyldithiophosphate additives in white oil, ASLE Trans. 24 (1981) 77–90.
[53] R.B. Jones, R.C. Coy, The chemistry of the thermal degradation of zinc dialkyldithiophosphate additives, Asle Trans. 24 (1981) 91–97.
[54] G. Hilgetag, H. Teichmann, The alkylating properties of alkyl thiophosphates, Angew. Chemie Int. Ed. English. 4 (1965) 914–922.
[55] M.L.S. Fuller, M. Kasrai, G.M. Bancroft, K. Fyfe, K.H. Tan, Solution decomposition of zinc dialkyl dithiophosphate and its effect on antiwear and thermal film formation studied by X-ray absorption spectroscopy, Tribol. Int. 31 (1998) 627–644.

[56] R.K. Brow, D.R. Tallant, S.T. Myers, C.C. Phifer, The short-range structure of zinc polyphosphate glass, J. Non. Cryst. Solids. 191 (1995) 45–55.
[57] M. Burkinshaw, A. Neville, A. Morina, M. Sutton, Lubrication of aluminium–silicon surfaces with ZDDP and detergents, Tribol. Surfaces Interfaces. 6 (2012) 53–58.
[58] N.J. Mosey, M.H. Müser, T.K. Woo, Molecular mechanisms for the functionality of lubricant additives, Science (80-.). 307 (2005) 1612–1615.
[59] S.T. John, Y. Song, Z. Liu, Effects of Temperature and Pressure on ZDDP, Tribol. Lett. 28 (2007) 45–49.

CHAPTER 4

Effect of Iron Oxides on Sliding Friction of Thermally Sprayed 1010 Steel Coated Cylinder Bores

4.1. Introduction

Mass reduction of automotive components has received significant attention in recent years due to its strong influence on improving fuel economy. In this context the use of linerless Al-Si alloys in some internal combustion engines is notable. Early efforts to develop linerless alloys resulted in a hypereutectic Al-Si alloy A390 with ~18 wt. % Si [1,2] where the presence of a high volume fraction of large (50-100 µm) primary Si particles in this alloy provided the primary mechanism for extended engine durability [3]. These engines, however, have the drawback of being difficult to cast and machine [4]. Hypo-eutectic Al-Si alloys with 6-10% Si on the other hand contain almost no primary Si, which makes them easier and more economical to manufacture but provide insufficient wear resistance [5]. While most hypo-eutectic aluminum engine blocks use an iron liner to meet durability requirements for wear, eliminating this cost of adding liner will be a significant advancement in lightweight engine technology [2]. The wear resistance of hypoeutectic Al-Si alloy engine blocks may be improved by using low carbon ferrous coatings deposited by thermal spray techniques [6]. PTWA spray thin oxide layer coatings produced this way have a lamellar structure consisting of iron splats, resulting from flattening of molten metal droplets as they hit the surface, separated by iron oxide (FeO) stringers [7].

The unlubricated sliding wear mechanisms of PTWA low carbon (1020) steel coatings deposited on 319 Al alloy at different velocities, loads and under varying relative humidity (RH) tested against M2 high speed tool steel have been studied [8–10]. The COF values of the 1020

steel coatings varied with changing RH: at 12% RH the COF was 0.62 which decreased to 0.48 at 90% RH. This was attributed to the "polishing" effect, on increasing RH, as a result of hydrated iron oxides being trapped between the contact surfaces. Oxidative wear occurred by Fe_2O_3 formation at low loads (<20 N) and low sliding velocities (<1 m/s) with the thickness of surface oxide layer generated during sliding increasing with increasing loading conditions. At high loads and low sliding velocities, the wear rates were high due to severe plastic deformation of the splat tips leading to fracture and fragmentation. It was suggested [7] that the low fracture toughness (0.2-1.0 MPa $m^{1/2}$) of the interfacial oxide phases in the thermal spray ferrous coatings could cause splat delamination during sliding contact. On increasing the sliding velocity, at high loads, the wear mechanisms shifted from mechanical to oxidative wear causing a decrease in the wear rates.

Self-mated plain carbon steel pins and disks tested under unlubricated sliding are known to reduce the wear rates over a critical speed attributed to the surface hardening as a result of frictional heating of the asperities in contact causing ferrite-to-austenite phase transformation and subsequent quench hardening as also observed in the case of PTWA 1020 steel coatings samples in the load range between 40-80 N and velocity range of 1.5-2.5 m/s [8,11]. Hwang et al. [12] studied the wear behaviour of plasma spray deposited ferrous coatings, with varying oxide (FeO) contents, against SAE 9254V spring steel under lubricated conditions. The ferrous coatings hardened by the addition of Al_2O_3-ZrO_2 powders showed the lowest wear rate at high loads (200 N) which was attributed to the high cohesive bonding between the coatings and the matrix. Nickel aluminum thermal wire-arc sprayed coatings [13] tested against 52100 steel pins under lubricated conditions, using hydraulic oil, showed high wear resistance and low friction which

was attributed to the formation of a transition lubricating film and porous microstructure assisting in lubricating oil retention—although no direct evidence was provided for the same.

For extended durability of the cylinder bore and piston ring assembly it is also important to consider the wear and friction behaviour of the counterface piston ring. A standard piston ring pack consists of a set of two compression rings, a scraper ring and a bottom oil-control ring [14–17]. The top compression rings (TCRs) serve as the gas seal between the combustion chamber and the crankcase and are often subjected to demanding tribological conditions (high loads and temperatures) and dry scuffing [15]. Scuffing resistance of piston coatings was studied against a 390 Al bore under lubrication starvation conditions at 12 Hz, 120 N load and 360 K [17]. It was found that while physical vapour deposited (PVD) diamond-like carbon (DLC) coating showed moderate scuffing resistance while Ni–P–BN coating produced least wear and highest scuffing resistance. Traditionally, gray cast iron has been used as TCR. In the past two decades, CrN and flame spray/plasma sprayed molybdenum coated steel rings have become popular. Amorphous diamond-like carbon coatings (DLCs) coated steel rings are also being used commercially as TCR [18].

The DLC coatings consist of a mixture of sp^2:sp^3 hybridized carbon atoms and have two principal grades: hydrogenated DLC (H-DLC) with typically 40 at.% H and non-hydrogenated DLC (NH-DLC) with <2 at.% H [19]. One of the main factors determining the friction reduction of DLC coatings is formation of a “transfer layer” on the counterface [20–22]. In the case of hydrogenated DLC (H-DLC) coatings with 40 at% H, the H-terminated carbon bonds in the coating and the transfer layer has repulsive interactions during sliding, leading to low coefficient of friction (COF) and wear, an effect that was more prominent in vacuum tests [23]. Unlubricated sliding of H-DLC coatings against M50 steel balls under 5.0 N load and dry N_2

atmosphere showed low COF values of 0.03-0.07 which was attributed to the formation of carbon rich transfer layers on the steel counterface having a disordered graphitic structure [24]. Tung and Gao [25] studied the wear and friction behaviour of Cr-plated and DLC coated rings tested against a cast iron cylinder segment under boundary lubricated conditions and observed that a lower running-in friction was observed for DLC coated rings compared to Cr-plated rings which was attributed to the solid lubricant properties of carbon films.

From the above review, it can be seen that the wear and friction study of the piston rings against thermal spray coatings on engine bores, especially under lubricated wear conditions, is missing in the literature and will prove to be useful for the automotive industry to assess the performance of the spray coatings. In this study, we report the friction and wear behaviour of thermally sprayed low carbon steel 1010 coating, deposited on Al 380 cylinder bore, sliding against selected top compression rings (TCR), namely, DLC coated, CrN, plasma sprayed molybdenum and cast iron piston rings. The evolution of microstructure and compositions of the contact surfaces during sliding have been characterized and used to delineate the friction and wear reduction mechanisms. This study will also provide a dry scuffing and durability evaluation of the ring coatings to be used against the ferrous thermal spray coatings.

4.2. Experimental

4.2.1 Spray Coatings

A cylinder bore made of cast hypo-eutectic (Al 380) Al-9.0% Si was mechanically roughened. The low carbon ferrous thermal spray coatings were deposited on the Al 380 bores using plasma transfer wire arc (PTWA) technology. This technology is a single wire based rotating spray process using an arc spray applied on the internal surface of the Al–Si engine bore. The wire stock was low carbon steel with nominal AISI 1010 composition. The deposited

coatings were 200±25 μm thick. The cross-hatched honed surfaces had an average surface roughness of R_a=195±20 nm as measured by an optical profilometer.

4.2.2 Tribological Tests

In order to simulate a reciprocating bore/piston ring sliding contact from an internal combustion engine, an Anton-Paar (formerly CSM) linear module reciprocating tribometer was used. The 1010 spray coated cylinder bores were sectioned and tested against piston rings while measuring friction. Two types of commercial piston rings were selected as counterfaces: i) DLC coated rings and CrN rings. The DLC coating is a plasma vapour deposited (PVD) hydrogenated coating with a 2.5 μm thick top carbon-rich layer followed by a 2.4 μm tungsten rich layer and a 0.1 μm Cr-interlayer. The PVD deposited CrN coating had an average thickness of 23-25 μm.

Reciprocating tests were performed at different stroke lengths of range 2.0-40.0 mm under a constant load of 5.0 N, corresponding to 2.0-5.0 MPa Hertzian contact pressure. The frequency was maintained between 5.0 Hz to 8.0 Hz, covering a velocity range of 0.02–0.60 m/s. The test conditions maintained in this study were according to the reciprocating testing standards [26,27]. Each sliding test performed using a grade of TCR was repeated three times and the average value was reported. The conformal contact of the bore and the piston rings was carefully maintained for all the tests to avoid edge wear. The volumetric wear loss measurements from different regions of the coating wear track were determined using optical profilometry techniques (Wyko NT1100) as described in [28–31].

Both dry and lubricated reciprocating wear tests were performed. The unlubricated wear tests were performed in ambient air (25-35% relative humidity, RH) while the lubricated tests were performed using a commercial engine oil, SAE 5W-30 (ILSAC GF-5). For all lubricated tests, 1 ml of oil was added onto the engine bore surface at the beginning of the test. The

lubrication regime, determined from the ratio (λ) of minimum film thickness (h_{min}) to the r.m.s roughness (r^*) of the contacting surfaces may be calculated using equations 1-3 [32]:

$$\frac{1}{E^*} = \frac{1-\nu_{1010}^2}{E_{1010}} + \frac{1-\nu_{DLC}^2}{E_{DLC}} \quad [4\text{-}1]$$

where E_{1010} is 115 GPa, E_{DLC} is 110 GPa, Poisson's ratio of 1010 coating ν_{1010} is 0.32 and Poisson's ratio of DLC coating ν_{DLC} is 0.22.

$$h_{min} = 1.79R^{0.47}\alpha^{0.49}{\eta_o}^{0.68}V^{0.68}(E^*)^{-0.12}P^{-0.07} \quad [4\text{-}2]$$

$$r^* = \sqrt{{r_{1010}}^2 + {r_{DLC}}^2} \quad [4\text{-}3]$$

where R is the radius of the counterface ring, V is the sliding speed, P is the applied normal load applied and α and η_o represent viscosity properties of the lubricating oil. At constant load and while using the same oil, changing the sliding velocity will change the lubrication regime as shown in Table 4.1.

4.2.3 Examination of Worn Surfaces during and After Sliding

The changes in composition of the wear tracks during the reciprocating sliding tests were observed using a micro-Raman spectrometer. The Horiba micro-Raman spectrometer that used a 50 mW Nd–YAG laser (532 nm excitation line) was mounted on the CSM reciprocating tribometer and the 50× objective lens of the spectrometer was focused on the wear track. The tests were interrupted after every 40 sliding cycles for 55 s to obtain a Raman spectrum. Subsequently, the reciprocating test was continued without any change of loading or environmental conditions on the same wear track. In this way, twenty Raman spectra were collected while conducting a typical friction test.

A FEI Quanta 200 FEG scanning electron microscope (SEM) equipped with an energy-dispersive X-ray EDAX (SiLi Detector) spectrometer was used to investigate the worn surfaces after the sliding tests. The surface texture parameters were measured using a Bruker optical profilometer in the vertical shift interferometry (VSI) mode. The changes in oxide debris compositions were monitored using a 50 mW Nd–YAG laser (532 nm excitation line) through the 50× objective lens of a Horiba Raman micro-spectrometer. Transmission electron microscopy (TEM) analyses were performed on cross-sections prepared by a focused ion beam (FIB) (Carl Zeiss NVision 40 CrossBeam) lift-out technique [33] using a gallium ion source operated at 30 kV. Prior to the ion milling process, the surfaces were protected by sputtering them with a layer of tungsten. The cross-sectional samples were ion-milled from both sides to a thickness about 100 nm for TEM observations made using a FEI Titan 80-300 HR-TEM operated at 80 kV to obtain high-resolution imaging and diffraction patterns of the tribolayers formed during sliding.

4.3. Results and Discussion

4.3.1 Characterization of 1010 Coatings

A typical optical profilometry image of the top surface of the 1010 spray coated bore is shown in Figure 4.1(a). The honing marks can be seen in a cross-hatched pattern with lines intersecting at a 45° angle. A typical SEM micrograph of a polished (to 0.1 μm roughness) cross-section of the 1010 spray coating is shown in Figure 4.1(b). It can be seen that the 1010 coatings were sprayed on a mechanically roughened surface following a dovetail profile providing mechanical interlocks with the Al-Si 380 substrate. A higher magnification SEM image of the 1010 spray coating cross-section can be seen in Figure 4.1(c). A network of oxide stringers and clusters (average width of 6.7±4.5 μm) separates the Fe splats with occasional round Fe particles.

The micro-Raman spectrum indicated that the oxide vein composition was FeO as shown in the inset of Figure 4.1(b). The effect of honing was investigated by studying the cross-sectional features of the 1010 steel coating. Figure 4.2(a) shows a low magnification cross-sectional TEM image of the 1010 steel coating where a distinct strain gradient could be observed. At a depth of ~500-900 nm from the top surface, parallel bands of elongated grains divided into smaller subgrains of size between 80 and 120 nm were observed and the strain was estimated as per [34] to be $\varepsilon>2$. In between the two FeO veins the grain size was relatively larger at 180-220 nm and the strain was lower at $\varepsilon\sim0.6$. At depths greater than 500 nm from the top surface the un-deformed grains of sizes between 400-900 nm were observed. The severe deformation in the immediate subsurface was attributed to the honing process whereas the moderate strain gradient was probably formed as a result of the coating deposition process involving splat depositions.

‘

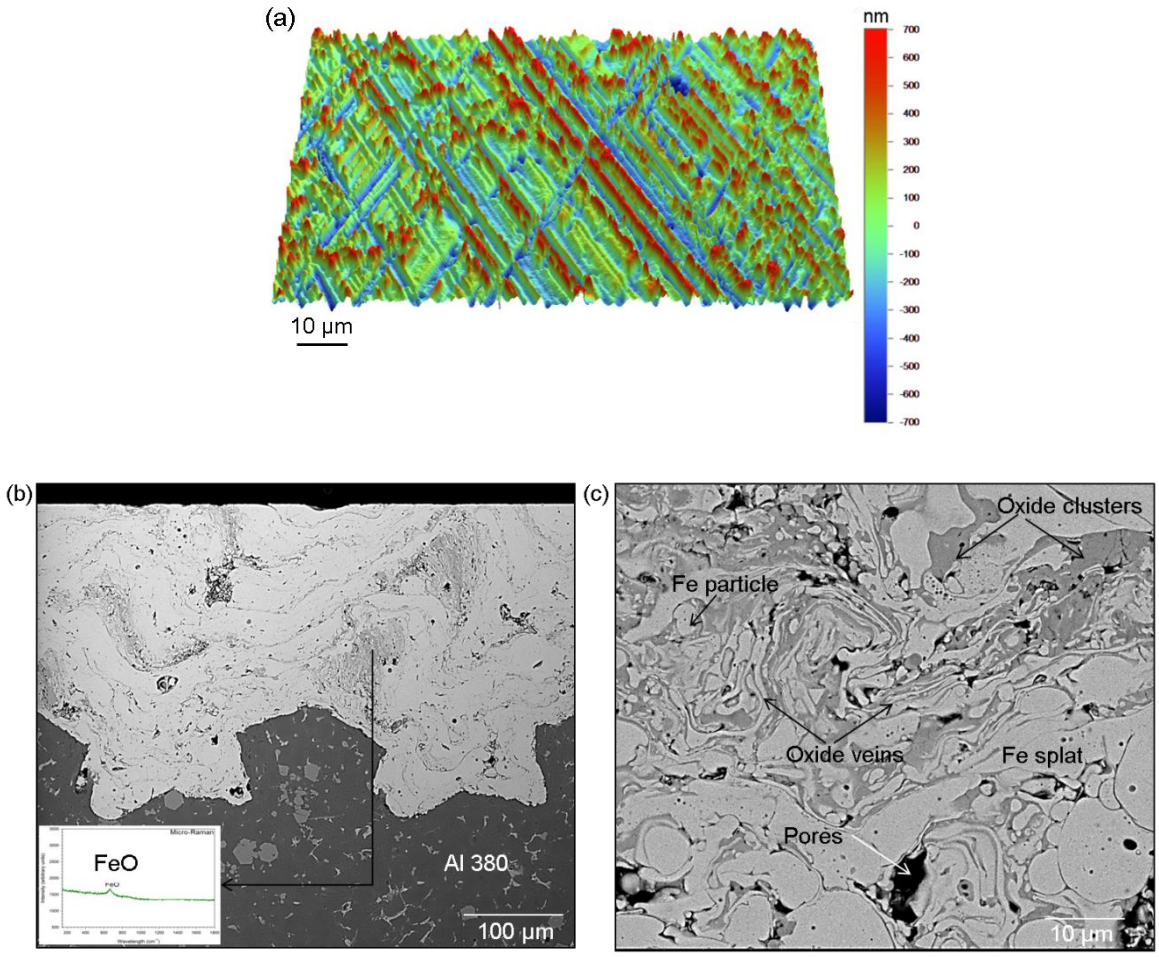

Figure 4.1. (a) Optical profilometry image showing cross-hatched honing marks on the 1010 spray coated engine bore with roughness parameters R_a=195±20 nm, R_q=250±20 nm and R_t=2.5±0.5 µm; (b) Backscattered SEM image of the cross-section of 1010 spray coating (inset shows Raman spectrum of FeO); (c) higher magnification backscattered SEM image of the 1010 spray coating.

The composition of the 1010 steel coating was studied using TEM whereby the HR-TEM images of the individual phases were identified using FFT generated SAED images. Figure 4.2(b) shows a high magnification STEM image of the 1010 steel coating where the phases were determined using the HR-TEM image (Figure 4.2c) and subsequent FFT generated SAED patterns which were identified as α-Fe (Figure 2d) and FeO veins (Figure 4.2e). The circular

features with inner granular structures (Figure 4.2f) were identified as α-Fe (Figure 4.2g). In summary, TEM cross-sectional analyses revealed the different strain gradients in the 1010 coating and identified α-Fe grains separated by FeO veins.

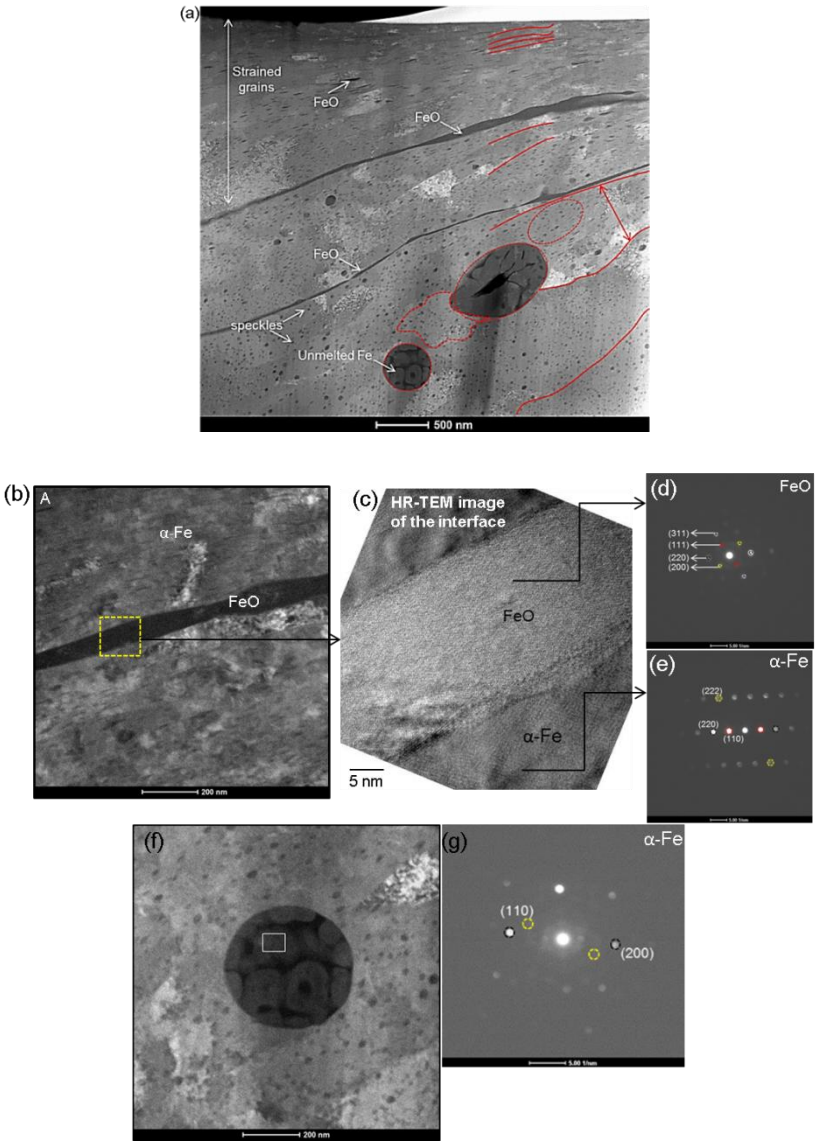

Figure 4.2: (a) Low magnification TEM image of cross-section of as deposited 1010 coating showing differences in the grain sizes and orientations; (b) Brightfield TEM image of a FeO vein separating α-Fe matrix; (c) High resolution TEM (HR-TEM) image of the region marked within a box in (b) showing crystalline regions corresponding to FeO vein and α-Fe; Selected area diffraction pattern (SAED) analyses revealed different phases of the as-deposited 1010 steel coating (d) FeO veins and (e) α-Fe substrate; (f) High-magnification TEM image and (g) corresponding SAED analyses of unmolten Fe.

4.3.2 Oxide Formations during Unlubricated Sliding: Microscopic and Spectroscopic Observations

Unlubricated sliding tests were performed to simulate the cold scuffing conditions of an engine bore-piston ring contact. The tests were performed under a 5.0 N load and 5.0 Hz frequency for a stroke length of 2.0 mm corresponding to 0.02 m/s. Typical COF curves are shown in Figure 4.3a. The friction curves can be divided into two parts; an initial running-in period of increasing COF followed by a plateau of constant COF indicating the steady state friction (μ_S) regime. The duration of the initial running-in friction period is designated as t_R. The CrN ring showed the highest steady state (μ_S) COF of 0.50 and a t_R of 1000 cycles. The lowest μ_S and shortest t_R was observed for the DLC coated ring at μ_S = 0.19 and t_R = 600 cycles. The performances of the piston rings when tested against 1010 spray coatings are summarized in a COF vs wear diagram (Figure 4.3b). The highest COF value of 0.52±0.05 of the 1010 spray coating was observed for tests against the CrN coated rings. The lowest volumetric wear (0.25±0.05 mm^3) and lowest μ_S (0.19±0.02) was observed for tests against the DLC coated rings. The unlubricated test results thus imply that a DLC coated ring would show highest wear resistance and lowest friction against 1010 spray coatings under cold scuffing conditions.

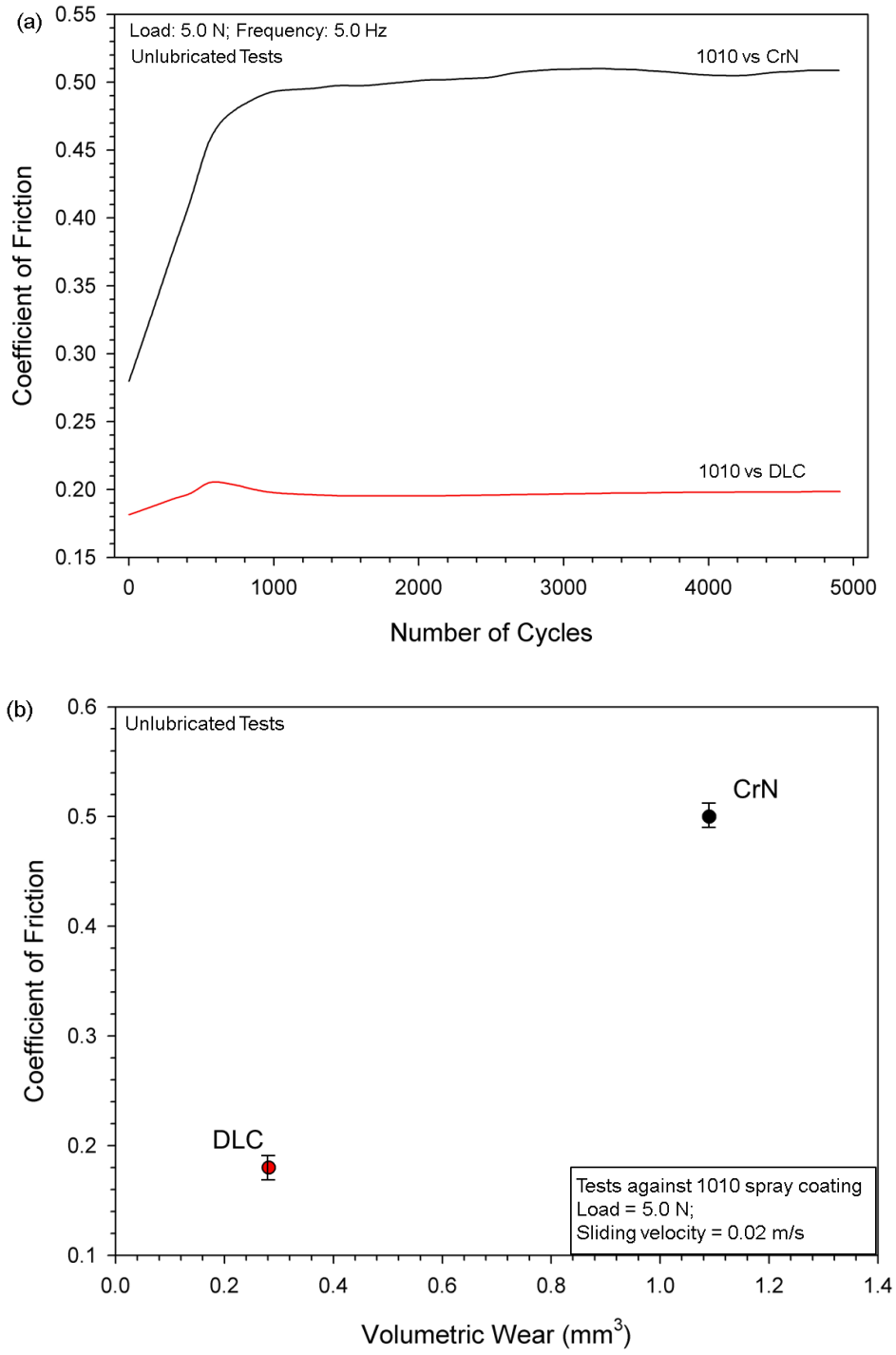

Figure 4.3. (a) Representative coefficient of friction plots for unlubricated tests; b) Average COF vs volumetric wear (mm^3) for unlubricated tests conducted on 1010 spray coating against CrN and DLC coated piston rings (load= 5.0 N, sliding velocity 0.02 m/s). Tests against each piston ring coating were performed three times and the average COF and wear rate values are reported.

Figure 4.4 shows the SEM micrographs of the worn surfaces of the 1010 spray coating against the DLC coated ring (Figure 4.4a) and the CrN ring (Figure4. 4c). The wear tracks of 1010 spray coating in the case of tests against the DLC coating had a width of 1.2 mm whereas the wear track of 1010 spray coating against CrN ring was 2.5 mm wide indicating higher wear loss in the case of tests against CrN ring. Micro-Raman spectra as shown in Figure 4.4b were useful for determining the changes in the oxide phases induced by sliding. The initial oxide consists of FeO as indicated by the Raman peak at 676 cm^{-1} [35]. A sliding induced oxide conversion was found to occur and was identified as Fe_2O_3 from the signature micro-Raman peaks in the A_{1g} and E_g modes at 225, 300, 412 and 625 cm^{-1} [35]. In the case of 1010 spray coating surfaces tested against DLC coated rings, two micro-Raman peaks at 1320 cm^{-1} and 1570 cm^{-1}, designated as the D band and the G band indicative of amorphous carbon structure [36] were detected. Thus in the case of tests against DLC coated rings amorphous carbon was transferred to the 1010 spray coating surface forming a carbonaceous transfer layer. The FeO to Fe_2O_3 conversion occurred at the surface of 1010 spray coating against CrN rings as well, as shown in the Raman spectra in Figure 4.4d—however, the amorphous carbon peaks were absent. It is thus conceivable that the carbonaceous transfer layer formed on the 1010 spray coating surface sliding against the DLC coated rings was responsible for COF reduction.

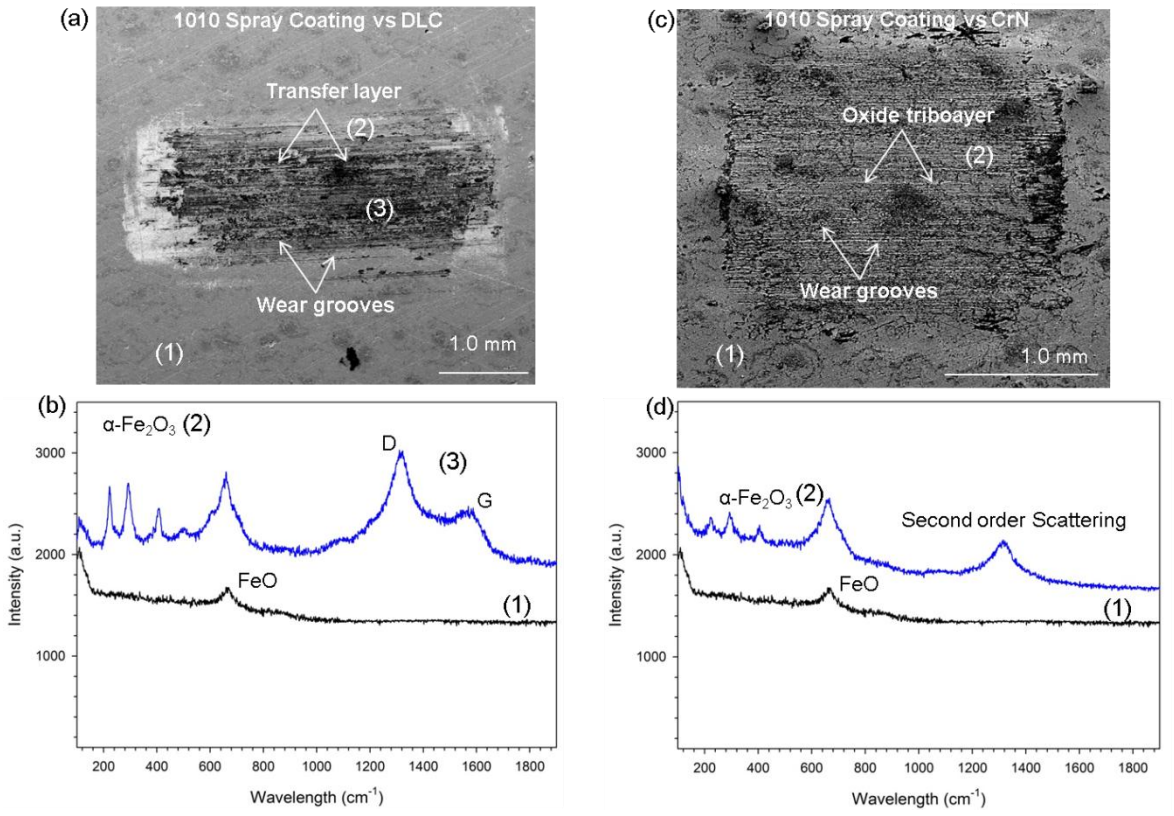

Figure 4.4. (a) Typical secondary electron image of wear track formed on the 1010 coating surface tested against DLC coated piston ring under unlubricated conditions for 5000 cycles; (b) Micro-Raman spectra obtained from the areas indicated by (1), (2) and (3) in (a) corresponding to FeO, Fe_2O_3 and amorphous carbon; (c) Typical secondary electron image of wear track formed on the 1010 spray coated engine bore surface when tested against CrN piston ring under unlubricated conditions for 5000 cycles (load= 5.0 N, sliding velocity 0.02 m/s); (d) Micro-Raman spectra obtained from the areas indicated by (1), and (2) in (c) corresponding to FeO and Fe_2O_3.

The progression of oxide formation was monitored using in-situ micro-Raman spectroscopic observations as shown in Figure 4.5. 1010 coating sliding against CrN TCR was chosen for this experiment as the CrN coating exhibited highest COF and oxide layer formations on the wear tracks that were visible to eye. Figure 4.5 shows a typical COF curve for 1010 coating sliding against CrN TCR. It can be seen that FeO to Fe_3O_4 transformation occurs after about 120-140 cycles and this change in iron oxide phases corresponds to the increase in COF. After about 600 sliding cycles, the Raman spectrum indicates another phase transformation where the Fe_3O_4 further changes to Fe_2O_3 often visible to the naked eye by its characteristic red colour. It is interesting to note that every stage of iron oxide phase transformation corresponds to changes in the COF values. The images shown in the inset of Figure 4.5 show how the wear tracks were slowly covered by an oxide layer. In order to capture the formation of the surface oxide layers on the wear tracks in-situ brightfield optical microscopic images were also taken at different sliding cycles.

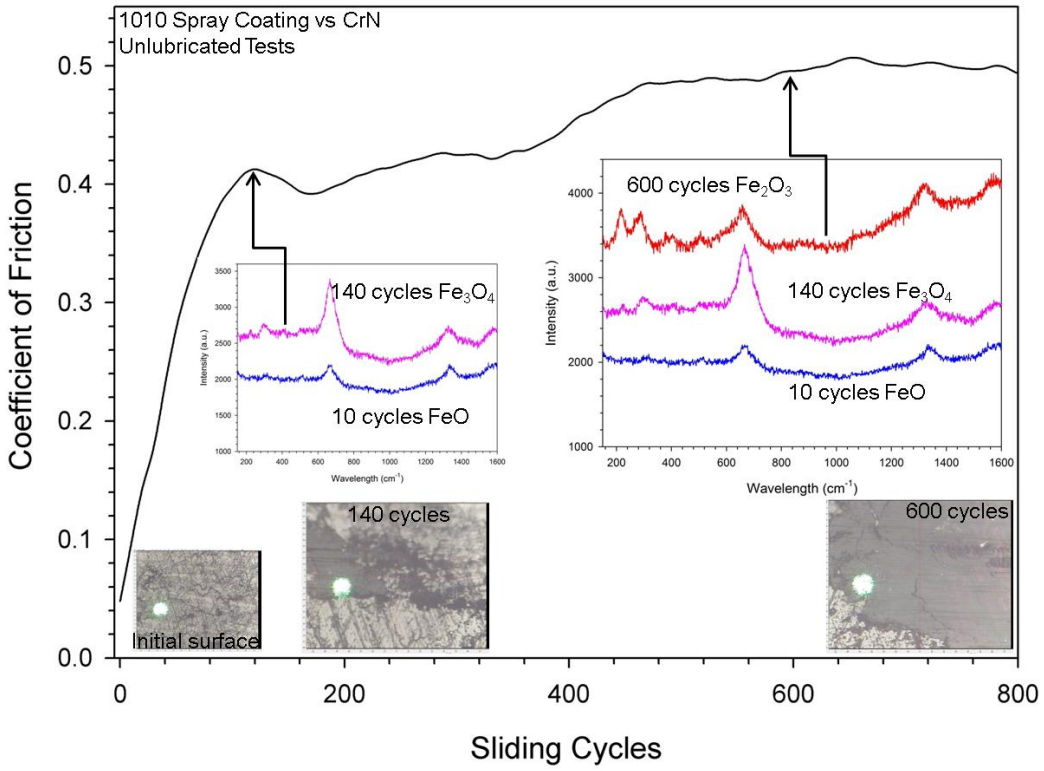

Figure 4.5: In-situ micro-Raman observations of progression of oxide on 1010 coating during siding contact against CrN TCR.

Figure 4.6 shows the oxide layers formed on the 1010 coatings tested against CrN TCR after 10, 90, 180 and 600 seconds and compares with that observed against DLC coated TCRs. It is evident that while in the case of tests of 1010 coating against the CrN coated TCR, the red iron oxide formed on the wear tracks as well as on the end of the wear tracks, whereas the formation of iron oxide was not so prominent in the case of tests against DLC coated TCRs. Further advantages of DLC coated rings became evident upon examining the ring contact surfaces (Figure 4.7). Figures 4.7a,b show the DLC coated ring contact surface where the wear track width was 0.8 mm and had low amounts of oxide debris adhered to the ring surface. On the other

hand, the CrN ring contact surface (Figures 4.7c,d) had a higher wear track width of 1.5 mm and showed large plates of Fe_2O_3 debris adhered to the ring surface.

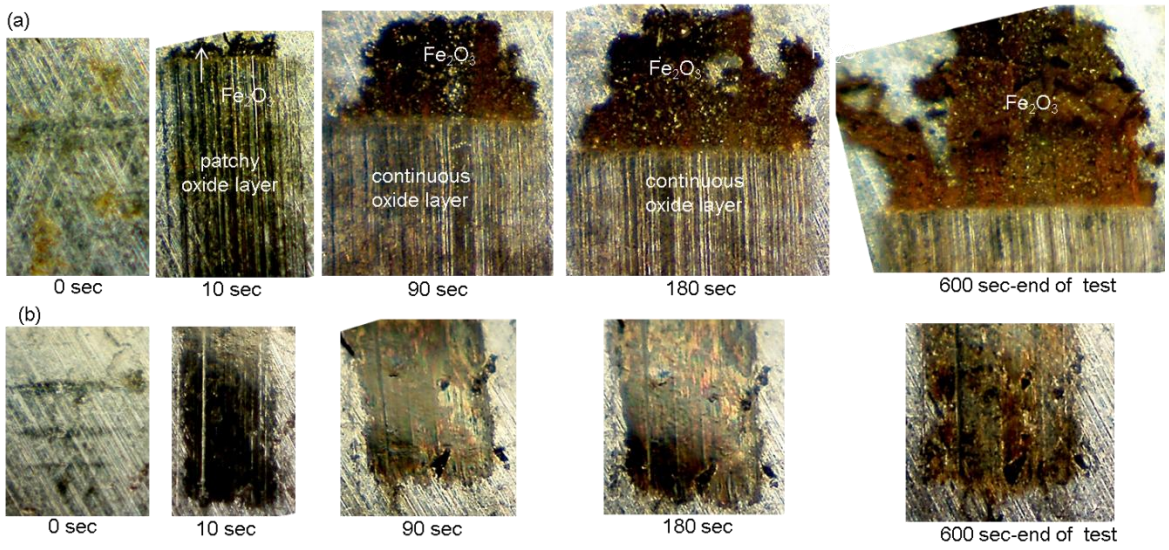

Figure 4.6: Progression of oxide formation during unlubricated tests of (a) 1010 vs CrN TCR and (b) 1010 vs DLC TCR.

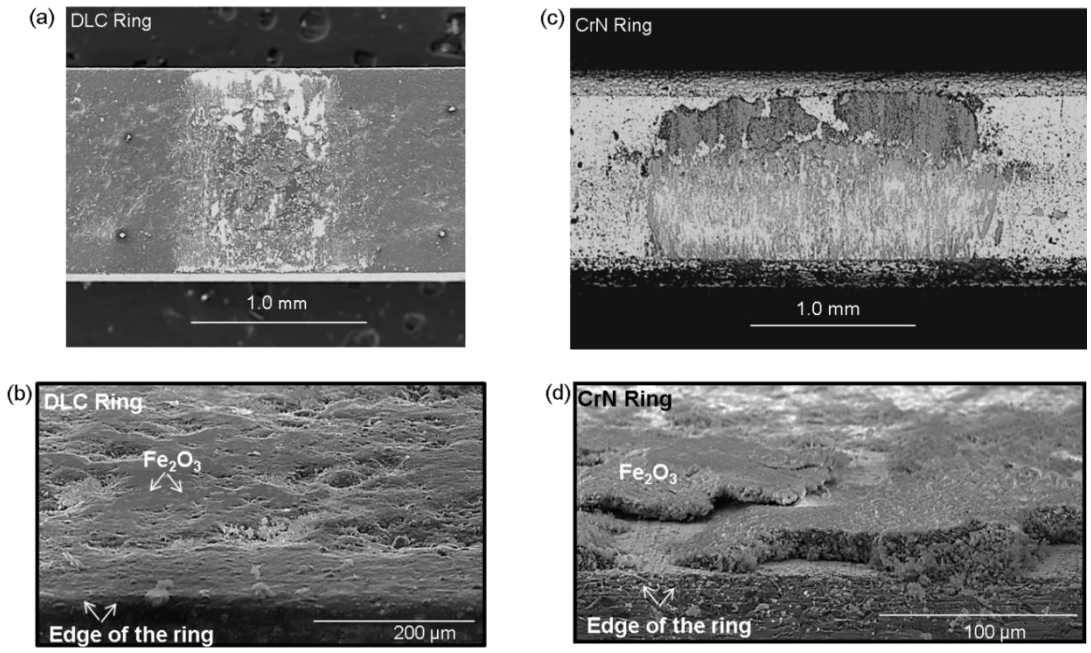

Figure 4.7. SEM images of (a) DLC coated piston ring and (b) wear debris formed on the DLC coated piston ring when tested against 1010 spray coated engine bore surface under unlubricated conditions for 5000 cycles; SEM images of (c) CrN piston ring and (d) oxide debris formed on the CrN piston ring when tested against 1010 spray coated engine bore surface under unlubricated conditions for 5000 cycles (load= 5.0 N, sliding velocity 0.02 m/s).

The reason behind lower oxide debris formation and consequent lower COF and wear behaviour of DLC coated ring was explored by examining the tribolayers formed on the 1010 coating contact surfaces by cross-section TEM microscopy. Figure 4.8 shows a STEM image of the typical section of the tribolayer formed on the 1010 coating after tests against the DLC coated TCR. The different phases of the as-deposited coating and the different phases of the tribolayer were identified using SAED pattern analyses. The 550±50 nm tribolayer formed on top of the 1010 coating was identified as a Fe_2O_3 layer with Fe particles randomly distributed in it. Interestingly, a 100 nm amorphous carbon layer on top of the Fe_2O_3 layer constituted the topmost layer that was in sliding contact with the piston ring. It is proposed that the carbon layer formed on the contact surface can be traced to the transferred material from the DLC coated piston ring. Accordingly, the DLC carbon atoms were in sliding contact with the top carbon layer supported by the Fe_2O_3 oxide layer. The tribolayers formed on 1010 coating contact surface sliding against the CrN rings was similar except for the lack of the top carbon layer. Therefore, in the case of CrN, plasma sprayed molybdenum coated and uncoated CI rings, once sliding contact ensued, the oxide conversion and Fe_2O_3 debris formation occurred and Fe_2O_3 debris was adhered to the piston ring contact surface causing high COF values in the range of 0.3-0.6 in the steady state friction regime. In the case of 1010 spray coated surfaces tested against DLC coated rings, the initial oxide conversion and debris formation was followed by the formation of an amorphous carbon transferred from the DLC coated ring which shortened the t_R and led to quick transition to the steady state friction regime. The formation of the amorphous carbon layer thus prevented further the oxide conversion to Fe_2O_3 and adhesion of Fe_2O_3 debris to the piston ring contact surface and resulted in low steady state COF values (0.18-0.22).

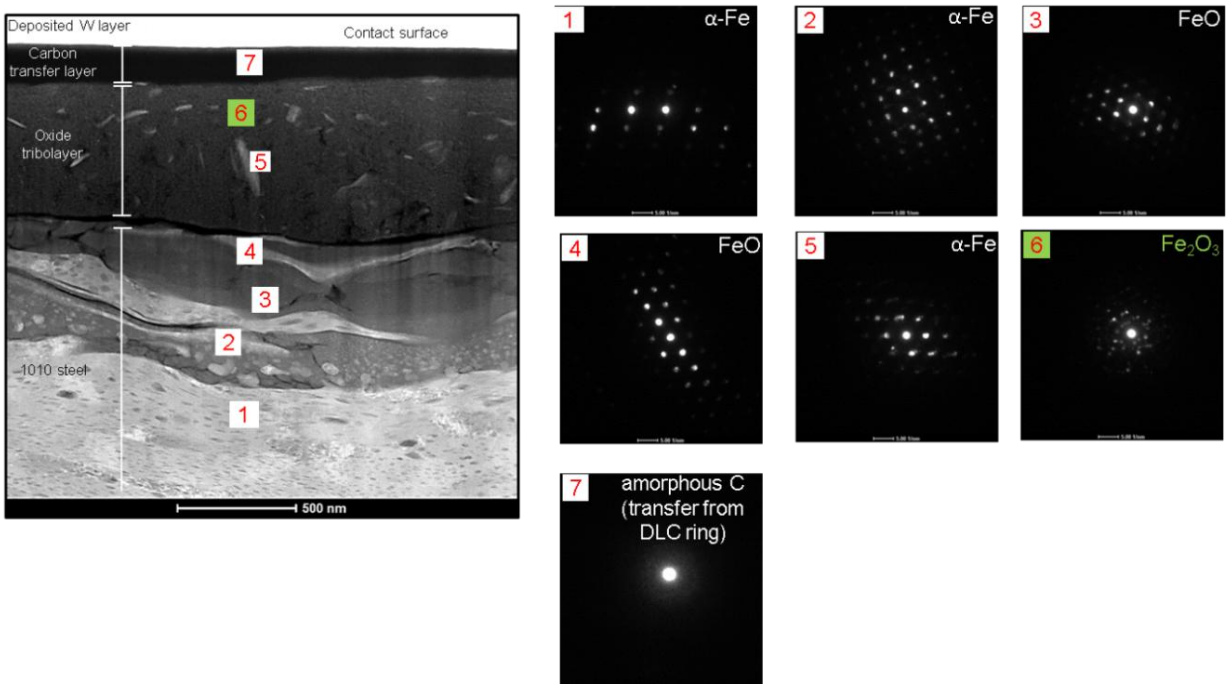

Figure 4.8: Cross-section TEM image of tribolayers formed on 1010 steel coating surface after test against DLC TCR and corresponding diffraction patterns identifying the various phases.

The specific role of the iron oxide transformations that occur during unlubricated sliding has been discussed in this section. Figure 5 shows that for 5130M sliding against CrN coated TCR after an initial change in oxide phase from FeO to Fe_3O_4, the COF curve reaches a plateau at an average value around 0.4. At longer cycles, the spinel Magnetite Fe_3O_4 phase transforms to the most stable oxide phase rhombohedral Hematite Fe_2O_3 [37,38]. As a result of the formation of Fe_2O_3, which adhered to the counterface TCR as oxide debris, the COF further increased to 0.48. The increase in COF from Fe_3O_4 phase to Fe_2O_3 phase is attributed to the fact that the Fe_3O_4 layer may adhere to surface better and acts as a better lubricant [39]. It is to be noted that the Fe_3O_4 and the Fe_2O_3 layers also form on 5130M sliding surfaces when sliding against DLC

coated counterfaces, However, against DLC coated counterfaces, an amorphous carbon layer transferred from the DLC coated piston ring forms on top of the oxide layers and this layer is responsible for reducing COF as evident in Figure 3. In summary, while the iron oxides greatly influence the friction and wear behaviour of the 1010 coated cylinder the specific tribolayers generated on the sliding surfaces depend on the counterface material.

4.3.3 Role of Oil Degraded Tribolayers during Lubricated Sliding Contact

Two types of lubricated tests were performed: continuous boundary lubricated tests, under a 5.0 N load and 5.0 Hz frequency for a stroke length of 2.0 mm corresponding to 0.02 m/s, where the lubricant was added at the beginning of the tests aimed towards simulating the normal running conditions of an IC engine and; discontinuous (unlubricated-lubricated) tests, aimed towards simulating the engine start condition, consisted of a brief initial period of 1200 cycles of unlubricated sliding (cold start) followed by addition of 1 ml of engine oil ensuing lubricated sliding (normal running) while the changes in the friction values were recorded.

4.3.3.1 Continuous Lubricated Tests

Typical friction curves are shown in Figure 4.9. The lowest μ_S of 0.10 was recorded in the case of DLC coated rings tested against 1010 spray coatings whereas CrN ring showed a μ_S of 0.12. The friction curves show that the steady state friction regime was reached within the first 400 cycles in the case of DLC coated rings running against 1010 spray coated surfaces. In case of CrN coated TCR the initial running-in period lasted for about 800 cycles.

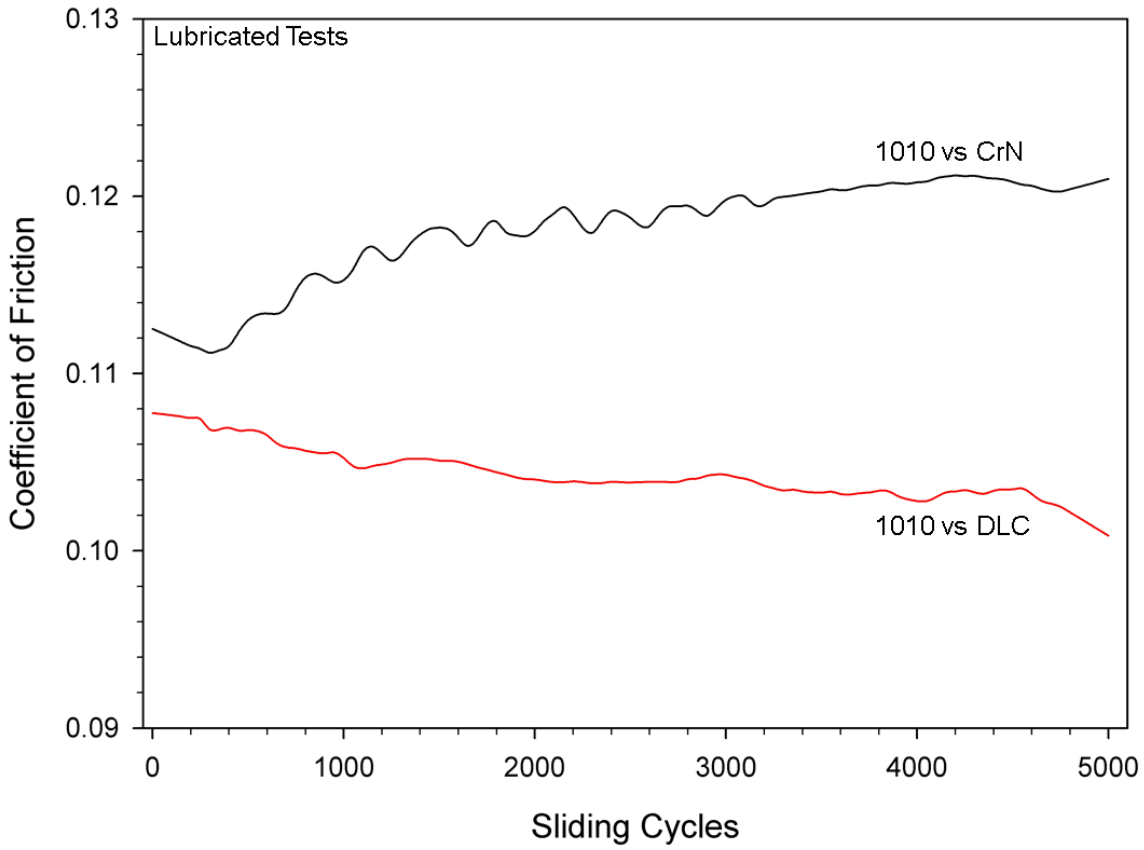

Figure 4.9. Representative coefficient of friction plots for continuous lubricated tests conducted on 1010 spray coating against uncoated CI and DLC coated piston rings (load= 5.0 N, sliding velocity 0.02 m/s).

The DLC coated piston rings were further used to study the frictional behaviour at different sliding velocities within the boundary lubricated regime. The purpose of these tests was to quantify the friction values at different sliding velocities within the boundary lubrication regime, as experienced during regular operations of an engine bore-piston ring contact. For this purpose, the 1010 spray coatings were tested against the DLC coated TCR under the sliding velocity range of 0.02-0.6 m/s at a constant load of 5.0 N. This was achieved by varying the stroke lengths between 2.0-40.0 mm and varying the frequency between 5.0-8.0 Hz. The changes in the sliding speed and correspondingly the λ values at different stroke lengths are listed in Table 4.1 and plotted as a Stribeck-type [40] curve as shown in Figure 10. It can be seen that compared to the unlubricated tests showing COF of 0.18 the COF progressively decreased with increasing sliding velocity (and correspondingly λ) to 0.09 at λ=0.58. On further increasing the sliding velocities, the COF further decreased to a low of 0.06 at λ=0.91. On increase in the sliding velocity, corresponding to λ>1, it was observed that the COF slightly increased to a range of 0.08-0.10. Thus it is seen from Figure 8 that in the boundary lubricated regime, λ<1, the μ_S values varied within the range of 0.06-0.18 with different sliding velocities. The low μ_S values at higher sliding velocities maybe attributed to the increase in the lubricant film (tribolayer) thickness as seen from Table 1—further microscopy based analyses is required to study the tribolayer morphology and formation mechanisms.

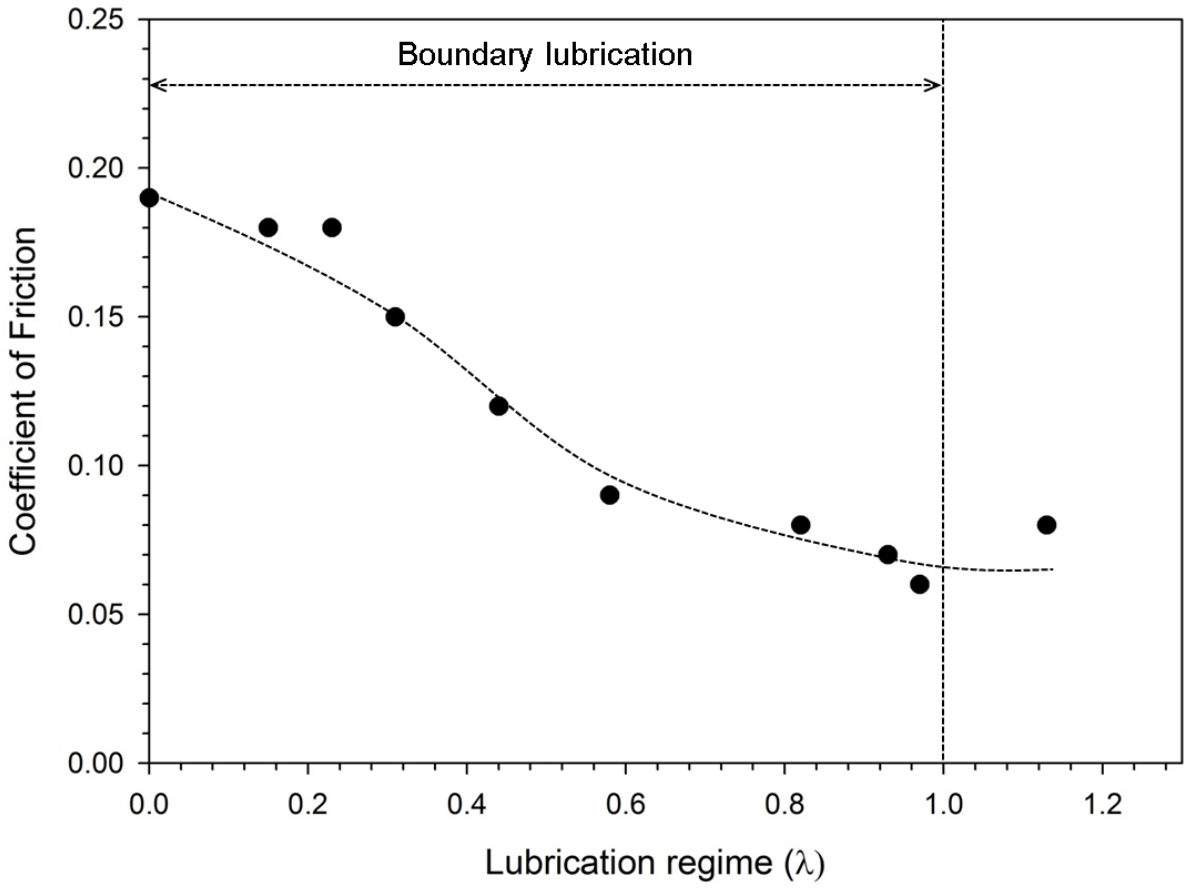

Figure 4.10. Comparison of coefficient of friction for 1010 spray coating tested DLC coated piston ring in oil (5W30) at λ values. The lubrication regime λ is determined from the ratio of minimum film thickness (hmin) to the r.m.s roughness (r*) of the contacting surfaces. The COF=0.18 at λ=0 was obtained from the unlubricated test results and was re-plotted here.

Table 4.1: Variation of linear speeds, h_{min} and λ values with changes in the stroke length and/or frequency.

Stroke length (mm), Hz	Linear Speed (m/s)	h_{min}	λ
2, 5	0.02	0.0297	0.15
4, 5	0.04	0.0476	0.23
6, 5	0.06	0.0628	0.31
10, 5	0.1	0.0889	0.44
15, 5	0.15	0.1171	0.58
25, 5	0.25	0.1657	0.82
30, 5	0.3	0.1876	0.93
20, 8	0.32	0.1960	0.97
25, 8	0.4	0.2281	1.13

4.3.3.2 Unlubricated-Lubricated Tests

The typical friction results for the unlubricated-lubricated tests are shown in Figure 4.11a while the average COF and wear results from three tests of 1010 spray coated surfaces against each TCR is shown in Figure 4.11b. It can be seen that the μ_S values for the TCR materials tested for unlubricated-lubricated tests show higher COF values compared to those observed during continuous lubrication tests (Figure 4.10)—thus the interrupted lubrication tests provide an estimate of the maximum wear and friction losses that might be expected when 1010 spray coated surfaces were tested against different TCR materials.

The DLC coated ring showed a low μ_S value of 0.14 during the unlubricated sliding period and further decreased to 0.11 during the lubricated sliding. The most prominent decrease in COF was observed for the tests of 1010 spray coating sliding against CrN ring from 0.55 to 0.16, as the oil starvation period against CrN ring led to highest generation of wear debris, adhesion and friction (as described in Section 3.2). Figure 4.11b shows that the CrN rings recorded the highest COF of 0.16±0.02 and a volumetric wear loss of 0.53±0.05 mm^3. The 1010 coatings tested against the DLC coated piston rings showed the lowest volumetric wear of 0.25±0.03 mm^3 and lowest COF of 0.11. The μ_S of DLC coated ring, tested against 1010 spray coatings, under continuous lubricated sliding was lower than the unlubricated-lubricated sliding by 9% and may be attributed to the initial period of unlubricated sliding resulting in the formation of an oxide layer. The oxide layer did not form in the case of the continuous lubricated tests. Overall, the DLC coated rings were found to show the lower friction and wear during unlubricated-lubricated and continuous lubricated tests compared to the CrN coated rings.

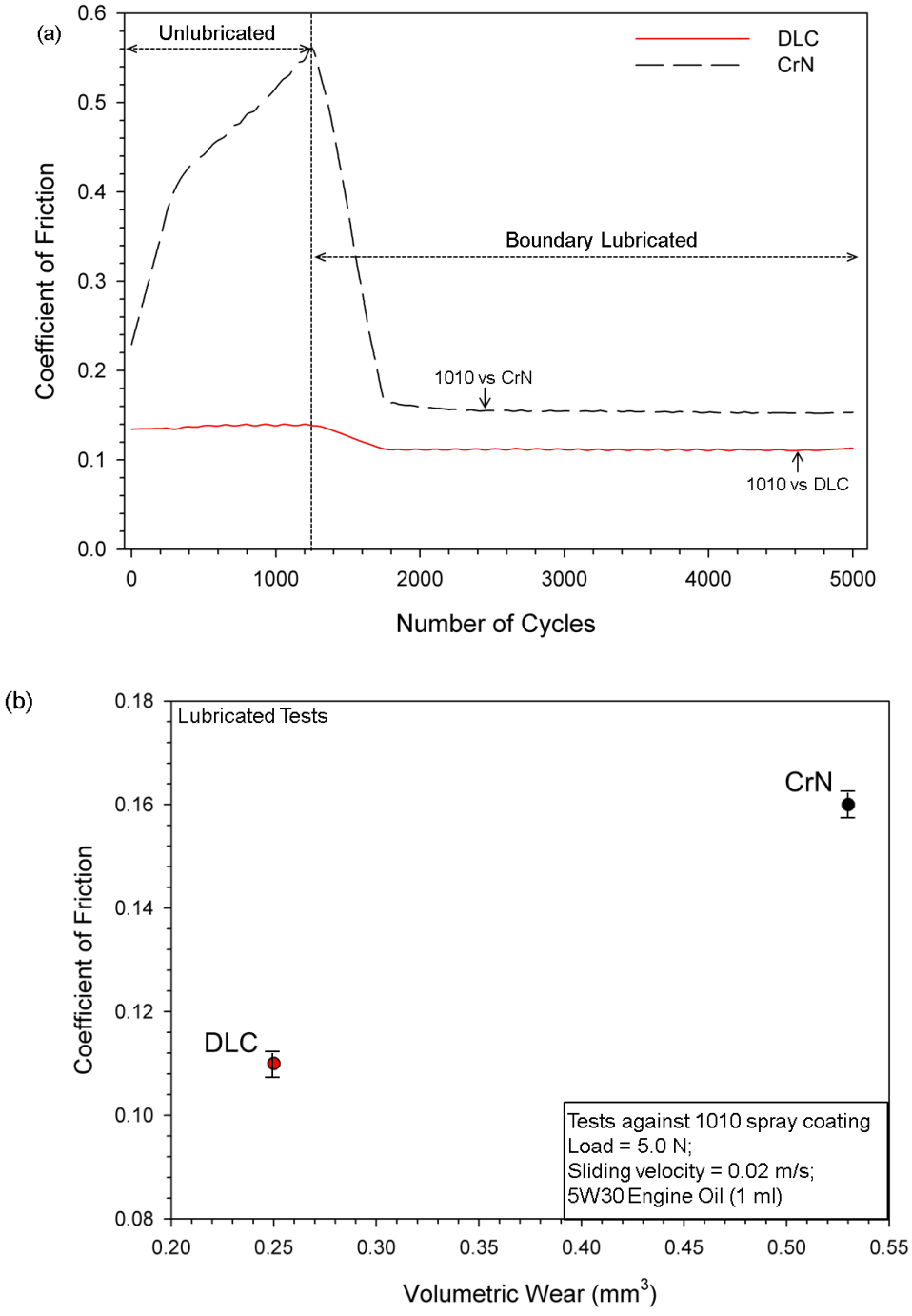

Figure 4.11. (a) Representative COF plots and (b) average COF vs volumetric wear (mm^3), for three tests, of 1010 spray coating tested against CrN and DLC coated piston rings under unlubricated-lubricated sliding conditions (load= 5.0 N, sliding velocity 0.02 m/s).

4.3.4 Wear and Friction Reduction Mechanisms during Lubricated Sliding

It has been shown that the DLC coated piston rings provide the lowest friction and wear loss when tested against the 1010 spray coatings. To rationalize the factors responsible for low COF of 1010 spray coating against DLC coated ring, it is important to investigate the tribolayers that are generated during the sliding process. Unlubricated sliding of 1010 spray coated surfaces against the DLC coated rings led to the formation of a carbon rich transfer layer on the 1010 spray coating worn surface as stated in Section 3.2.

TEM observations (Figure 4.12) made on cross-sections of the wear track of 1010 spray coated bore tested against the DLC coated ring showed the formation of a composite tribolayer. This tribolayer consisted of a carbon layer on top of an oil degraded tribolayer or an oil residue layer (ORL). The ORL that was not formed during unlubricated sliding was comprised of compounds formed by the decomposition of SAE 5W-30 engine oil during sliding. The top carbon layer that also formed on 1010 spray coated surfaces during unlubricated sliding against DLC coated rings is shown in the bright-field TEM image (Figure 4.12a). It can be seen that the carbon layer had a thickness of 30±5 nm while the ORL had a thickness of 100±40 nm. High magnification and high resolution TEM (HR-TEM) images of the carbon layer and the ORL are shown in Figures 4.12b, c. It can be seen that the carbon layer had an amorphous structure. The ORL consisted of random distribution of nano-crystalline particles within an amorphous matrix. Figure 4.12c shows that the ORL was formed on top of a FeO vein of the 1010 spray coating and ultra-fine (~50-100 nm) grains of iron beneath it. A fast Fourier transform (FFT) derived diffraction pattern of the HR-TEM image obtained from the ORL (Figure 4.12d) is shown in Figure 4.12e. Measurement of the d-spacing values of the nano-crystalline regions marked in Figure 4.12d using the FFT-derived diffraction pattern and indexing of these d-spacing distances

indicated that the nano-crystalline particles consisted of α-ZnS (hexagonal) and $FePO_4$. The zinc sulphide and the iron phosphate components of the tribolayer may be traced to the sliding induced degradation of the zinc dilakyldithiophosphate (ZDDP) additive in the engine oil and subsequent reaction with the substrate. The phosphates and the sulphides formed from ZDDP are known to be antiwear components responsible for reducing wear [41]. It is implied that the amorphous carbon layer formed on top of the ORL transferred from the DLC coated TCR, as found for unlubricated sliding as well, on interaction with the DLC coated piston ring led to low friction. The sequence of tribolayer formation during sliding contact needs to studied in further detail, using electron microscopy and micro-Raman spectroscopy; however, it is evident from the current experiments that an amorphous carbon layer is essential for reducing friction, and tests against DLC coated piston rings have led to in-situ generation of such a double tribolayer (amorphous layer on ORL). The critical aspect of friction reduction study is to investigate the tribolayers generated during sliding. As the current results demonstrate, DLC-coated top compression rings tested against 1010 spray coated bores appeared to reduce the steady state coefficient of friction and improve wear resistance compared to what can be achieved using standard Mobil Oil against other TCRs. In future, it will be important to study the evolution of tribolayers and compare friction performance of DLC-coated TCRs tested against cast iron liners. This will allow the selection of an optimum composition of the tribocouple consisting of the appropriate grade of engine bore material sliding against a suitable TCR material.

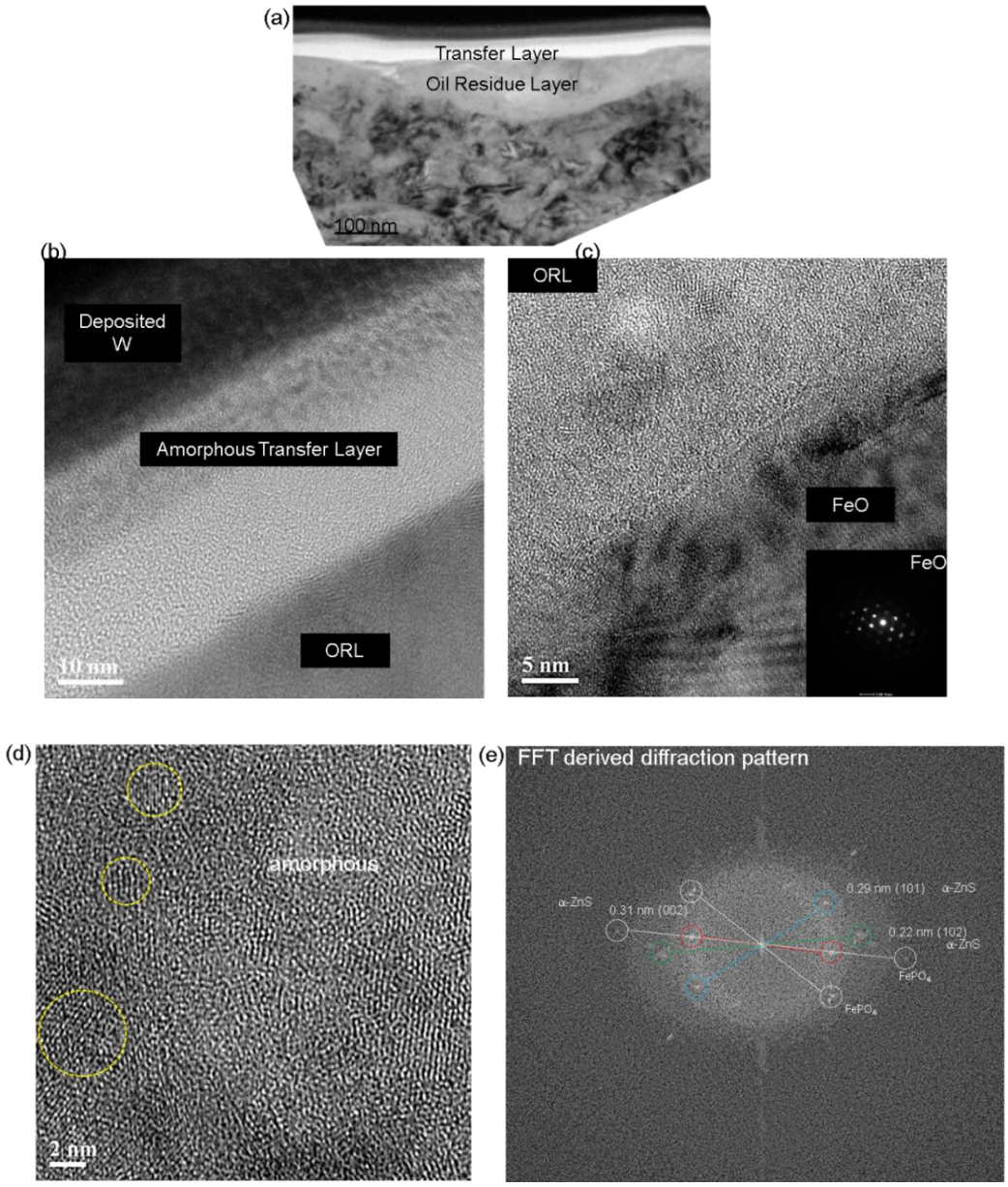

Figure 4.12. (a) Low magnification TEM image of the cross-section of the 1010 surface tested against DLC coated piston ring under boundary lubricated conditions; (b) high magnification, HR-TEM image of the amorphous layer transferred from DLC coating formed on top of ORL. The top tungsten (W) layer was deposited prior to FIB milling to protect the features of interest; (c) HR-TEM image of the interface between the ORL and the FeO vein—inset shows the SAED pattern corresponding to the FeO crystals; (d) HR-TEM image of the ORL showing nano-crystalline regions within an amorphous matrix; (e) FFT-derived diffraction pattern of the regions indicated in white circles in (d) showing the formation of $FePO_4$ and ZnS.

Conclusions

The friction and wear behaviour of 1010 spray coatings, deposited on Al 380 engine bore surfaces using plasma transfer wire arc (PTWA) technology, were investigated by conducting unlubricated and boundary tests using lubricated tests and scuffing resistance. Two top compression piston ring (TCR) coatings were selected for this purpose, namely, DLC coated and CrN coated TCRs. The main results arising from this work are summarized as follows:

1. In-situ Raman spectroscopy conducted on 1010 steel indicated that FeO was transformed to Fe_2O_3 during unlubricated sliding.

2. 1010 sliding against DLC coated TCR resulted in the formation of an amorphous carbon rich transfer layer, on top of the Fe_2O_3 oxide layer, which prevented further oxide conversion and adhesion to TCR contact surface resulting in a low COF of 0.18 and wear loss compared to the CrN coated TCR.

3. Boundary lubricated sliding tests, with an initial period of unlubricated sliding, aimed at simulating engine start up and normal engine running conditions resulted in low steady state COF values that ranged between 0.10 (for DLC) and 0.16 (for CrN).

4. An oil residue layer (ORL) incorporating ZnS and $FePO_4$ nanoparticles embedded in an amorphous matrix formed on 1010 steel coating during boundary lubricated sliding and was responsible for the low wear.

5. The low friction of 1010 steel coating observed during boundary lubricated sliding against DLC coated TCR was due to a composite tribolayer consisting of an amorphous carbon layer formed on top of ORL.

Bibliography

[1] J.L. Jorstad, The hypereutectic aluminum-silicon alloy used to cast the Vega engine block, Mod. Cast. 60 (1971) 59–64.

[2] A.K. Sachdev, R.K. Mishra, A. Mahato, A. Alpas, Vehicle lightweighting: challenges and opportunities with aluminum, in: ICAA13 13th Int. Conf. Alum. Alloy., Wiley Online Library, 2012: pp. 609–622.

[3] S.K. Dey, T.A. Perry, A.T. Alpas, Micromechanisms of low load wear in an Al–18.5% Si alloy, Wear. 267 (2009) 515–524.

[4] S. Bhowmick, A. Banerji, A.T. Alpas, Tribological behavior of Al–6.5%,–12%,–18.5% Si alloys during machining using CVD diamond and DLC coated tools, Surf. Coatings Technol. 284 (2015) 353–364.

[5] H.W. Doty, Aluminum alloy for engine blocks, (2005).

[6] G. Barbezat, Advanced thermal spray technology and coating for lightweight engine blocks for the automotive industry, Surf. Coatings Technol. 200 (2005) 1990–1993.

[7] A. Rabiei, D.R. Mumm, J.W. Hutchinson, R. Schweinfest, M. Rühle, A.G. Evans, Microstructure, deformation and cracking characteristics of thermal spray ferrous coatings, Mater. Sci. Eng. A. 269 (1999) 152–165.

[8] A. Edrisy, A.T. Alpas, T. Perry, Wear mechanism maps for thermal-spray steel coatings, Metall. Mater. Trans. A. 36 (2005) 2737–2750.

[9] A. Edrisy, T. Perry, A.T. Alpas, Investigation of scuffing damage in aluminum engines with thermal spray coatings, Wear. 259 (2005) 1056–1062.

[10] A. Edrisy, T. Perry, Y.T. Cheng, A.T. Alpas, The effect of humidity on the sliding wear of plasma transfer wire arc thermal sprayed low carbon steel coatings, Surf. Coatings Technol. 146 (2001) 571–577.

[11] N.C. Welsh, The dry wear of steels I. The general pattern of behaviour, Philos. Trans. R. Soc. London A Math. Phys. Eng. Sci. 257 (1965) 31–50.

[12] B. Hwang, J. Ahn, S. Lee, Correlation of microstructure and wear resistance of ferrous coatings fabricated by atmospheric plasma spraying, Metall. Mater. Trans. A. 33 (2002) 2933–2945.

[13] L. Prchlik, S. Sampath, Effect of the microstructure of thermally sprayed coatings on friction and wear response under lubricated and dry sliding conditions, Wear. 262 (2007) 11–23.

[14] M. Priest, D. Dowson, C.M. Taylor, Predictive wear modelling of lubricated piston rings in a diesel engine, Wear. 231 (1999) 89–101.

[15] E.P. Becker, Trends in tribological materials and engine technology, Tribol. Int. 37 (2004) 569–575.

[16] S.C. Tung, M.L. McMillan, Automotive tribology overview of current advances and challenges for the future, Tribol. Int. 37 (2004) 517–536.

[17] Y. Wang, S.C. Tung, Scuffing and wear behavior of aluminum piston skirt coatings against aluminum cylinder bore, Wear. 225 (1999) 1100–1108.

[18] T. Iwashita, N. Yamashita, Piston ring, (2001).

[19] A. Erdemir, C. Donnet, Tribology of diamond-like carbon films: recent progress and future prospects, J. Phys. D. Appl. Phys. 39 (2006) R311.

[20] S. Bhowmick, A. Banerji, M.J. Lukitsch, A.T. Alpas, The high temperature tribological behavior of Si, O containing hydrogenated diamond-like carbon (aC: H/a-Si: O) coating against an aluminum alloy, Wear. 330 (2015) 261–271.
[21] A. Banerji, S. Bhowmick, A.T. Alpas, High temperature tribological behavior of W containing diamond-like carbon (DLC) coating against titanium alloys, Surf. Coatings Technol. 241 (2014) 93–104.
[22] E. Konca, Y.-T. Cheng, A.T. Alpas, Sliding wear of non-hydrogenated diamond-like carbon coatings against magnesium, Surf. Coatings Technol. 201 (2006) 4352–4356.
[23] J. Andersson, R.A. Erck, A. Erdemir, Friction of diamond-like carbon films in different atmospheres, Wear. 254 (2003) 1070–1075.
[24] S. Bhowmick, A. Banerji, A.T. Alpas, Friction reduction mechanisms in multilayer graphene sliding against hydrogenated diamond-like carbon, Carbon N. Y. 109 (2016) 795–804.
[25] S.C. Tung, H. Gao, Tribological characteristics and surface interaction between piston ring coatings and a blend of energy-conserving oils and ethanol fuels, Wear. 255 (2003) 1276–1285.
[26] W. Conshohocken, Standard Practice for Conducting Friction Tests of Piston Ring and Cylinder Liner Materials Under Lubricated Conditions 1, Test. i (2010) 1–9. doi:10.1520/G0181-04R09.2.
[27] P.M. Lee, R.J. Chittenden, Consideration of test parameters in reciprocating tribometers used to replicate ring-on-liner contact, Tribol. Lett. 39 (2010) 81–89.
[28] A. Banerji, M.J. Lukitsch, A.T. Alpas, Friction reduction mechanisms in cast iron sliding against DLC: Effect of biofuel (E85) diluted engine oil, Wear. 368 (2016) 196–209.
[29] A. Banerji, H. Hu, A.T. Alpas, Sliding wear mechanisms of magnesium composites AM60 reinforced with Al 2 O 3 fibres under ultra-mild wear conditions, Wear. 301 (2013) 626–635.
[30] A. Banerji, A. Edrisy, V. Francis, A.T. Alpas, Effect of bio-fuel (E85) addition on lubricated sliding wear mechanisms of a eutectic Al–Si alloy, Wear. 311 (2014) 1–13.
[31] M. Chen, X. Meng-Burany, T.A. Perry, A.T. Alpas, Micromechanisms and mechanics of ultra-mild wear in Al–Si alloys, Acta Mater. 56 (2008) 5605–5616.
[32] I.M. Hutchings, P. Shipway, Tribology: friction and wear of engineering materials, (1992).
[33] X. Meng-Burany, A.T. Alpas, FIB and TEM studies of damage mechanisms in DLC coatings sliding against aluminum, Thin Solid Films. 516 (2007) 325–335.
[34] J. Zhang, A.T. Alpas, Transition between mild and severe wear in aluminium alloys, Acta Mater. 45 (1997) 513–528.
[35] D.L.A. De Faria, S. Venâncio Silva, M.T. De Oliveira, Raman microspectroscopy of some iron oxides and oxyhydroxides, J. Raman Spectrosc. 28 (1997) 873–878.
[36] A.C. Ferrari, J. Robertson, Interpretation of Raman spectra of disordered and amorphous carbon, Phys. Rev. B. 61 (2000) 14095.
[37] U. Schwertmann, J. Friedl, H. Stanjek, From Fe (III) ions to ferrihydrite and then to hematite, J. Colloid Interface Sci. 209 (1999) 215–223.
[38] L. Xiang, C. Gao, Y. Wang, Z. Pan, D. Hu, Tribological and tribochemical properties of magnetite nanoflakes as additives in oil lubricants, Particuology. 17 (2014) 136–144.
[39] S.R. Pearson, P.H. Shipway, J.O. Abere, R.A.A. Hewitt, The effect of temperature on wear and friction of a high strength steel in fretting, Wear. 303 (2013) 622–631.

[40] E.R.M. Gelinck, D.J. Schipper, Calculation of Stribeck curves for line contacts, Tribol. Int. 33 (2000) 175–181.
[41] H. Spikes, The history and mechanisms of ZDDP, Tribol. Lett. 17 (2004) 469–489.

CHAPTER 5

High Temperature Tribological Behaviour of W Containing Diamond-Like Carbon (DLC) Coating against Titanium Alloys

5.1. Introduction

Diamond-like carbon (DLC) coatings are promising candidates for protecting contact surfaces during manufacturing operations including stamping, and machining as well as in tribological systems like the piston rings running against cylinder bores of aluminum internal combustion engines [1–4]. DLC coatings show no or very small adhesion against aluminum (and magnesium) alloys [5–10]. A drawback of most DLC coatings is that they tend to show high friction and adhesion at temperatures typically higher than 200 ˚C [11–14]. Konca et al. [15] observed that non-hydrogenated DLC (NH-DLC), with 40 at % H, tested against an Al-6.5% Si (319 Al) alloy at 120 ˚C produced a coefficient of friction, COF, of 0.30 that was nearly two times higher than the COF at 25 ˚C (measured under an atmosphere with 15% RH). Similarly the wear rate (3.08×10^{-5} mm^3/m) at 120 ˚C was an order of magnitude higher than that at 25 ˚C. The wear rate increased further to 3.36×10^{-4} mm^3/m at 300 ˚C where the coating was almost completely removed from the surface of the steel substrate. It was suggested that the low COF of NH-DLC coatings tested in ambient air (25 ˚C) was due to passivation of the dangling carbon bonds at the contact surface by –OH dissociated from themoisture in the ambient air [8,16]. A carbon rich transfer layer that was also –OH passivated was detected on the counterface. The lack of moisture at elevated temperatures was thought to deprive the surface carbon atoms from the beneficial effect of passivation and as such causing adhesion of aluminum to the DLC surface [12-14]. A comparative study [17] of the tribological behaviour of H-DLC and NH-DLC (with less than 2% H) coatings against the same aluminum alloy (319 Al) found that at 25 ˚C

both the coatings showed low COF values of 0.11-0.12 with very low adhesion. The low COF observed in H-DLC at room temperature could be attributed to hydrogen termination of dangling carbon bonds, in a way similar to -OH passivation [8, 16]. As H-DLC does not require atmospheric moisture for passivation, its low COF can be retained at higher temperatures compared to NH-DLC [18,19]. At 300 ˚C, significant aluminum adhesion was noted regardless of coating composition. At 300 ˚C and above, graphitization of DLC occurred consistent with findings from other studies [18, 19]. DLC coatings modified by Si, F, W and other elements have been considered to promote high temperature and environmental stability [20–25]. Tungsten (W) addition was shown to be particularly beneficial for the high temperature tribological behaviour of the DLC coatings [21-25]. Baba and Hatada [21] performed room temperature ball (WC)-on-disk (W-DLC) tests and reported a low COF of 0.10 of W-DLC due to the WC precipitates present on the coating surface as determined using XRD and X-ray photoelectron spectroscopy (XPS) studies. Transmission electron microscopy conducted by Meng and Gillispie [22], who studied mechanical properties of W-DLC, revealed the presence of nanocrystalline (nc) WC embedded in an amorphous carbon matrix. DLC coatings incorporating carbide particles including TiC, TiBC and WC when tested against AISI 52100 steel [23] showed that the harder TiBC containing DLC had highest wear rate (5×10^{-5} mm^3/Nm) due to the formation of brittle TiB_2 (hexagonal), as determined by XRD. The WC-DLC system maintained a good compatibility between the mechanical properties (Hardness=15-20 GPa) and tribological properties (μ~0.2; wear rates 10^{-7}-10^{-8} mm^3/Nm). Voevodin et al. [24] observed that the COF of coatings with nc WC embedded in a DLC matrix decreased from 0.70 to 0.30 as the carbon content of DLC increased from 30 at.% to 90 at.% when tested in an ambient air atmosphere (50% RH) at 25 °C. Raman analyses found evidence for the formation of tungsten oxide and the

authors noted that the oxide layer led to self-lubrication of coatings. Fervel et al. [25] studied thermal sprayed WC-17% Co run against Al_2O_3 (with 13-40% TiO_2) and recorded a COF of 0.20 and observed formation of a WO_3 layer detected by XPS. In a study on the tribological behaviour W-DLC tested against 319 Al counterface a similar low COF of 0.18 was observed at 400 ˚C [26] whereby the COF remained low (0.12) at 500 ˚C . Micro-Raman analyses indicated the formation of tungsten oxide rich layers both on the W-DLC surface and in the transfer layers on the 319 Al counterface. The formation of WO_3 on W-DLC surface was proposed to be responsible for the low COF. On the other hand under lubricated sliding conditions the improved scuffing resistance of W-DLC was discussed in terms of the formation of WS_x type tribofilms on their sliding surfaces [27–29].

In summary, the incorporation of W in DLC was shown to improve the tribological properties of DLC coatings at elevated temperatures. Although the tribological performances of DLC coatings have been studied against steel, Al and Mg as reviewed above, performances of DLC coatings against titanium alloys are yet to be explored. NH-DLC coatings tested at room temperature against Ti-6Al-4V under an ambient atmosphere exhibited a COF of 0.11 [30]. Another study [31] found also a low COF of 0.10 when NH-DLC coatings were tested against commercially pure titanium (>99.3 wt.%) under the ambient conditions, but in an argon atmosphere a high COF of 0.52 was measured. When studying friction and wear of W-DLC sliding against Ti-6Al-4V alloy consideration should be given to their elevated temperature behaviour. These studies are expected to contribute to improving the efficiency of high temperature forming process of Ti-6Al-4V as well their machining performance by improving the tool and die life. Accordingly the current study evaluates the high temperature tribological performance of H-DLC and W-DLC coatings against Ti-6Al-4Vand compares the performace of

these coatings with more conventional caotings. Surface characterization studies were carried out for the rationalization of the tribological mechanisms responsible for friction, wear and material transfer during elevated temperature sliding contact.

5.2. Experimental Details

Pin-on-disk tests were performed using Ti-6Al-4V alloy pins of 15 mm in length with one end machined into a hemisphere of 4.05 mm in diameter. Ti-6Al-4V had the following composition (in wt.%): 5.50-6.75% Al, ≤ 0.08% C, ≤ 0.4% Fe, ≤ 0.03% N, ≤ 0.2% O, ≤ 0.02% H, 3.50-4.50% V and the balance Ti. The microhardness of the alloy was 380.00 ± 3.01 HV. M2 grade tool steel of 2.54 cm in diameter and with a hardness of 64 ± 3 HRC was used as the substrate for all the coatings tested. The M2 steel disks were polished to 0.1 μm prior to the deposition processes.

5.2.1 N- Based Coatings: TiN, TiAlN and TiCN

TiN coatings of 0.80 μm in thickness were deposited on the polished M2 steel disks using cathodic arc vapour deposition (CAVD) process that employed a Ti target and N_2 gas (2-5 Pa). The hardness and elastic modulus of the coatings were measured using a Hysitron TI 900 Triboindenter equipped with a Berkovich type nano-indenter. Accordingly, the hardness and elastic modulus of the as deposited TiN coatings were calculated to be 13.90 GPa and 278.00 GPa. Similarly, TiAlN coatings of 0.82 μm in thickness were deposited using the CAVD method where a Ti-Al target was used in an N_2 atmosphere (Ti:Al:N=35:15:50 at%). The hardness of the TiAlN coatings was 14.21 GPa and their elastic modulus was 257.00 GPa. TiCN coatings were also deposited from a Ti target by CAVD method to a thickness of 0.87 μm in an atmosphere consisting of N_2 and C_2H_2. The TiCN coatings deposited in this way had a hardness of 14.50 GPa and an elastic modulus of 250.00 GPa.

5.2.2 C-Based Coatings: H-DLC and W-DLC

The H-DLC coatings were deposited using an unbalanced magnetron sputtering system. The physical vapour deposition (PVD) system used had one chromium target and two graphite targets. The M2 steel substrate surfaces were first cleaned by Ar glow discharge and then an approximately 0.10 μm thick Cr interlayer was deposited to promote adhesion of the coating to the steel surface. The power to the Cr target was decreased gradually while increasing the power to graphite targets to obtain 1.50 μm thick DLC coatings. Butane precursor gas was used to achieve the desired 40 at.% of hydrogen content of the coating as confirmed by Elastic Recoil Detection analyses. This coating is designated as H-DLC; the hardness and the elastic modulus of H-DLC were 11.40 GPa and 103 GPa. The average surface roughness of the H-DLC was 19.45 ± 0.80 nm as determined using an optical surface profilometer.

The W-DLC coatings were deposited on M2 steel coupons using a cathodic arc PVD system. The substrate surfaces were first cleaned by Ar glow discharge following which the Cr layer was deposited. The hardness of the W-DLC coating was 8.70 ± 1.70 GPa, and its elastic modulus was 104.31 ± 18.81 GPa. The average surface roughness of the W-DLC was 20.01 ± 1.02 nm as determined using an optical surface profilometer. The W content of the coating was 20 at. % and the H concentration was kept < 2 at.%. Cross-sections made by focused ion beam (FIB) milling method (Carl Zeiss NVision 40 CrossBeam) were examined by SEM and TEM. The specific locations where the cross-sections are taken were prepared by coating the area of interest with 35 μm × 2 μm × 2 μm strips of Pt to protect the sample surface from ion beam damage during milling. Ion milling and polishing were then performed on the both sides of the area protected by the Pt strip to reduce the thickness of the cross-sectional sample below 100 nm (in-situ lift out method [32]). Then two narrow trenches (6 μm thick and 22 μm long) were

cut parallel to each other on either side of the area of interest, using FIB milling. A thin membrane (1 μm thick and 20 μm long), left between the two trenches, was then removed using a lift-out device with an end effector and placed on a Cu-grid for TEM observations. Fig.5.1(a) shows the SEM cross-sectional microstructure of the W-DLC coating with ~1 μm thick Cr interlayer. Energy-dispersive X-ray spectroscopy (EDS) maps were taken using FEI Quanta 200 FEG scanning electron microscopes equipped with an energy-dispersive X-ray EDAX SiLi Detector spectrometer and showed the distributions of W and C across the thickness of the coating as represented in Fig. 5.1(b, c). The high resolution TEM micrograph in Fig. 5.1(d) and the corresponding diffraction pattern in Fig. 5.1(e) show the nanocrystalline WC particles (15.0±5.2 nm) dispersed in an amorphous carbon matrix.

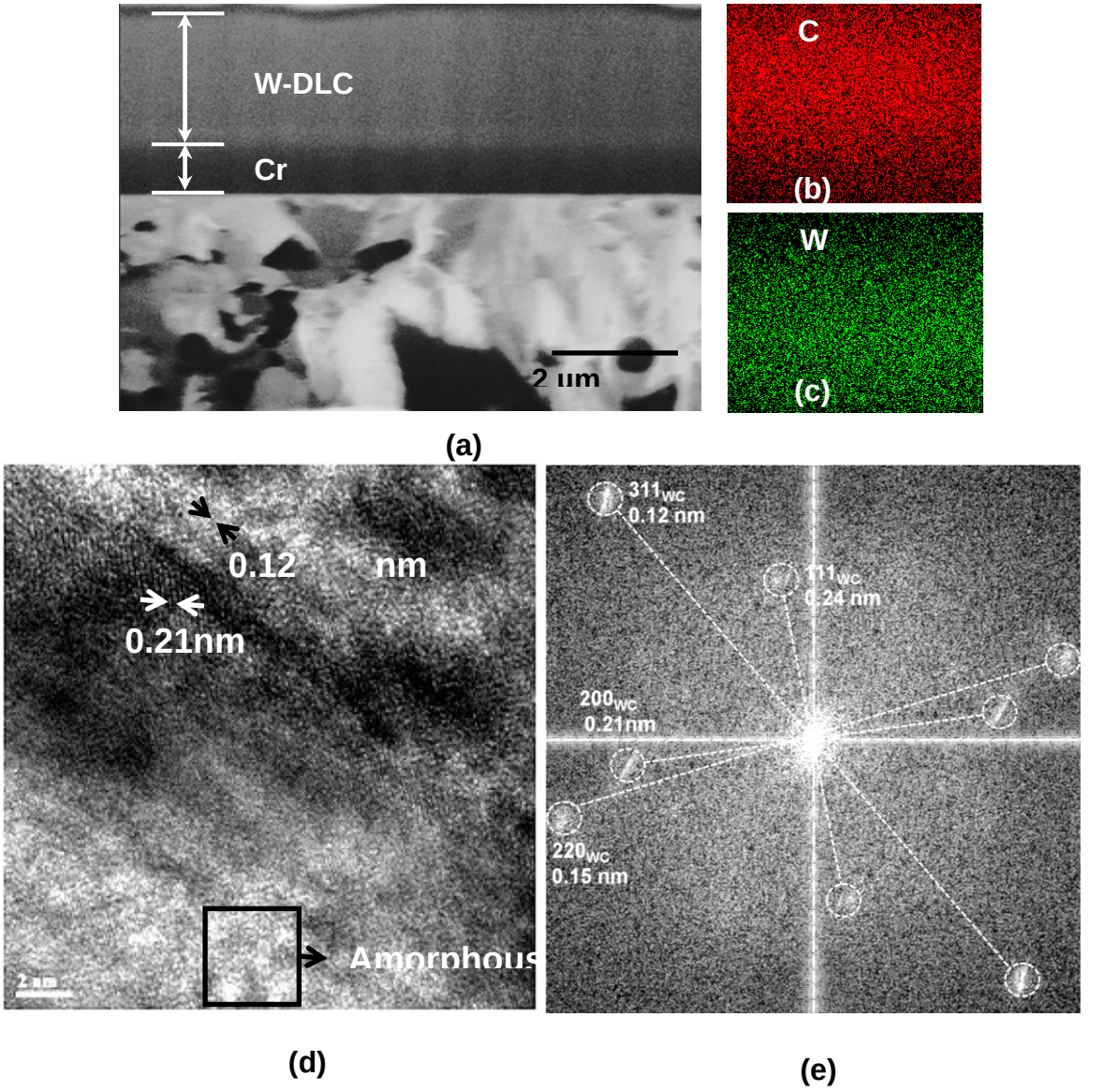

Figure 5.1. Cross-sectional micrographs of W-DLC: (a) FIB/SEM micrograph showing the W-DLC and the Cr interlayer deposited on M2 steel substrate; (b, c) EDS maps of C and W; (d) HR-TEM micrograph showing FCC crystalline structure of nano scale WC particles dispersed in an amorphous matrix; (e) selected area diffraction pattern showing WC particles in an amorphous matrix.

5.2.3. Pin-on-Disk tests and Wear Rate Calculations

A high temperature pin-on-disk tribometer was used to measure the COF and the volumetric wear of N- and C-based coatings (and the uncoated M2 steel) at 0.12 m/s and a normal load of 5.00 N for 1.00×10^3 – 3.00×10^3 revolutions. Whenever steady state COF was attained the average COF value of steady-state stage of the friction curve was calculated from the arithmetic mean of COF signals typically after 2.00×10^2 revolutions. For tests where no steady state COF occurred, the data was recorded up to 15.00×10^2 revolutions and the average of the fluctuating COF curve was reported. The COF values were recorded separately for each test at a specific constant temperature. The steady state COF value reported for each temperature is the average of the steady state values obtained from three tests conducted for that constant temperature. The standard deviation of an individual COF curve was calculated by determining the dispersion (fluctuations) from average COF value for each test. The arithmetic mean of the standard deviation values from three tests conducted at each constant temperature has been reported as the overall standard deviation of the COF curve at that temperature. The average steady state COF along with the standard deviations for three tests performed at each constant test temperature has been presented in Table 5.1. Sliding tests for all coatings were carried out at 25 ˚C (47% RH). H-DLC and W-DLC coatings were subjected to high temperature tests. These two coatings were tested at several constant temperatures up to 500 ˚C. Sliding tests were conducted on a polycrystalline (35° rhombic) diamond, PCD, insert with a hardness of ~80 GPa, against the same Ti-6Al-4V pins. The PCD was selected for comparison of its tribological properties with the coating because PDC tools are extensively used in the manufacturing of titanium alloys and known to have high wear resistance [33].

The wear losses of the N- and C-based coatings were calculated from the volume of the material removed as measured from the area of the wear track at eight different locations along a circular sliding track of radius 1.5 mm. A white light interferometry technique—a Wyko NT 1100 optical surface profilometer—was used for this purpose in a way similar to that described in [34]. When material transfer (from Ti-6Al-4V) occurred to the coating surface the adhered material was removed by boiling HNO_3 prior to conducting the surface profilometery on the sliding track. The reported wear rates were the average values (and the corresponding standard deviations) obtained from three tests at each temperature and loading condition.

An EDS mapping technique was used to determine the areal distribution of titanium transferred to the sliding track formed on the coating surface. The compositional contrast provided by EDS served to differentiate between the composition of the transferred material and that of the coating. The coating surface area covered by titanium was determined using an image analysis program using four EDS maps obtained from each sliding track. The Raman spectra of the transfer layers were obtained using a 50 mW Nd-YAG solid state laser (532.0 nm excitation line) through the 50× objective lens of a Horiba Raman micro-spectrometer.

Table 5.1: Summary of average coefficient of friction of H-DLC and W-DLC coatings against Ti-6Al-4V at different test temperatures.

	H-DLC				
(°C)	25 ˚C	100 ˚C	200 ˚C	300 ˚C	400 ˚C
Test 1	0.11±0.01	0.07±0.01	0.05±0.001	0.45±0.15	0.57±0.08
Test 2	0.11±0.02	0.06±0.01	0.05±0.002	0.43±0.11	0.56±0.12
Test 3	0.12±0.01	0.07±0.01	0.04±0.001	0.45±0.12	0.58±0.13

	W-DLC					
(°C)	25 ˚C	100 ˚C	200 ˚C	300 ˚C	400 ˚C	500 ˚C
Test 1	0.10±0.01	0.06±0.001	0.03±0.006	0.35± 0.10	0.06±0 .04	0.08± 0.01
Test 2	0.11±0.01	0.07±0.002	0.03±0.007	0.34± 0.10	0.08± 0.02	0.09± 0.01
Test 3	0.09±0.01	0.05±0.001	0.03±0.006	0.37±0 .09	0.06±0 .03	0.07± 0.01

5.3. Results and Analyses

5.3.1 Evaluation of Coatings and Ranking of their Performance

Initially three types of N-based coatings were tested against Ti-6Al-4V in order to compare their performance with C-based coatings at 25 ℃ . All N-based coatings tested, TiN, TiAlN and TiCN, exhibited high COFs and large fluctuations from the mean values of the recorded COF. Typical friction curves showing the variations in their COF with the number of revolutions are presented in Fig. 5.2(a), for TiN and TiAlN together with the uncoated M2 steel substrate. The

M2 steel and the N-based coatings exhibited similar friction behaviour; the initial COFs were low i.e., 0.29 for M2 steel, 0.31 for TiAlN and 0.33 for TiN (and 0.31 for TiCN not shown as it was almost identical to other coatings). This was followed by an increase in COFs for all coatings and the substrate. The COF values for number of revolutions exceeding 4.00×10^2 were 0.39 ± 0.02 for the M2 steel, 0.46 ± 0.02 for TiN, 0.41 ± 0.04 for TiAlN and 0.41 ± 0.03 for TiCN.

In almost total contrast to the friction behaviour of the N-based coatings, the C-based coatings exhibited an initial high peak, which was followed by a decrease to low and steady-state COF characterized by low fluctuations. The initial COF of PCD was as high as 0.41 but after sliding for about 1.60×10^2 revolutions a very low and stable COF of 0.05 ± 0.01 was attained, a behaviour that was was maintained for the rest of the test. Note that in addtion to the low average value the fluctuations in the COF curve were also negligibly small (±0.01) indicating a steady state COF regime. The high COF at low sliding cycles (number of revolutions) was thus regarded as the running-in period which preceded the stead state COF. A similar behaviour was observed during the sliding of H-DLC coatings for which an initial COF 0.60 was recorded for the running-in period that lasted less than 20 revolutions. The COF then decreased to a low and stable value of 0.11 ± 0.01 (Fig. 5.2a).

The coatings were ranked according to their average COF values obtained (Fig. 5.2b) when they reach a high COF plateau (for N-based coatings) or a low steady-state plateau (for C-based coatings). For the comparisons made in Fig. 5.2(b) an average COF of three friction tests were considered. The low COFs of PCD and H-DLC coatings compared to the N-based coatings become evident from Fig. 5.2(b). As a result of this ranking H-DLC coating emerged as a candidate for further evaluation of its tribological performance against Ti-6Al-4V at elevated

temperatures as will be discussed in detail in section 3.2 . It was observed that the COF of W-DLC coating (0.08) was as low as that of the H-DLC coating and hence this coating too was considered for elevated temperature tests (see section 3.3.).

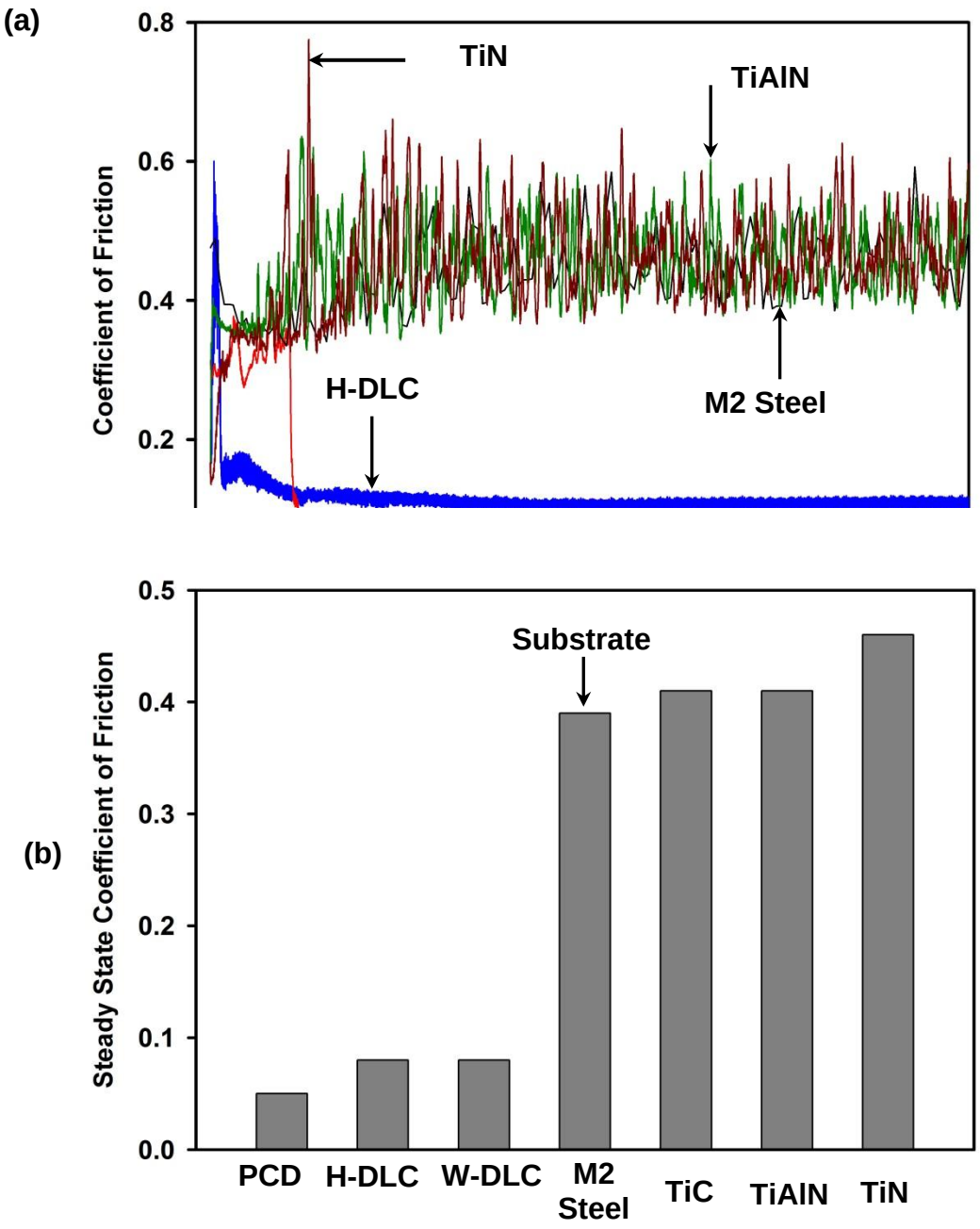

Figure 5.2. (a) Variations of the COF with the number of revolutions for uncoated M2 steel, TiN, TiAlN, PCD and H-DLC tested against Ti–6Al–4V at 25 °C in ambient air atmosphere. (Load = 5.00 N and speed = 0.12 m/s). (b) The variation of the average COF and standard deviation values for uncoated M2 steel, TiN, TiAlN, PCD, H-DLC, W-DLC and TiCN against Ti–6Al–4V-as determined from three tests performed for each coating.

5.3.2 Changes in Tribological Behaviour of H-DLC with Temperature

Fig. 5.3 shows the variation of COF of H-DLC with the number of revolutions for the tests conducted at 100, 200 and 300 ˚C. At 100 ˚C a COF of 0.14 was recorded during the running-in period followed by a decrease to a steady state value of 0.07 ± 0.01, i.e. a lower COF value than that was observed at 25 ˚C. (The friction curve at 25 °C is reproduced in Fig. 5.3 for comparison.) A low running-in COF followed by a low steady state COF of 0.05 ± 0.001 was also observed at 200 ˚C. This was the highest (test) temperature where a low steady state COF was obtained for H-DLC. Sliding tests conducted at 300 ˚C showed an unstable COF that increased with the number of revolutions; after 1.90 × 102 revolutions a high COF of 0.44 ± 0.13 with large fluctuations was recorded. Microscopic observations of the wear track indicated that H-DLC coating was completely removed and detached from the contact surface during sliding at 300 ˚C. Sliding tests conducted at 400 ˚C resulted in a higher COF of 0.57 ± 0.11, where the coatings were found to be removed from the wear track exposing the steel substrate.

The wear tracks formed on the H-DLC surfaces were examined using SEM and the representative secondary electron images (SEI) are shown in Fig. 5.4. No significant transfer of material from Ti-6Al-4V to the H-DLC could be detected for the tests performed in the temperature range between 25 ˚C and 200 ˚C (Figs. 5.4 [a-c]). Traces of titanium transfer could be found occasionally along the wear tracks as marked on these images. On the other hand, a considerable amount of titanium transfer occurred to the H-DLC surface both at 300 ˚C and 400 ˚C and the wear tracks were entirely covered by the adhered titanium layers (Figs. 5.4 [d-e]). As per previously described process, the wear track was examined by dissolving the transferred material and it was found the adhesion indeed occurred on the steel substrate. Hence the COF

recorded for 300 ˚C and 400 ˚C were at least as high as that of the M2 steel as indicated in Fig. 5.2(a).

The Ti-6Al-4V pin contact surfaces were examined by SEM in the secondary electron image (SEI) mode to reveal the morphological features of the worn area while the elemental composition of this area was determined using EDS. It was observed for tests conducted at 25 ˚C, 100 ˚C and 200 ˚C that the contact surfaces at the tips of the Ti-6Al-4V pins were covered with patches of materials transferred from the H-DLC. An example is given in Fig. 5.5(a) that shows the contact surface of Ti-6Al-4V pin for test conducted at 200 ˚C and reveals that the tip was entirely covered by a transfer layer. The corresponding EDS elemental maps show the distributions of the elements, namely Ti, Al, and V that belong to the pin as well as C transferred from the coating and O due to oxidation Figs. 5.5 (b-f). It can be seen that the contact area was devoid of the pin elements Ti, Al and V but a transfer layer which was rich in C was formed (Fig. 5.5e). The formation of carbonaceous transfer layers on Ti-6Al-4V correlated well with the fact that almost no Ti transfer to the H-DLC coating surface occurred (Fig. 5.4c) and this was consistent with low COF recorded during sliding (Fig. 5.3).

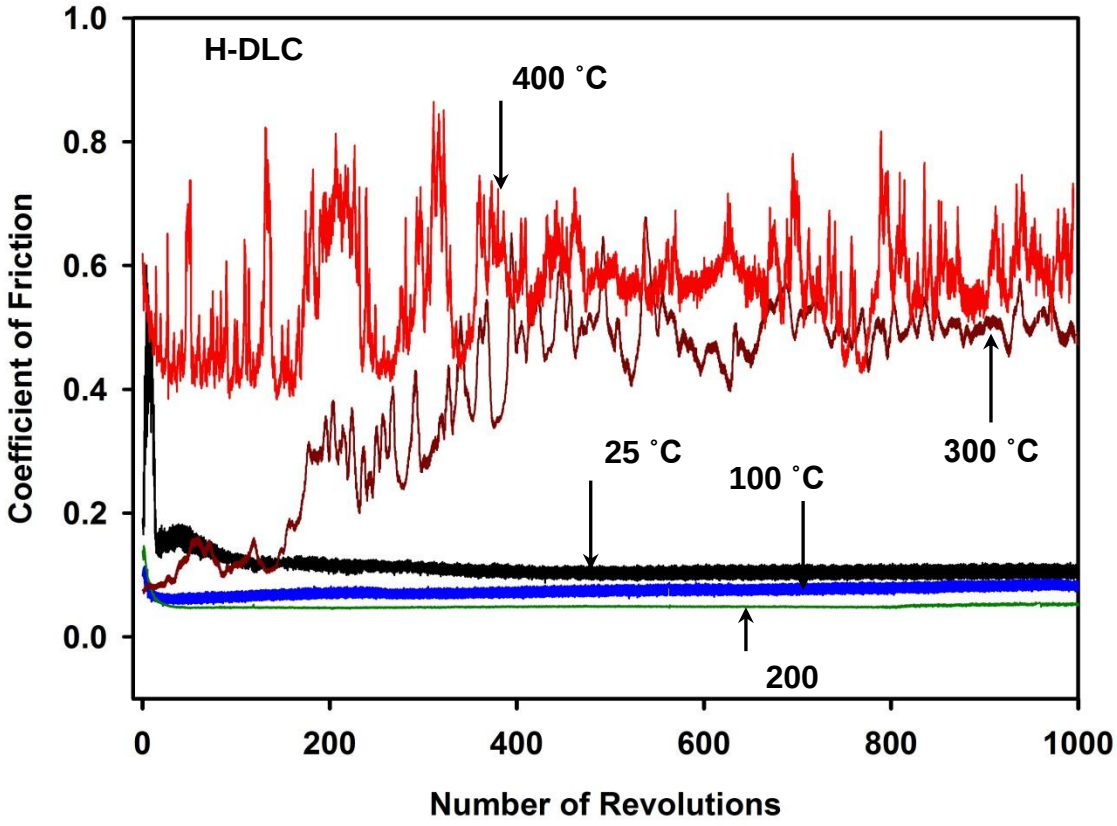

Figure 5.3. Variations of the COF with the number of revolutions when the H-DLC coating was tested against Ti–6Al–4V at 25 °C, 100 °C, 200 °C, 300 °C and 400 °C.

The wear track on the coating surface was smooth (Fig. 5.4c) and as evident from the lack of Fe at the sliding interface (Fig. 5.5g) the H-DLC coating was still intact with only slight wear. For tests conducted at 300 ˚C and 400 ˚C there were no transfer layers formed on the Ti-6Al-4V pin's contact surface. The tip of the Ti-6Al-4V pin tested at 400 ˚C and the corresponding EDS maps of relevant elements, Ti, Al, V, C, O and Fe, are shown in Figs. 5.5(h-n). The Ti-6Al-4V contact surface was subjected to wear and had the same composition as the rest of the pin with no significant evidence for C transfer, Fig. 5.5(l). In contrast to the tests done at 200 ˚C and at lower

temperatures however, large amount of Fe was found on the worn contact surface of Ti-6Al-4V, which possibly occurred after the removal of the coating as a result of wear exposing the M2 substrate. In summary, H-DLC coatings showed low and stable COFs up to 200 ˚C, which was accompanied by the formation of a carbonaceous transfer layer on the Ti-6Al-4V alloy's contact surface. The high COF values were observed when the tests were performed at 300 ˚C and 400 ˚C where no such transfer layer was formed on the Ti-6Al-4V pin.

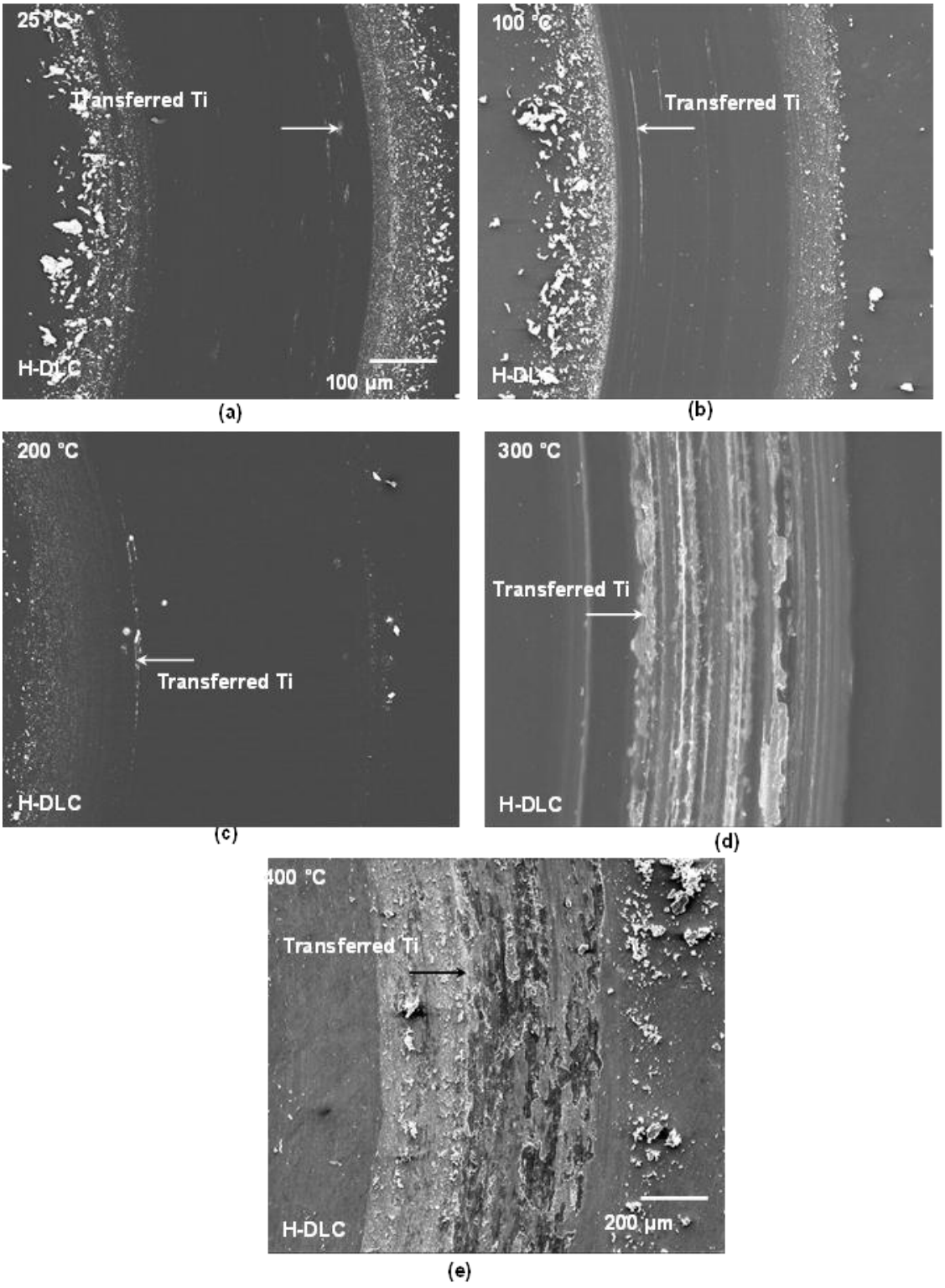

Figure 5.4. Typical secondary electron images of wear tracks formed on the H-DLC surface when tested against Ti–6Al–4V at (a) 25 °C, (b) 100 °C, (c) 200 °C, (d) 300 °C and (e) 400 °C.

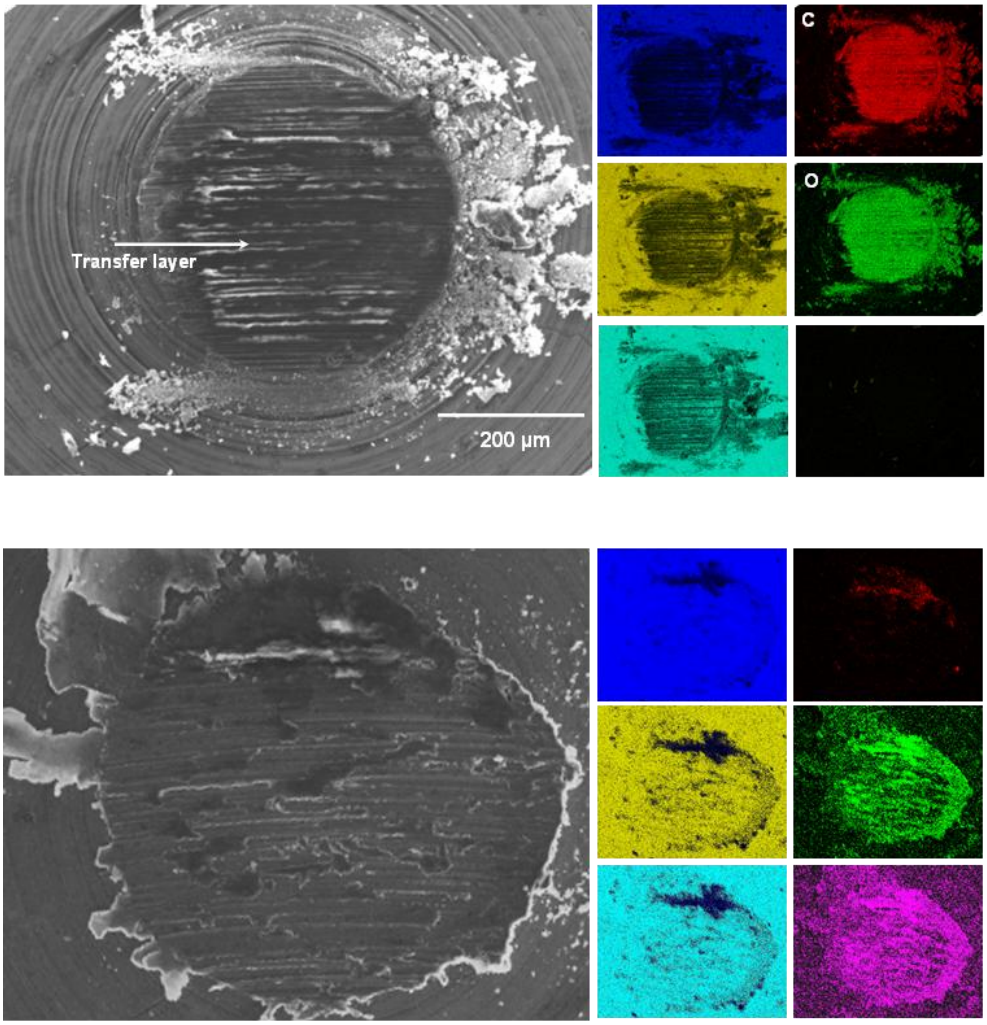

Figure 5.5. (a) Secondary electron image of the Ti–6Al–4V pin surface taken after sliding against H-DLC coating at 200 °C. The elemental EDS maps taken from the whole area shown in (a) are for (b) Ti, (c) Al, (d) V, (e) C, (f) O and (g) Fe. (h) Secondary electron image of Ti–6Al–4V pin surface after the sliding test against H-DLC coating at 400 °C. The elemental EDS maps taken from the whole area shown in (h) are for (i) Ti, (j) Al, (k) V, (l) C, (m) O and (n) Fe.

5.3.3 Changes in Tribological Behaviour of W-DLC with Temperature

As tribological properties of H-DLC were found to deteriorate at high temperature, as reported in Section 3.2., an alternative DLC coating namely W-DLC was considered for potential high temperature sliding applications of Ti-6Al-4V. Fig. 5.2(b) already demonstrated that W-DLC had a COF that was as low as that of H-DLC at 25 C. Shown in Figs. 5.6(a, b) are the COF values of W-DLC coating as a function of number of revolutions at testing temperatures where H-DLC exhibited a low COF and a steady state behaviour. At the beginning of the tests performed at 25 ˚C, the COF initially increased similar to the other C-based coatings and reached a high value of 0.49, fluctuated at this value for about 4.00×10^2 revolutions and decreased to a low value of 0.09 for a few cycles and increased again to 0.30. Following this running-in period, which was more torturous than H-DLC, a low COF value of 0.10 ± 0.01was attained and maintained for the rest of the test. The duration of running-in period of W-DLC was further extended to 9.00×10^2 revolutions when the tests were done at 100 ˚C. At this temperature the COF in the running-in period was about 0.45 and the ensuing steady state COF was 0.06 ± 0.001 that was constant for the duration of last 20.00×10^2 revolutions. The running-in period of W-DLC was the longest, i.e., 1.50×10^2 revolutions for the test conducted at 200 ˚C. A running-in COF of 0.49 was reached and then the friction curve showed the typical decrease to the steady state value of 0.03 ± 0.006 for the last 15.00×10^2 revolutions. The steady state COF of 0.03 ± 0.006 at this temperature was the lowest among all temperatures considered. Therefore, the temperature dependence of COF of both W-DLC and H-DLC showed very similar trends up to 200 ˚C but deviations occurred in favour of W-DLC at higher temperatures.

At 300 ˚C, an initially high COF that lent itself to a lower COF stage was observed for W-DLC. However, no steady state COF could be achieved as high fluctuations were observed in

entire test range at this temperature. A COF value of 0.35 ± 0.10 can be measured for sliding cycles between 1000 and 2000 (Fig. 5.6b) but the COF showed a decreasing trend at high sliding cycles.

For the tests conducted at 400 ˚C and 500 ˚C, the COF behaviour changed once more with lower and stable COF values almost similar to those at temperatures lower than 200 ˚C. Although the general trends of friction curves were similar to those in Fig. 5.6(a) there were notable differences too. At 400 ˚C, the COF increased to 0.21 initially and then decreased to 0.07 ± 0.03 after 8.00×10^2 cycles. The initial increase was 60% lower than the running-in COF at 25 ˚C and also the subsequent drop in COF was not as abrupt. The higher fluctuations about the low COF stage could be noted for tests at 400 ˚C compared to those in Fig 5.6(a). These differences infer that the mechanisms for the low COFs at temperatures between 25 ˚C and 200 ˚C and those at 400 ˚C and 500 ˚C are expected to be different. The COF curve of W-DLC obtained at 500 ˚C was essentially similar to that at 400 ˚C and had a low COF of 0.08 ± 0.01 for the last 2.50×10^3 revolutions.

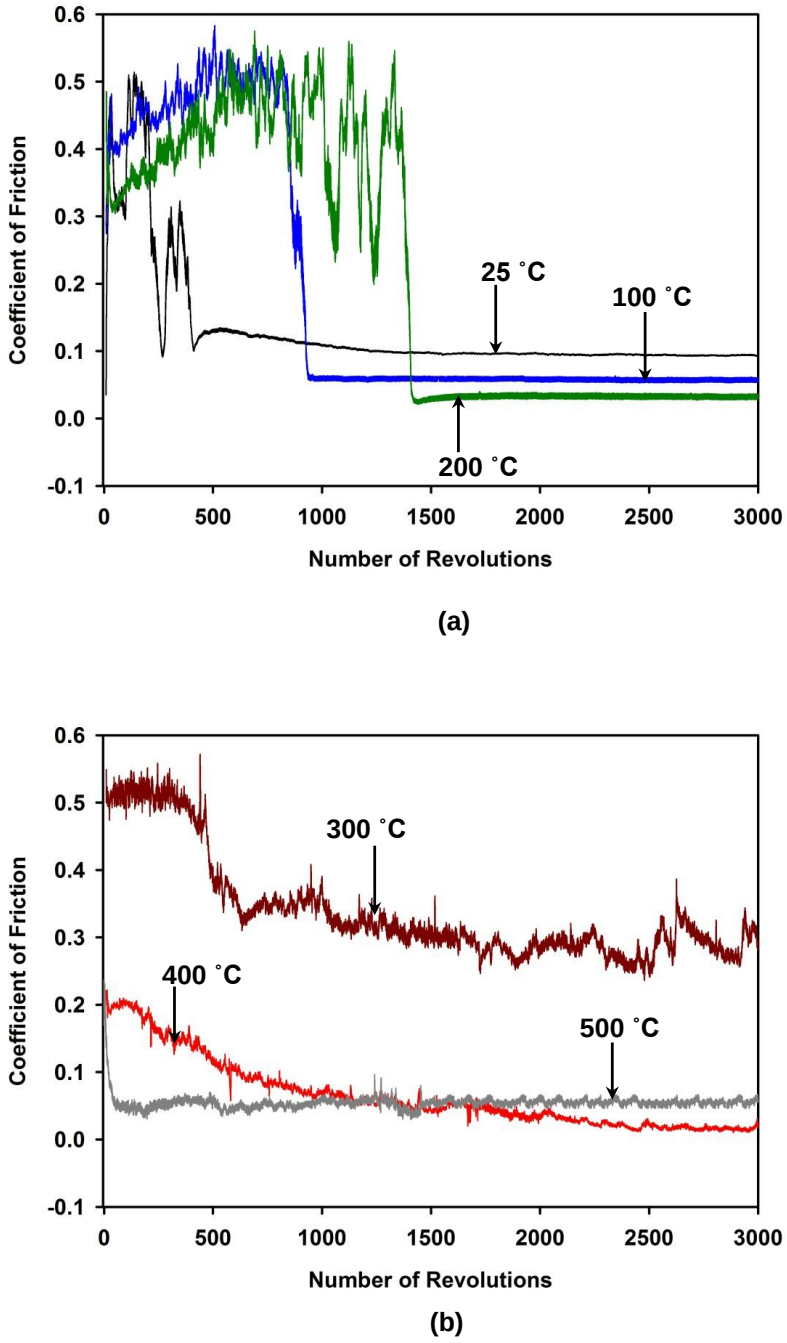

Figure 5.6. Variation of the COF with the number of revolutions when the W-DLC coating was tested against the Ti–6Al–4V pin at (a) 25 °C, 100 °C and 200 °C; (b) 300 °C, 400 °C and 500 °C.

The average COF values of H-DLC and W-DLC are presented as a function of testing temperature in Fig. 5.7. Very similar COF trends of W-DLC and H-DLC up to 300 ˚C can be identified clearly. An increase in the average COF was observed for both H- DLC and W-DLC for temperatures higher than 200 ˚C. While the COF of H-DLC continued to increase at 300 ˚C and at 400 ˚C the COF of the W-DLC interestingly decreased to 0.07 ± 0.01 when tested at 400 ˚C. The low COF of 0.08 ± 0.01 persisted at 500 ˚C.

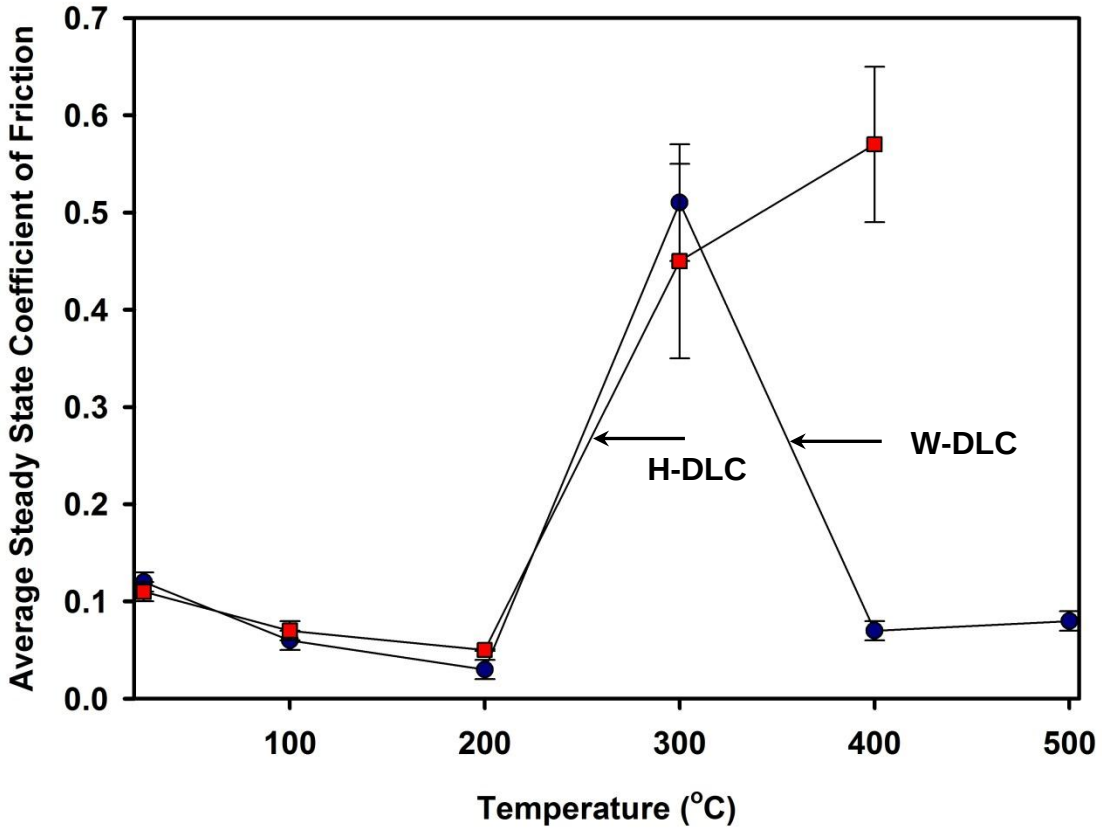

Figure 5.7. Variation of average steady state COF with the test temperature for H-DLC and WDLC coatings. The sliding wear tests were performed at a temperature interval of 25 °C up to 400 °C for H-DLC and up to 500 °C for W-DLC.

SEM images of W-DLC shown in Figs. 5.8 (a, b) did not provide evidence for significant titanium transfer to the wear tracks on the coatings for tests conducted at 25 ˚C and 100 ˚C. At 200 ˚C, some titanium adhesion was observed inside the wear track (Fig. 5.8c) but this was in the form of occasional patches with most of the wear track having a smooth appearance, much like the wear tracks of H-DLC in Figs 5.4a-c. W-DLC tested at 300 ˚C exhibited extensive titanium transfer to coating surface (Fig. 5.8d) similar to H-DLC (Figs 4d). At higher testing temperatures of 400 ˚C and 500 ˚C, interestingly, there was no evidence for titanium adhesion inside the wear tracks of W-DLC (Fig. 5.8 [e, f]). It was also noted that the resulting wear tracks were narrower compared to those formed at 25 ˚C, indicating an overall improvement in the tribological properties of W-DLC in the 400-500 ℃ range.

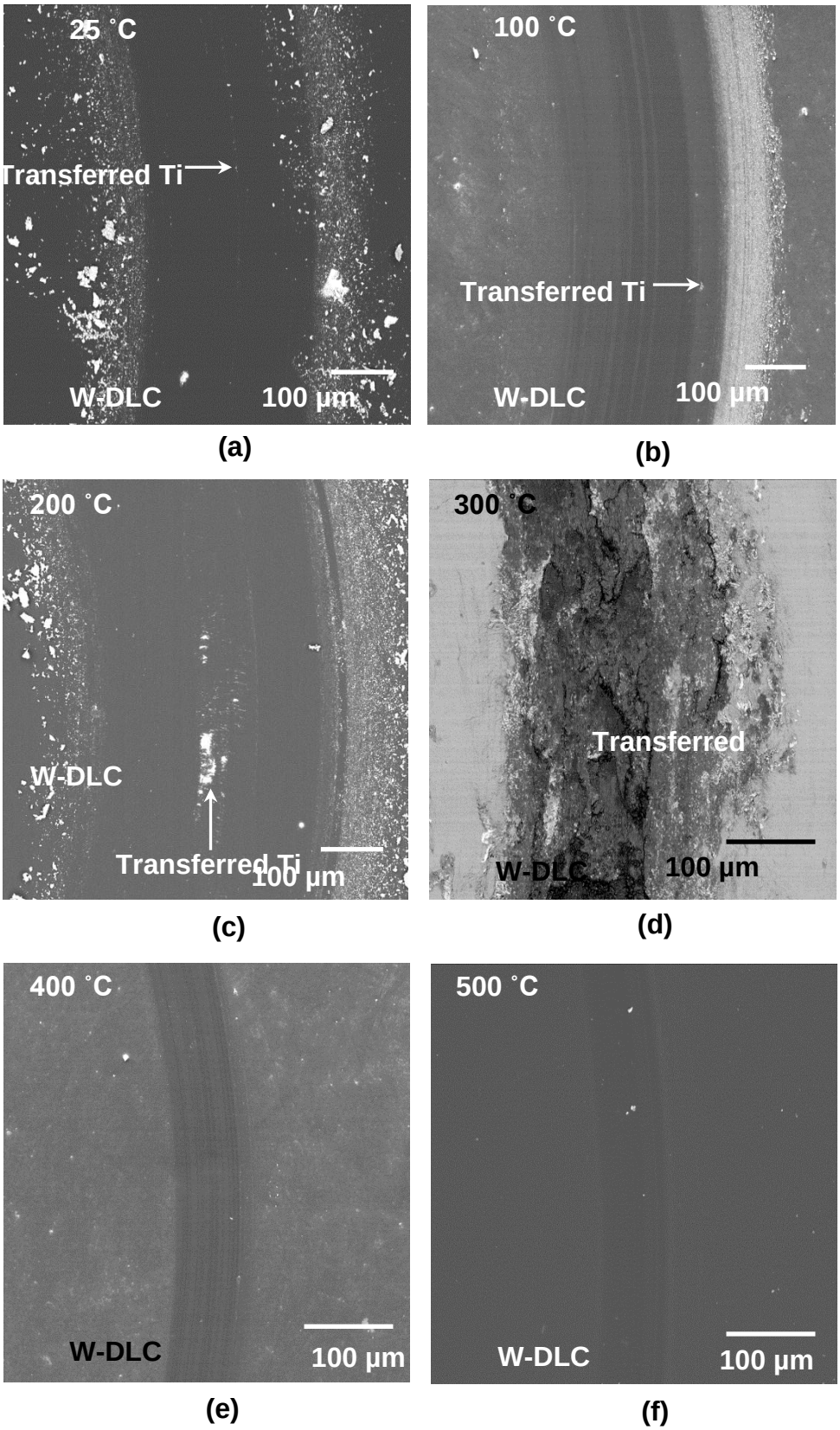
25 ˚C
Transferred Ti
W-DLC
100 µm
(a)
100 ˚C
Transferred Ti
W-DLC
100 µm
(b)
200 ˚C
W-DLC
Transferred Ti
100 µm
(c)
300 ˚C
Transferred
W-DLC
100 µm
(d)
400 ˚C
W-DLC
100 µm
(e)
500 ˚C
W-DLC
100 µm
(f)

Figure 5.8. Typical secondary electron images of sections of W-DLC wear tracks when W-DLC was tested against Ti–6Al–4V at (a) 25 °C, (b) 100 °C, (c) 200 °C, (d) 300 °C, (e) 400 °C, (f) 500 °C.

Fig. 5.9(a) shows results of the quantitative metallographic analyses carried out in order to determine the amount of material transfer to the H-DLC and W-DLC coatings. The area of coating surface covered by transferred material (mainly Ti) was very small (2%) at 25 ˚C and only increased to 5-8% at 200 °C for both H-DLC and W-DLC. The rate of transfer increased between 200 ˚C and 300 ˚C such that 75-82% (300 ˚C) of the surface was covered with transferred material layers. Consistent with the reduction in COF, a notable drop in the amount of material transfer (~1%) occurred at 400 ˚C as well as at 500 ˚C for W-DLC, whereas for the H-DLC tested at 400 ˚C, 80% of the wear track was covered by material transferred from Ti-6Al-4V. As discussed before, the COF appears to correlate well with the amount of material transferred to the coating surface. It is noted that for the W-DLC coating the lowest area coverage is observed at elevated temperatures (>400 ˚C) corresponding to the lowest COF. Fig. 5.9(b) shows the variation of the steady state COF with the area of W-DLC and H-DLC coatings' surface covered by the transferred material for . The COF increased linearly with the amount of material transferred to the coating for the surface coverage between 20-80%. For low (<20%) and high (> 80%) percentages of the surface coverage the slope of the curve changed, with both regions showing high slopes. Within the large region between 20% and 80% surface coverage the variation of COF with the fraction of material adhered (x) obeys the following equation:

$$COF = 0.19 + 0.38x$$

The wear rates of H-DLC and W-DLC coatings at different temperatures are shown in Fig. 5.10. For H-DLC, the normalized wear rate was 2.02×10^{-5} mm^3/Nm at 25 ˚C, and increased to 3.73×10^{-5} mm^3/Nm at 100 ˚C. A slight decrease in wear to 1.11×10^{-5} mm^3/Nm was observed for the test conducted at 200 ˚C (consistent with the lowest observed COF for the coating at this temperature). At 300 ˚C a rapid increase in wear occurred to 1.85×10^{-4} mm^3/Nm with a further increase to 4.29×10^{-4} mm^3/Nm at 400 ˚C. Optical surface profilometery measurements performed on the H-DLC's wear tracks determined a maximum wear depth of 2.18 µm at 300 ˚C and 3.10 µm and 400 ˚C, confirming that the coatings (with initial thickness of 1.50 µm) were removed during sliding, exposing the substrate to the titanium adhesion in agreement with the EDS maps in Fig. 5.5(n) showing presence of Fe transferred from the substrate. Volumetric wear loss of W-DLC increased between 25 ˚C and 300 ˚C. At 25 ˚C, the wear loss was 2.73×10^{-5} mm^3/Nm and slightly increased to 5.86×10^{-5} mm^3/Nm at 100 ˚C. At 200 ˚C the wear loss increased by an order of magnitude to 2.09×10^{-4} mm^3/Nm and reached 4.25×10^{-4} mm^3/Nm at 300 ˚C with a wear depth of 5.1 µm. At higher temperatures the decrease in wear rates were evident as wear rate of 1.05×10^{-5} mm^3/Nm was recorded at 400 ˚C and 3.62×10^{-5} mm^3/Nm at 500 ˚C.

A transfer layer rich in C was formed on the Ti-6Al-4V pin surface when tested against W-DLC between 25 ˚C and 200 ˚C. The Ti-6Al-4V pin tested at 300 ˚C showed scuffing marks along the sliding direction but no significant material transfer (Fig. 5.11a) occurred. The sliding interface was composed of alloying elements of the pin, Ti, Al and V, and there was evidence for oxidation as indicated by the O map as well as some C could be detected mostly towards the periphery of the contact area (Fig. 5.11 [b-f]). Fe transfer was the notable feature of the W-DLC tested at 300 ˚C (Fig. 5.11g) and it is conceivable that iron oxide was formed on the pin surface.

At 400 ˚C and 500 ˚C, a tribolayer covered the contact surface of the Ti-6Al-4V pin, as shown in Fig. 5.11(h). Note that the contact area became smaller indicating less wear. The transfer layer that was formed on the contact surface of Ti-6Al-4V pin was conspicuous and had a dark colour in SEI of Fig. 5.11(h). It was depleted in Ti, Al and V Fig. 11(i,j,k). The layer had high carbon concentration Fig. 5.11(l). The oxidation of the contact area was evident from the prominently high O concentration in Fig. 5.11(m). A particularly important feature of the compositional analyses was the fact that the transfer layer was rich in W (Fig. 11n). The role of W in reducing the COF, or the more specifically the role of WO_3 that formed at high temperatures, is discussed in Section 4.

.

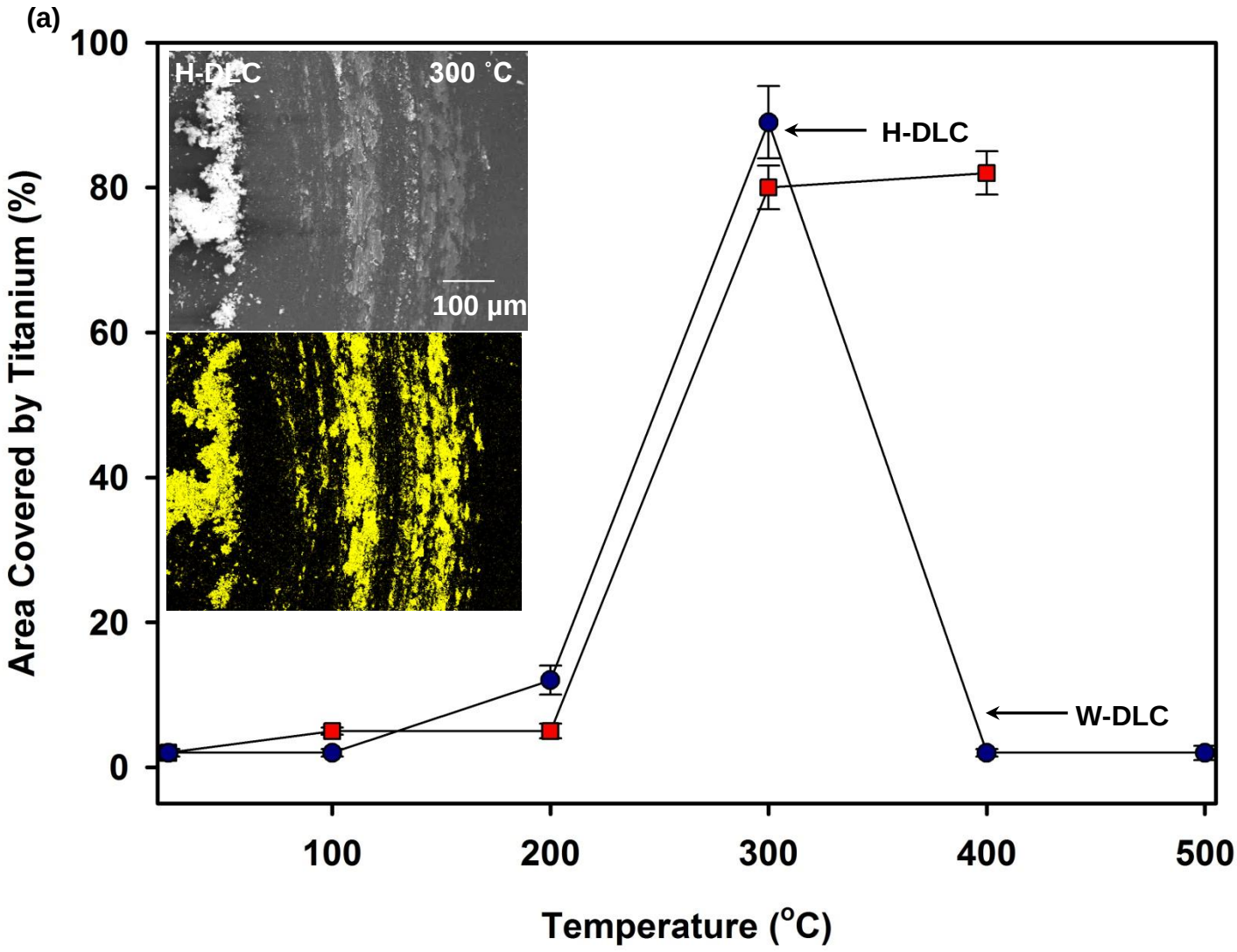
(a)
H-DLC
300 ˚C
100 µm
H-DLC
W-DLC
Area Covered by Titanium (%)
Temperature (°C)
0
20
40
60
80
100
100
200
300
400
500

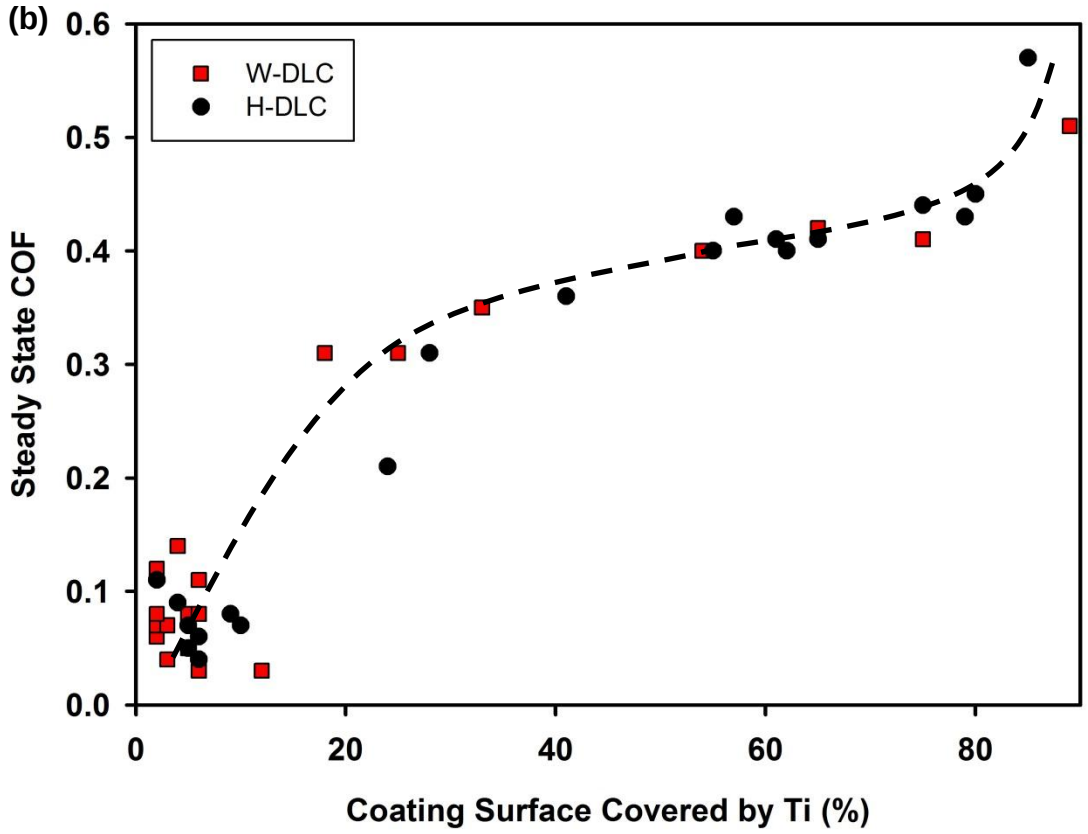

Figure 5.9. (a) Percentage of area covered of the H-DLC and W-DLC wear tracks (by material transferred from Ti–6Al–4V as estimated from EDS maps of titanium (see Sections 3.2 and 3.3)) as a function of temperature. Insets show secondary electron images of wear tracks of H-DLC at 300 °C and corresponding EDS map of adhered titanium. (b) The variation of steady state COF with the percent area of the coating wear track covered by adhered material transferred from Ti–6Al–4V. Sliding wear tests were performed at an interval of 25 °C in the temperature range of 25–400 °C for H-DLC and in the temperature range of 25–500 °C for W-DLC. For H-DLC at N300 °C no steady state COF was obtained and the average COFs from the friction curves recorded up to 15.00×10^2 revolutions are reported.

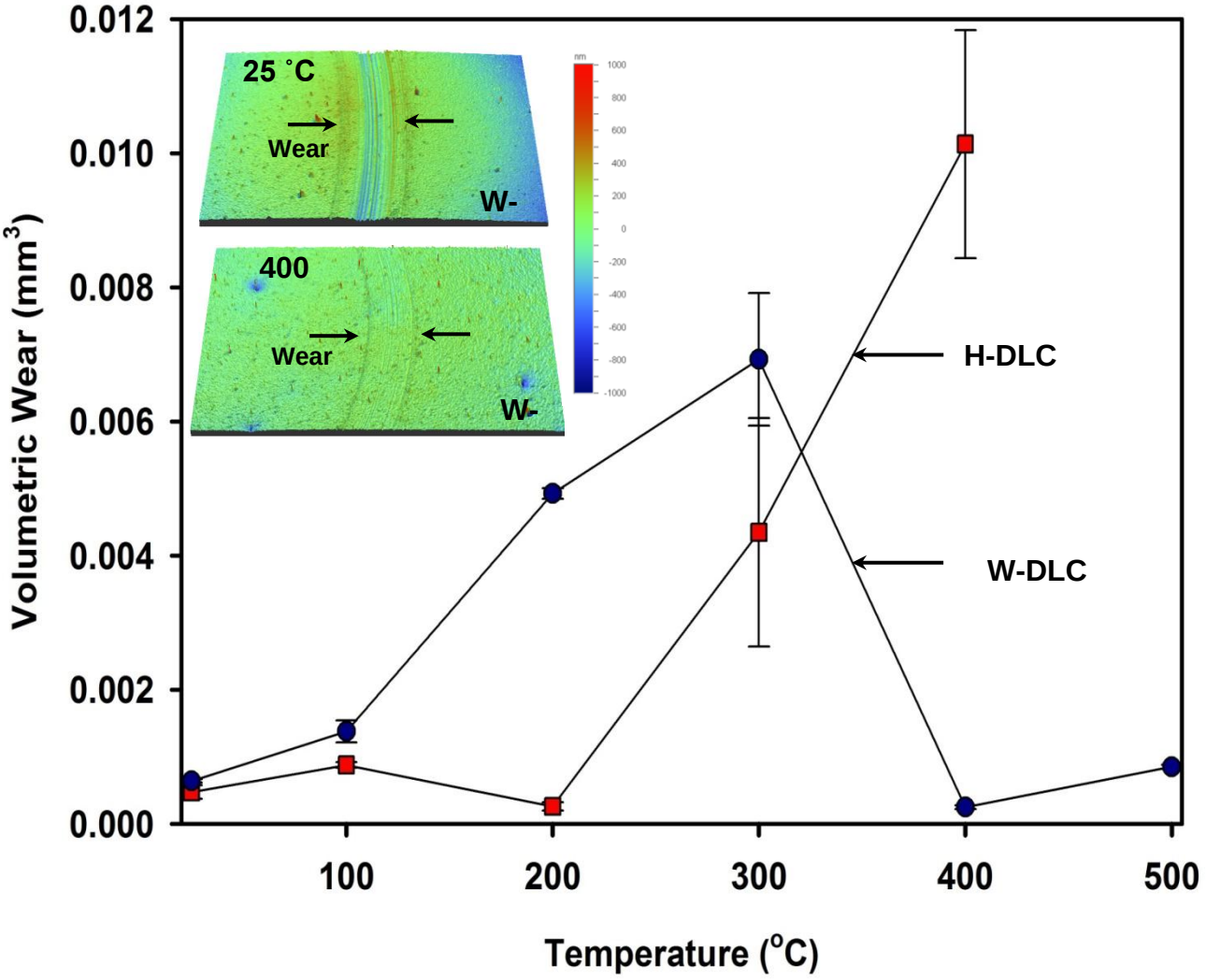

Figure 5.10. The variations of wear rates (mm3 /N-m) of H-DLC and W-DLC against Ti–6Al–4V with test temperature. Insets show 3-D surface profile images of the wear tracks of W-DLC tested at 25 °C and 400 °C.

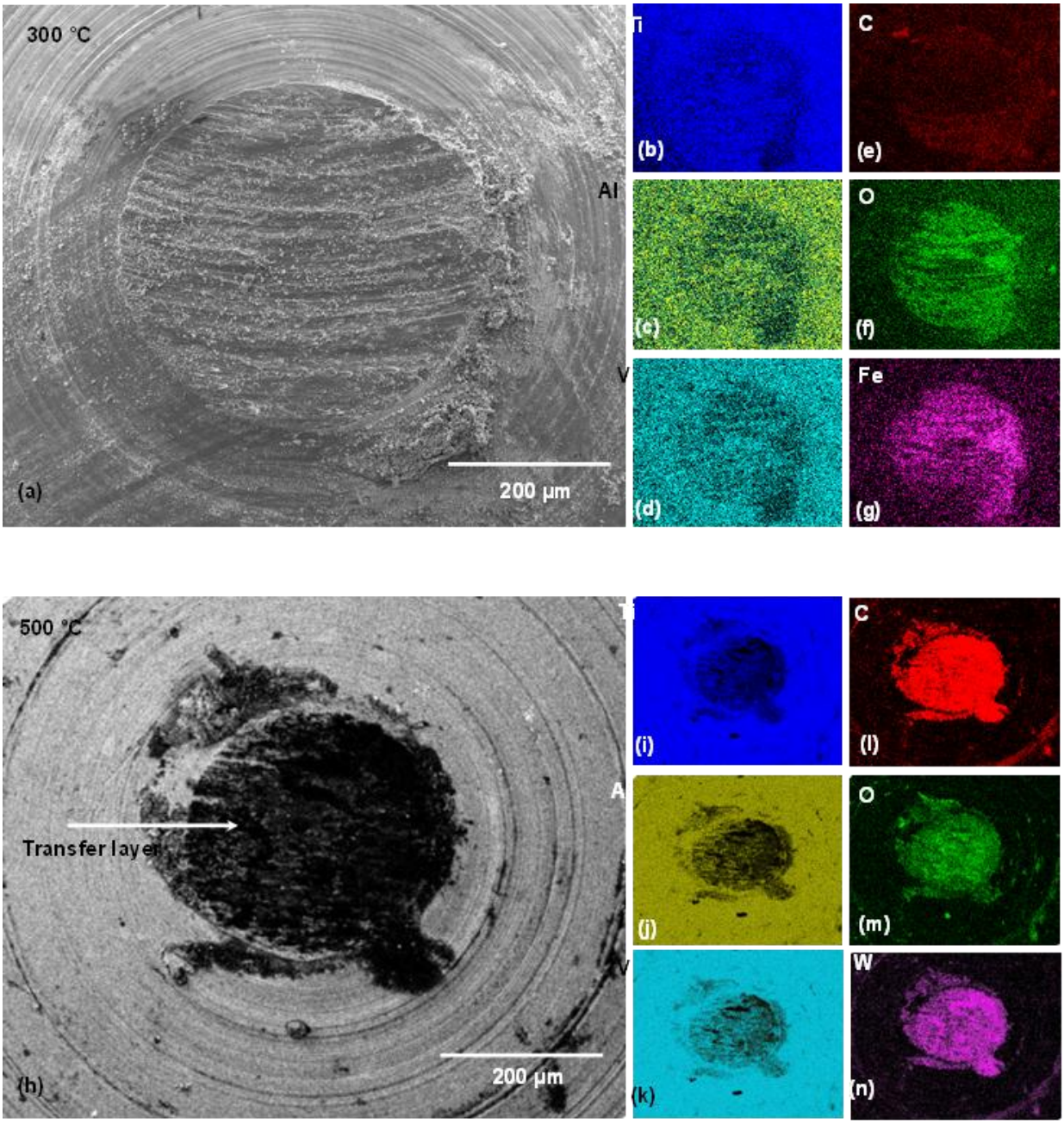

Figure 5.11. (a) Secondary electron image of Ti–6Al–4V pin surface taken after sliding against W-DLC coating at 300 °c. the elemental eds maps taken from the whole area shown in (a) are for (b) Ti, (c) Al, (d) V, (e) C, (f) O and (g) Fe. (h) secondary electron image of pin surface after the sliding against w-dlc coating at 500 °c. the elemental EDS maps taken from the whole area shown in (h) are for (i) Ti, (j) Al, (k) V, (l) C, (m) O and (n) W.

5.4. Discussion

5.4.1 Titanium Adhesion Mitigation by H-DLC and W-DLC (25 ˚C to 200 ˚C)

The H-DLC/Ti-6Al-4V tribological system exhibited a very low and stable COF in the temperature range of 25 ˚C and 200 ˚C. The room temperature COF of 0.11 decreased to 0.05 at 200 ˚C. The H-DLC had an excellent titanium adhesion mitigation capability at this temperature range. The coating was subjected to small amount of wear at temperatures between 25 ˚C and 200 ˚C. In this temperature range the formation of the carbon rich transfer layers on the Ti-6Al-4V was a common feature of the sliding contact surface . During the initial stages of the wear tests the COF was always high [6] concurrent with the formation of the transfer layers. Thus the running-in can be considered as the sliding time period where the carbonaceous layers do form on the Ti-6Al-4V surfaces. The low COF of the H-DLC, for tests <200 ˚C, could be attributed the interactions between the H-DLC's sliding interface and carbonaceous transfer layers [16, 19, 31] --possibly containing H-terminated carbons.

For W-DLC/Ti-6Al-4V sliding system, carbonaceous layers were formed on the Ti-6Al-4V contact surface when the tests were conducted at 25-200 ˚C range and also at temperatures above 400 ˚C, with the exception of tests done around 300 ˚C. The sequence of changing events at different temperatures is important. W-DLC does not contain more than 2% H in its composition—hence the passivation mechanism suggested for H-DLC, i.e., passivation of C atoms at the surfaces by H atoms, is not feasible. However, it is conceivable that the C bonds were passivated by OH from the testing environment [35]. At 25 ˚C the W-DLC surface as well as the carbonaceous transfer layers on Ti-6Al-4V were possibly passivated by OH. On the other hand, the wear rates of W-DLC showed an increase at lower temperatures compared to H-DLC because of lack of moisture necessary to sustain this type of passivation process (Fig 10). It is

plausible that the adsorbed OH at the beginning of the test would still maintain the COF almost at par with that of H-DLC, as shown in Fig. 5.7. This point requires further investigation.

For experiments conducted at 300 ˚C, a high COF along with coating wear and Ti adhesion (to steel substrate underneath the parts of the coating that are removed) were observed for both coatings. The sliding induced graphitization process of carbon through the transformation of sp^3 (diamond-like) to sp^2 (graphite-like) which occurs above 250 ˚C [11-13] could be cited as the possible reason for high temperature coating wear.

5.4.2 Titanium Adhesion Mitigation by W-DLC (400 ˚C to 500 ˚C)

In case of the tests conducted at 400 ˚C - 500 ˚C, the COF values of (Fig. 7) of W-DLC unexpectedly dropped while for the H-DLC they continued to increase. At 400 ˚C - 500 ˚C temperature range not only did W-DLC exhibit a low COF but this coating also experienced low volumetric wear losses (Fig. 5.10). Moreover, no evidence of Ti adhesion to the coating surface was found (Figs. 5.8 [e, f]). The transfer layers at 400 ˚C -500 ˚C were rich in tungsten and oxygen, implying the formation of an oxide phase. To confirm the nature of the oxide phase micro Raman tests were conducted on the transfer layers. The Raman spectra taken from the transfer layers formed on the Ti-6Al-4V after sliding against W-DLC at 25 ˚C, 100 ˚C, 200 ˚C are presented in Fig. 5.12(a). Raman spectra of the transfer layers formed on the Ti-6Al-4V after sliding against W-DLC at 400 ˚C and 500 ˚C are presented in Fig. 5.12(b). Fig. 12(b) indicates that the transfer layers formed at 400 ˚C and 500 ˚C contained a tungsten trioxide (WO_3) phase. The presence of WO_3 is evidenced by the peaks generated at 257, 600, and 806 cm^{-1} [36–38]. In addition, the transfer layers contained carbon transferred from the coating, as indicated by the presence of D and G peaks at 1354 cm^{-1} and 1588 cm^{-1} respectively [39,40]. The prominent D and G peaks observed at temperatures >200 ˚C suggested possibility of sliding induced

graphitization at elevated temperatures . The increase in sp^2 peak can be taken as an indication of graphitization, which would cause highcoating wear at elevated temperatures (250 ˚C≤T≤400 ˚C)) only to be circumvented by the formation of tungsten trioxide at 400 ˚C. .

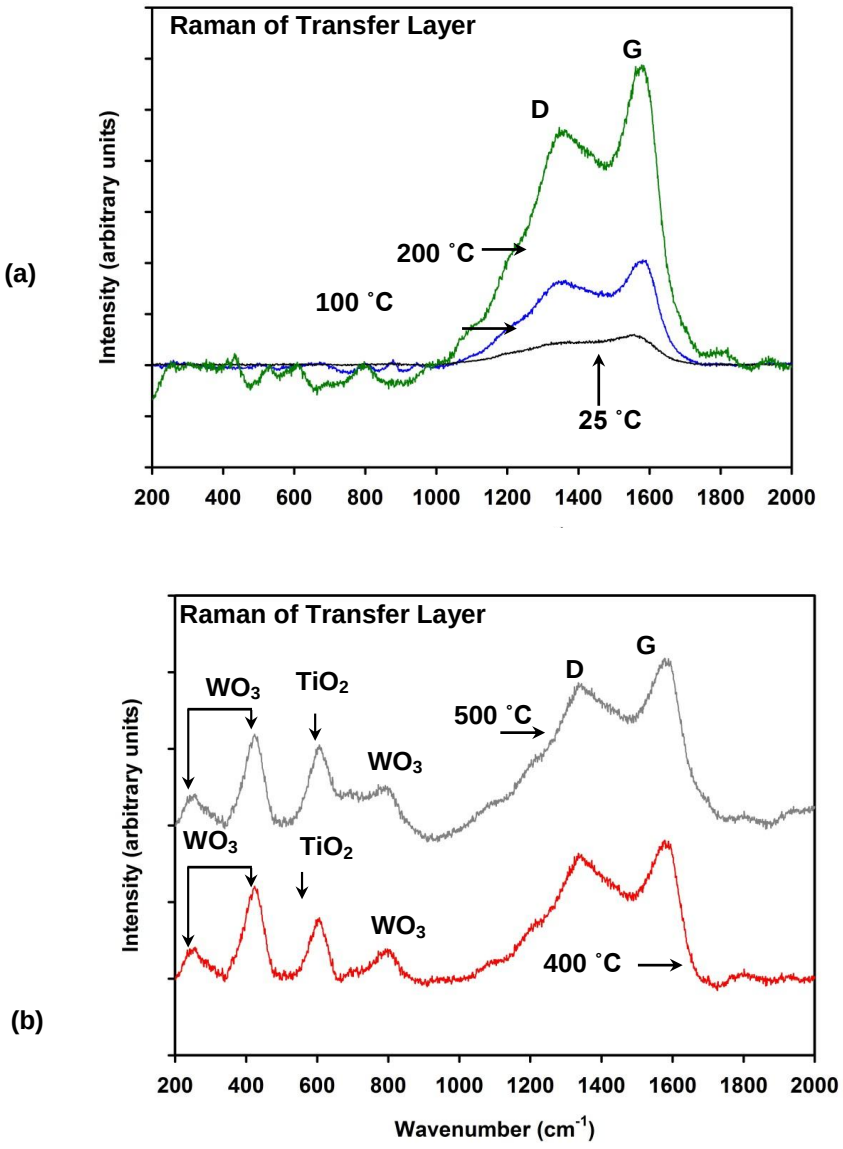

Figure 5.12. Micro-Raman spectra of the transfer layer formed on Ti–6Al–4V pins tested against W-DLC coating (a) at 25 °C, 100 °C, 200 °C and (b) at 400 °C and 500 °C.

The low frictional properties of WO_3 have been discussed in literature [41–44]; a crystalline WO_3 film deposited on sapphire substrate tested against 440 C stainless steel sliders [44] was reported to be responsible for the low COF of 0.18. In a previous investigation of the chemical compositions of transfer layers that were formed at 400 ˚C and 500 ˚C on an Al-6.5% Si alloy run against W-DLC [26] it was shown that sliding contact triggered the formation of a tungsten oxide rich layer. Thus, the formation of WO_3 may not depend on the counterface material. It can be suggested that the it was the W in DLC that came in contact with the oxygen was probably responsible for its formation. To confirm the formation of WO_3 on W-DLC surfaces micro-Raman studies on the W-DLC coatings heated to different temperatures were conducted. Raman spectra shown in Figs. 5.13 a and b are taken from W-DLC samples that were heated to different temperatures. The Raman spectra presented in Fig. 5.13(b) show the appearance of WO_3 peaks (at 257, 600, and 806 cm^{-1} [33-35]) for annealing temperatures of 400 ˚C and 500 ˚C that was not seen at 25 ˚C, 100 ˚C, 200 ˚C and 300 ˚C (Fig. 5.13a). This is in agreement with the thermodynamic equilibrium calculations of WO_3 formation as a result of the reaction between O_2 and W [42, 43]. Thus WO_3 detected in the transfer layers (Fig. 5.12b) originated from the WO_3 formed on the coating surface. It is important to emphasize that the oxide layers can form on W-DLC surface by heating the samples to 400 ˚C and above without the need of the application of siding process. On the other hand, high temperature alone is not sufficient to cause the sp^3 to sp^2 transformation as seen in the micro-Raman spectra in Fig. 5.13. The transformation to sp^2 requires sliding contact at elevated temperatures as indicated by the micro-Raman spectra of the transfer layers (Fig. 5.12).

The high temperature tribological stability of the W-DLC coating is technologically important and may expand the use of these coatings in new applications for Ti-6Al-4V

machining. It can be proposed that a thermally assisted machining that can be conducted by heating the W-DLC coated cutting tools would reduce the cutting forces and as the COF of the coating is expected to remain low long tool life and good surface finish quality can be achieved. It should be noted that this method could potentially eliminate the use of coolants, which would be significantly beneficial from the economical point of view. One point of consideration however will be the prevention of large temperature increase during the machining operation as for temperatures exceeding 500 ˚C WO_3 layers may not be stable—thus methods for maintaining the workpiece temperature low should be considered. The feasibility of applying a thermally activated machining that makes use of the W-DLC coated tools are being examined in a concurrent study [45].

‘

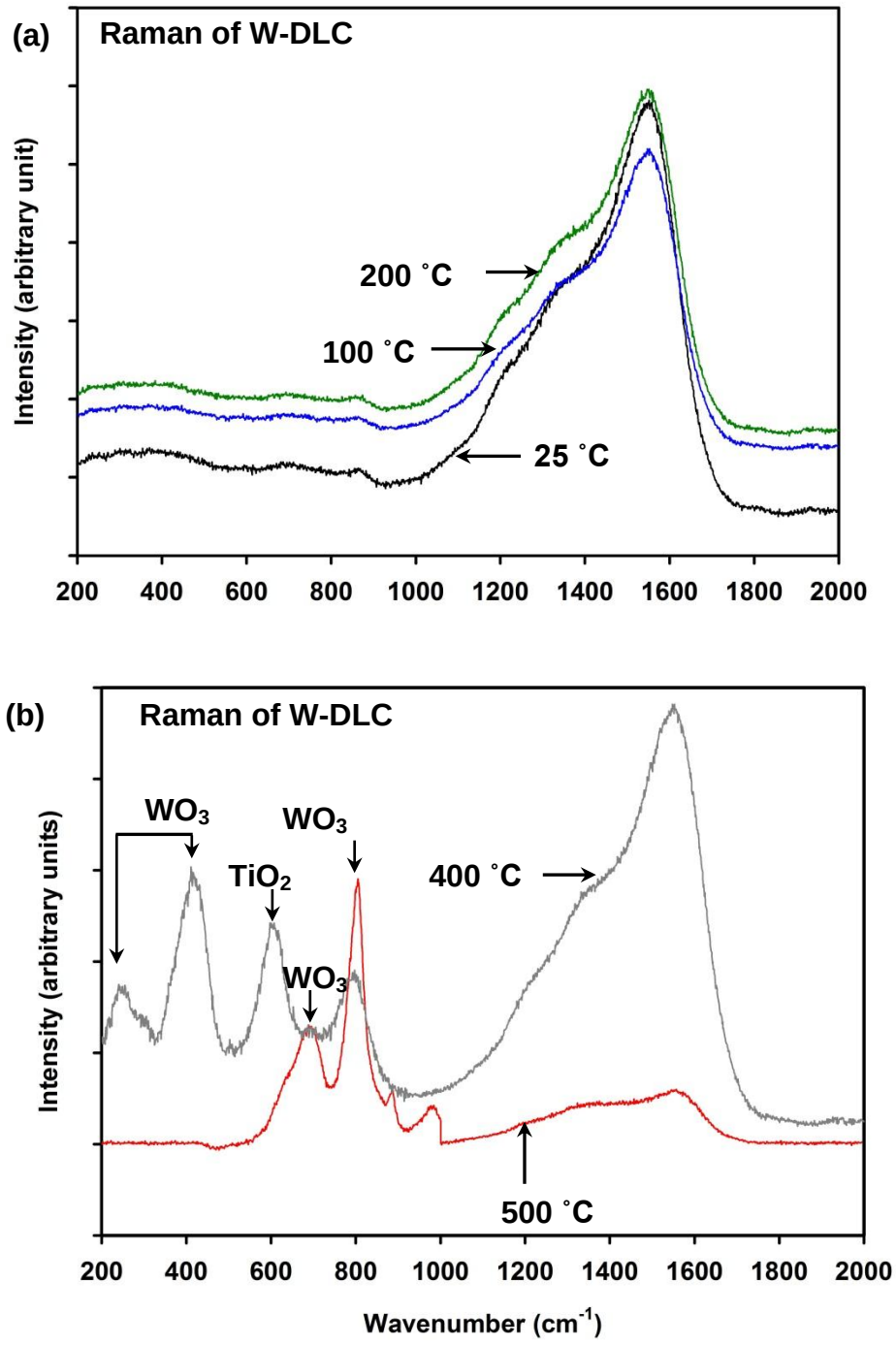

Figure 5.13. Micro-Raman spectra of W-DLC coating surface (taken outside the wear track corresponding to an annealing time of 180 s) at (a) 25 °C, 100 °C, 200 °C and (b) at 400 °C and 500 °C.

Summary and Conclusions

1. N-based coatings showed high COF (>0.45) when tested against Ti-6Al-4V at 25 ˚C due to the adhesion of titanium to the coating surface.

2. Sliding of W-DLC against Ti-6Al-4V alloy at 25 ˚C W-DLC showed a low COF (0.10) and a low wear rate, which was attributed to the formation of a carbon rich transfer layer on the Ti-6Al-4V alloy counterface.

3. At intermediate temperatures of 200 ˚C and 300 ˚C, sliding between W-DLC and Ti-6Al-4V alloy led to high COF values (0.46-0.51) and volumetric wear losses; no transfer layer was formed on Ti-6Al-4V surface.

4. At 400 ˚C and 500 ˚C, very low COF (0.07-0.08) values were recorded with minimum titanium adhesion to the coating surface. The low magnitudes of COF and wear rates were attributed to the formation of a tungsten trioxide layer on W-DLC surface.

Bibliography

[1] A. Erdemir, Review of engineered tribological interfaces for improved boundary lubrication, Tribol. Int. 38 (2005) 249–256.

[2] J. Andersson, R.A. Erck, A. Erdemir, Friction of diamond-like carbon films in different atmospheres, Wear. 254 (2003) 1070–1075.

[3] S. Bhowmick, A.T. Alpas, The performance of hydrogenated and non-hydrogenated diamond-like carbon tool coatings during the dry drilling of 319 Al, Int. J. Mach. Tools Manuf. 48 (2008) 802–814.

[4] S. Bhowmick, A.T. Alpas, Minimum quantity lubrication drilling of aluminium–silicon alloys in water using diamond-like carbon coated drills, Int. J. Mach. Tools Manuf. 48 (2008) 1429–1443.

[5] E. Konca, Y.-T. Cheng, A.M. Weiner, J.M. Dasch, A.T. Alpas, Effect of test atmosphere on the tribological behaviour of the non-hydrogenated diamond-like carbon coatings against 319 aluminum alloy and tungsten carbide, Surf. Coatings Technol. 200 (2005) 1783–1791.

[6] F.G. Sen, X. Meng-Burany, M.J. Lukitsch, Y. Qi, A.T. Alpas, Low friction and environmentally stable diamond-like carbon (DLC) coatings incorporating silicon, oxygen and fluorine sliding against aluminum, Surf. Coatings Technol. 215 (2013) 340–349.

[7] F.G. Sen, Y. Qi, A.T. Alpas, Material transfer mechanisms between aluminum and fluorinated carbon interfaces, Acta Mater. 59 (2011) 2601–2614.

[8] F.G. Sen, Y. Qi, A.T. Alpas, Surface stability and electronic structure of hydrogen-and fluorine-terminated diamond surfaces: A first-principles investigation, J. Mater. Res. 24 (2009) 2461–2470.

[9] E. Konca, Y.-T. Cheng, A.T. Alpas, Sliding wear of non-hydrogenated diamond-like carbon coatings against magnesium, Surf. Coatings Technol. 201 (2006) 4352–4356.

[10] S. Bhowmick, A.T. Alpas, The role of diamond-like carbon coated drills on minimum quantity lubrication drilling of magnesium alloys, Surf. Coatings Technol. 205 (2011) 5302–5311.

[11] S. Sattel, T. Gieβen, H. Roth, M. Scheib, R. Samlenski, R. Brenn, H. Ehrhardt, J. Robertson, Temperature dependence of the formation of highly tetrahedral aC: H, Diam. Relat. Mater. 5 (1996) 425–428.

[12] S. Sattel, J. Robertson, H. Ehrhardt, Effects of deposition temperature on the properties of hydrogenated tetrahedral amorphous carbon, J. Appl. Phys. 82 (1997) 4566–4576.

[13] S. Sattel, M. Weiler, J. Gerber, T. Giessen, H. Roth, M. Scheib, K. Jung, H. Ehrhardt, J. Robertson, Nucleation during deposition of hydrocarbon ions as a function of substrate temperature, Diam. Relat. Mater. 4 (1995) 333–336.

[14] S. Bhowmick, M.J. Lukitsch, A.T. Alpas, Tapping of Al–Si alloys with diamond-like carbon coated tools and minimum quantity lubrication, J. Mater. Process. Technol. 210 (2010) 2142–2153.

[15] E. Konca, Y.-T. Cheng, A.M. Weiner, J.M. Dasch, A.T. Alpas, Elevated temperature tribological behavior of non-hydrogenated diamond-like carbon coatings against 319 aluminum alloy, Surf. Coatings Technol. 200 (2006) 3996–4005.

[16] Y. Qi, E. Konca, A.T. Alpas, Atmospheric effects on the adhesion and friction between non-hydrogenated diamond-like carbon (DLC) coating and aluminum–A first principles investigation, Surf. Sci. 600 (2006) 2955–2965.

[17] W. Ni, Y.-T. Cheng, A.M. Weiner, T.A. Perry, Tribological behavior of diamond-like-

carbon (DLC) coatings against aluminum alloys at elevated temperatures, Surf. Coatings Technol. 201 (2006) 3229–3234.

[18] A. Grill, Tribology of diamondlike carbon and related materials: an updated review, Surf. Coatings Technol. 94 (1997) 507–513.

[19] A.A. Gharam, M.J. Lukitsch, M.P. Balogh, A.T. Alpas, High temperature tribological behaviour of carbon based (B 4 C and DLC) coatings in sliding contact with aluminum, Thin Solid Films. 519 (2010) 1611–1617.

[20] M.-C. Chiu, W.-P. Hsieh, W.-Y. Ho, D.-Y. Wang, F.-S. Shieu, Thermal stability of Cr-doped diamond-like carbon films synthesized by cathodic arc evaporation, Thin Solid Films. 476 (2005) 258–263.

[21] K. Baba, R. Hatada, Deposition and characterization of Ti-and W-containing diamond-like carbon films by plasma source ion implantation, Surf. Coatings Technol. 169 (2003) 287–290.

[22] W.J. Meng, B.A. Gillispie, Mechanical properties of Ti-containing and W-containing diamond-like carbon coatings, J. Appl. Phys. 84 (1998) 4314–4321.

[23] J.C. Sánchez-López, D. Martínez-Martínez, M.D. Abad, A. Fernández, Metal carbide/amorphous C-based nanocomposite coatings for tribological applications, Surf. Coatings Technol. 204 (2009) 947–954.

[24] A.A. Voevodin, J.P. O'neill, J.S. Zabinski, Tribological performance and tribochemistry of nanocrystalline WC/amorphous diamond-like carbon composites, Thin Solid Films. 342 (1999) 194–200.

[25] V. Fervel, B. Normand, H. Liao, C. Coddet, E. Beche, R. Berjoan, Friction and wear mechanisms of thermally sprayed ceramic and cermet coatings, Surf. Coatings Technol.

111 (1999) 255–262.

[26] A.A. Gharam, M.J. Lukitsch, M.P. Balogh, N. Irish, A.T. Alpas, High temperature tribological behavior of W-DLC against aluminum, Surf. Coatings Technol. 206 (2011) 1905–1912.

[27] B. Podgornik, D. Hren, J. Vižintin, Low-friction behaviour of boundary-lubricated diamond-like carbon coatings containing tungsten, Thin Solid Films. 476 (2005) 92–100.

[28] M. Ban, M. Ryoji, S. Fujii, J. Fujioka, Tribological characteristics of Si-containing diamond-like carbon films under oil-lubrication, Wear. 253 (2002) 331–338.

[29] K. Vercammen, K. Van Acker, A. Vanhulsel, J. Barriga, A. Arnsek, M. Kalin, J. Meneve, Tribological behaviour of DLC coatings in combination with biodegradable lubricants, Tribol. Int. 37 (2004) 983–989.

[30] Y. Liu, R. Asthana, P. Rohatgi, A map for wear mechanisms in aluminium alloys, J. Mater. Sci. 26 (1991) 99–102.

[31] E. Konca, Y.-T. Cheng, A.T. Alpas, Dry sliding behaviour of non-hydrogenated DLC coatings against Al, Cu and Ti in ambient air and argon, Diam. Relat. Mater. 15 (2006) 939–943.

[32] X. Meng-Burany, A.T. Alpas, FIB and TEM studies of damage mechanisms in DLC coatings sliding against aluminum, Thin Solid Films. 516 (2007) 325–335.

[33] D.A. Stephenson, J.S. Agapiou, Metal cutting theory and practice, CRC press, 2016.

[34] M. Chen, X. Meng-Burany, T.A. Perry, A.T. Alpas, Micromechanisms and mechanics of ultra-mild wear in Al–Si alloys, Acta Mater. 56 (2008) 5605–5616.

[35] A.A. Gharam, M.J. Lukitsch, Y. Qi, A.T. Alpas, Role of oxygen and humidity on the tribo-chemical behaviour of non-hydrogenated diamond-like carbon coatings, Wear. 271

(2011) 2157–2163.

[36] J.A. Horsley, I.E. Wachs, J.M. Brown, G.H. Via, F.D. Hardcastle, Structure of surface tungsten oxide species in the tungsten trioxide/alumina supported oxide system from x-ray absorption near-edge spectroscopy and Raman spectroscopy, J. Phys. Chem. 91 (1987) 4014–4020.

[37] K. Nonaka, A. Takase, K. Miyakawa, Raman spectra of sol-gel-derived tungsten oxides, J. Mater. Sci. Lett. 12 (1993) 274–277.

[38] M.A. Vuurman, I.E. Wachs, In situ Raman spectroscopy of alumina-supported metal oxide catalysts, J. Phys. Chem. 96 (1992) 5008–5016.

[39] M.J. Pelletier, Analytical applications of Raman spectroscopy, Wiley-Blackwell, 1999.

[40] I. Pócsik, M. Hundhausen, M. Koós, L. Ley, Origin of the D peak in the Raman spectrum of microcrystalline graphite, J. Non. Cryst. Solids. 227 (1998) 1083–1086.

[41] C. Donnet, A. Erdemir, Tribology of diamond-like carbon films: fundamentals and applications, Springer Science & Business Media, 2007.

[42] H.A. Wriedt, The OW (oxygen-tungsten) system, Bull. Alloy Phase Diagrams. 10 (1989) 368–384.

[43] T.W. Scharf, I.L. Singer, Role of the transfer film on the friction and wear of metal carbide reinforced amorphous carbon coatings during run-in, Tribol. Lett. 36 (2009) 43–53.

[44] O.D. Greenwood, S.C. Moulzolf, P.J. Blau, R.J. Lad, The influence of microstructure on tribological properties of WO 3 thin films, Wear. 232 (1999) 84–90.

[45] S. Bhowmick, A.T. Alpas, The Performance of Diamond-Like Carbon Coated Drills in Thermally Assisted Drilling of Ti-6Al-4V, J. Manuf. Sci. Eng. 135 (2013) 61019.

CHAPTER 6

Role of Temperature on Tribological Behaviour of Ti containing MoS_2 Coating against Aluminum Alloys

6.1. Introduction

Tribological problems of high friction and adhesion are commonly encountered during high temperature manufacturing processes, including warm and hot aluminum alloy sheet metal forming where the operating temperatures range between 200 and 500 ˚C [1–5]. High temperature tribology is also important in automotive engine powertrain systems that operate in the temperature range of 100-200 °C [6–8], where the increasing use of light weight components made of aluminum alloys amplify friction and adhesion problems. On the other hand, in order to eliminate or significantly reduce the use of metal removal fluids both dry and minimum quantity lubricant (MQL) machining of lightweight alloys were attempted but these efforts were hampered by complications (short tool lives, high energy expenditure) arising from of material transfer and adhesion of aluminum or magnesium to the tool surfaces [9–13]. Damage caused by adhesion during high temperature sliding processes may be reduced by the use of tool and die coatings that exhibit low friction, and adhesion at elevated working temperatures.

Transition metal dichalcogenides are well-known for their lubricating properties. MoS_2 is a prevalent solid lubricant for tribological applications in vacuum and inert gas environments [14–17]. Tribological tests performed on MoS_2 coatings against SAE 52100 grade steel under ultra-high vacuum (5×10^{-8} Pa) resulted in a very low coefficient of friction, COF, of 0.003 [18]. Low COF values ranging between 0.01 and 0.04 were also reported under high vacuum conditions in other studies [19,20]. Tests conducted under ambient air (40% RH) on the other hand showed a COF of 0.15 [18]. Martin et al. [15] attributed the ultra-low friction of MoS_2 coatings to the

“easy shear" of basal planes that are oriented parallel to the sliding direction and suggested that under humid atmospheres water vapour could diffuse into the inter-lamella gap and thus impede shear of basal planes [21,22]. A few studies have focused on the high temperature friction behaviour of MoS_2 coating. Existing studies were usually conducted against steel or ceramic based counterfaces. Kubart et al [23] tested MoS_2 coatings against 52100 steel at 28 ˚C (50% RH) and 100 ˚C and found that the COF decreased from 0.14 to 0.04. Arslan [24] showed that the COF values of MoS_2 coatings tested against Al_2O_3 counterfaces decreased from 0.07 at 25 ˚C to 0.03 at 300 ˚C but increased abruptly to above 0.45 at 500 ˚C. Wong et al. [25] reported that MoS_2 coatings run against A2 steel at 35% RH showed a low COF of $\leq$0.11 at temperatures up to 320 ˚C, which was attributed to the formation of a sulphur-rich transfer layer on the counterface. At temperatures higher than $\geq$400 ˚C, the MoS_2 layers oxidized completely to MoO_3 due to combined effects of high temperature and sliding resulting in an increase of the COF to above 0.35.

Although MoS_2 coatings exhibit low friction and wear under a dry atmosphere, their tribological properties are sensitive to moisture as indicated in the previous paragraph. It was found that incorporation of Ti in MoS_2 (Ti-MoS_2) using a magnetron sputtering deposition technique reduced the sensitivity of the coating to moisture [26]. Ti-MoS_2 when tested against WC-Co in an atmosphere with 50% RH maintained a low COF of 0.07 [26]. Ding et al. [27] tested Ti-MoS_2 coatings with varying Ti content against Al_2O_3 counterfaces. It was suggested that the presence of Ti atoms in MoS_2 may reduce the propensity of water vapour entering between the inter-lamellar spaces. Two distinct friction regimes were found depending on Ti percentage. MoS_2 coatings containing up to 15.2 at.% Ti showed low COF values between 0.04-0.11 when tested in atmospheres with RH between 0%-80%. It was noted that MoS_2 coatings

with 9.5 at.% Ti showed low COF (0.03-0.05) even in 100% RH. Higher COF values in the range of 0.2-0.6 were observed for the MoS_2 coatings with higher Ti concentrations between 20.2-29.7 at.%. Wang et al. [28] observed that pure MoS_2 tested against Si_3N_4 counterfaces at room temperature and 38% RH had a high COF of about 0.82, which was reduced to 0.16 under the same test conditions when 15.3 at.% Ti was added to MoS_2. Mechanical properties of MoS_2 coatings were also found to improve upon addition of Ti to the coating [29]. For example, the hardness of MoS_2 increased from 4.9 GPa to 8.3 GPa with the addition of 15.3 at.% Ti and to 10.35 GPa with 19.5 at.% Ti [28]. The addition of Ti in the MoS_2 coating is also expected to improve the adhesion of the coating to the substrate which in turn increased its' wear resistance. 25% Ti containing MoS_2 deposited on a Ti-6Al-4V substrate showed the lowest mass loss and COF when tested against 52100 steel compared to the uncoated Ti-6Al-4V blocks [30]. In summary, MoS_2 coatings showed low wear and friction in inert atmospheres and in vacuum but their ambient air performance is relatively poor. Ti-MoS_2 has shown to have the advantages of having higher hardness, higher wear resistance and low COF in humid air. In this study, friction and adhesion mechanisms of Ti-MoS_2 coatings are investigated at temperatures ranging between 25 ˚C and 400 ˚C. The Ti-MoS_2 coatings were tested against a common lightweight material, namely hypoeutectic Al-6.5% Si alloy. SEM, TEM and XPS analyses of the pristine coating and worn surfaces have been performed to delineate the friction mechanisms of Ti-MoS_2 coatings at different temperatures.

6.2. Experimental Procedure

6.2.1. Materials

The Ti containing MoS_2 coatings, designated as Ti-MoS_2, were deposited on M2 grade tool steel substrates. The Ti-MoS_2 coatings were produced by Miba (Teer) Coatings Group

(Worcestershire, UK) using an unbalanced magnetron sputtering technique. During deposition, an argon sputtering pressure of 3.0×10^{-3} Torr was used. The distance between the substrates and the targets was maintained at 150 mm. Substrates were rotated in front of each of the targets at a speed of 4.0 rpm. A pulsed DC power supply provided 45 V bias during deposition. A thin interlayer of Ti was deposited first followed by the deposition of the Ti–MoS_2 coating producing "low titanium" variety of MoST [26]. The substrate temperature during the deposition process was maintained at < 200 °C. The hardness of the coating was measured using a Hysitron TI 900 TriboIndenter equipped with a Berkovich nano-indenter tip with an indenter contact depth of 150 nm. Accordingly, the Ti-MoS_2 had a hardness of 3.51±0.10 GPa (harder than conventional MoS_2 coating with a hardness of 1.20 GPa [29]). The microstructure of Ti-MoS_2 was studied by transmission electron microscopy (TEM) by observing cross-sections excised using focused ion beam (FIB) milling. Carl Zeiss NVision 40 Cross-Beam instrument was used for preparing FIB lift out samples [31–33] which were subsequently analyzed using high resolution TEM (FEI Titan 80-300).

The counterface used for friction and wear tests was 15 mm long 319 Al alloy pins with one end machined into a hemisphere of 4.05 mm in diameter. 319 Al had the following composition (in wt.%): 5.5–6.5% Si, 3.0–4.0% Cu, 1.0% Fe, 0.10% Mg, 0.5 Mn, 0.35% Ni, 1.0% Zn, 0.25% Ti and the balance Al. The bulk hardness of 319 Al was 72.40 HR-15 T, in Rockwell superficial hardness scale measured using a 1/16 in (1.59 mm) diameter ball. Substrates for coating deposition were machined from an annealed M2 tool steel (AISI type M2) bar of 2.54 cm in diameter. The M2 steel bar was first cut into 1 cm thick discs. The discs were then subjected to a heat treatment procedure that consisted of austenizing at 1200 °C for 3-4 minutes followed by air cooling to 25 °C and then tempering at 560 °C for 120 minutes. The final hardness of the M2

steel discs was 63 ± 2 HRC. The substrates were polished with 0.10 μm diamond suspension prior to deposition of the coatings.

6.2.2. Pin-on-Disk Tests: COF Measurements and Wear Rate Calculations

A high temperature pin-on-disk tribometer was used to measure the COF values and the wear rates of the Ti-MoS_2 coatings. The Ti-MoS_2 coatings were subjected to high temperature tests between 25 and 500 °C, at constant temperatures with 50 °C interval between each. The steady state COF (μ_S) was measured after a steady state friction region on a COF vs. sliding distance (number of revolutions) curve was attained, which typically took about 1500 revolutions. The maximum COF value during the initial running-in period of a friction curve was reported as μ_R. For tests during which no steady state region occurred, the mean value of the entire friction curve (typically with high fluctuations) was reported. Every sliding friction test was repeated three times at each test temperature, the average of thee COF values were reported (e.g., see Fig. 6.2).

All tests were performed under ambient conditions (45% RH) using a constant speed of 0.12 m/s and a normal load of 5.0 N for 5000 revolutions. The wear tracks of the Ti-MoS_2 were examined after dissolving the transferred material (in 10% NaOH) to calculate the volumetric wear loss using 2D profiles of the wear tracks generated. A non-contact white light interferometry technique was used for this purpose [34,35]. The volumetric wear loss of the Ti-MoS_2 coating was calculated from the 2D profiles obtained from six different locations on each wear track and the corresponding wear rate was determined by averaging these measurements.

6.2.3. Determination of Morphological and Compositional Features of Transfer Layers

The morphological and compositional features of surfaces subjected to sliding wear damage were examined by scanning electron microscope SEM, energy-dispersive X-ray, EDS, and

micro-Raman spectroscopy. The details of surface damage features were studied using FEI Quanta 200 FEG SEM equipped with a SiLi Detector EDS detector. Micro-Raman spectra of the transfer layers were obtained using a 50 mW Nd–YAG laser (532 nm excitation line) through the 50× objective lens of a Horiba Raman micro-spectrometer. The diameter of the laser spot for Raman on the specimen surface was 1 μm. Chemical analyses of the transfer layers formed on the counterface were also conducted using X-ray photoelectron spectroscopy (XPS) using Kratos Axis Ultra X-ray photoelectron spectrometer with spatial resolution of 5 μm, which can probe the surface of the samples to a depth of 7–10 nm with elemental detection limit of 0.1 at.% and with an area of acquisition of 15 microns in diameter. High-resolution scans for elements of interest were taken to determine chemical bonding information. The survey scans were performed at 160 eV pass energy while the high resolution scans were performed at 40 eV.

6.3. Results

6.3.1 Microstructure of Ti-MoS_2 Coating

Fig. 6.1 (a) shows a cross-sectional FIB/SEM image of the as-deposited Ti-MoS_2 coating. The coating has a thickness of 1.2 μm. A 40 nm thick Ti interlayer deposited on M2 type steel substrate can be seen in Fig. 6.1 (a). Fig. 6.1 (b) is a TEM/EDS image of the Ti-MoS_2 coating that revealed the distribution of Mo, S, Ti within the cross-section of the coating. According to Fig. 6.1 (b) the Ti content in the coating gradually decreased with distance moving away from the Ti interlayer. A higher magnification TEM image shown in Fig. 6.1 (c) indicated that the Ti-MoS_2 coating had a modulated microstructure consisting of successive Ti and Mo rich layers with 5 nm interlayer spacing. Fig. 6.1 (d) is an HR-TEM image indicating the interface between

the Ti-MoS_2, that appeared to have an amorphous structure, and the α-Ti interlayer.

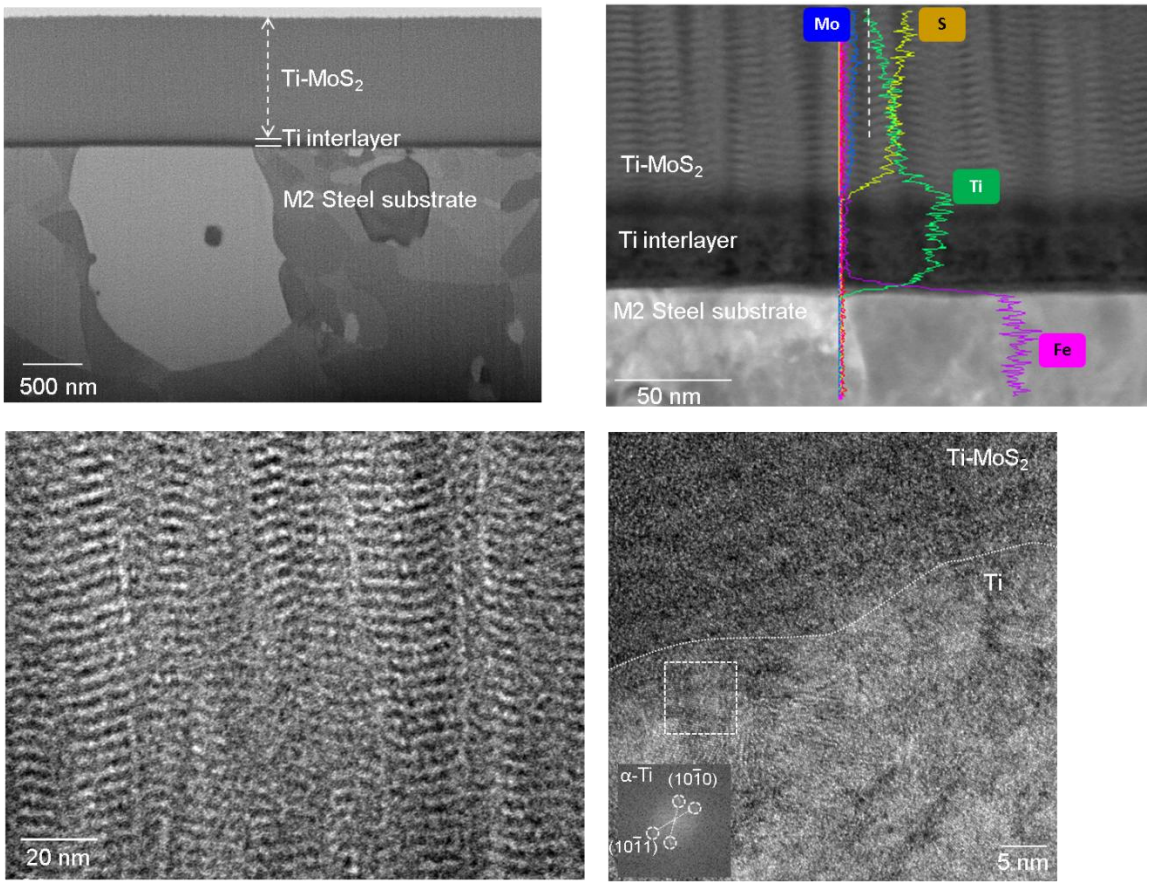

Figure 6.1: (a) Cross-sectional FIB/SEM (secondary electron) image of Ti-MoS_2 coating with a Ti interlayer and the M2 steel substrate; (b) bright-field cross-sectional TEM image of the Ti-MoS_2 coating and EDS line scans showing the distributions of the Mo, S, Ti and Fe (in the substrate); (c) high magnification bright-field TEM image showing the different layers of the Ti-MoS_2 coating with interlayer spacing of 5 nm; (d) HR-TEM image of the interface between the Ti-MoS_2 coating and the Ti interlayer. The FFT generated SAED shown in the inset is obtained from the marked region within the Ti interlayer showing a crystalline structure in contrast to the Ti-MoS_2 layers which have an amorphous appearance.

6.3.2. Variation of Coefficient of Friction with Temperature

As indicated in Section 2.2. three tests were performed at each test temperature and the average values of maximum running-in COF (μ_R) and steady state COF, μ_S are determined. The mean values of μ_R and μ_S obtained at different temperatures are shown in Fig. 6.2. According to

Fig. 6.2 μ_R and μ_S of Ti-MoS_2 at 25 ˚C were 0.13 and 0.11. Both μ_R and μ_S decreased between 25 ˚C and 200 ˚C. At 200 ˚C μ_R and μ_S were 0.07 and 0.06. The low μ_R and μ_S values were maintained up to 350 ˚C. At T ≥ 400 ˚C, the COF curves changed significantly, as will be discussed later in this section, but neither a peak running in COF nor a steady state region could be detected. The average COF values calculated as explained in Section 2.2 were significantly higher than those observed at lower temperatures. In the following paragraphs the typical trends in the COF curves of Ti-MoS_2 tested at different temperatures will be presented and the corresponding damage features will be described.

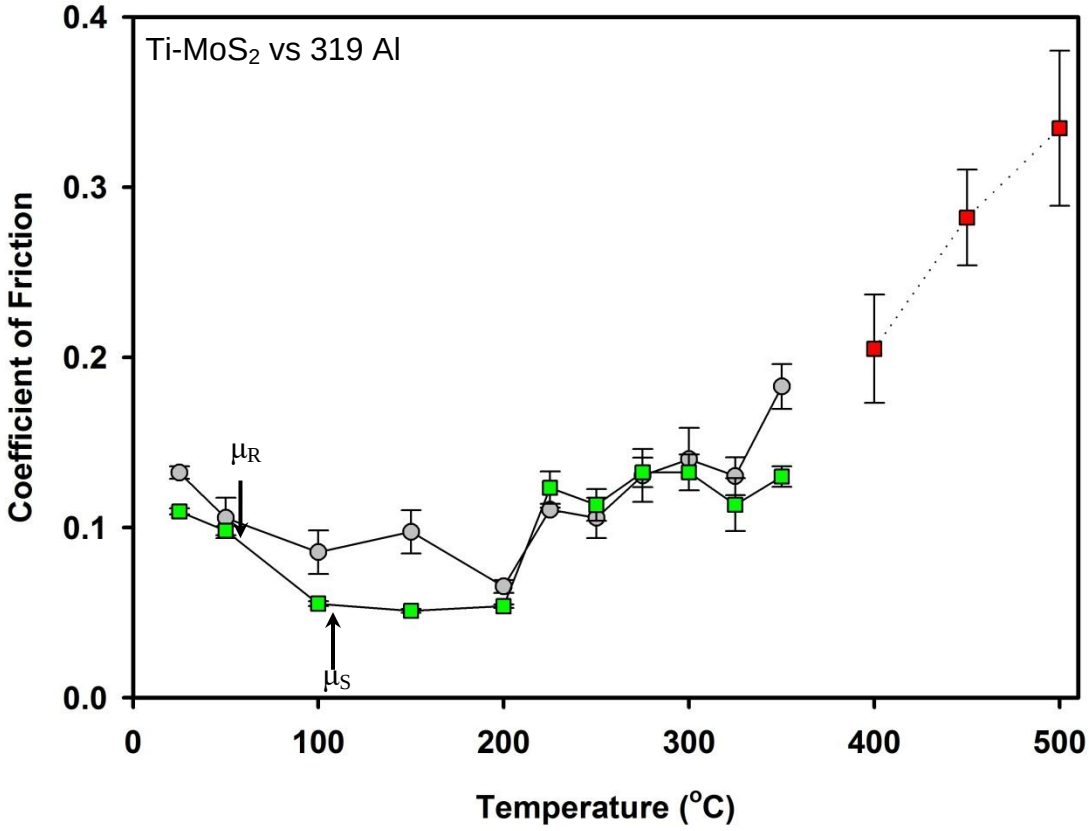

Figure 6.2: Variations of the COF of Ti-MoS_2 coating at different testing temperatures. The maximum running-in COF is designated as μ_R and steady state COF as μ_S. Each data point corresponds to average value determined from friction results of three tests performed on Ti-MoS_2 coating at each temperature. A 50 °C interval was maintained between each test for temperatures up to 200 °C whereas a 25 °C interval was maintained between 250 °C - 350 °C to measure the accurately changes in COF at elevated temperatures. At temperatures higher than 400 °C no μ_R or μ_S could be detected as the COF curves showed large fluctuations.

Fig. 6.3 (a) shows representative friction curves as a function of the number of revolutions for Ti-MoS_2 coatings tested at temperatures between 25 ˚C to 200 ˚C. According to the friction curve shown in Fig. 6.3 (a) at 25 °C, an initial μ_R of 0.15 was obtained in this particular test and the COF immediately decreased to a low μ_S value of 0.11 which was maintained for the rest of the test. The μ_R values were 0.11 and 0.07 for tests conducted at 100 ˚C and 200 ˚C and the μ_s

values were 0.05 and 0.06. Thus the friction trends in this temperature range were virtually the same with a slightly higher running in COF followed by a low and persistent steady state region with very small fluctuations.

The wear tracks formed on the contact surfaces of Ti-MoS_2 were examined using SEM and the representative secondary electron images (SEIs) are shown in Figs. 6.3 (b, c). Some aluminum oxide debris particles were formed on the side of the wear tracks during the tests at 200 °C. However, no Al transfer from the counterface to the wear tracks occurred during sliding in the temperature range between 25 °C and 200 °C.

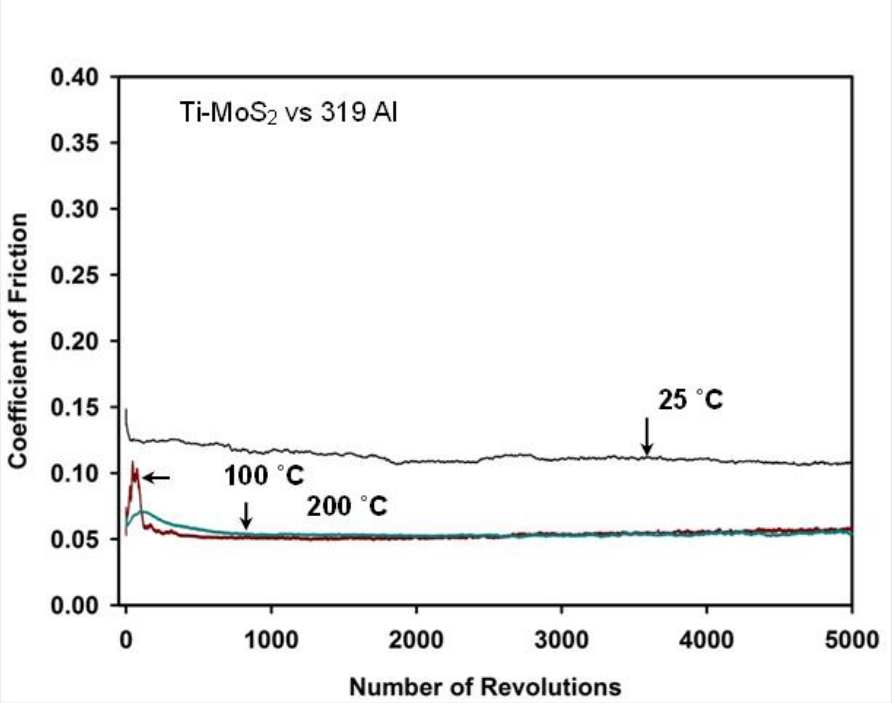

(a)

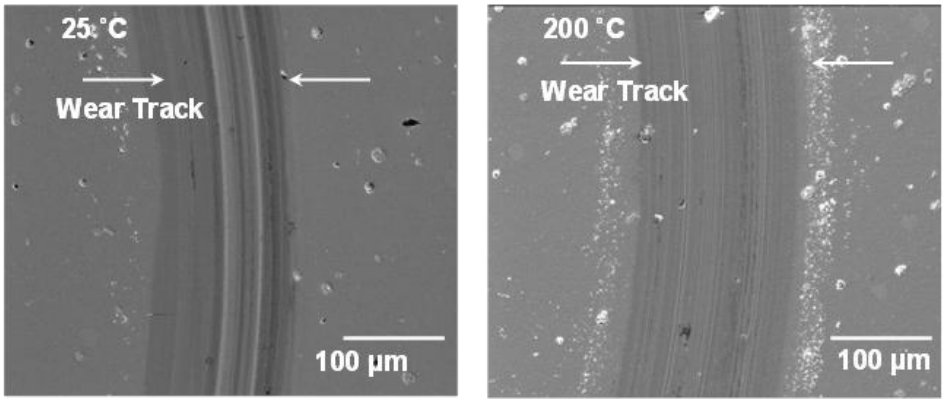

(b) (c)

Figure 6.3: (a) Variation of the COF with the number of revolutions when the Ti-MoS_2 coating was tested against the 319 Al pin at 25 °C, 100 °C and 200 °C. Typical secondary electron images of wear tracks formed on the Ti-MoS_2 surface when tested against 319 Al at (b) 25 °C and (c) 200 °C.

The COF curves shown in Fig. 6.4 (a) are representative of the friction behaviour between 250 ˚C and 350 ˚C. During the test conducted at 250 °C, the typical friction curve of the Ti-MoS_2 coating was characterized by a running in period (with μ_R of 0.14) followed by lower plateau (with μ_S of 0.10 for the tests shown in Fig. 6.4a) . Higher μ_R values were observed during the tests carried out at 300 °C and 350 °C according to the curves of Fig. 6.4 (a) the recorded μ_R were 0.17 and 0.21 respectively. The general shape of the curves were not much different than each other with a lower steady state plateau with μ_S values of 0.12 and 0.14 at 300 °C and 350 °C. It is however noted that there is an increase in the fluctuations about the mean μ_S values with the temperature. In summary between the 25 °C and 350 °C the general characteristics of friction curves were similar and they all led to a low steady state region.

A backscattered SEM image and the corresponding compositional EDS maps of Ti-MoS_2 wear track showed that coating was still intact at 350 °C (Figs. 6.4 b-f) with sliding wear damage remaining limited to the coating, without penetrating to the substrate. It is also noted meanwhile that the sliding tests performed at 350 °C marked the beginning of aluminum transfer to the coating surface as evident from traces of Al adhered on the Ti-MoS_2 wear tracks (Fig. 6.4f) and Al adhesion was responsible for the slightly higher μ_S value (and larger fluctuations) compared to the tests performed at 300 °C where there was no Al adhesion on the wear tracks.

Sliding tests conducted at temperatures $\geq$ 400 °C generated distinctly different friction curves characterized by an unstable behaviour and large fluctuations dominated the friction plots, as shown in Fig. 6.5a. The instability in the friction curve at 400 °C is marked by an initial COF of 0.10 which was followed by a steep rise to 0.27. At 450 °C and 500 °C, the friction increased abruptly with the start of the test and COF values fluctuated widely between 0.28 and 0.35 (Fig. 6.5a).

The occurrence of large fluctuations suggested material transfer to the counterface. The backscattered SEM image (Fig. 6.5b) of wear track of Ti-MoS_2 coating tested at 450 °C exhibited streaks of Al transferred to the coating surface. EDS compositional maps showed that Al adhesion to the coating occurred at locations where the Ti-MoS_2 coating was partially removed while other regions of the wear tracks were oxidized (Figs. 6.5 c-f).

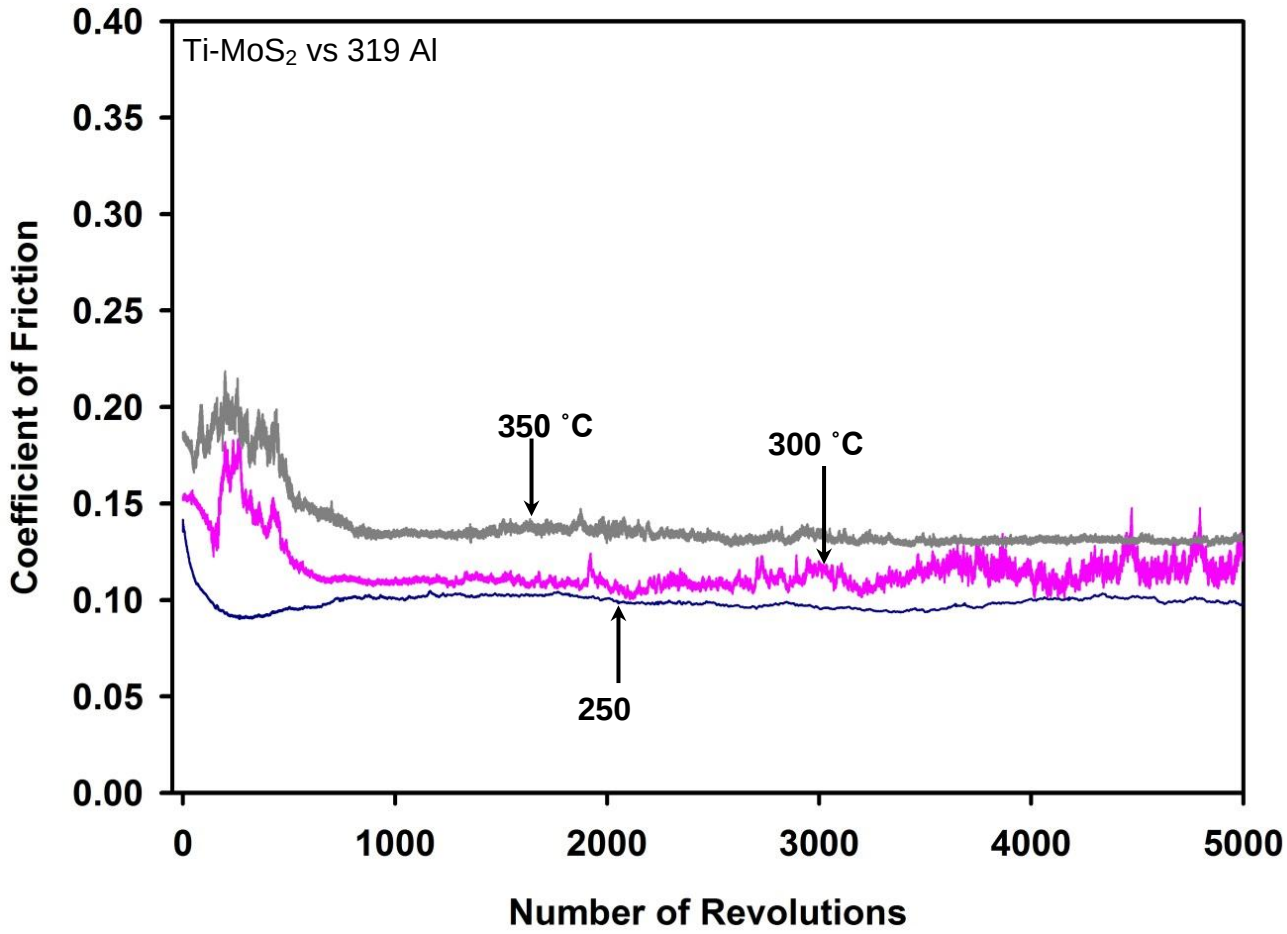
Ti-MoS2 vs 319 Al
Coefficient of Friction
0.40
0.35
0.30
0.25
0.20
0.15
0.10
0.05
0.00
350 ˚C
300 ˚C
250
0
1000
2000
3000
4000
5000
Number of Revolutions

(a)

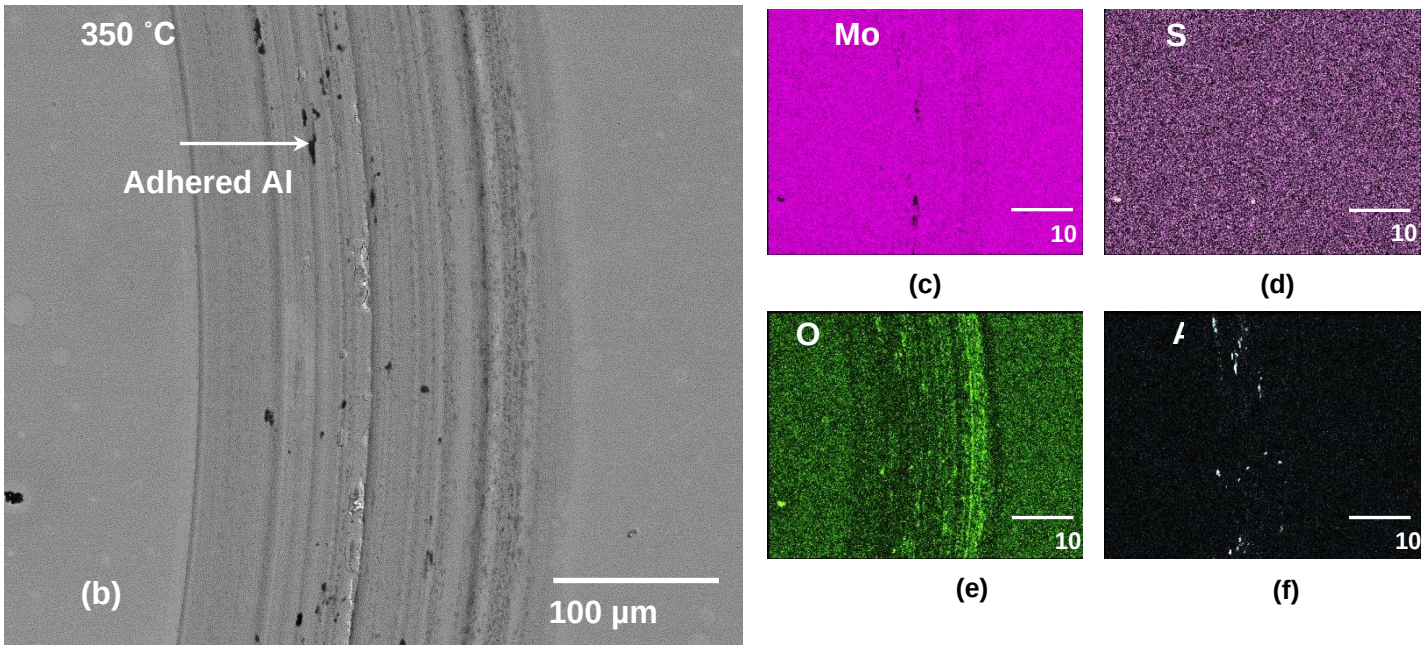

Figure 6.4: (a) Variation of the COF with the number of revolutions when the Ti-MoS_2 coating was tested against the 319 Al pin at 250 °C, 300 °C and 350 °C. (b) Typical secondary electron images of wear tracks formed on the Ti-MoS_2 surface when tested against 319 Al at 350 °C. The elemental EDS maps taken from the area shown in (b) are for (c) Mo, (d) S, (e) O and (f) Al.

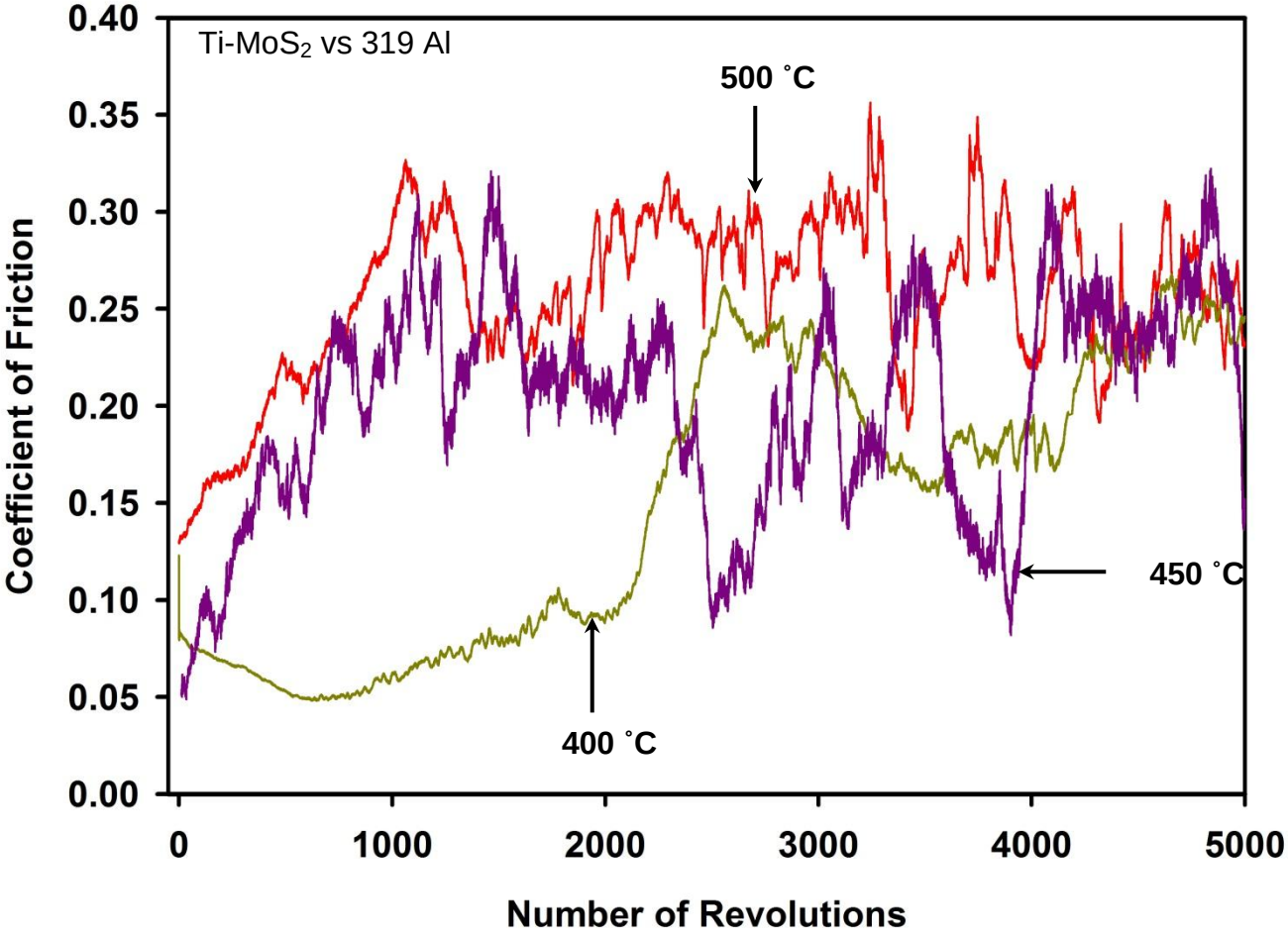
Ti-MoS2 vs 319 Al
500 ˚C
450 ˚C
400 ˚C
Coefficient of Friction
0.40
0.35
0.30
0.25
0.20
0.15
0.10
0.05
0.00
0
1000
2000
3000
4000
5000
Number of Revolutions

(a)

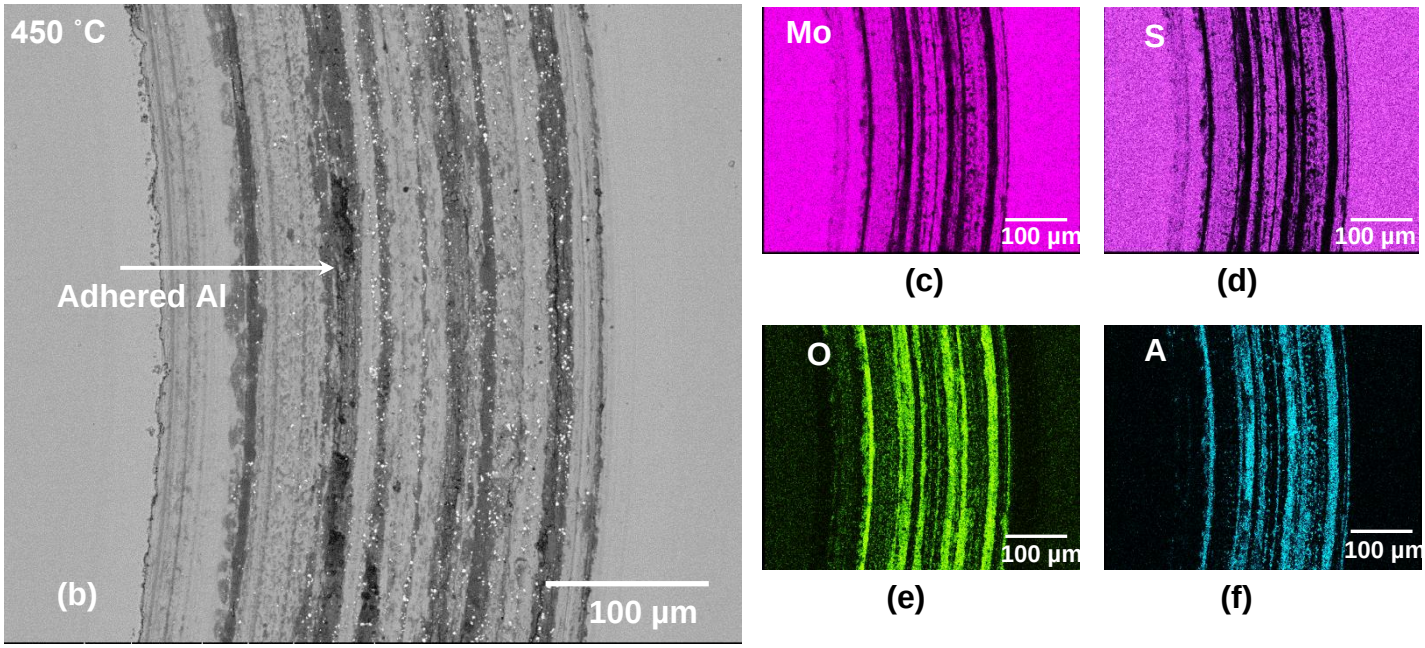

Figure 6.5: (a) Variation of the COF with the number of revolutions when the Ti-MoS_2 coating was tested against the 319 Al pin at 400 °C, 450 °C and 500 °C. (b) Typical secondary electron images of wear tracks formed on the Ti-MoS_2 surface when tested against 319 Al at 450 °C. The elemental EDS maps taken from the area shown in (b) are for (c) Mo, (d) S, (e) O and (f) Al.

6.3.3. Transfer Layer Formation on 319 Al Counterfaces

Contact surfaces of the 319 Al pins were examined by SEM in the backscattered electron mode to observe the morphological features of the worn area. For the tests conducted at 25 °C, 100 °C and 200 °C the contact surfaces of the 319 Al counterfaces were covered with patches of materials transferred from the Ti-MoS_2 coating. Fig. 6.6 (a) shows that the contact surface of the 319 Al subjected to sliding against Ti-MoS_2 coating at 25 °C was covered by the transfer layers and the transfer layers were also evident at 200 °C, Fig. 6.6 (e). The EDS elemental maps (Fig.

6.6 b-d at 25 °C and f-h at 200 °C) show the distributions of the Mo and S, originating from Ti-MoS_2 coating and reveal the presence of oxygen in these transfer layers. As pointed out earlier no Al transfer to the Ti-MoS_2 coating surface occurred up to 200 ˚C resulting in low COF recorded during sliding in this temperature range (Fig. 6.2).

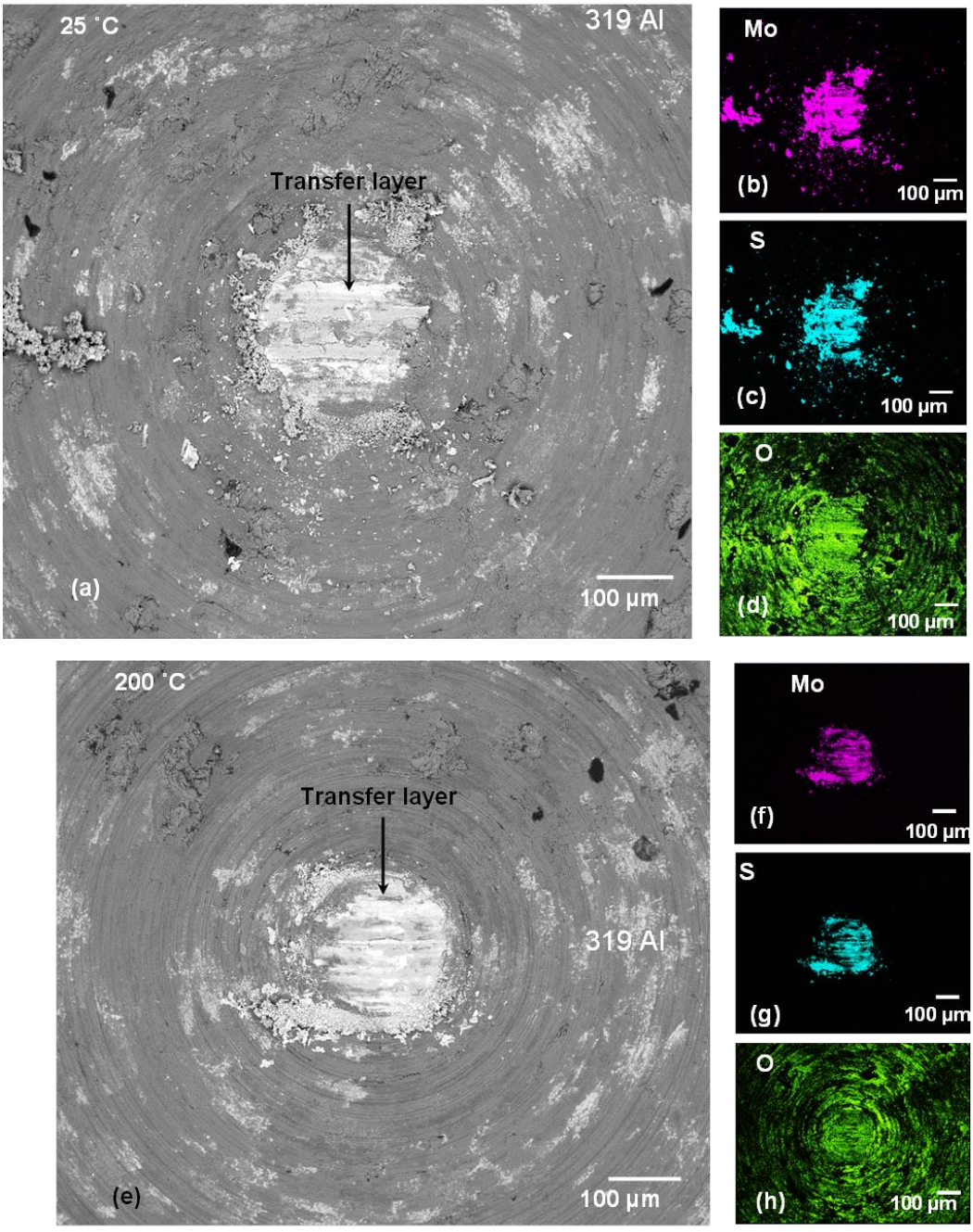

Figure 6.6: (a) Secondary electron image of the 319 Al pin surface taken after sliding against Ti-MoS_2 coating at 25 °C. The elemental EDS maps taken from the area shown in (a) are for (b) Mo, (c) S and (d) O. (e) Secondary electron image of 319 Al pin surface after the sliding against Ti-MoS_2 coating at 200 °C. The elemental EDS maps taken from the area shown in (e) are for (f) Mo, (g) S and (h) O.

At 350 °C, a tribolayer was also found to cover the contact surface of the 319 Al counterface as shown in Fig. 6.7 (a). EDS maps in Figs. 6.7 (b, c) show that while the tribolayers had a high Mo concentration almost no S was observed in the transfer layer. The traces of S observed in Fig. 6.7 (c) were located at the periphery of the contact surface. The tribolayer on 319 Al counterface contact surface incorporated O as shown in Fig. 6.7 (d). The effects of the changes in the compositions of the transfer layers on friction will be discussed in Section 4.

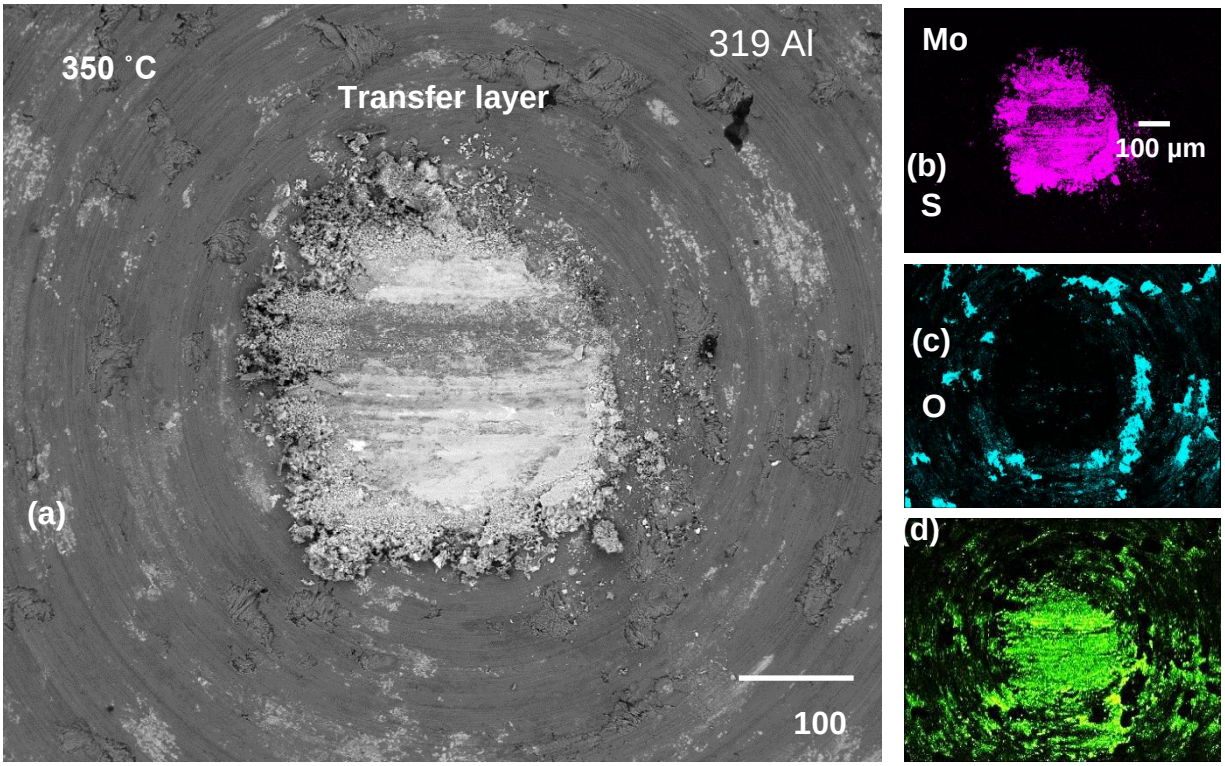

Figure 6.7: (a) Secondary electron image of the 319 Al pin surface taken after sliding against Ti-MoS_2 coating at 350 °C. The elemental EDS maps taken from the area shown in (a) are for (b) Mo, (c) S and (d) O.

6.3.4. Characterization of Contact Surfaces using Raman and XPS

Micro-Raman spectra obtained from the wear tracks of Ti-MoS_2 are shown in Fig. 6.8 (a). The Raman spectrum of the as-deposited Ti-MoS_2 coating showed typical peaks at 375 and 410 cm^{-1}, which were interpreted as the E_{2g} and A_{1g} bands arising from the vibrational modes within the S–Mo–S layer [36,37]. The Raman spectrum of the wear track of Ti-MoS_2 tested at

200 ˚C was characterized with Raman peaks that were similar to those in the as-deposited coating. The Raman spectrum acquired from the wear tracks generated at 350 ˚C showed a different set of peaks appearing at 81 (A_g), 115 (B_{1g}), 155 (B_{2g}), 285 (B_{3g}), 335 (B_{2g}), 660 (B_{3g}), 815 (A_g, B_{1g}) and 990 cm^{-1} (A_g, B_{1g}), which suggested formation of MoO_3 [37] via oxidation of MoS_2. The Raman peaks that characterized wear tracks of Ti-MoS_2 tested at 350 ˚C were typical for other tests performed between 200 ˚C and 350 ˚C but not those below 200 ˚C indicating that MoO_3 formation occurred at temperatures above 200 ˚C. MoO_3 increasingly covered larger portions of the contact surfaces at test temperatures above 350 ˚C. The Raman spectrum at 450 ˚C showed a strong Si peak and some small peaks belonging to MoO_3. The Si peaks arise from the adhesion of the 319 Al-Si alloy to the Ti-MoS_2 coating surface at ≥ 450 ˚C as observed in the SEM image of the Ti-MoS_2 wear track in Fig. 6.5 (a).

Fig. 6.8 (b) shows typical Micro Raman spectra obtained from the transfer layers formed on 319 Al counterfaces recorded at different test temperatures. Peaks belonging to MoS_2 were detected in the temperature range of 25 °C–200 °C similar to those of the wear tracks. For test performed at 350 °C peaks that appeared between 100 cm^{-1} and 1000 cm^{-1} were assigned to MoO_3 [37]. Raman spectrum of 319 Al counterfaces tested at 450 °C showed weak MoO_3 peaks with a prominent peak at 500 cm^{-1} attributed to the Si particles in the 319 Al indicating that the Si particles were mostly exposed as the transfer layer was not well formed.

(a)

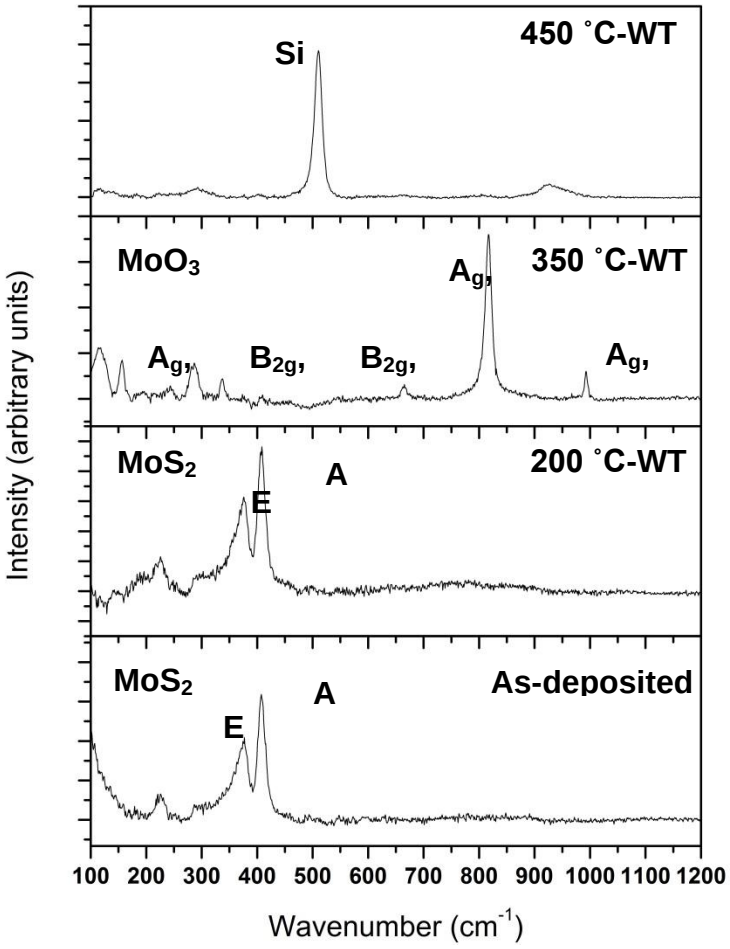
450 ˚C-WT
Si
MoO3
350 ˚C-WT
Ag,
Ag,
B2g,
B2g,
Ag,
MoS2
200 ˚C-WT
A
E
MoS2
As-deposited
A
E
Intensity (arbitrary units)
100 200 300 400 500 600 700 800 900 1000 1100 1200
Wavenumber (cm-1)

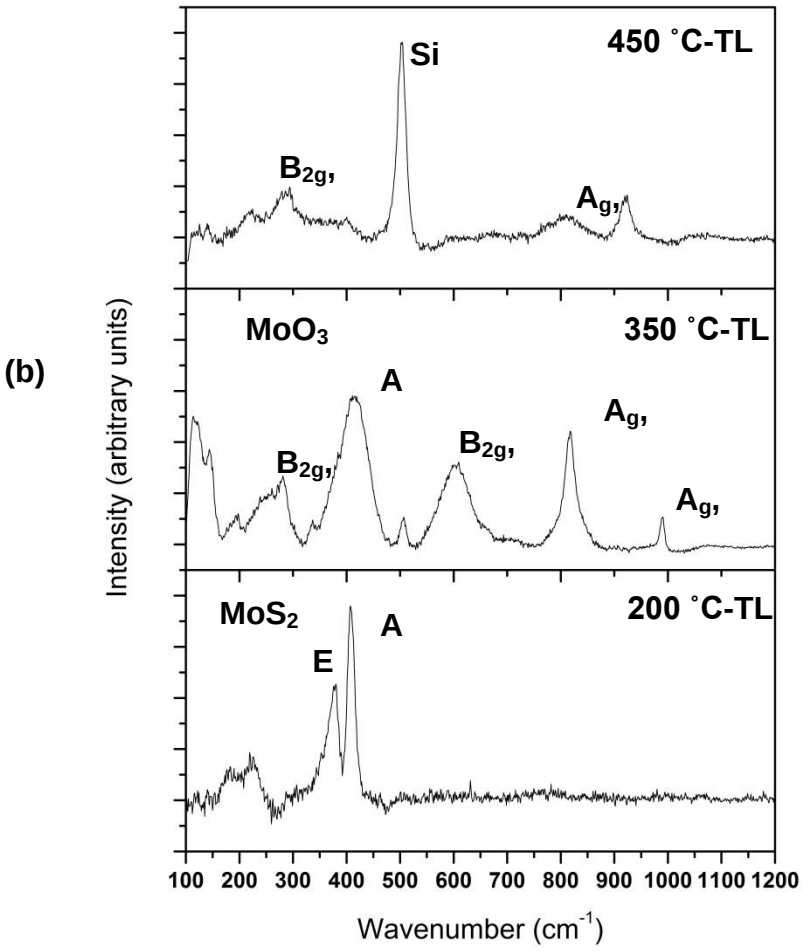

Figure 6.8: Raman spectra of (a) the wear tracks (WT) formed on Ti-MoS_2 and (b) transfer layers (TL) formed on 319 Al surface at 200 °C, 350 °C and 450 °C. The Raman spectrum of unworn Ti-MoS_2 is given for comparison. At 200 °C the Raman spectra of the WT and the TL appeared to be similar to that of the as-deposited coating and corresponded to MoS_2 layers. At 350 °C the Raman peaks corresponded to MoO_3 layers. The Raman spectrum at 450 °C showed prominent Si peaks which were attributed to Al-Si adhesion to WT in (a) and Si particles exposed on the 319 counterface surface in (b) as the transfer layer was not well formed.

Quantitative elemental compositional analyses performed using XPS survey scans on the tribolayers formed on the 319 Al c ounterfaces at 200 °C and 350 °C. Fig. 6.9 shows the changes in surface compositions of tribolayers at 200 °C and 350 °C. Fig. 6.9 (a) indicates that the transfer layer formed at 200 °C comprised of 2.8 at.% Mo, 28.4 at.% O and 3.4 at.% S at the section analyzed. The transfer layers formed at 350 °C (Fig. 6.9b) revealed the different quantities of the elements, namely 3.5 at.% Mo, 37.2 at.% O and 0.6 at.% S. Consequently the XPS results indicated a notable reduction in the atomic percentage of S at 350 ˚C compared to that at 200 ˚C. When the XPS results are compared with micro-Raman (Fig. 6.8) and SEM/EDS results of the 319 Al counterface (Fig. 6.7) they suggest that the Ti-MoS_2 coating was almost completely oxidized to MoO_3 at > 200 ˚C.

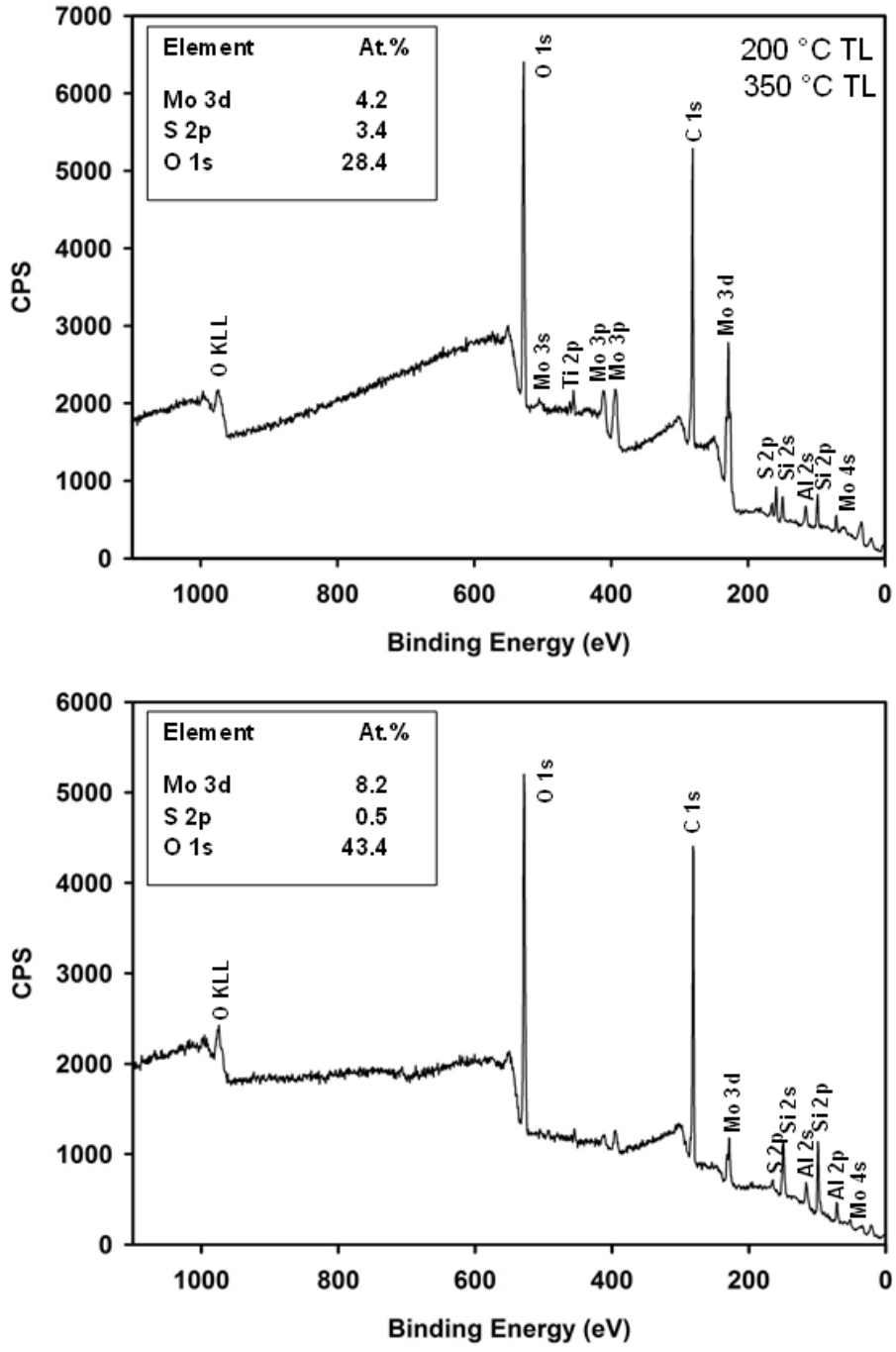

Figure 6.9: X-ray photoelectron spectroscopy (XPS) spectra of transfer layers (TL) formed on 319 Al during sliding against Ti-MoS_2 at (a) 200 °C and (b) 350 ˚C.

6.4. Discussion: Friction and Wear mechanisms of Ti-MoS_2 Coating at Different Temperatures

It is pertinent to discuss the elevated temperature tribological behaviour of Ti-MoS_2 in comparison with those of DLC coatings that are used to reduce friction and mitigate adhesion of Al-Si alloys to tool/die surfaces [38–40]. The hydrogenated and non-hydrogenated grades of DLC (H-DLC and NH-DLC) coatings can provide low friction to aluminum alloys by minimizing adhesive transfer of aluminum to counterfaces under ambient conditions [38–43]. However, at temperatures higher than 200 ˚C the tribological properties of these DLC coatings deteriorate [31,40,44]. In fact, high COF values are reported for NH-DLC at temperatures as low as 100 ˚C [44]. As shown in Fig. 6.10, the NH-DLC's COF is 0.18 at room temperature but its' COF immediately increases to 0.32 at 100 °C [44]. The H-DLC coatings survived at higher temperatures but again failed at a relatively low temperature of ≥200 °C [39, 40]. On the other hand, the Ti-MoS_2 coatings showed a low and steady state COF between 0.05 and 0.15 in the temperature range of 25 ˚C - 350 ˚C. The low friction of NH-DLC is primarily due to the passivation of the dangling carbon bonds at the contact surface by moisture in humid environments [45–47]. Consequently at temperatures above 100 ˚C high friction and wear occurs as this passivation mechanism becomes inactive [44] and graphitization leads to coating removal at higher temperatures. Both the NH- and H-DLC coatings are subjected to graphitization and softening at temperatures > 200 ˚C [32, 39]. At temperatures above 200 ˚C the H atoms, terminating the surface carbon bonds of the H-DLC coating [32, 39], would undergo desorption resulting in high COF ≥ 0.35. The Ti-MoS_2 coatings studied in this work exhibit low COF values in the range of 0.05-0.14 (Fig. 6.2) in dry atmospheres and thus do not necessarily need a moisture dissociation mechanism (to OH and H) to passivate their surface to achieve low friction. Accordingly, at temperatures between 100 ˚C and 350 ˚C the Ti-MoS_2 coatings provided

low friction. The purpose for the comparison of Ti-MoS_2 coatings with that of DLC was to show that while DLC coatings are beneficial at room temperature, their low friction and adhesion mitigating properties deteriorate at higher temperatures > 100°C. The results presented in this manuscript shows that in the temperature range of 100-350 °C the Ti-MoS_2 coatings maintained low friction and would be beneficial for elevated temperature applications of engineering components sliding against aluminum alloy counterfaces.

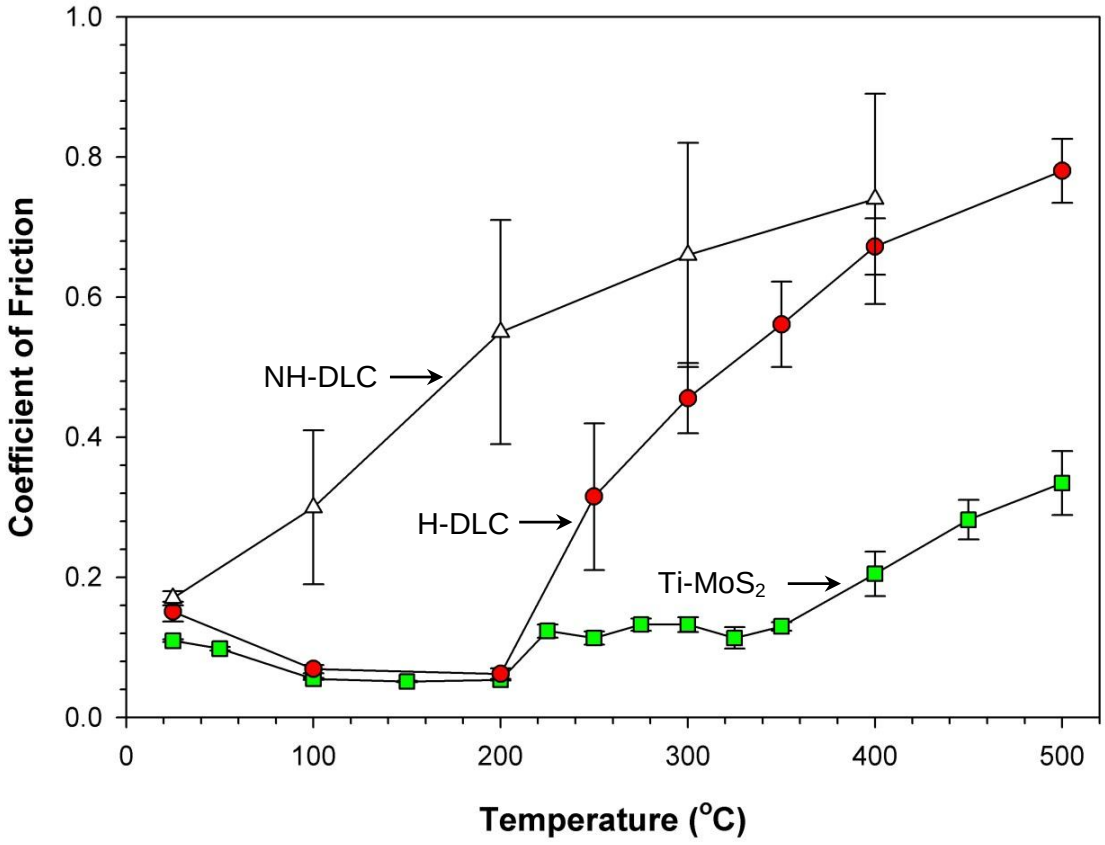

Figure 6.10: Variation of COF (μ) with the test temperature for H-DLC, NH-DLC and Ti-MoS_2 coatings subjected to high temperature tests at constant temperatures between 25 and 500 °C. Note that $\mu = \mu_S$ (steady state COF) up to 400 °C for Ti-MoS_2, up to 200 °C for H-DLC and up to 100 °C for NH-DLC.

The micromechanisms controlling the tribological behaviour of the Ti-MoS_2 coatings at different temperatures can be discussed with the aid of a COF vs. wear rate diagram shown in Fig. 6.11. According to Fig. 6.11 three different regimes exist as demarcated by changes of COF values and wear rates in different temperature ranges. The three regimes demarcated in Fig. 6.11 are as follows: i) 25 ˚C and 200 ˚C: in this temperature range MoS_2 transfer layers are formed on the counterface provide low friction; ii) 225 ˚C and 350 ˚C: in this temperature range both MoS_2 and MoO_3 co-exist on the contact surfaces and control friction and wear; and iii) above 400 ˚C extensive Al adhesion to the Ti-MoS_2 coatings occur.

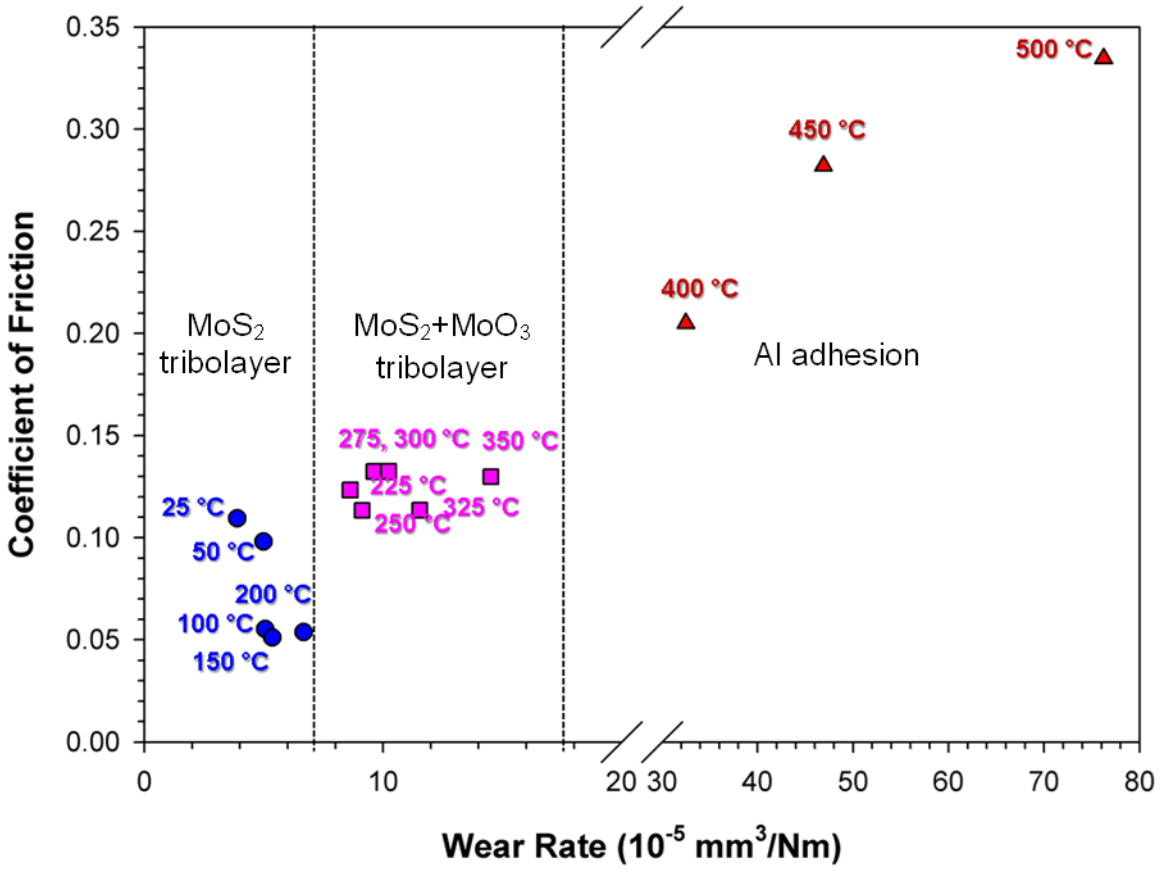

Figure 6.11: COF vs wear rate plot for Ti-MoS_2 tested against 319 Al at different temperatures. Low COF and wear rates were observed for temperatures between 25 °C and 200 °C where a MoS_2 transfer layer formed. In the temperature range of 200-350 °C the increase in COF and wear rates were attributed to formation of MoO_3 and transfer to counterface. At above 400 °C localized areas of coating removal and Al-Si adhesion led to significant increase in COF and wear rates.

In case of the tests performed between 25 ˚C and 200 ˚C, the COF progressively decreased from 0.11 to a minimum value of 0.05 while the wear rates were less sensitive to the test temperature and varied in a narrow range of 3.89×10^{-5} - 6.67×10^{-5} mm^3/Nm. SEM/EDS (Fig. 6.6) and micro-Raman (Fig. 6.8) observations suggested that the formation of transfer layers consisting of MoS_2 on Al-Si counterfaces, was responsible for the low friction and wear. The

higher COF at 25 ˚C compared to that at 200 ˚C was due to presence of moisture (45% RH) in the environment. The increase in COF of MoS_2 in a humid environment has been attributed to either oxidation to MoO_3 [16] or water adsorption on MoS_2 layers [48]. Yet, the addition of Ti to the MoS_2 coatings resulted in a relatively low steady state COF of 0.11 at 45% RH than the COF values reported of 0.14 and 0.15 reported for monolithic MoS_2 coatings [18, 23] tested at room temperature under ambient conditions against 52100 steel. The improved friction behaviour has been attributed to the presence of the Ti atoms in interstitial sites between the S planes preventing adsorption of water molecules [27]. With an increase in temperature the moisture was removed and the COF values decreased to 0.05 until above 200 ˚C.

At temperature range between 225 ˚C and 350 ˚C, a slight increase in COF to values between 0.10 and 0.15 was observed. The coating wear tracks were largely covered by layers consisting of a mixture of MoS_2 and MoO_3 which were also transferred to the counterface. The change in the lamellar lubricious MoS_2 structure [16] to an orthorhombic and brittle MoO_3 [37] was the likely reason for the increase in COF and wear rates. At temperatures above 350˚C, the wear rates increased sharply i.e. 32.48×10^{-5} mm^3/Nm at 400 ˚C, 46.89×10^{-5} mm^3/Nm at 450 ˚C and 76.23×10^{-5} mm^3/Nm at 500 ˚C. This rapid increase was attributed to partial removal of the coating from wear tracks, as seen in Fig. 6.5. Adhesion of 319 Al counterface to the coating surfaces contributed to higher wear rates observed. The COF values also increased rapidly to 0.34 at 500 ˚C (Fig. 11).

In summary, the COF vs. wear rate diagram in Fig. 6.11 was useful to reveal the temperature induced changes in the tribological behaviour of Ti-MoS_2 coating sliding against Al-Si alloys. Accordingly, it can be suggested that the safe operation window for use of Ti-MoS_2 coating against Al-Si alloys ranges between 25 ˚C and 350 ˚C.

Summary and Conclusions

The main results arising from this work can be summarized as follows:

(1) At temperatures between 25 ˚C and 200 ˚C Ti-MoS_2 coatings showed low friction of 0.05-0.11 and wear rates against Al-6.5% Si (Al 319) which were attributed to the formation of MoS_2 transfer layers formation on the counterface contact surfaces.

(2) At ≥ 200 ˚C the COF and wear behaviour were controlled by the formation of a mixture of MoS_2 and MoO_3 on the contact surface. Slight increase in the wear rates and COF values (0.11-0.15) were observed.

(3) At above 400 ˚C, the Ti-MoS_2 coating began to disintegrate and adhesion of 319 Al to the coating surface occurred.

In conclusion, Ti-MoS_2 offers high thermal stability, high wear resistance and low friction for dry sliding contact applications against aluminum alloys at temperatures up to 350˚C.

Bibliography

[1] M. Kleiner, M. Geiger, A. Klaus, Manufacturing of lightweight components by metal forming, CIRP Ann. Technol. 52 (2003) 521–542.
[2] R. Neugebauer, T. Altan, M. Geiger, M. Kleiner, A. Sterzing, Sheet metal forming at elevated temperatures, CIRP Ann. Technol. 55 (2006) 793–816.
[3] T. Naka, G. Torikai, R. Hino, F. Yoshida, The effects of temperature and forming speed on the forming limit diagram for type 5083 aluminum–magnesium alloy sheet, J. Mater. Process. Technol. 113 (2001) 648–653.
[4] S. Bhowmick, A.T. Alpas, The role of diamond-like carbon coated drills on minimum

quantity lubrication drilling of magnesium alloys, Surf. Coatings Technol. 205 (2011) 5302–5311.
[5] S. Mahabunphachai, M. Koç, Investigations on forming of aluminum 5052 and 6061 sheet alloys at warm temperatures, Mater. Des. 31 (2010) 2422–2434.
[6] E.P. Becker, Trends in tribological materials and engine technology, Tribol. Int. 37 (2004) 569–575.
[7] S.C. Tung, M.L. McMillan, Automotive tribology overview of current advances and challenges for the future, Tribol. Int. 37 (2004) 517–536.
[8] A. Banerji, A. Edrisy, V. Francis, A.T. Alpas, Effect of bio-fuel (E85) addition on lubricated sliding wear mechanisms of a eutectic Al–Si alloy, Wear. 311 (2014) 1–13.
[9] S. Bhowmick, A.T. Alpas, The performance of hydrogenated and non-hydrogenated diamond-like carbon tool coatings during the dry drilling of 319 Al, Int. J. Mach. Tools Manuf. 48 (2008) 802–814.
[10] S. Bhowmick, A.T. Alpas, Minimum quantity lubrication drilling of aluminium–silicon alloys in water using diamond-like carbon coated drills, Int. J. Mach. Tools Manuf. 48 (2008) 1429–1443.
[11] S. Bhowmick, M.J. Lukitsch, A.T. Alpas, Tapping of Al–Si alloys with diamond-like carbon coated tools and minimum quantity lubrication, J. Mater. Process. Technol. 210 (2010) 2142–2153.
[12] S. Bhowmick, A. Banerji, A.T. Alpas, Tribological behavior of Al–6.5%,–12%,–18.5% Si alloys during machining using CVD diamond and DLC coated tools, Surf. Coatings Technol. 284 (2015) 353–364.
[13] W.M. Silva, L.M. Jesus, J.R. Carneiro, P.S. Souza, P.S. Martins, V.J. Trava-Airoldi, Performance of carbide tools coated with DLC in the drilling of SAE 323 aluminum alloy, Surf. Coatings Technol. 284 (2015) 404–409.
[14] H.E. Sliney, Solid lubricant materials for high temperatures—a review, Tribol. Int. 15 (1982) 303–315.
[15] J.M. Martin, C. Donnet, T. Le Mogne, T. Epicier, Superlubricity of molybdenum disulphide, Phys. Rev. B. 48 (1993) 10583.
[16] J.K.G. Panitz, L.E. Pope, J.E. Lyons, D.J. Staley, The tribological properties of MoS2 coatings in vacuum, low relative humidity, and high relative humidity environments, J. Vac. Sci. Technol. A Vacuum, Surfaces, Film. 6 (1988) 1166–1170.
[17] C. Donnet, J.M. Martin, T. Le Mogne, M. Belin, Super-low friction of MoS2 coatings in various environments, Tribol. Int. 29 (1996) 123–128.
[18] C. Donnet, Advanced solid lubricant coatings for high vacuum environments, Surf. Coatings Technol. 80 (1996) 151–156.
[19] T. Spalvins, Lubrication with sputtered MoS2 films: principles, operation, limitations, (1991).
[20] V.R. Johnson, G.W. Vaughn, Investigation of the mechanism of MoS2 lubrication in vacuum, J. Appl. Phys. 27 (1956) 1173–1179.
[21] J.-F. Yang, B. Parakash, J. Hardell, Q.-F. Fang, Tribological properties of transition metal di-chalcogenide based lubricant coatings, Front. Mater. Sci. 6 (2012) 116–127.
[22] G. Levita, P. Restuccia, M.C. Righi, Graphene and MoS 2 interacting with water: A comparison by ab initio calculations, Carbon N. Y. 107 (2016) 878–884.
[23] T. Kubart, T. Polcar, L. Kopecký, R. Novak, D. Novakova, Temperature dependence of tribological properties of MoS 2 and MoSe 2 coatings, Surf. Coatings Technol. 193 (2005)

230–233.
[24] E. Arslan, Y. Totik, O. Bayrak, I. Efeoglu, A. Celik, High temperature friction and wear behavior of MoS2/Nb coating in ambient air, J. Coatings Technol. Res. 7 (2010) 131.
[25] K.C. Wong, X. Lu, J. Cotter, D.T. Eadie, P.C. Wong, K.A.R. Mitchell, Surface and friction characterization of MoS 2 and WS 2 third body thin films under simulated wheel/rail rolling–sliding contact, Wear. 264 (2008) 526–534.
[26] N.M. Renevier, V.C. Fox, D.G. Teer, J. Hampshire, Performance of low friction MoS 2/titanium composite coatings used in forming applications, Mater. Des. 21 (2000) 337–343.
[27] X. Ding, X.T. Zeng, X.Y. He, Z. Chen, Tribological properties of Cr-and Ti-doped MoS 2 composite coatings under different humidity atmosphere, Surf. Coatings Technol. 205 (2010) 224–231.
[28] X. Wang, Y. Xing, S. Ma, X. Zhang, K. Xu, D.G. Teer, Microstructure and mechanical properties of MoS 2/titanium composite coatings with different titanium content, Surf. Coatings Technol. 201 (2007) 5290–5293.
[29] P. Stoyanov, R.R. Chromik, D. Goldbaum, J.R. Lince, X. Zhang, Microtribological performance of Au–MoS2 and Ti–MoS2 coatings with varying contact pressure, Tribol. Lett. 40 (2010) 199–211.
[30] L. Wu, B.C. Holloway, D.P. Beesabathina, C. Kalil, D.M. Manos, Analysis of diamond-like carbon and Ti/MoS 2 coatings on Ti–6Al–4V substrates for applicability to turbine engine applications, Surf. Coatings Technol. 130 (2000) 207–217.
[31] A. Banerji, S. Bhowmick, A.T. Alpas, High temperature tribological behavior of W containing diamond-like carbon (DLC) coating against titanium alloys, Surf. Coatings Technol. 241 (2014) 93–104.
[32] S. Bhowmick, A. Banerji, M.J. Lukitsch, A.T. Alpas, The high temperature tribological behavior of Si, O containing hydrogenated diamond-like carbon (aC: H/a-Si: O) coating against an aluminum alloy, Wear. 330 (2015) 261–271.
[33] A. Banerji, H. Hu, A.T. Alpas, Sliding wear mechanisms of magnesium composites AM60 reinforced with Al 2 O 3 fibres under ultra-mild wear conditions, Wear. 301 (2013) 626–635.
[34] S. Bhowmick, A. Banerji, A.T. Alpas, Tribological Behaviour of W-DLC against an Aluminium Alloy Subjected to Lubricated Sliding., Tribol. Ind. 37 (2015).
[35] S. Bhowmick, F.G. Sen, A. Banerji, A.T. Alpas, Friction and adhesion of fluorine containing hydrophobic hydrogenated diamond-like carbon (FH-DLC) coating against magnesium alloy AZ91, Surf. Coatings Technol. 267 (2015) 21–31.
[36] H. Li, Q. Zhang, C.C.R. Yap, B.K. Tay, T.H.T. Edwin, A. Olivier, D. Baillargeat, From bulk to monolayer MoS2: evolution of Raman scattering, Adv. Funct. Mater. 22 (2012) 1385–1390.
[37] B.C. Windom, W.G. Sawyer, D.W. Hahn, A Raman spectroscopic study of MoS2 and MoO3: applications to tribological systems, Tribol. Lett. 42 (2011) 301–310.
[38] F. Wang, Z. Lu, L. Wang, G. Zhang, Q. Xue, Effect of tribochemistry on friction behavior of fluorinated amorphous carbon films against aluminum, Surf. Coatings Technol. 304 (2016) 150–159.
[39] A.A. Gharam, M.J. Lukitsch, M.P. Balogh, A.T. Alpas, High temperature tribological behaviour of carbon based (B 4 C and DLC) coatings in sliding contact with aluminum, Thin Solid Films. 519 (2010) 1611–1617.

[40] S. Bhowmick, A. Banerji, M.Z.U. Khan, M.J. Lukitsch, A.T. Alpas, High temperature tribological behavior of tetrahedral amorphous carbon (ta-C) and fluorinated ta-C coatings against aluminum alloys, Surf. Coatings Technol. 284 (2015) 14–25.
[41] J.M. Dasch, C.C. Ang, C.A. Wong, Y.T. Cheng, A.M. Weiner, L.C. Lev, E. Konca, A comparison of five categories of carbon-based tool coatings for dry drilling of aluminum, Surf. Coatings Technol. 200 (2006) 2970–2977.
[42] H. Fukui, J. Okida, N. Omori, H. Moriguchi, K. Tsuda, Cutting performance of DLC coated tools in dry machining aluminum alloys, Surf. Coatings Technol. 187 (2004) 70–76.
[43] N. Wain, N.R. Thomas, S. Hickman, J. Wallbank, D.G. Teer, Performance of low-friction coatings in the dry drilling of automotive Al–Si alloys, Surf. Coatings Technol. 200 (2005) 1885–1892.
[44] E. Konca, Y.-T. Cheng, A.M. Weiner, J.M. Dasch, A.T. Alpas, Elevated temperature tribological behavior of non-hydrogenated diamond-like carbon coatings against 319 aluminum alloy, Surf. Coatings Technol. 200 (2006) 3996–4005.
[45] S. Bhowmick, A. Banerji, A.T. Alpas, Tribological behavior and machining performance of non-hydrogenated diamond-like carbon coating tested against Ti–6Al–4V: Effect of surface passivation by ethanol, Surf. Coatings Technol. 260 (2014) 290–302.
[46] E. Konca, Y.-T. Cheng, A.M. Weiner, J.M. Dasch, A.T. Alpas, Effect of test atmosphere on the tribological behaviour of the non-hydrogenated diamond-like carbon coatings against 319 aluminum alloy and tungsten carbide, Surf. Coatings Technol. 200 (2005) 1783–1791.
[47] S. Bhowmick, G. Sun, A.T. Alpas, Low friction behaviour of boron carbide coatings (B 4 C) sliding against Ti–6Al–4V, Surf. Coatings Technol. 308 (2016) 316–327.
[48] X. Zhao, S.S. Perry, The role of water in modifying friction within MoS2 sliding interfaces, ACS Appl. Mater. Interfaces. 2 (2010) 1444–1448.

CHAPTER 7

Role of Humidity in Reducing Sliding Friction of Multilayered Graphene

7.1. Introduction

Minimizing friction and wear losses remains one of the greatest challenges for components operating under sliding contact conditions and requires development new surface coatings, as well as liquid and solid lubricants [1–3]. Graphite and other carbon based materials such as diamond like carbon coatings are also being used to reduce friction [4–6]. The friction behaviour of graphene, a new carbon based material, has attracted interest and is currently being studied [7–11].

Kim et al. [8] investigated the frictional characteristics of CVD grown graphene under a normal load of 70 mN and in an atmosphere with 33 % RH and observed that the COF was affected by the substrate as the graphene grown on Ni substrate demonstrated low COF of 0.10 compared to the coatings grown on Cu with a COF of 0.20. Berman et al. [9] conducted tribological tests on graphene flakes suspended in ethanol for stainless steel sliding against itself at 2.0 N whereby low COF of 0.15 was recorded. In another study [10], a low COF of 0.15 was observed during sliding of stainless steel lubricated by ethanol processed graphene in a dry N_2 atmosphere and the low friction of graphene was attributed to the occurrence of 'easy shear' at the contact interface.

Some studies investigated the frictional characteristics of graphene using atomic force microscope (AFM) tips using very low loads [12–17]. Lee et al. [12] studied friction behaviour of exfoliated graphene and graphite in ambient air using a lateral force microscope (LFM) with a SiN tip under low normal force of 0.5 nN and a low scanning velocity 10 μm/s. It was observed that the friction of 1.5 nm thin graphene layer was greater than the friction force observed on the

thick graphite (multilayered graphene) surface which was attributed to the higher van der Waal's interactions in the latter. Filleter et al. [13] using friction force microscopy (FFM) experiments found that a bilayer graphene grown epitaxially on SiC substrate showed lower friction force compared to a single layer graphene, which was attributed to a lower electron-phonon coupling effect in the bilayer. Lee et al. [14] found that frictional behaviour of graphene produced by mechanical exfoliation depended on the layer thickness. FFM studies were conducted in an ambient atmosphere (25-50% RH) using low speeds of 1-10 μm/s and low normal loads of 0.1-2.0 nN. Lower friction force values were observed with increasing the graphene layer thickness (>4 layers) compared to a monolayer graphene due to an increased resistance to out-of-plane deformation [14]. Yan et al. [15] investigated the friction behaviour of CVD grown graphene transferred to polyethylene teraphthalate substrate at 20 mN and 50 μm/s against fused silica; although the graphene was partially worn out after 25 tests, a low steady state COF of 0.09 was maintained. Wählisch et al. [16] and Marchetto et al. [17] studied friction of a single layer graphene grown on SiC wafer with a carbon rich interlayer against a ruby sphere using a normal force of 0.1 mN and the maximum velocity of 50 μm/s, under an ambient atmosphere (40-60% RH). The initial COF of 0.02 increased to 0.07 after 100 cycles. The low initial COF was attributed to contact with the top graphene layer, while for higher cycles the top layer was delaminated and the friction behaviour was governed by the interactions between the counterface asperities and carbon rich interface layer.

These studies shed light on the frictional behaviour of graphene and suggested possibility of using graphene for reducing friction during sliding. However, none studied the effect of atmospheric humidity as an independent variable. It is known that the wear and friction behaviour of carbon based materials, namely graphite and amorphous diamond-like carbon

surfaces are strongly influenced by the humidity in the test environment [18–22]. The low friction behaviour of graphite at high humidity was attributed to the moisture that ‘saturated the carbon dangling bonds’ of the graphite [18]. The COF of non-hydrogenated diamond-like carbon (NH-DLC) surfaces was shown to decrease with increasing the moisture in the surrounding environment [19, 20]. The decrease in friction of the non-hydrogenated diamond-like carbon coating in moist air was attributed to the passivation of the dangling carbon bonds by the OH (and H) groups dissociated from the water vapour in the atmosphere during the tribological contact [21, 22].

Tribological tests exploring the role of humidity on friction behaviour of graphene are yet to be performed and in this study aims to conduct sliding friction experiments at different test atmospheres with controlled humidity levels and analyse the results using analytical microscopy and spectroscopy to shed light on the mechanisms of friction reduction observed in humid atmospheres.

7.2. Experimental Procedure

Sliding wear tests were performed on commercially available (Graphene Supermarket Inc., NY, USA) graphene grown on 0.5 mm thick Ni foils under atmospheric pressure using a chemical vapour deposition (CVD) process with methane gas as the source of carbon. Morphological features of graphene and the microstructures of the transfer layers were studied using FEI Quanta 200 FEG scanning electron microscope (SEM) equipped with an energy dispersive spectroscopy (EDS) having SiLi detector. The Ni foils, on which the graphene was deposited, were mounted on a steel plate using carbon tape and were placed in sliding contact against counterface made of 4.0 mm diameter Ti-6Al-4V balls on which a constant load of 1.0 N was applied. The corrosion resistance of Ti-6Al-4V was the reason for its selection. A pin-on-

disk type CSM tribometer was used to perform the sliding friction tests. The tribometer used consisted of a stationary pin under an applied load in contact with a rotating disc located inside an environmental chamber for measuring friction and wear under controlled humidity atmospheres, monitored using a hygrometer with a sensitivity of ±0.1 of the desired % RH level. A description of the tribometer is provided in [23]. Sliding tests were conducted at a low constant speed of 0.05 m/s. The specific load and sliding speed values used in the sliding tests were determined from the previous tests conducted on DLC coatings using similar humidity levels [19-22]. Experiments conducted under low sliding speed and low load allowed friction measurements on graphene layers without causing excessive damage and wear—consistent with other studies on friction behaviour of graphene carried at low speeds [12-17]. The graphene is expected to act as a boundary lubricant at low speeds (and low loads) used. The effect of humidity on the COF was studied by conducting the tests in an enclosed environmental chamber with controlled relative humidity (RH) levels of 10, 32 and 45% RH and in a dry nitrogen (0% RH) environment. The moisture content in the environmental chamber was reduced purging dry argon gas.

At least three sliding tests were performed under each test environment and a new counterface was used for each test. For each friction curve, the value of COF in the steady-state (μ_S) stage was calculated from the arithmetic mean of the COF signals, typically after 6.00 $\times 10^2$ revolutions. The average μ_S values obtained from three tests under a specific test environment and their standard deviations were reported.

The samples for transmission electron microscopy (TEM) investigations were prepared by a focused ion beam (FIB) lift out technique using a Ga^+ ion source sputtered at 30 kV and a beam current of 80 pA using Carl Zeiss NVision 40 dual beam. Prior to the ion milling process, the

surfaces were protected by sputtering them with a layer of carbon. The cross-sectional samples were ion-milled from both sides to a thickness of about 100 nm. The final milling of the samples was conducted at a low beam current of 40 pA to minimize beam damage on the cross-sections. TEM observations were performed using FEI Titan 80-300 HR-TEM, having a lateral resolution < 1Å, operated at 300 kV was used to obtain high-resolution imaging and diffraction patterns. Micro-Raman studies on the graphene surfaces were carried out using a 50 mW Nd–YAG laser (532 nm excitation line) through the 50× objective lens (diameter of the laser spot for Raman on the specimen surface was 1 μm) of a Horiba Raman micro-spectrometer. Chemical analyses of the transfer layers formed on the counterface were conducted by X-ray photoelectron spectroscopy (XPS) using Kratos Axis Ultra X-ray photoelectron spectrometer with spatial resolution of 5 μm, which can probe the surface of the samples to a depth of 7-10 nm with elemental detection limit of 0.1 at.% and area of acquisition of 15 microns in diameter. High-resolution scans of elemental peaks of interest were taken to determine chemical bonding information. The survey scans were performed at 160 eV pass energy while the high resolution scans were performed at 40 eV.

7.3. Results

7.3.1. Deposition and Characterization of CVD Grown Graphene

The graphene grown on Ni foils formed a multilayered structure as platelets with different thicknesses. Figure 7.1 shows the Raman spectra of the graphene platelets acquired from three different locations indicated in the inset of Figure 7.1a. The Raman spectra show the characteristic G (1580 cm^{-1}) and 2D (2705 cm^{-1}) peaks with peak intensity ratios, I_G/I_{2D} of 2.18-2.68 indicating multilayered graphene. A slightly broadened 2D peak, generated due to double resonance of phonons having opposite momentum, is also considered as a Raman fingerprint of

multilayered graphene [24,25]. Raman D-band at 1330 cm^{-1} is known as the disorder band [24]. As there was no evidence for the formation of D-band on the pristine graphene it could be suggested that the defect density of the graphene films was extremely low.

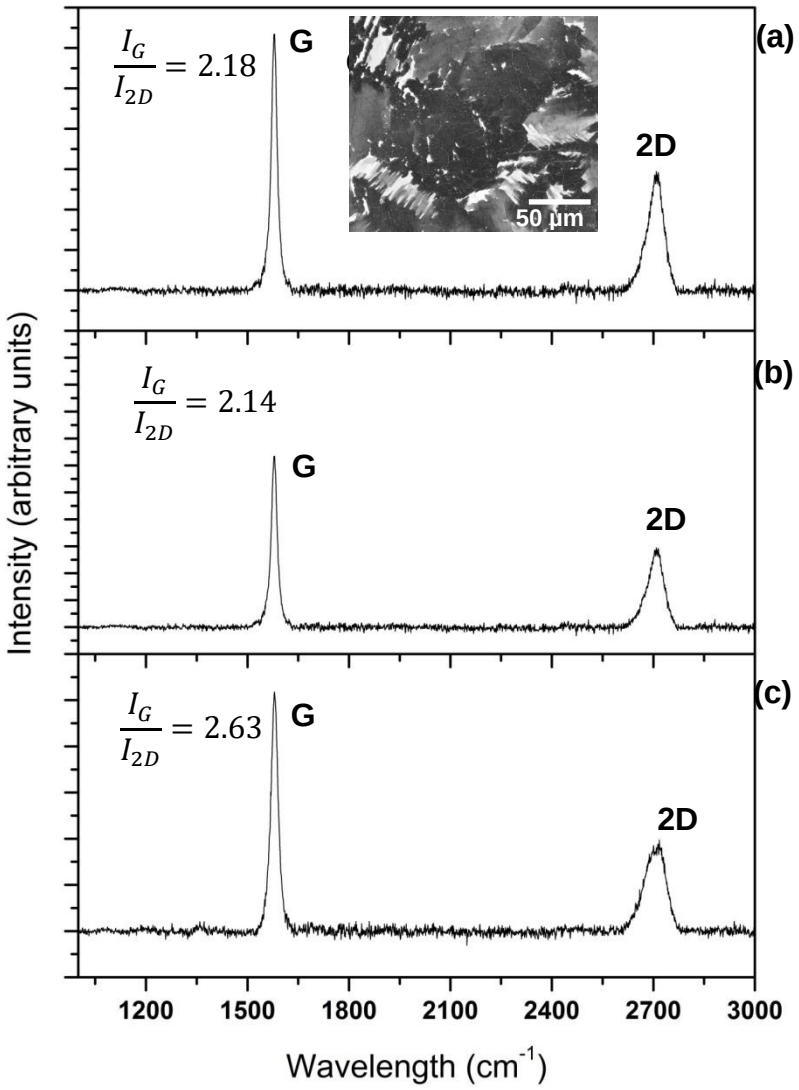

Figure 7.1—Micro-Raman spectra of the graphene on Ni substrate taken at three different locations shown in the secondary electron image in the inset. The ratio of G and 2D bands indicate the graphene flakes deposited by the CVD process form more than single layer. (The ambient atmosphere consisted of 45 % RH).

7.3.2. COF Behaviour of Graphene under Different Test Environments

The typical trends in the COF (μ) values of graphene tested under dry nitrogen (N_2) atmosphere with 0% RH and in air with 10% RH, are shown in Figure 7.2 (a) as a function of number of revolutions. Accordingly, testing the graphene in a dry N_2 atmosphere produced a high maximum running COF, μ_R, reaching 0.51. Following running-in period the COF decreased to 0.38 ± 0.06 for a short sliding period of 60 cycles in this test and then increased again to 0.59 ± 0.2 and after 400 cycles it exhibited large fluctuations until the test was stopped at 10^3 cycles. Thus no μ_S was observed in this condition and the large fluctuations are indicative of adhesion of counterface material to the sample. Under an ambient air atmosphere with 10% RH a running–in period occurred with μ_R of 0.17 (at 10 cycles) followed by a decrease to 0.09. The running-in period lasted for 2.20×10^2 revolutions and the rest of the curve was characterized by a low a stable COF indicating attainment of a steady state friction with a μ_S of 0.17 ± 0.01 that was maintained for the rest of the test. The running-in period was observed in tests conducted at higher RH values, yet the μ_R decreased when the RH of the environmental chamber increased. Sliding tests conducted on graphene samples tested in an air atmosphere with 32% RH resulted in μ_R of 0.11 followed by a low μ_S of 0.16 ± 0.01 as shown in Figure 7.2b (with a larger COF axis for clarity). The μ_R decreased to 0.05 for graphene tested in air with 45% RH and subsequently to a μ_S of 0.11 ± 0.01 which was the lowest steady state COF observed in all humidity atmospheres considered. As indicated before at each testing environment three tests were performed and the COF curves presented in Figs. 3a, b re the typical trends. A plot of μ_R and average μ_S values obtained from the three tests at each environment is shown in Figure 7.2c which emphasizes that the compared to dry sliding, the COF values (both μ_R and μ_S) of graphene

decreased significantly (67%) when 10% RH introduced in the test environment and a slight decrease in COF was recoded when the humidity was increased in the range of 32% to 45% RH.

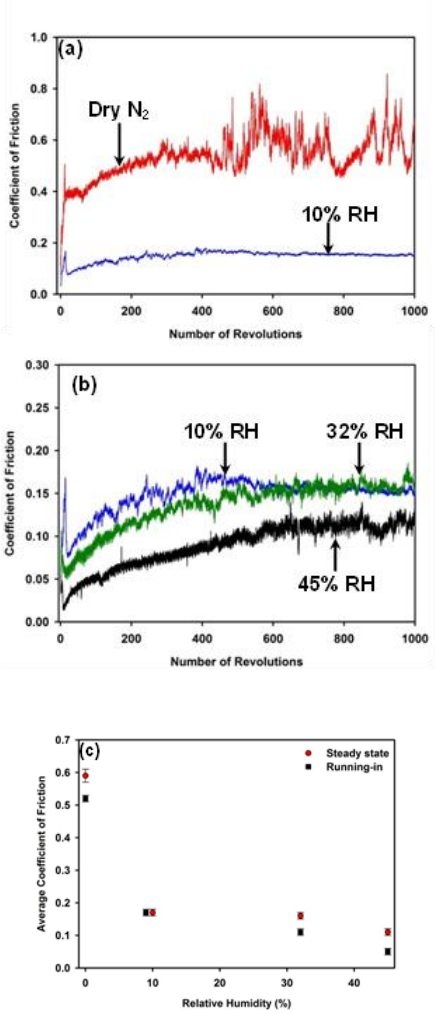

Figure 7.2—Variation of the coefficient of friction (COF) with the number of revolutions when the graphene was tested against the Ti-6Al-4V ball at (a) dry N_2 and ambient air with 10% RH (b) 10%, 32% and 45% RH. The data obtained 10% RH are re-plotted in Figure 3 (b) for comparison. (c) Variation of peak running in (μ_r) and steady state COF (μ_s) with RH. Each point in the plot represents the average value of three tests performed at a particular RH. The error bars represent the variation about the mean COF values from the three tests.

7.3.3. Microscopic Observations of Wear Tracks

The wear tracks formed on the graphene surfaces were examined using SEM. A back scattered electron image (BSEI) of the sliding track shown in Figure 7.3a, obtained after 10^3

revolutions, indicated that material transfer occurred from Ti-6Al-4V counterface to the graphene and Ni substrate surface when tests were conducted in a dry N_2 atmosphere. No graphene plates could be observed on the wear track in Figure 7.3a, which shows a section covered completely by the adhered material transferred from the counterface. Quantitative metallography was used to determine the amount of material transferred to the wear track under each test condition. The graphene wear tracks were examined using FEI Quanta 200 FEG scanning electron microscope (SEM, operated at 10 kV). The areal distribution of titanium transferred to the sliding track formed on the graphene surface was determined using an energy dispersive spectroscopy (EDS, with SiLi detector) technique that served to differentiate between the areas covered by the transferred titanium and the rest the wear track [26]. The percentage of wear track surface covered by the transferred titanium was determined using an image analysis program (Image J image processing program, NIH) by examining three separate sliding tracks obtained under each test condition (dry, 10% RH, 32 %RH and 45% RH as described in Section 2). Four different locations from each sliding wear track were analysed. The average values representing the area of graphene wear track covered by titanium are thus the results of 12 measurements. It was found that 86% of the total contact area was covered with the transferred Ti-6Al-4V. The width of the wear track (105 ± 2.11 μm) when the tests were conducted in air with 10% RH (Figure 7.3b) was smaller compared to those conducted in dry N_2 atmosphere for which the width of wear track in sections covered by adhered material was 1006 ± 2.53 μm. Only 12% of the sample surface was covered by a thin layer of adhered Ti-6Al-4V while in other areas graphene flakes could be detected on the wear track with the top surfaces exhibiting longitudinal scratches, as shown in Figure 7.3b. The material transfer from the counterface was drastically reduced to less than 1% when the tests were conducted in an atmosphere with 32% RH, with the

graphene flakes subjected to sliding wear damage clearly be visible on the wear track (Figure 7.3c). The amount of Ti-6Al-4V transfer to the graphene surface was less than 0.5% for the test performed at highest humidity of 45% RH (Figure 7.3d). The width of wear track at 32% RH and 45 % RH was comparable with the latter wear track exhibiting graphene with longitudinal scratches extending in the direction of sliding similar to sliding wear damage at 32% RH.

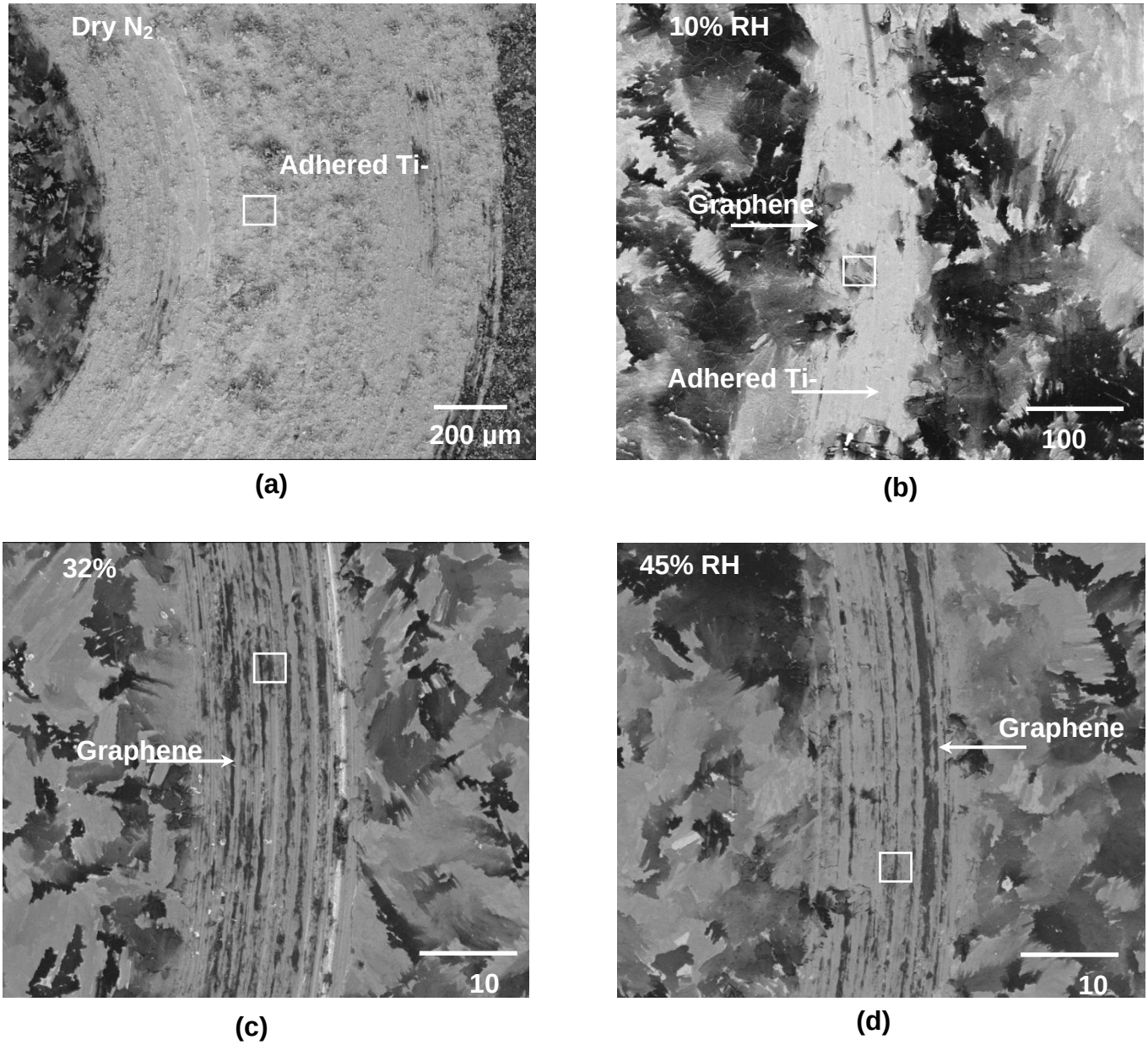

Figure 7.3—Secondary electron images of typical sections of graphene wear tracks when graphene was tested against Ti-6Al-4V at (a) dry N_2, (b) 10% RH, (c) 32% RH, and (d) 45% RH. Extensive transfer and adhesion of Ti-6Al-4V occurred within the wear track when the sliding tests were conducted in dry N_2. Graphene flakes were still evident within the wear track after the sliding tests at 10%, 32% and 45% RH. The white boxes in each figure indicate the specific locations from which Raman spectra (Figure 7a) were obtained.

7.3.4. Characterization of Transfer Layers

Ti-6Al-4V counterface contact surfaces were examined by SEM for wear damage and also for possible occurrence of transfer layers. When the COF was high the counterface was subjected to wear damage in a dry N_2 atmosphere. As shown in Figure 7.4a tests in dry N_2 atmosphere produced a wear scar of diameter of 1.1 mm and exhibited scuffing marks extending along the sliding direction. There was no evidence for material transfer from the graphene surface. The EDS maps in Figs. 7.4 (b, d) indicate that the lighter gray area that covered most part of worn Ti contact surface consisted of Ni transferred from the Ni substrate while it was in sliding contact with the Ti-6Al-4V ball. Carbon map is given as a reference but no carbon was detected by EDS as the graphene surface was covered by Ti from the counterface as previously shown in Figure 7.3a. The wear in a dry atmosphere was too severe for graphene to play a role in reducing friction and adhesion between Ni and Ti. In contrast, for the tests conducted at 45% RH resulted in the formation of carbonaceous transfer layers from the graphene at the contact surface of the Ti-6Al-4V (Figure 7.4e). The elemental EDS map for C is shown in Figure 7.4f. The EDS maps of the Ti and Ni are also provided in Figures 7.4 (g, h) that indicate metallic contact and adhesive transfer between Ti and Ni was virtually eliminated by the graphene. The contact surface area was smaller (and had a roughly elliptical shape of 100 µm by 400 µm) compared to tests in dry N_2.

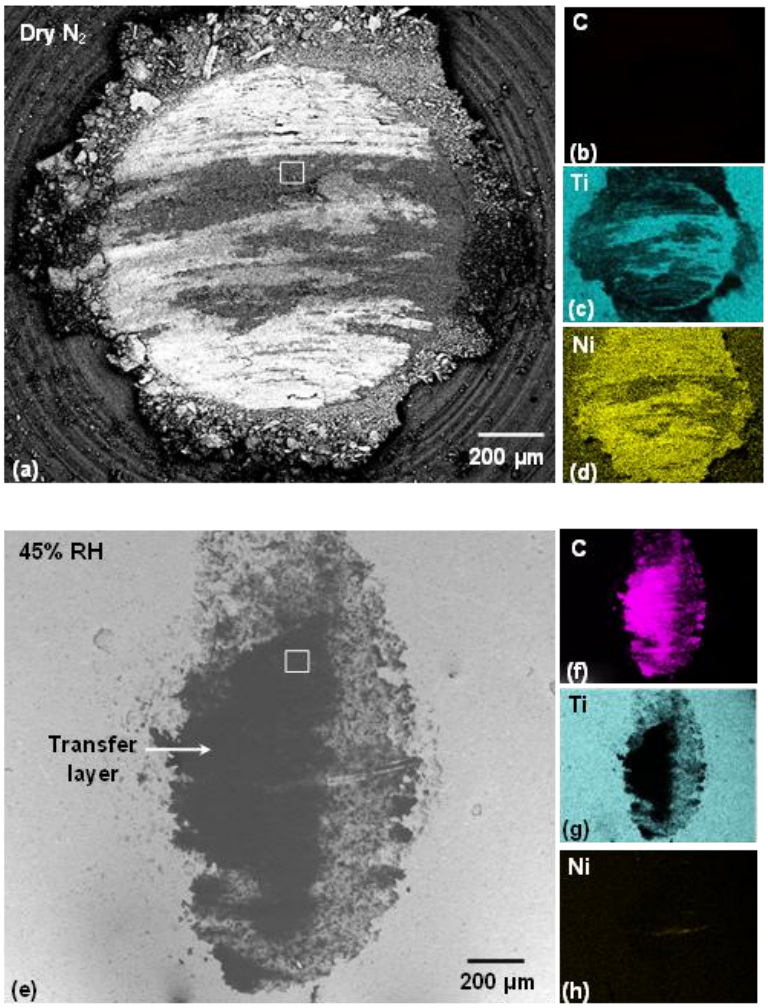

Figure 7.4—(a) Secondary electron image of Ti-6Al-4V ball contact surface taken after sliding against graphene in a dry N_2 atmosphere. The elemental EDS maps taken from the whole area shown in (a) are for (b) C, (c) Ti and (d) Ni. (e) Secondary electron image of ball contact surface after the sliding against graphene at 45% RH. The elemental EDS maps taken from the area shown in (e) are for (f) C, (g) Ti and (h) Ni. The white boxes in each SEM figure indicate the specific locations from which Raman spectra (Figure 7b) were obtained.

A cross-sectional FIB image (Figure 7.5a) of the transfer layer generated on the Ti-6Al-4V counterface during sliding tests performed in a 45% RH atmosphere revealed that the layer was 940±40 nm. The low magnification cross-sectional TEM image of the transfer layer shown in Figure 7.5b exhibits a rather featureless morphology incorporating a network of stringer type

linear structures of length. High resolution TEM (HR-TEM) images (Figure 7.5c-f) identified these structures as layers of monoatomic graphene stacked on top of each other and embedded in an amorphous carbon matrix. The thickness of the graphene layers in each stack varied between 2-6 nm and thus comprised 4-21 individual monatomic graphene layers. The d-spacing values of the graphene layers varied between 0.34 - 0.38 nm, which changed with the number of graphene layers in each stack. Figure 7.5d shows two regions one with 4 stacking layers and the other with 5 stacking layers with graphene layer d-spacing = 0.38 nm, while a region with 21 stacking layers (Figure 7.5e) showed a smaller d-spacing = 0.35 nm as determined from Fast Fourier Transform (FFT) derived diffraction patterns. Figure 7.5f shows an HR-TEM image of the interface between the graphene transfer layers (with d=0.36 in a stack of 20 layers) and the α-Ti from the Ti-6Al-4V pin surface. The interface was free of porosity and continuous and did not reveal mixing between the elements at each side of the interface. It is important to note here that the d-spacing values of the graphene nano-layers detected in the transfer layers were larger than that of pristine graphite with d (002) = 0.33 nm [27]. The increase in the interlayer spacing may be attributed to adsorption of passivating molecules.

XPS analyses of the graphene transfer layers that were formed on Ti-6Al-4V at 45% RH are presented in Figure 7.6. The O 1s spectra show peaks appearing at 532.78 eV, 531.61 eV, and 529.74 eV which may be attributed to H_2O, OH and oxide (TiO_2) respectively as shown in Figure 7.6 (a) [28–30].The C 1s peaks appearing at binding energies of 284.80, 286.30, and 288.80 eV (Figure 7.6b) may be assigned to the –C-C/-C-H, -C-OH/-C-O-C and –O-C=O respectively [28, 30]. These results suggest that the surface carbon atoms in the graphene transfer layers were terminated by O, H and OH.

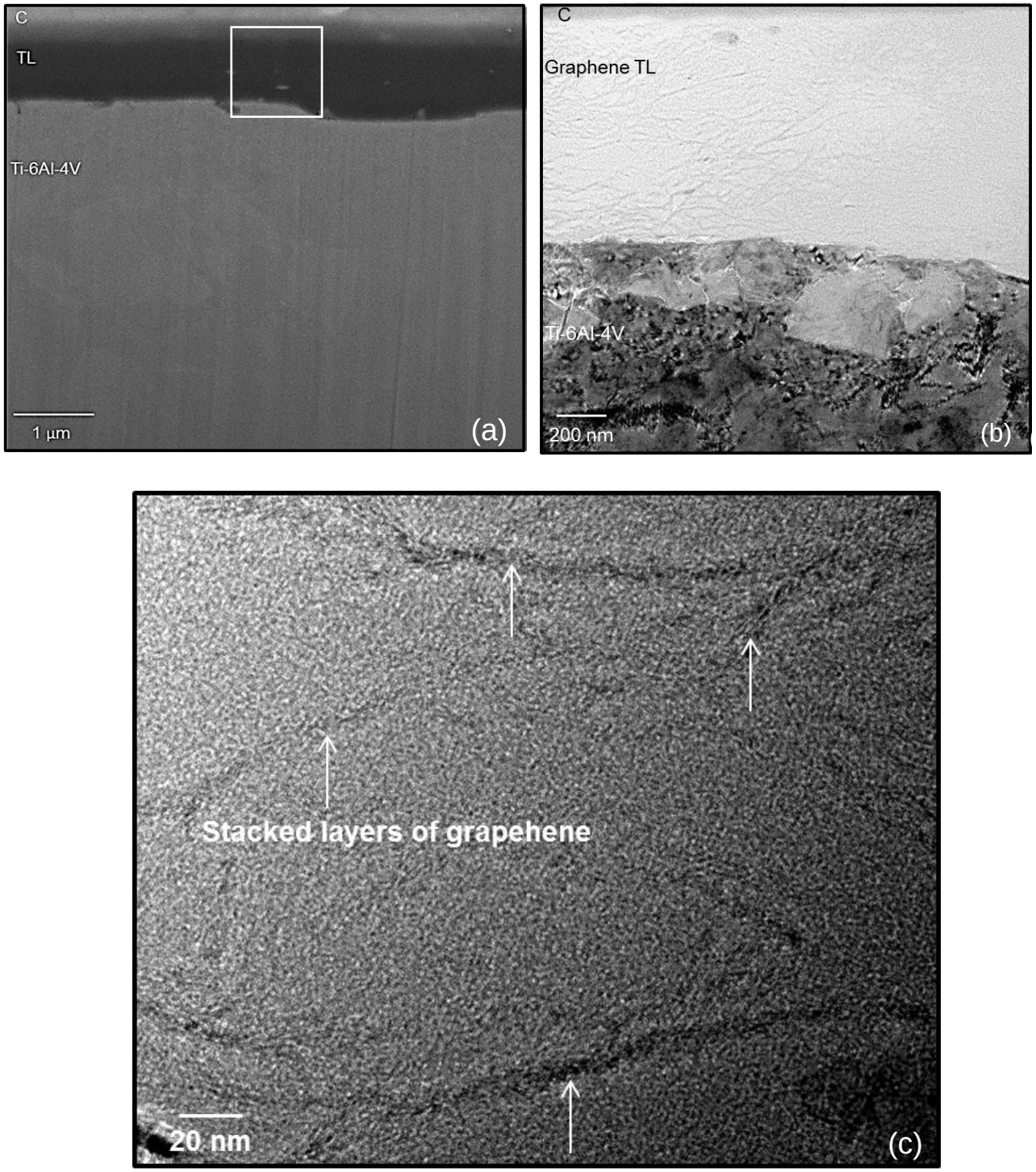
C
TL
Ti-6Al-4V
1 µm
(a)
C
Graphene TL
Ti-6Al-4V
200 nm
(b)
Stacked layers of grapehene
20 nm
(c)

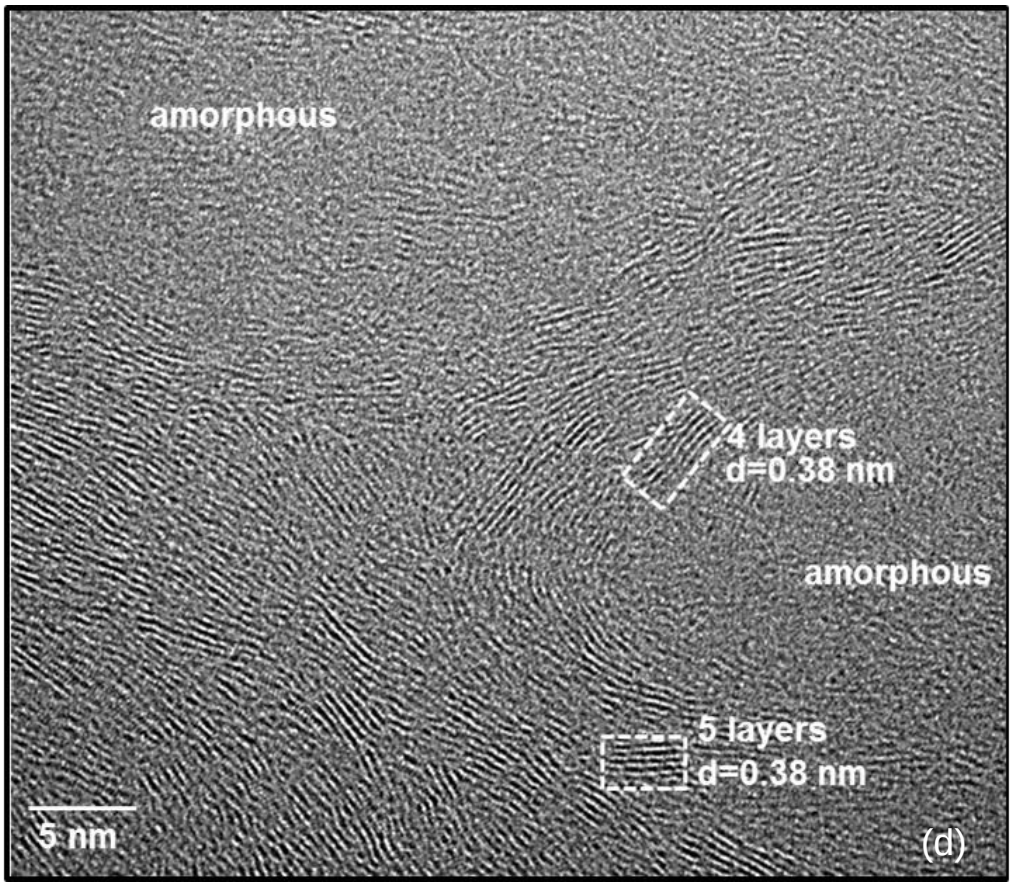
amorphous
4 layers
d=0.38 nm
amorphous
5 layers
d=0.38 nm
5 nm
(d)

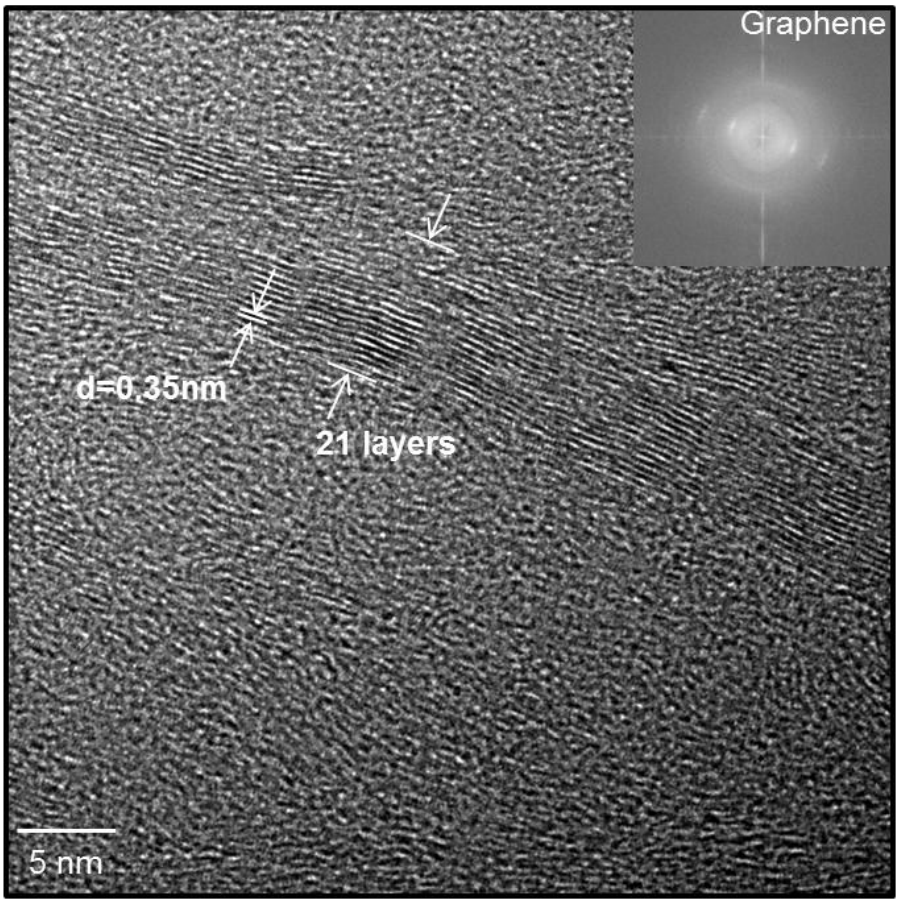

(e)

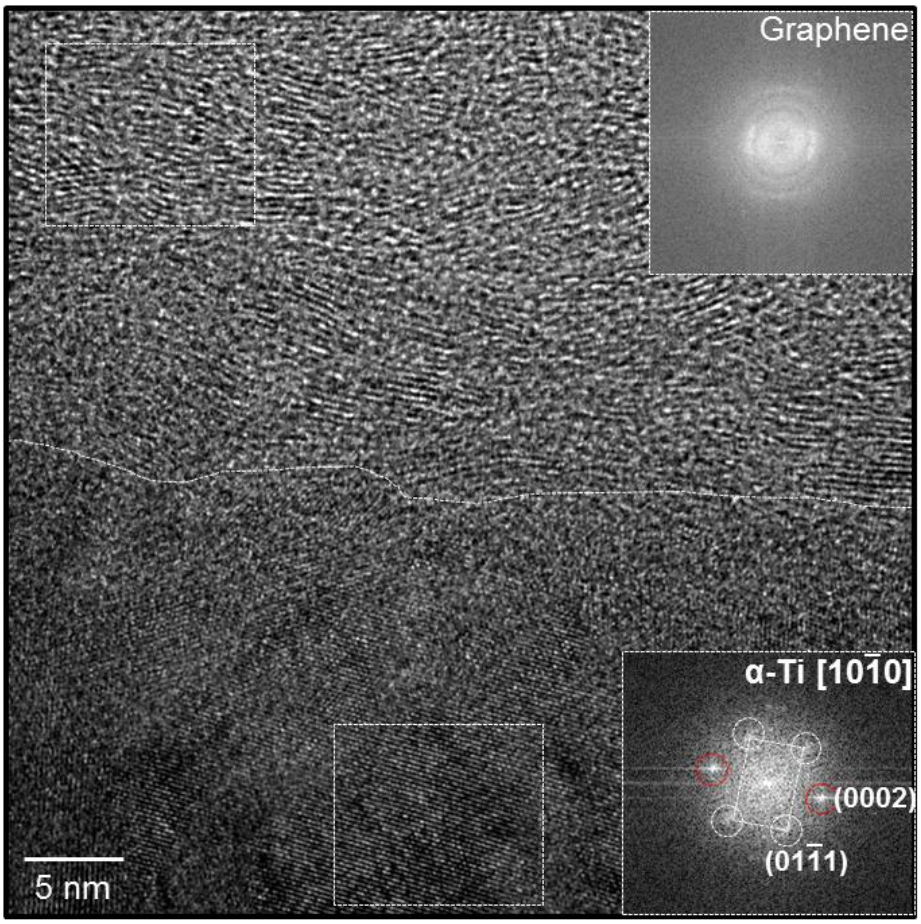

(f)

Figure 7.5—a) Cross-sectional FIB image of the transfer layer (TL) on Ti-6Al-4V contact surface for a test performed in 45% RH atmosphere, obtained using a Ga^+ ion source sputtered at 30 kV and a beam current of 80 pA. (b) Cross-sectional TEM image of the transfer layer, acquired from the region indicated as (b) in (a), showing a network of graphene stringers. (c), High magnification image of graphene stacks forming the stringers extending in an amorphous C matrix. (d) High resolution TEM (HR-TEM) image of graphene layers consisting of 4-5 stacks with d spacings of 0.38 nm within an amorphous matrix. (e) HR-TEM image showing graphene layers consisting of 21 stacks with d spacing of 0.34 nm within an amorphous matrix. (f) HR-TEM image of the interface between transferred graphene layer and top surface of the Ti-6Al-4V counterface. The images in the inset shows the Fast Fourier Transform (FFT) derived diffraction patterns indicating graphene in transfer layer and α-Ti counterface.

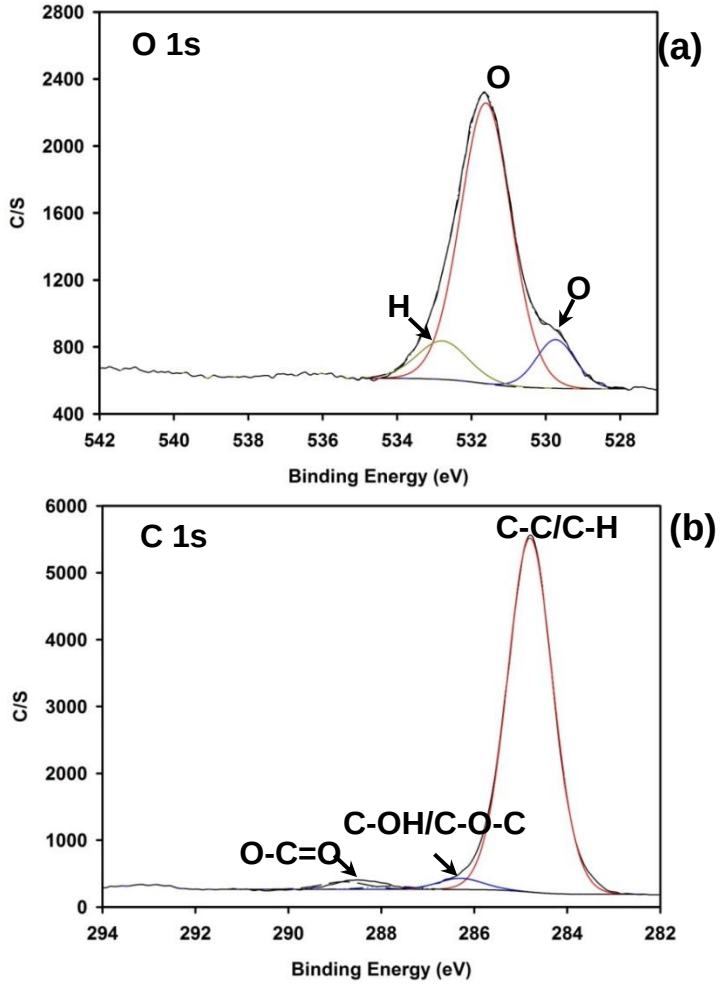

Figure 7.6—X-ray photoelectron spectroscope (XPS) spectra of transfer layers that formed on Ti-6Al-4V ball surface during sliding against graphene in ambient air with 45% RH for (a) O 1s and, (b) C 1s. High-resolution scan of Ti (not shown in the manuscript) $2p_{1/2}$ and $2p_{3/2}$ shows binding energy values of 463.98 eV and 458.26 eV, which when considered together with O 1s value of 529.74 eV corresponds to TiO_2 [29].

7.3.5. Micro-Raman Analyses of Graphene in Transfer Layer and Wear Tracks

For sliding tests performed in humid atmospheres (10%-45% RH), the micro-Raman spectra (Figure 7.7a) of the transfer layers formed on the Ti-6Al-4V surfaces showed a G band at 1580 cm^{-1} (appearing as a split peak) and weak 2D band at 2705 cm^{-1} similar to that observed for unworn graphene (Figure 7.1). Additionally, a distinct D-band appearing at 1342 cm^{-1} (Figure 7.7a) along with small intensity peaks at 2920 cm^{-1} labelled as D+G and at 3250 cm^{-1} labelled as 2D' bands were also observed for tests performed in humid atmosphere. The intensity of D band increased when the RH increased in the test chamber. To confirm the nature of the D, D+G and 2D' bands, micro-Raman analyses were conducted on the wear track of graphene surfaces for each test performed at different RH (Figure 7.7b). The Raman spectra of the worn graphene surfaces also showed a distinct D band, the intensity of which increased on increasing the RH. The important trend of increasing D band intensity of the graphene surfaces with increasing RH is thus observed both in transfer layer and in the worn coating. On the other hand, micro-Raman spectra obtained from the transfer layers and the worn coating for graphene tested in dry N_2 environment showed a featureless plot which was consistent with the lack of C transfer to the Ti-6Al-4V and absence of graphene on the wear track.

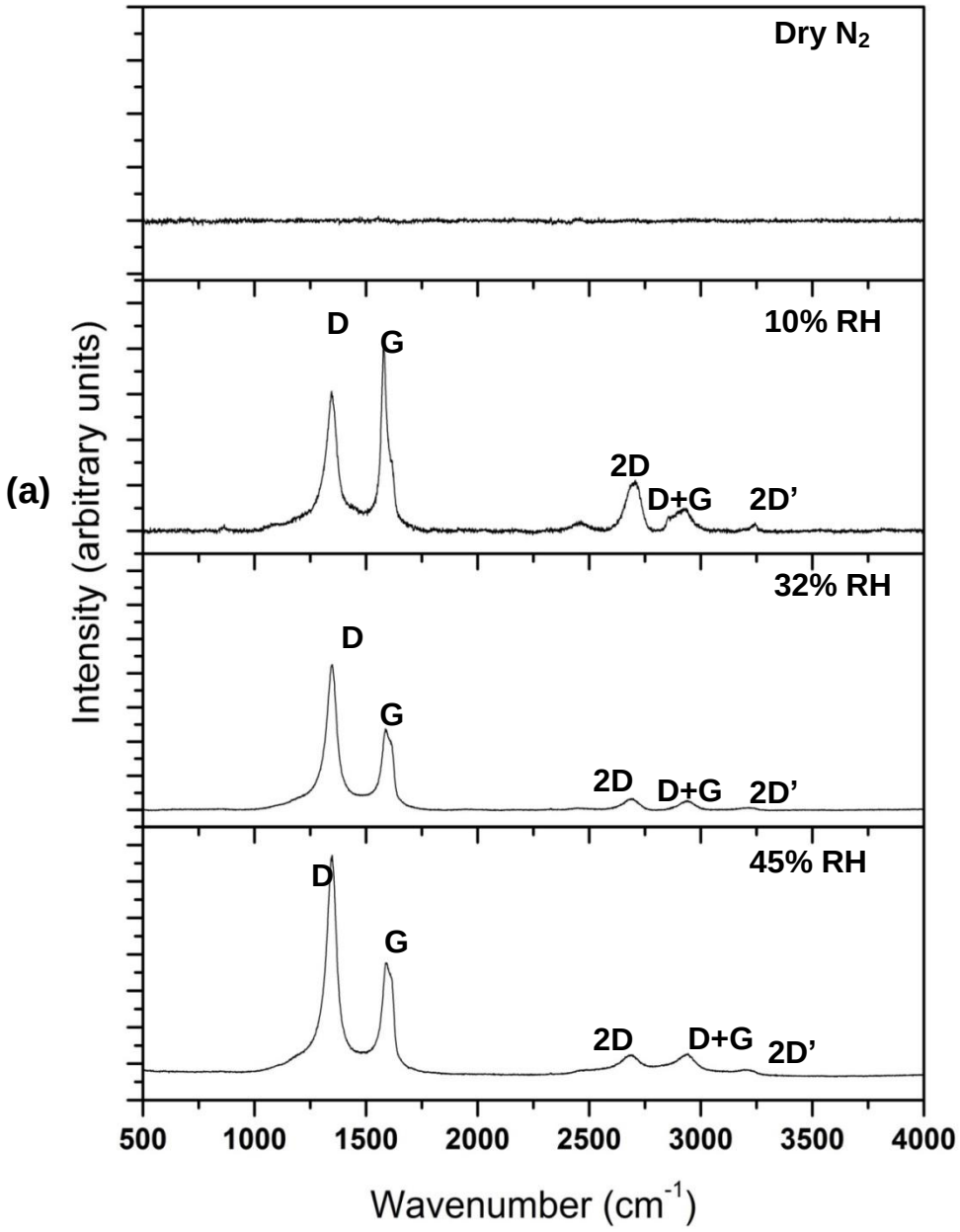
(a)
Dry N_2
10% RH
32% RH
45% RH
D
G
2D
D+G
2D'
Intensity (arbitrary units)
500
1000
1500
2000
2500
3000
3500
4000
Wavenumber (cm^{-1})

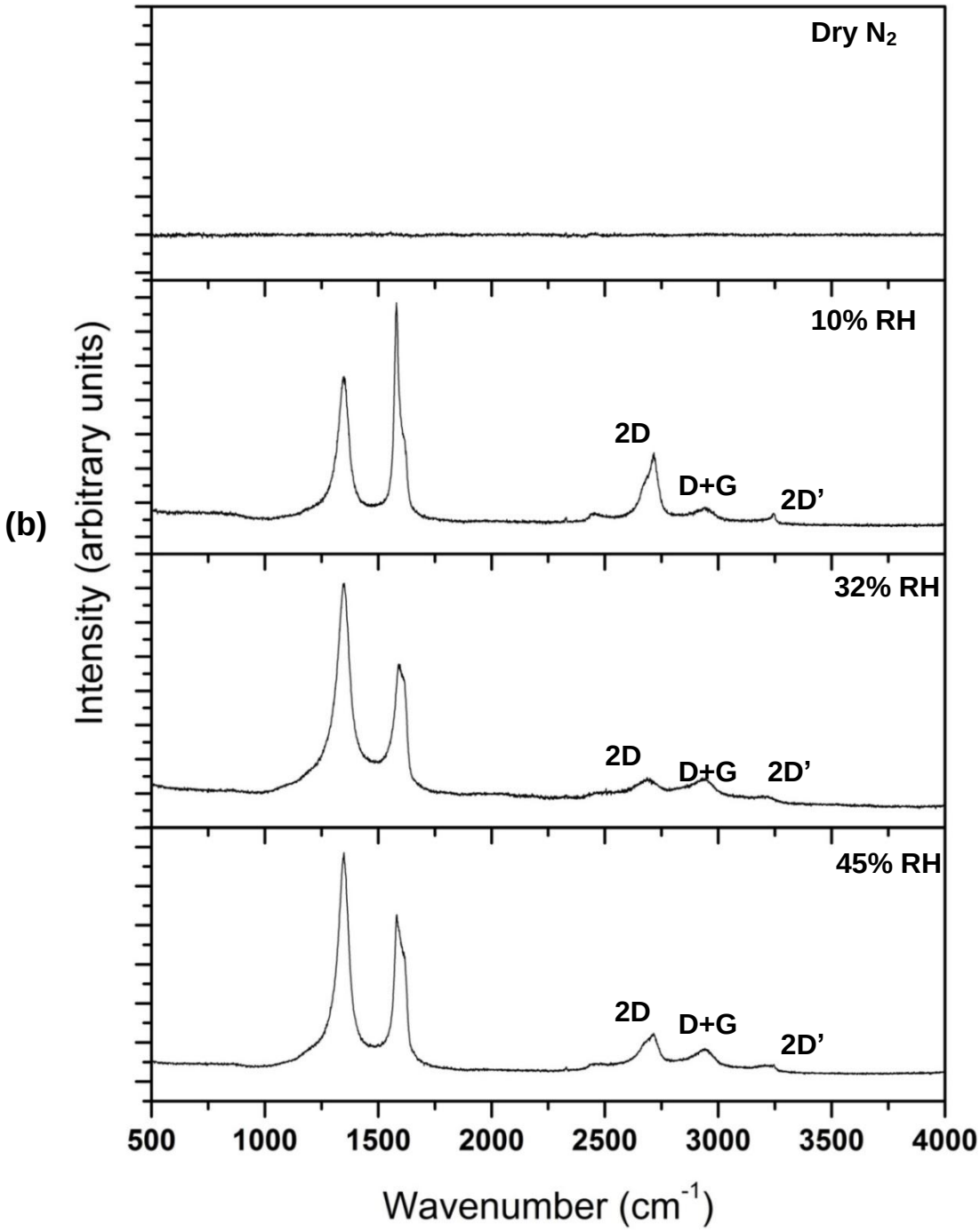

Figure 7.7—(a) Micro-Raman spectra of the transfer layer formed on counterface sliding against graphene at dry N_2, 10% RH, 32% RH and 45% RH conditions. (b) Micro-Raman spectra of the graphene wear track after the sliding tests at dry N2, 10% RH, 32% RH and 45% RH conditions. (Compare the wear track spectra generated at 45% RH with Figure 7.1, of unworn graphene surface before the sliding test).

The salient point of the results presented in Section 3 was that graphene showed high COF in N_2 atmosphere (0% RH) but when humidity is introduced in testing atmosphere graphene's COF was reduced and both μ_R and μ_s decreased slightly with an increase in atmospheric humidity.

Raman spectroscopy may be used to examine the disorder of C-network as interpreted from appearances of defect activated D, split G, D+G and the 2D' bands [24,25,31–34]. The hydrogenation of pristine graphene [32, 33] led to sp^3 C-H bond formation causing defects as a result of a breakdown of translational symmetry of the sp^2 C network and appeared as D, D' (split G) and D+G bands in the Raman spectra of hydrogenated graphene [32].When tests were done at humid atmospheres, the micro-Raman spectra of graphene wear tracks showed a prominent D-band (1350 cm^{-1}) and split G-band (1580-1600 cm^{-1}), along with D+G (2920 cm^{-1}) and 2D' (3250 cm^{-1}) bands (Figure 7.7b). The corresponding spectra of the transfer layer were exactly the same (Figure 7.7a). It may be suggested that sliding induced defects were introduced as a result of sp^2 to sp^3 transformation possibly leading to amorphization of graphene. The defects in graphene C-network can be thus attributed to C-H and C-OH bond formations (Figure 7.6) that occurred during sliding in contrast to the low defect C-network of the unworn graphene surface (Figure 7.1).

The chemisorption of H and OH molecules, derived from the moisture in humid air, on the C atoms during sliding could be cited as possible reason for the transformation of sp^2 (C=C bonds) to sp^3 (C-C) hybridization. The chemisorption of H and OH atoms and the resulting structural changes in the C atom hybridization from sp^2 to sp^3 are schematically represented in Figure 7.8. The D-band recorded in the micro-Raman of graphene in both the transfer layer and

the wear tracks for tests at 10%, 32% and 45% RH showed increasing intensity with increasing RH (Figure 7.7). Consequently an increase in the density of sp^3 C atoms, which may coalesce and form clusters [33], can be suggested as a possible reason for an increase in the structural disorder generated during sliding causing amorphization (Figures 7.5d-f). It may also be inferred that the adsorption of H and OH in the graphene layers imposed repulsive interactions possibly resulting in the increase in the lattice spacing (Figure 7.5) and led to detachment of graphene layers facilitating transfer to the counterface.

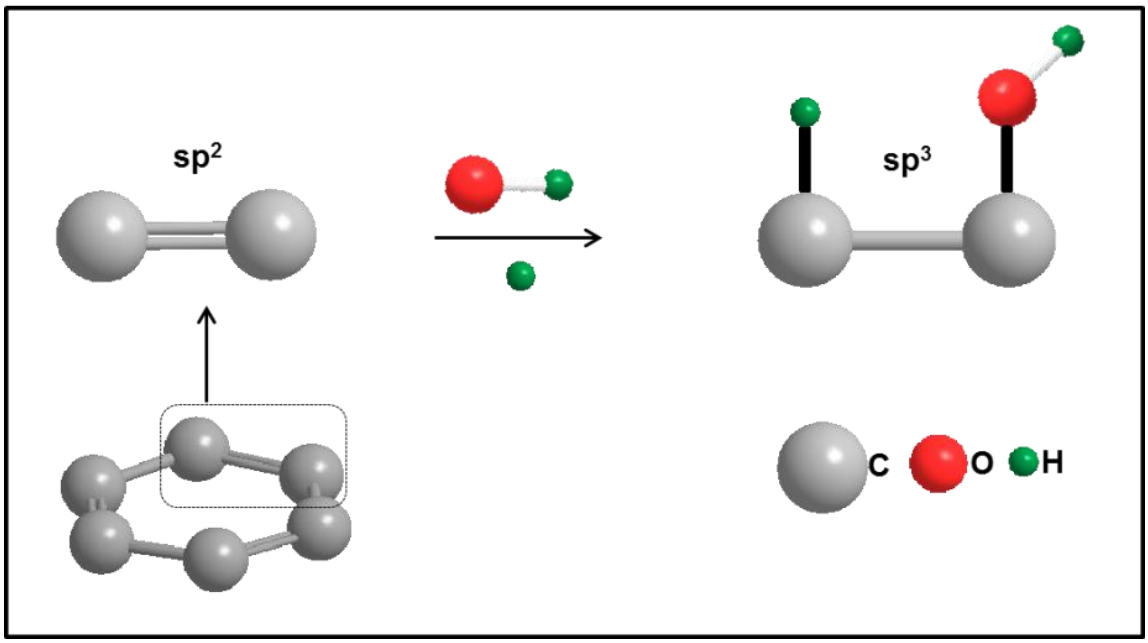

Figure 7.8—Schematic representation of adsorption of OH and H molecules dissociated from moisture, by the sp^2 C=C atoms of graphene and formation of sp^3 C-C atoms.

Although the exact mechanisms of graphene damage and transfer are yet to be understood, the sequence of events is clear: the increase of the initial COF (μ_R) during the running in period may be taken as an indication of sliding induced damage to graphene. Molecular dynamics simulations [35,36] revealed that unsaturated carbon atoms on the counterface and in the film undergo a bond-breaking and bond-forming process that governs the run-in friction. AFM

studies of epitaxial graphene on SiC [16, 17] showed that the graphene layer can be damaged during reciprocating wear and suggested that a carbon interlayer could reduce friction. In this study we find that the value of μ_R reaches a peak (Figure 7.2), which possibly coincides with the material transfer to the counterface. The formation of sp^3 C atoms and ensuing amorphization is followed by a subsequent decrease in COF to a minimum where friction occurs between two carbon surfaces. The role of H and OH adsorption on the carbon surfaces becomes critical at this stage as passivation of H and OH on the carbon surfaces is known to reduce COF [21, 22].

First principle calculations showed [37] that under moisture laden tribological test conditions the water molecules can dissociate to form H and OH which subsequently gets adsorbed to the carbon surfaces. On the other hand the N_2 molecule does not dissociate and hence no adsorption is expected for tests performed in dry N_2 atmosphere causing high COF. Graphene tested in dry N_2 atmosphere showed high friction which is consistent with the mechanism predicted from first principle studies [37]. At 45% RH, where the lowest μ_R and μ_S is observed, it can be argued that with an increase in the moisture a larger number of C-H and C-OH bond formation would occur on both sides of the interface, i.e, on the surfaces of worn graphene and the transfer layers. Repulsive interactions between H-H, H-OH and OH-OH groups would reduce the COF and as long as the passivated transfer layers persisted, a low steady state COF, μ_S, will be maintained.

It is useful to present a brief comparison of friction reduction mechanisms of DLC and graphene under humid environments. DLC coatings containing about 40% H (H-DLC) showed very low COF values (0.004-0.02) in vacuum and when tested under dry (RH< 0.1%) gas atmospheres due to H terminated surface carbon atoms [38–40]. Under the same conditions NH-DLC coatings consistently displayed high friction (0.5-0.8) accompanied by adhesion of

counterface materials [41]. When tested under ambient conditions (30-50% RH) [19, 20], and in aqueous solutions [22], NH-DLC coatings however exhibited low COF values (0.1-0.2). The friction reduction mechanisms consisted of formation of amorphous carbonaceous transfer layers on the counterface and passivation of the unsaturated C atoms on both sliding interfaces by H and OH [21, 35-38], that were dissociated from water molecules in the surrounding atmosphere. The current work revealed generation of carbonaceous transfer layers on the counterface sliding against graphene in a way similar to the DLC coatings. However, these layers were not completely amorphous but incorporated stacks of conjugated graphene layers (as shown in Figure 5) with interlayer spacing larger than that of the pristine graphite, as discussed earlier in this section. The observations suggested that several layers of graphene were subjected to OH passivation. This friction reduction mechanism was peculiar to multilayered graphene as in DLC coatings the passivation was restricted to the top surface.

In summary, this paper shows that H and OH molecules can passivate graphene under high RH conditions leading to low friction when tested against Ti-6Al-4V. This opens up prospects of achieving low friction for lubricated tests performed on graphene when submerged in OH enriched lubricants. Furthermore, the technological implications of the current results may extrapolated to more severe engineering applications like machining where water or OH based lubricants might be used on graphene coated tool materials.

Conclusions

Tribological tests exploring the role of humidity on friction behaviour of a multilayered graphene sliding against Ti-6Al-4V were performed. Tests conducted at dry N_2 atmosphere resulted in a high and unsteady coefficient of friction of 0.52, which was reduced to low steady state value of 0.11 when the same tests were conducted in a humid atmosphere with 10% RH. Both the average running-in and the steady state coefficient of friction further decreased with an increase in relative humidity. Micro-Raman of the worn graphene showed generation of defect induced peaks D, split G, D+G and 2D' bands which suggested an increased disorder in the carbon network as a result of sp^2 to sp^3 transformation and amorphization during sliding. Transferred material on the counterface had an amorphous C matrix that incorporated stringers of graphene stacks with increased d-spacing due to the repulsion between the adsorbed molecules incorporated between the graphene layers. The friction reducing mechanisms comprised of establishment of transfer layers on counterface and passivation of surfaces by H and OH, as revealed by XPS, adsorbed by the C atoms at each sides of sliding interface.

Bibliography

[1] C. Donnet, A. Erdemir, Historical developments and new trends in tribological and solid lubricant coatings, Surf. Coatings Technol. 180–181 (2004) 76–84. doi:10.1016/j.surfcoat.2003.10.022.

[2] C. Donnet, a Erdemir, Solid Lubricant Coatings: Recent Developments and Future Trends, Tribol. Lett. 17 (2004) 389–397. doi:10.1023/B:TRIL.0000044487.32514.1d.

[3] H.E. Sliney, t h e compounds such as molybdenum disulfide (, (1982) 55–81.

[4] J. Spreadborough, The frictional behaviour of graphite, Wear. 5 (1962) 18–30.

[5] J. Robertson, Diamond-like amorphous carbon, Mater. Sci. Eng. R Reports. 37 (2002) 129–281.

[6] S. Bhowmick, F.G. Sen, A. Banerji, A.T. Alpas, Friction and adhesion of fluorine

containing hydrophobic hydrogenated diamond-like carbon (FH-DLC) coating against magnesium alloy AZ91, Surf. Coatings Technol. 267 (2015) 21–31.
[7] D. Berman, S.A. Deshmukh, S.K.R.S. Sankaranarayanan, A. Erdemir, A. V Sumant, Extraordinary macroscale wear resistance of one atom thick graphene layer, Adv. Funct. Mater. 24 (2014) 6640–6646.
[8] K.-S. Kim, H.-J. Lee, C. Lee, S.-K. Lee, H. Jang, J.-H. Ahn, J.-H. Kim, H.-J. Lee, Chemical vapor deposition-grown graphene: the thinnest solid lubricant, ACS Nano. 5 (2011) 5107–5114.
[9] D. Berman, A. Erdemir, A. V Sumant, Few layer graphene to reduce wear and friction on sliding steel surfaces, Carbon N. Y. 54 (2013) 454–459.
[10] D. Berman, A. Erdemir, A. V Sumant, Reduced wear and friction enabled by graphene layers on sliding steel surfaces in dry nitrogen, Carbon N. Y. 59 (2013) 167–175.
[11] P. Egberts, G.H. Han, X.Z. Liu, A.T.C. Johnson, R.W. Carpick, Frictional behavior of atomically thin sheets: hexagonal-shaped graphene islands grown on copper by chemical vapor deposition, ACS Nano. 8 (2014) 5010–5021.
[12] H. Lee, N. Lee, Y. Seo, J. Eom, S. Lee, Comparison of frictional forces on graphene and graphite, Nanotechnology. 20 (2009) 325701.
[13] T. Filleter, J.L. McChesney, A. Bostwick, E. Rotenberg, K. V Emtsev, T. Seyller, K. Horn, R. Bennewitz, Friction and dissipation in epitaxial graphene films, Phys. Rev. Lett. 102 (2009) 86102.
[14] C. Lee, Q. Li, W. Kalb, X.-Z. Liu, H. Berger, R.W. Carpick, J. Hone, Frictional Characteristics of Atomically Thin Sheets, Science (80-.). 328 (2010) 76–80. doi:10.1126/science.1184167.
[15] C. Yan, K.-S. Kim, S.-K. Lee, S.-H. Bae, B.H. Hong, J.-H. Kim, H.-J. Lee, J.-H. Ahn, Mechanical and environmental stability of polymer thin-film-coated graphene, ACS Nano. 6 (2011) 2096–2103.
[16] F. Wählisch, J. Hoth, C. Held, T. Seyller, R. Bennewitz, Friction and atomic-layer-scale wear of graphitic lubricants on SiC (0001) in dry sliding, Wear. 300 (2013) 78–81.
[17] D. Marchetto, C. Held, F. Hausen, F. Wählisch, M. Dienwiebel, R. Bennewitz, Friction and wear on single-layer epitaxial graphene in multi-asperity contacts, Tribol. Lett. 48 (2012) 77–82.
[18] B.K. Yen, B.E. Schwickert, M.F. Toney, Origin of low-friction behavior in graphite investigated by surface x-ray diffraction, Appl. Phys. Lett. 84 (2004) 4702–4704.
[19] E. Konca, Y.-T. Cheng, A.T. Alpas, Dry sliding behaviour of non-hydrogenated DLC coatings against Al, Cu and Ti in ambient air and argon, Diam. Relat. Mater. 15 (2006) 939–943.
[20] E. Konca, Y.-T. Cheng, A.M. Weiner, J.M. Dasch, A.T. Alpas, Effect of test atmosphere on the tribological behaviour of the non-hydrogenated diamond-like carbon coatings against 319 aluminum alloy and tungsten carbide, Surf. Coatings Technol. 200 (2005) 1783–1791.
[21] S. Bhowmick, A. Banerji, A.T. Alpas, Tribological behavior and machining performance of non-hydrogenated diamond-like carbon coating tested against Ti–6Al–4V: Effect of surface passivation by ethanol, Surf. Coatings Technol. 260 (2014) 290–302.
[22] A.A. Gharam, M.J. Lukitsch, Y. Qi, A.T. Alpas, Role of oxygen and humidity on the tribo-chemical behaviour of non-hydrogenated diamond-like carbon coatings, Wear. 271 (2011) 2157–2163.

[23] M. Chen, T. Perry, A.T. Alpas, Ultra-mild wear in eutectic Al–Si alloys, Wear. 263 (2007) 552–561.
[24] A.C. Ferrari, J.C. Meyer, V. Scardaci, C. Casiraghi, M. Lazzeri, F. Mauri, S. Piscanec, D. Jiang, K.S. Novoselov, S. Roth, Raman spectrum of graphene and graphene layers, Phys. Rev. Lett. 97 (2006) 187401.
[25] L.M. Malard, M.A.A. Pimenta, G. Dresselhaus, M.S. Dresselhaus, Raman spectroscopy in graphene, Phys. Rep. 473 (2009) 51–87.
[26] A. Banerji, S. Bhowmick, A.T. Alpas, High temperature tribological behavior of W containing diamond-like carbon (DLC) coating against titanium alloys, Surf. Coatings Technol. 241 (2014) 93–104.
[27] C.-H. Park, F. Giustino, M.L. Cohen, S.G. Louie, Electron− Phonon Interactions in Graphene, Bilayer Graphene, and Graphite, Nano Lett. 8 (2008) 4229–4233.
[28] A. Banerji, A. Edrisy, V. Francis, A.T. Alpas, Effect of bio-fuel (E85) addition on lubricated sliding wear mechanisms of a eutectic Al–Si alloy, Wear. 311 (2014) 1–13.
[29] X. Wang, Q. Xiang, B. Liu, L. Wang, T. Luo, D. Chen, G. Shen, TiO2 modified FeS nanostructures with enhanced electrochemical performance for lithium-ion batteries, Sci. Rep. 3 (2013) 2007.
[30] C.C. Chusuei, D.W. Goodman, M.J. Van Stipdonk, D.R. Justes, E.A. Schweikert, Calcium phosphate phase identification using XPS and time-of-flight cluster SIMS, Anal. Chem. 71 (1999) 149–153.
[31] L.G. Cançado, A. Jorio, E.H.M. Ferreira, F. Stavale, C.A. Achete, R.B. Capaz, M.V.O. Moutinho, A. Lombardo, T.S. Kulmala, A.C. Ferrari, Quantifying defects in graphene via Raman spectroscopy at different excitation energies, Nano Lett. 11 (2011) 3190–3196.
[32] B.R. Matis, J.S. Burgess, F.A. Bulat, A.L. Friedman, B.H. Houston, J.W. Baldwin, Surface doping and band gap tunability in hydrogenated graphene, ACS Nano. 6 (2012) 17–22.
[33] Z. Luo, T. Yu, Z. Ni, S. Lim, H. Hu, J. Shang, L. Liu, Z. Shen, J. Lin, Electronic structures and structural evolution of hydrogenated graphene probed by Raman spectroscopy, J. Phys. Chem. C. 115 (2011) 1422–1427.
[34] Z. Sun, Z. Yan, J. Yao, E. Beitler, Y. Zhu, J.M. Tour, Growth of graphene from solid carbon sources, Nature. 468 (2010) 549–552.
[35] G.T. Gao, P.T. Mikulski, J.A. Harrison, Molecular-scale tribology of amorphous carbon coatings: effects of film thickness, adhesion, and long-range interactions, J. Am. Chem. Soc. 124 (2002) 7202–7209.
[36] L. Pastewka, S. Moser, M. Moseler, Atomistic insights into the running-in, lubrication, and failure of hydrogenated diamond-like carbon coatings, Tribol. Lett. 39 (2010) 49–61.
[37] Y. Qi, E. Konca, A.T. Alpas, Atmospheric effects on the adhesion and friction between non-hydrogenated diamond-like carbon (DLC) coating and aluminum–A first principles investigation, Surf. Sci. 600 (2006) 2955–2965.
[38] H.I. Kim, J.R. Lince, O.L. Eryilmaz, A. Erdemir, Environmental effects on the friction of hydrogenated DLC films, Tribol. Lett. 21 (2006) 51–56.
[39] A.R. Konicek, D.S. Grierson, P. Gilbert, W.G. Sawyer, A. V Sumant, R.W. Carpick, Origin of ultralow friction and wear in ultrananocrystalline diamond, Phys. Rev. Lett. 100 (2008) 235502.
[40] C. Donnet, J. Fontaine, T. Le Mogne, M. Belin, C. Héau, J.P. Terrat, F. Vaux, G. Pont, Diamond-like carbon-based functionally gradient coatings for space tribology, Surf.

Coatings Technol. 120 (1999) 548–554.
[41] E. Konca, Y.-T. Cheng, A.M. Weiner, J.M. Dasch, A.T. Alpas, Vacuum tribological behavior of the non-hydrogenated diamond-like carbon coatings against aluminum: effect of running-in in ambient air, Wear. 259 (2005) 795–799.

CHAPTER 8

Friction Behaviour of Multilayered Graphene against Steel

8.1. Introduction

Graphene is a two dimensional monolayer of carbon atoms that serve as building blocks of graphite [1]. The nano and micro-scale friction behaviour of graphene is of interest and is currently being studied [2–4]. Lee et al. [2] demonstrated using friction force microscopy (FFM) experiments (25-50% RH) on mechanically exfoliated graphene that friction values of more than four layers of graphene was as low as that of bulk graphite while a monolayer graphene plane showed higher friction. Friction behaviour of graphene also depends on other factors such as graphene-substrate adhesion, as well as on environmental conditions. Kim et al. [3] found that the COF of CVD grown graphene was affected by the substrate as the graphene grown on Ni showed a low COF of 0.10 compared to graphene grown on Cu (COF = 0.20) under a normal load of 70 mN (33% RH). Berman et al. [4] reported a COF of 0.18 for ethanol processed graphene used as lubricant for steel vs. steel sliding in a dry N_2 atmosphere. Bhowmick et al. [5] reported the role of humidity in determining the friction behaviour of multilayered graphene by performing macro scale experiments in air with different relative humidity (RH) levels (10–45% RH) against a Ti alloy counterface. It was shown that progressively lower friction values were observed when the RH of the atmosphere was increased, with the lowest COF of 0.11 reached at 45% RH which was attributed to the chemisorption of H and OH molecules in the graphene stacks [5].

Diamond-like carbon (DLC) coatings can improve the performance of the machining tools and dies by reducing the coefficient of friction (COF); minimizing adhesion to workpieces made of steel, aluminum, magnesium and titanium alloys [6–13]. However, the tribological properties

of DLC coatings are highly dependent on their composition and working environment. The tribological behaviour of the hydrogenated (H-DLC) and non-hydrogenated DLC (NH-DLC) coatings were found to differ under vacuum and inert (i.e. N_2 or Ar) atmospheres. Erdemir [14] tested H-DLC and NH-DLC coatings in dry N_2 atmosphere against H-DLC coated H13 steel disks and observed that the H-DLC generated very low COF of 0.005, while the NH-DLC produced a high COF of 0.75. The very low COF value in case of H-DLC was attributed to the C-H σ-bond termination of the surface carbon atoms. Konca et al. [15] observed a high COF of 0.52 while testing an Al-6.5% Si alloy against NH-DLC, under vacuum condition. The same NH-DLC when tested in an ambient atmosphere produced a low COF of 0.16, which was attributed to passivation of dangling carbon bonds by hydrogen (H) and hydroxyl (OH) groups due to dissociation of moisture. In a vacuum environment the dangling σ carbon bonds at the NH-DLC contact surface interacted with the Al-6.5% Si pin counterface and promoted aluminum transfer to the coating wear track, leading to the high values of COF. The DLC coatings are thus known to be sensitive to changes in relative humidity (RH).

It becomes clear from the above review that moisture in the test environment reduces friction of carbon based materials. In this work, we describe the differences in the friction characteristics of graphene and DLC coatings tested against a common tool steel (M2) counterface. Results of microscopic and spectroscopic investigations are presented to highlight the differences in the running-in and steady state friction mechanisms.

8.2. Materials and Experiments

The graphene used for sliding experiments was deposited on Ni foil substrates using a chemical vapour deposition (CVD) process with methane gas as the source of carbon. Micro-Raman spectroscopy of the as deposited graphene was carried out using a 50 mW Nd–YAG laser

(532 nm excitation line) through the 50× objective lens of a Horiba Raman micro-spectrometer showed a characteristic G (1580 cm^{-1}) and 2D (2705 cm^{-1}) peaks with peak intensity ratio (I_G/I_{2D}) > 1 suggesting a multilayered structure. The absence of D-band (1330 cm^{-1}) was indicative of very low defect density of graphene. The NH-DLC coatings were deposited using an unbalanced magnetron sputtering system. A 0.10 µm thick Cr interlayer was deposited to promote adhesion of the coating to the M2 steel surface followed by the deposition of 1.50 µm thick NH-DLC coating on top. The hydrogen content of the NH-DLC coating measured using elastic recoil detection (ERD) of < 2.00 at.%. The hardness and the elastic modulus of NH-DLC were 13.0 GPa and 158.55 GPa. The Raman spectra of the as deposited NH-DLC coating had a broad peak between 1250 and 1530 cm^{-1} indicating an amorphous carbon structure.

A pin-on-disk tribometer was used to measure the COF values of multilayered graphene and NH-DLC against 15 mm long M2 steel pins with one end in the shape of a of 4.05 mm diameter hemisphere. Unlubricated tests were conducted using a speed of 0.05 m/s and a normal load of 2.00 N for 1000 revolutions. All friction tests were conducted under ambient conditions at constant relative humidity (RH) levels of 52%, 25% and 10% RH. During the sliding experiments the highest magnitude of COF reached during the running-in stage (μ_R) and the duration of the running-in friction regime (t_R) were noted while the COF of the steady state friction (μ_S) regime was determined from the average COF values of the plateau that followed the running-in period, typically after 500 revolutions.

The M2 steel pin counterface contact surfaces were investigated using scanning electron microscopic (SEM) and a EDS was used to determine the areal distribution of carbon transferred to the counterface from the graphene and DLC surface during the sliding tests. The transfer layer generated on the M2 steel surface during sliding against graphene tested at 52% RH was further

investigated by transmission electron microscopy (TEM). The sample for TEM investigations were prepared using a focused ion beam (FIB) lift out technique and by milling them at 30 kV in a Carl Zeiss NVision 40 dual beam work station. The details of FIB and TEM techniques can be found in [16,17]. Micro-Raman spectroscopy studies were performed on the sliding contact surfaces to differentiate the pristine carbon structure from the sliding induced changes in the coating surface and the transfer layer structures.

8.3. Results

Typical COF curves of graphene where the variations in friction are plotted against the number of revolutions are shown in Fig. 8.1. Accordingly, testing the graphene under an ambient air atmosphere with 10% RH produced a high μ_R of 0.51. Following the running-in period, the COF decreased to a μ_S of 0.11 ± 0.02 for a sliding period of 400 cycles in this test and this was maintained for 1000 cycles - until the end of the test. Sliding tests conducted at 25% RH recorded a μ_R of 0.45 that lasted for 140 revolutions followed by a μ_s of 0.09 ± 0.01. The μ_R decreased to 0.34 under 52% RH and the μ_s was also low at 0.08. The NH-DLC showed a μ_R of 0.42 when the tests were conducted under a RH of 10%. The friction continued to increase following a brief drop without reaching a steady state. The COF at the end of the test was 0.47. The μ_R decreased to 0.40 when the RH of the environmental chamber increased to 25% and a steady state of 0.33 was observed after 600 revolutions. A μ_R = 0.32 was recorded at 52% RH and a μ_s of 0.25 at 52% RH, indicating the beneficial effects of humidity in decreasing the COF.

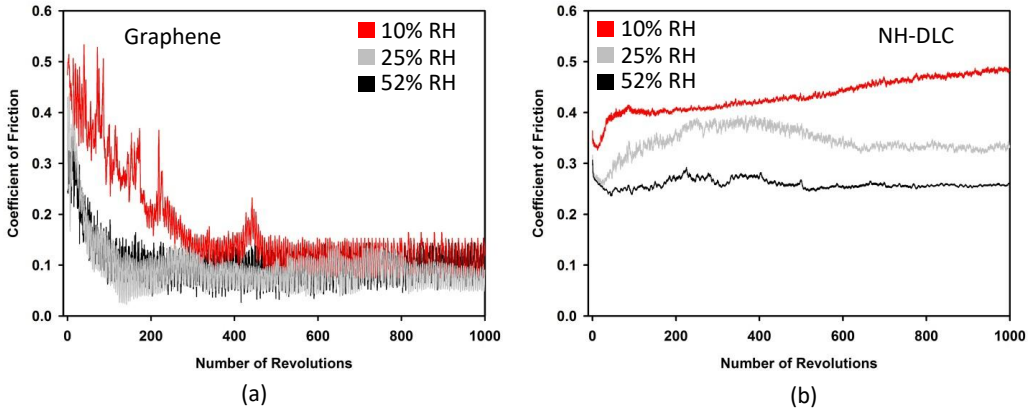

Figure 8.1: Variation of the coefficient of friction (COF) with the number of revolutions when (a) multilayered graphene (b) NH-DLC were tested against the M2 steel counterface in ambient air with 10%, 25% and 52% RH.

A general trend emerged such that the COF of graphene and that of the NH-DLC depended on the moisture content as it was observed that the μ_R and μ_S values decreased with an increase in the RH. A plot of μ_R and μ_S values obtained from the tests at different RH values is shown in Figs. 8.2 (a-b). Fig. 8.2c shows the changes in the duration of the running-in period, t_R, with RH% in the test atmosphere. The μ_R values of graphene and NH-DLC were almost similar at all RH whereas the t_R values of graphene were shorter compared to that of NH-DLC indicating earlier transition to steady state friction for graphene compared to NH-DLC. The μ_s values of graphene were lower by about 75% compared to those of NH-DLC for all tests. It is to be noted that the trend observed in Fig. 2, namely the reduction in μ_R, t_R and μ_S values for graphene with an increase in the RH is independent of the counterface as similar trends were observed for tests of graphene against Ti-6Al-4V counterface when tested at different RH values [5]. The μ_R, t_R

and μ_S values, however, depend on the composition of the counterface and whether the counterface was oxidized during sliding.

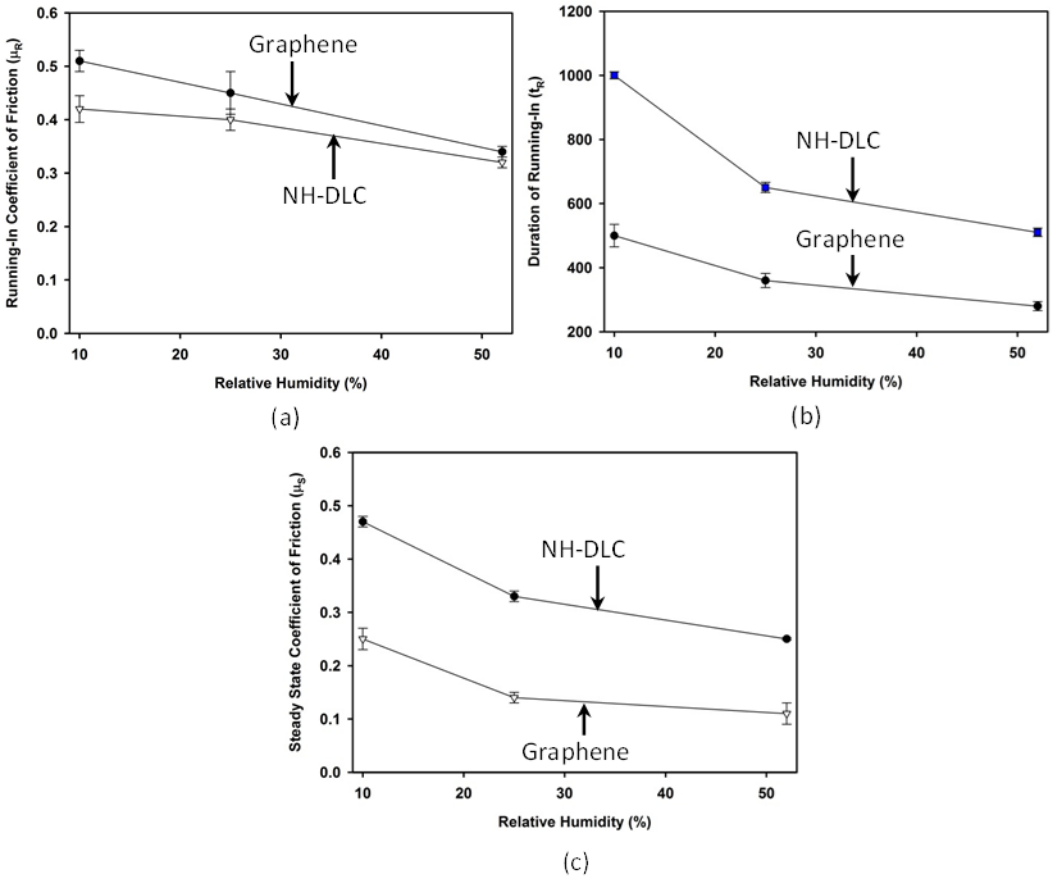

Figure 8.2: Variations of (a) peak running in (μ_R); (b) duration of running-in COF (t_R) and (c) steady state COF (μ_s) with RH (no steady state COF was reached for NH-DLC at 10% RH)

The M2 steel counterface contact surfaces tested against graphene at 52% RH revealed a wear scar with diameter of about 90 µm as indicated in the SEI image in Fig. 8.3 (a). EDS mapping of the contact surface revealed that carbon and oxygen rich layers were formed (Fig. 8.3 b, c) with low concentrations of Fe Fig. 8.3d. The SEM and EDS analyses of the counterface contact surfaces tested against NH-DLC at 52% RH also showed presence of a carbon-rich transfer in addition to the Fe and O [Figs. 8.4 (a-d)]. The wear on M2 steel was wider (120 µm). This initial data indicates that graphene could reduce the wear of M2 steel more effectively compared to the NH-DLC. More studies are needed to develop wear maps of graphene at different loads, speeds and environment.

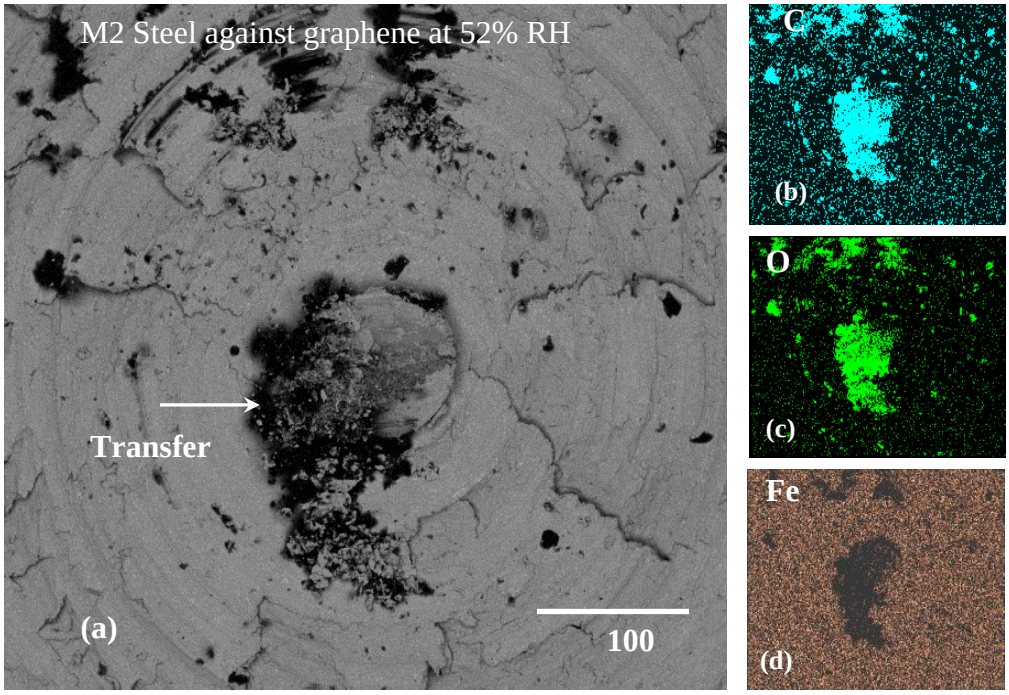

Figure 8.3: (a) Secondary electron image of the M2 steel pin surface taken after sliding against graphene at 25% RH. The elemental EDS maps taken from the whole area shown in (a) are for (b) C, (c) O and (d) Fe.

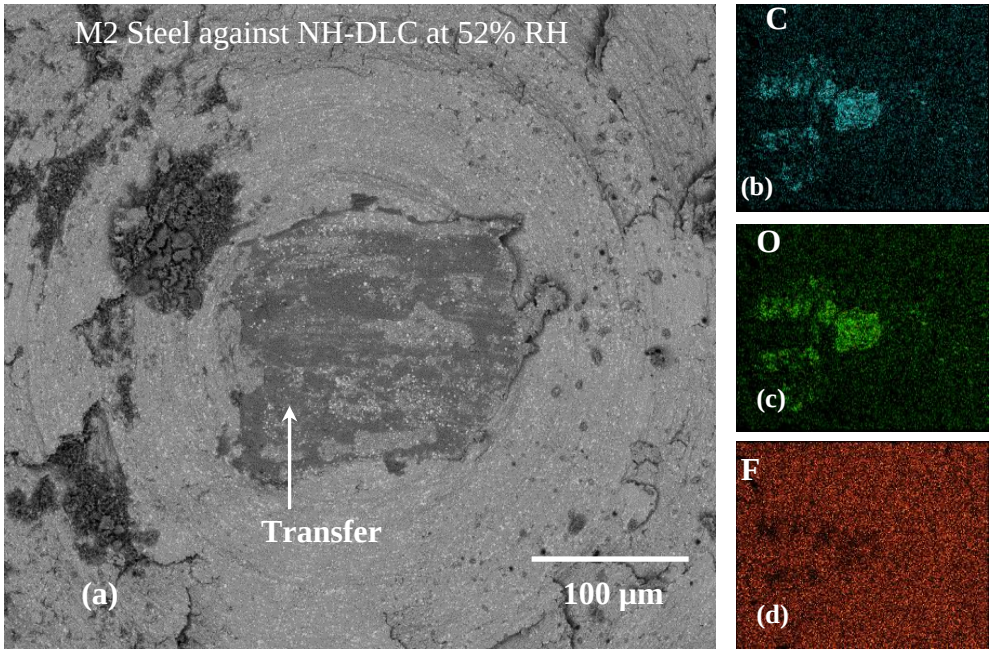

Figure 8.4: (a) Secondary electron image of the M2 steel pin surface taken after sliding against NH-DLC at 25% RH. The elemental EDS maps taken from the whole area shown in (a) are for (b) C, (c) O and (d) Fe.

8.4. Discussion

The results presented in the previous sections showed that μ_R, t_R and μ_S for multilayered graphene tested against a ferrous counterface decreased with an increase in atmospheric humidity and the effect of humidity on graphene's friction properties was more pronounced than those of NH-DLC. This section focuses on the friction reduction mechanisms of graphene by considering the tribo-chemical and structural changes that occur at the contact interface.

The low friction behaviour of graphene and NH-DLC coatings is associated with the formation of carbon containing transfer layers on the counterfaces [5,15]. In this study, the transfer layers were observed on counterfaces running against both graphene and NH-DLC (Figs. 8.3 and 8.4). Once the carbon transfer layers are formed on the steel counterfaces, the steady state friction regime commences and a low μ_S was maintained until the end of the test. A detailed study of the graphene transfer layer, using cross-sectional TEM microscopy revealed that the transfer layer comprised of stacked graphene layers surrounded by amorphous regions. The d-spacing between the stacked layers of graphene were measured as d = 0.35-0.36 nm, using fast Fourier transform (FFT) indexing, and found to be larger than the d spacing of pristine graphite d = 0.33 nm. Thus graphene undergoes a sliding contact induced structural transformation. In contrast, the DLC transfer layer would form an amorphous carbon structure mixed with nanoscale debris particles (from counterface) as inclusions.

Some aspects of sliding-induced structural transformation were demonstrated using micro-Raman spectra of the transfer layers formed on the steel counterface from graphene (and NH-DLC) tested in ambient air with 10% RH, 25% RH and 52% RH. The micro-Raman spectra of the graphene transfer layer formed during tests in ambient air with 52% RH (Fig. 8.5a) showed a sharp D-band appearing at 1342 cm^{-1} along with a small intensity (D + G) band at 2920 cm^{-1}

which were not present in pristine graphene. Other distinct peak shifts included a reduction in intensity of the 2D-band (2705 cm^{-1}) and a split G-band (1580–1600 cm^{-1}). These sliding-induced Raman D, split G, D + G and 2D′ peaks for graphene first appeared for tests performed in 10% RH. The appearance of these bands maybe attributed to the transformation of graphene sp^2 bonded atoms to sp^3 bonded carbon atoms [18–20]. The detailed mechanisms of the defect generation in graphene are yet to be studied but it could be suggested that if defects are formed they would assist with dissociation of moisture [21]. Dissociated H and OH radicals would form bonds with the surface graphene layers as well as intercalations between the graphene stacks resulting in the increase in the d-spacing between them.

The decrease in μs with the increase in humidity by OH passivation of C atoms of the transfer layers is consistent with previous findings for amorphous DLC coatings [22–25]. A typical micro-Raman spectrum of the transfer layer generated on M2 steel tested against NH-DLC (Fig. 8.5b) tested at 52% RH showed broad peaks at 1363 (D) and 1586 cm^{-1} (G) typical of amorphous carbon with disordered graphitic rings [19,22,23]. This spectrum is different from that of Raman spectrum obtained from the as-deposited NH-DLC as it shows an increase in the intensity of the D-band indicating disorder generated in the carbon network during sliding. The structural transformation observed in NH-DLC was due to the sp^2 ring cluster formations, as a result of sliding, as evident from the sharp D-band [19]. In NH-DLC only the surface dangling carbon atoms could form bonds with H and OH groups dissociated from moisture.

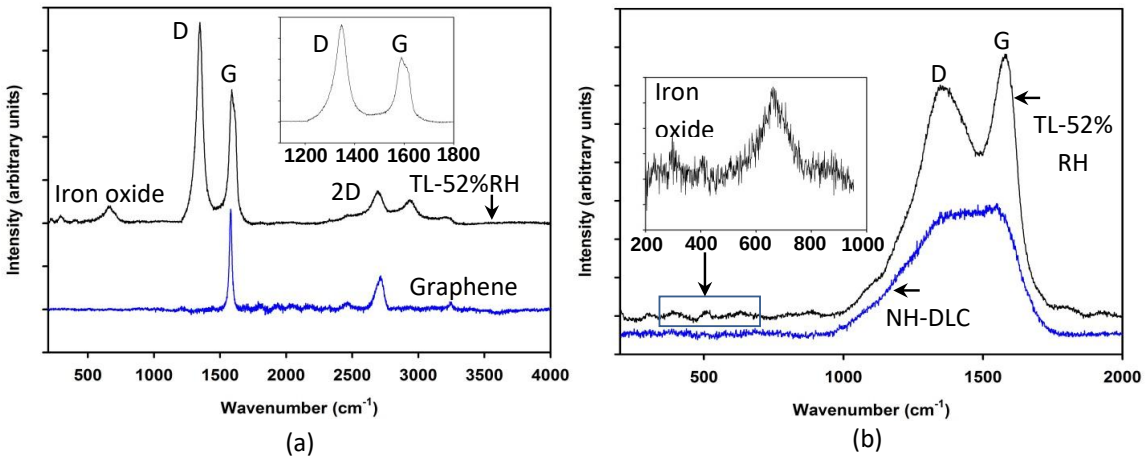

Figure 8.5: a) Micro-Raman spectra of the transfer layer formed on M2 counterface sliding against graphene in air with 52% RH. Micro-Raman of unworn graphene surface before the sliding test was also provided for the comparisons. An enlarged view of the D and G peaks is shown in inset; (b) Micro-Raman spectra of the transfer layer formed on counterface sliding against NH-DLC in air with 52% RH. Micro-Raman of unworn NH-DLC was also provided for the comparisons. The Raman spectrum of iron oxide is showing in inset.

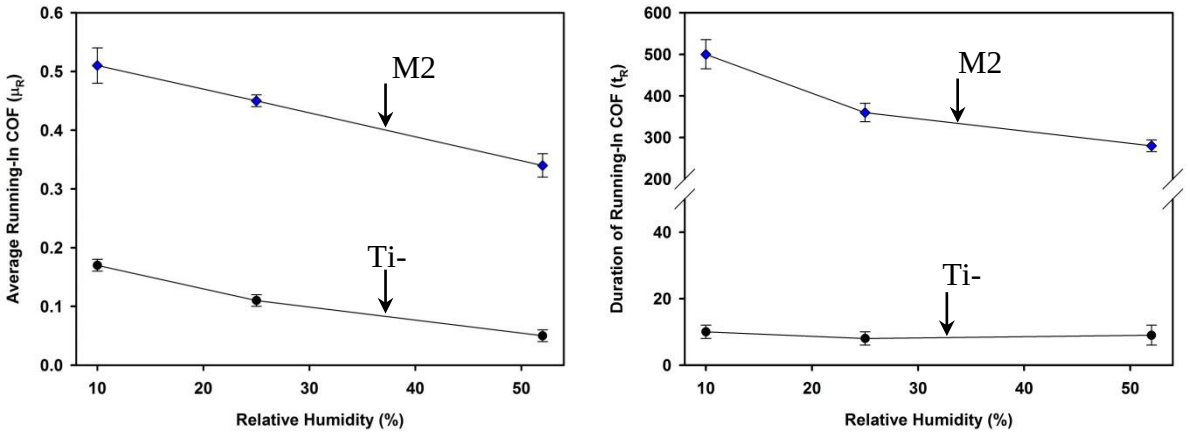

(a) (b)

Figure 8.6: Comparisons of (a) maximum running-in COF (b) average duration of running-in COF of M2 steel and Ti-6Al-4V against graphene at different humidity levels.

It is instructive to compare the running-in friction behavior of graphene against steel and Ti-6Al-4V [5]. Fig. 8.6 a,b shows that the graphene tested against M2 steel has a higher μ_R (and t_R) compared to tests made against Ti-6Al-4V [5]. The high μ_R and longer t_R values of graphene tested against steel might rationalized considering the iron oxides present on the steel surface that needs to be depleted before the graphene transfer layer forms and the friction stabilizes. The Raman peaks in Fig. 8.5a, b appearing below 700 cm^{-1} may be attributed to the characteristic peaks of iron oxide (haematite) incorporated in the transfer layer during sliding. In case of graphene sliding against inert Ti-6Al-4V surfaces, the graphene becomes transferred more readily showing low μ_R and short t_R. In both cases, however, increase in the atmospheric RH decreases the μ_R values. This mechanism needs to be further studied, but these results show that the friction behaviour of graphene depends on the counterface as well as on the test environment.

Conclusions

In this work, we have shown that coefficient of friction of graphene tested against a ferrous counterface in ambient air with was reduced with an increase in humidity. The transfer layer formed on the counterface had stacked layers with larger d-spacing compared to pristine graphene. It was proposed that sliding-induced defect formation facilitated the dissociation of moisture and the subsequent adsorption of H and OH groups caused structural transformations in graphene. The transfer layer formed from NH-DLC was amorphous and the structural changes due to sliding and moisture adsorption involved graphitic cluster formations. The overall lower steady state COF observed in graphene compared to DLC was attributed to the water intercalation in graphene as compared to surface passivation in case of NH-DLC.

Bibliography

[1] A.K. Geim, K.S. Novoselov, The rise of graphene, Nat. Mater. 6 (2007) 183–191. doi:10.1038/nmat1849.

[2] C. Lee, Q. Li, W. Kalb, X.-Z. Liu, H. Berger, R.W. Carpick, J. Hone, Frictional Characteristics of Atomically Thin Sheets, Science (80-.). 328 (2010) 76–80. doi:10.1126/science.1184167.

[3] K. Kim, H. Lee, C. Lee, S. Lee, H. Jang, J. Ahn, J. Kim, H. Lee, CVD – Grown Graphene : The Thinnest Solid Lubricant, Mater. Sci. (2011) 5107–5114. doi:10.1021/nn2011865.

[4] D. Berman, A. Erdemir, A. V. Sumant, Few layer graphene to reduce wear and friction on sliding steel surfaces, Carbon N. Y. 54 (2013) 454–459. doi:10.1016/j.carbon.2012.11.061.

[5] S. Bhowmick, A. Banerji, A.T. Alpas, Role of humidity in reducing sliding friction of multilayered graphene, Carbon N. Y. 87 (2015) 374–384.

[6] K. Bobzin, T. Brögelmann, K. Stahl, K. Michaelis, J. Mayer, M. Hinterstoißer, Friction reduction of highly-loaded rolling-sliding contacts by surface modifications under elasto-hydrodynamic lubrication, Wear. 328–329 (2015) 217–228. doi:10.1016/j.wear.2015.02.033.

[7] H. Ronkainen, S. Varjus, K. Holmberg, Friction and wear properties in dry, water- and oil-lubricated DLC against alumina and DLC against steel contacts, Wear. 222 (1998) 120–128. doi:10.1016/S0043-1648(98)00314-7.

[8] S. Bhowmick, A.T. Alpas, The performance of hydrogenated and non-hydrogenated diamond-like carbon tool coatings during the dry drilling of 319 Al, Int. J. Mach. Tools

Manuf. 48 (2008) 802–814. doi:10.1016/j.ijmachtools.2007.12.006.

[9] S. Bhowmick, A.T. Alpas, Minimum quantity lubrication drilling of aluminium-silicon alloys in water using diamond-like carbon coated drills, Int. J. Mach. Tools Manuf. 48 (2008) 1429–1443. doi:10.1016/j.ijmachtools.2008.04.010.

[10] S. Bhowmick, A.T. Alpas, The role of diamond-like carbon coated drills on minimum quantity lubrication drilling of magnesium alloys, Surf. Coatings Technol. 205 (2011) 5302–5311. doi:10.1016/j.surfcoat.2011.05.037.

[11] S. Bhowmick, A.T. Alpas, The Performance of Diamond-Like Carbon Coated Drills in Thermally Assisted Drilling of Ti-6Al-4V, J. Manuf. Sci. Eng. 135 (2013) 61019. doi:10.1115/1.4025739.

[12] S. Bhowmick, M.J. Lukitsch, A.T. Alpas, Tapping of Al-Si alloys with diamond-like carbon coated tools and minimum quantity lubrication, J. Mater. Process. Technol. 210 (2010) 2142–2153. doi:10.1016/j.jmatprotec.2010.07.032.

[13] Y. Liu, A. Erdemir, E.I. Meletis, A study of the wear mechanism of diamond-like carbon films 1, Surf. Coatings Technol. 82 (1996) 48–56. doi:10.1016/0257-8972(95)02623-1.

[14] A. Erdemir, The role of hydrogen in tribological properties of diamond-like carbon films, Surf. Coatings Technol. 146 (2001) 292–297.

[15] E. Konca, Y.-T. Cheng, A.M. Weiner, J.M. Dasch, A.T. Alpas, Vacuum tribological behavior of the non-hydrogenated diamond-like carbon coatings against aluminum: effect of running-in in ambient air, Wear. 259 (2005) 795–799.

[16] A. Banerji, S. Bhowmick, a. T. Alpas, High Temperature Tribological Behaviour of W Containing Diamond-Like Carbon (DLC) Coating against Titanium Alloys, Surf. Coatings Technol. 241 (2013) 93–104. doi:10.1016/j.surfcoat.2013.10.075.

[17] S. Bhowmick, A. Banerji, M.J. Lukitsch, A.T. Alpas, The high temperature tribological behavior of Si, O containing hydrogenated diamond-like carbon (aC: H/a-Si: O) coating against an aluminum alloy, Wear. 330 (2015) 261–271.

[18] C.-H. Park, F. Giustino, M.L. Cohen, S.G. Louie, Electron-Phonon Interactions in Graphene, Bilayer Graphene, and Graphite, (2008) 4–9. doi:10.1021/nl801884n.

[19] A.C. Ferrari, J.C. Meyer, V. Scardaci, C. Casiraghi, M. Lazzeri, F. Mauri, S. Piscanec, D. Jiang, K.S. Novoselov, S. Roth, A.K. Geim, Raman spectrum of graphene and graphene layers, Phys. Rev. Lett. 97 (2006) 1–4. doi:10.1103/PhysRevLett.97.187401.

[20] L.M. Malard, M.A. Pimenta, G. Dresselhaus, M.S. Dresselhaus, Raman spectroscopy in graphene, Phys. Rep. 473 (2009) 51–87. doi:10.1016/j.physrep.2009.02.003.

[21] P. Cabrera-Sanfelix, G.R. Darling, Dissociative adsorption of water at vacancy defects in graphite, J. Phys. Chem. C. 111 (2007) 18258–18263.

[22] S. Bhowmick, F.G. Sen, A. Banerji, A.T. Alpas, Friction and adhesion of fluorine containing hydrophobic hydrogenated diamond-like carbon (F-H-DLC) coating against magnesium alloy AZ91, Surf. Coatings Technol. 267 (2015) 21–31. doi:10.1016/j.surfcoat.2014.11.047.

[23] S. Bhowmick, A. Banerji, A.T. Alpas, Tribological behavior and machining performance of non-hydrogenated diamond-like carbon coating tested against Ti–6Al–4V: Effect of surface passivation by ethanol, Surf. Coatings Technol. 260 (2014) 290–302.

[24] A.R. Konicek, D.S. Grierson, A. V. Sumant, T.A. Friedmann, J.P. Sullivan, P.U.P.A. Gilbert, W.G. Sawyer, R.W. Carpick, Influence of surface passivation on the friction and wear behavior of ultrananocrystalline diamond and tetrahedral amorphous carbon thin films, Phys. Rev. B - Condens. Matter Mater. Phys. 85 (2012).

doi:10.1103/PhysRevB.85.155448.

[25] Y. Qi, E. Konca, A.T. Alpas, Atmospheric effects on the adhesion and friction between non-hydrogenated diamond-like carbon (DLC) coating and aluminum–A first principles investigation, Surf. Sci. 600 (2006) 2955–2965.

CHAPTER 9

General Summary and Conclusions

9.1 Summary and Impact of the Studies Undertaken

Only a small fraction of the fuel energy is expended in running the vehicle. The frictional losses in the components of an IC engine can consume as much as 20% of the available energy. In order to address the frictional losses in the tribological components of an automobile engine, it is important to have a clear understanding of the underpinning surface damage mechanisms at the microstructural level. The scope of the work undertaken in this dissertation was to identify the wear and surface damage mechanisms associated with lightweight internal combustion (IC) engines, with an emphasis on reduction of friction losses in order to increase engine efficiency. This work addresses the tribological design and performance improvement aspects of powertrain components made of lightweight alloys and coatings that are compatible with them. Both lightweight IC engines made of Al-Si alloys and those that are being developed with thermal spray coating bore surfaces were considered. The primary objective of this dissertation was optimization of cylinder/bore assembly surfaces and the reduction of frictional losses. Property sets of tribologically sustainable coatings (low COF, and wear resistant, and/or adhesion-mitigating) were examined. A common methodology adopted in this dissertation was to examine the micro-mechanisms of the friction behaviour of each material sets by seeking out the origin of tribolayers formed in each tribosystem. Interfacial microstructural properties, tribolayers, material transfer events, and compound formation processes were determined by using cross-sectional SEM/EDS, FIB-TEM, and XPS methods. Carefully designed tribological experiments were performed measuring the friction and wear as a function of the applied load, environment,

temperature and lubricant. The overall impact of the studies undertaken in this dissertation has been summarized below.

Tribological experiments aimed at determining interfacial mechanism that reduce the friction were performed on standard type A grey cast iron (CI) liners. The friction performance was evaluated using a suit of tribological tests at different environments to demonstrate the role of humidity. Sliding friction tests were performed against a novel piston ring coating non-hydrogenated DLC, which is known for providing minimum material adhesion. The role of boundary lubrication sliding in improving the tribological properties was studied using high-resolution TEM microscopy that showed the formation of an ORL on the cast iron contact surface, thicker than those formed on Al-Si but with similar compositions. The results suggested that NH-DLC (with <2 at.% H) would show 20% reduction in friction (and wear) when tested against CI in diluted oil compared to engine oil and thus reveals a potential low friction coating to replace the traditional role of nitride and molybdenum sprayed cast iron top compression rings. Cross-sectional TEM/EELS studies of the O-K 1s core loss peak acquired from the top of the surface of the NH-DLC coating showed a distinct peak and provided for the first time a direct evidence for OH termination of carbon bonds and hence surface passivation.

The elimination of cast iron cylinder liners in aluminum engine block bores has been identified as a critical strategy for engine mass reduction. Near eutectic Al-Si alloys derive their ultra-mild wear (UMW) resistance from the formation of stabilized surfaces consisting of the combined effects of oil-residue tribolayers, Si particle exposure and a zone of ultra-fine grain size Al grains that generated under the tribolayers. Thorough characterization of the ORL formed under boundary lubricated tests involving engine oil and engine oil diluted with E85 fuel indicated that ethanol played a significant role in facilitating degradation of engine oil additive

ZDDP. This study reveals that linerless engines made of near eutectic Al-Si alloys maybe durable and efficient for the engine lifecycle—the wear resistance is further improved on dilution of engine oil with E85.

Lightweight internal combustion (IC) engines represent one of the most significant technological advances in automotive technology. A suitable wear surface in the bore is needed to resist the scuffing action of the piston and ring pack and provide low friction during the normal engine operating conditions. Thermally sprayed steel coatings have been identified as a low mass alternative to cast iron liners. Systematic tribological tests have been performed on the 1010 thermal spray coatings under unlubricated, lubricated and transient lubricated conditions. Microscopic and spectroscopic analyses of the worn cylinder bore surfaces indicate a phase transformation from FeO to Fe_2O_3 during the unlubricated sliding. The detailed mechanism of the phase transformation process has been further investigated using in-situ micro-Raman (sensitive to oxide and structural changes) characterization technique. Selected top compression piston ring (TCR) materials made of cast iron, CrN coated steel, molybdenum sprayed steel and DLC coated steel (also supplied by GM) were chosen as the counterface. The friction reductions afforded by piston rings were ranked and the coatings that showed low friction in both unlubricated and lubricated conditions were determined. A significant achievement of this study was the revelation that DLC coated TCRs can eliminate dry scuffing altogether during reciprocating sliding test performed at laboratory scale. This technology, once put to large scale use may lead to elimination of use of engine oils altogether as it can potentially provide low friction and wear throughout the lifetime of the engine bore.

Thus the DLC coatings provide very exciting prospects in terms of reducing friction, wear and adhesion. However, an impediment to the widespread application of DLC coatings in

powertrain systems is their poor elevated temperature friction performance. Two separate studies, involving W-DLC and Ti-MoS_2 were undertaken in this dissertation that has been shown to maintain their low friction at elevated temperatures. Careful characterization using microscopic and spectroscopic techniques have been used to investigate the friction reduction mechanisms at elevated temperatures. It can be seen that modification of conventional DLC with W may significantly improve its themal stability at 400-500 C while Ti-MoS_2 provided low friction at all tested temperatures.

Finally, it has been shown that multilayer graphene can act as a potential lubricant whereby minimum amounts of graphene platelets maybe instrumental in reducing friction. The friction behaviour of multilayered graphene was studied as a solid lubricant. Specifically, the role of humidity in determining its macro-scale friction behaviour in air with different relative humidity (RH) levels (10–45% RH) was considered. Progressively lower friction values were observed with increasing the RH of the atmosphere, with the lowest COF of 0.11 reached at 45% RH. Defect characterization, using non-invasive micro Raman spectroscopy provided the fundamental scientific basis for friction reduction of the graphene layers under moisture laden conditions.

All the above studies revealed that understanding of interfacial tribology—namely compositional changes of tribolayer, subsurface evaluation as well as the role of transfer layers—during sliding is essential for selection of appropriate ring coatings for standard and lightweight combustion engines.

9.2 Original/Important contributions made by the author

1. Understand the effects of oil dilution by ethanol in terms of wear and friction.

With the increasing use of biofuels it is becoming more and more important that the effects of ethanol on engine wear and friction are critically evaluated. In this dissertation the author has reported works from two publications whereby the effects of ethanol mixed with oil on wear and friction has been assessed in combination with particular grade of DLC as the counterface. While there have been many studies evaluating ZDDP degradation mechanisms and many studies involving DLC passivation mechanisms there are no studies, to the best of author's knowledge, that evaluate the effects of ethanol on ZDDP degradation while at the same time also evaluate the effects ethanol dilution on friction of NH-DLC.

2. In-situ Raman spectroscopy study of iron oxide transformations during dry sliding of thermal spray coatings.

The use of Raman spectroscopic study for tribological purposes exists in the current literature. However, an in-situ Raman spectroscopy study of iron oxide phase transformations during unlubricated reciprocating sliding of thermal spray coatings against top compression ring materials is novel, to the best of author's knowledge, and the analyses of the effects of these iron oxides phases changes on friction behaviour of ferrous thermal spray coatings used in engine bores is of great importance.

3. Elimination of scuffing during dry sliding due to use of DLC coated top compression rings.

Scuffing during cold start is a common problem. In this dissertation the author has shown that the use of DLC coated top compression rings can potentially eliminate scuffing by maintaining low friction under unlubricated sliding conditions. However, this is true for the reciprocating tests conducted in the lab and would need further validation from dynamometer testing under actual engine running conditions.

4. Macroscale friction reduction mechanisms in graphene.

The role that atmospheric humidity plays in reducing friction of graphene has been studied. The dissertation provides detailed surface analyses to account for the mechanisms responsible for the low coefficient of friction of graphene in humid atmospheres. Sliding induced structural changes, defect formations (transformations in the C atom hybridizations), amorphization and formation of transfer layers were analyzed using a combination of analytical techniques including HR-TEM/FIB, micro-Raman and XPS. Particularly, the analyses of intercalation mechanisms of water molecules in between graphene layers is a major contribution and was appreciated by the journals in which the works were submitted for the detailed TEM evidences presented to support the proposed friction reduction mechanisms.

9.3 General Conclusions

1. Use of NH DLC counterface against CI system was beneficial to reduce friction and wear. Ethanol dilution of engine oil facilitated ORL formation and promoted decomposition of anti-wear components. As the COF of CI was the lowest when OH passivation of NH-DLC coating occurred it can be recommended that piston rings coated with NH-DLC run against cast iron liners would be advantageous.

2. The role of biofuel (E85) addition to synthetic engine oil during ultra-mild wear of an Al-12.6% Si alloy was investigated in details by applying an E85-synthetic oil mixture—E85/oil (1:1) blend. A lower cumulative volumetric wear was obtained in tests that used the E85/oil (1:1) blend. A tribochemical model explaining the ZDDP degradation, in presence of the E85/oil (1:1) blend, was suggested based on the spectroscopic and microscopic evidence. The hydroxyl groups present in the ethanol molecule in the E85 biofuel were suggested to facilitate the ligand exchange of the degraded ZDDP molecule, leading to the formation of antiwear polyphosphates.

3. Oxide transformation and role of DLC coated counterfaces on friction behaviour of 1010 spray coatings, deposited on Al 380 engine bore surfaces were investigated by conducting unlubricated. In-situ Raman spectroscopy indicated that FeO was transformed to Fe_2O_3 during unlubricated sliding. 1010 sliding against DLC coated TCR resulted in the formation of an amorphous carbon rich transfer layer, on top of the Fe_2O_3 oxide layer, which prevented further oxide conversion and adhesion to TCR contact surface resulting in a low COF of 0.18 and eliminated scuffing opposite to that experienced when using a CrN coated TCR.

4. An oil residue layer (ORL) incorporating ZnS and $FePO_4$ nanoparticles embedded in an amorphous matrix formed on 1010 steel coating during boundary lubricated sliding and was responsible for the low wear.

5. The friction reduction mechanisms of W-DLC and Ti-MoS_2 coatings were investigated. The W-DLC coating sustained its room temperature low friction properties up to 400°C which was attributed to WO_3 formation. Ti-MoS_2 offers high thermal stability, high wear resistance and low friction for dry sliding contact applications against aluminum alloys at temperatures up to 350˚C. At temperatures between 25 ˚C and 200 ˚C the low friction was attributed to the formation of MoS_2 transfer layers on the counterface contact surfaces while at ≥ 200 ˚C the COF and wear behaviour were controlled by the formation of a mixture of MoS_2 and MoO_3 on the contact surface.

6. The role of atmospheric humidity in determining the COF of multilayered graphene (MLG) was investigated and found that COF decreased drastically from when MLG was tested in air with RH between 10% and 45% compared to the tests performed in dry N_2. TEM and XPS observations performed following the sliding tests conducted under high humidity atmosphere revealed transfer of graphene to the counterface consisting of graphene stacks with 2e21 layers

and non-crystalline regions between the stacks, whereas when tested under a nitrogen atmosphere the graphene was subjected to severe wear damage and no transfer occurred to the counterface. The decrease in COF of MLG with humidity was attributed to the passivation of graphene layers in the wear track and in the transfer layers by molecules dissociated from the atmospheric moisture.

In conclusion, an important implication of this work is that delineating the micromechanisms that are responsible for reduction in friction and wear, is critical for development of appropriate materials and coatings for powertrain components.

9.4 Future Work

Using the directions adopted in this dissertation, the friction reduction strategies can be further studied in different ways. One major focus of this dissertation is to improve the friction reducing capabilities of the engine oil beyond what is currently achieved. Towards this end, engine oil containing graphene nano-platelets can be investigated whereby further reductions in friction as well as formation of a graphitic tribolayer that will provide long term durability is expected. Additives, other than ethanol, that may provide OH functional groups for passivation of DLC coated counetrfaces may be investigated, namely, ester based functional groups. Modifications in the spray coated Al-Si linerless bore maybe made with the variations in the iron oxide content. The dry scuffing resistance of these modified spray coated linerless cylinder bores may be tested with focus on the oxide transformation and its' effect on friction and wear. Surface texture may play a significant role in the friction and wear behaviour of cylinder bores/liners. Cylinder liners with different surface finish may be investigated and their dry scuffing resistance as well as oil retention capabilities will be evaluated.

In all the above future methodologies it is important to remember the underlying principle—the micromechanisms of friction and wear can be best understood when the tribolayers formed during sliding are characterized in details.

APPENDIX: Copyright Releases from Publications

Chapter 2

Friction reduction mechanisms in cast iron sliding against DLC: Effect of biofuel (E85) diluted engine oil

ELSEVIER LICENSE
TERMS AND CONDITIONS

Mar 19, 2017

This Agreement between ANINDYA BANERJI ("You") and Elsevier ("Elsevier") consists of your license details and the terms and conditions provided by Elsevier and Copyright Clearance Center.

License Number	4072680271742
License date	Mar 19, 2017
Licensed Content Publisher	Elsevier
Licensed Content Publication	Wear
Licensed Content Title	Friction reduction mechanisms in cast iron sliding against DLC: Effect of biofuel (E85) diluted engine oil
Licensed Content Author	A. Banerji,M.J. Lukitsch,A.T. Alpas
Licensed Content Date	15 December 2016
Licensed Content Volume	368
Licensed Content Issue	n/a
Licensed Content Pages	14
Start Page	196
End Page	209
Type of Use	reuse in a thesis/dissertation
Portion	full article
Format	both print and electronic
Are you the author of this Elsevier article?	Yes
Will you be translating?	No
Order reference number	
Title of your thesis/dissertation	Friction Reduction in Engine Materials: Role of Tribolayers
Expected completion date	Mar 2017
Estimated size (number of pages)	400
Elsevier VAT number	GB 494 6272 12
Requestor Location	ANINDYA BANERJI Canada Attn: ANINDYA BANERJI
Total	0.00 USD
Terms and Conditions	

INTRODUCTION

1. The publisher for this copyrighted material is Elsevier. By clicking "accept" in connection with completing this licensing transaction, you agree that the following terms and conditions apply to this transaction (along with the Billing and Payment terms and conditions established by Copyright

Clearance Center, Inc. ("CCC"), at the time that you opened your Rightslink account and that are available at any time at http://myaccount.copyright.com).

GENERAL TERMS

2. Elsevier hereby grants you permission to reproduce the aforementioned material subject to the terms and conditions indicated.

3. Acknowledgement: If any part of the material to be used (for example, figures) has appeared in our publication with credit or acknowledgement to another source, permission must also be sought from that source. If such permission is not obtained then that material may not be included in your publication/copies. Suitable acknowledgement to the source must be made, either as a footnote or in a reference list at the end of your publication, as follows:
"Reprinted from Publication title, Vol /edition number, Author(s), Title of article / title of chapter, Pages No., Copyright (Year), with permission from Elsevier [OR APPLICABLE SOCIETY COPYRIGHT OWNER]." Also Lancet special credit - "Reprinted from The Lancet, Vol. number, Author(s), Title of article, Pages No., Copyright (Year), with permission from Elsevier."

4. Reproduction of this material is confined to the purpose and/or media for which permission is hereby given.

5. Altering/Modifying Material: Not Permitted. However figures and illustrations may be altered/adapted minimally to serve your work. Any other abbreviations, additions, deletions and/or any other alterations shall be made only with prior written authorization of Elsevier Ltd. (Please contact Elsevier at permissions@elsevier.com). No modifications can be made to any Lancet figures/tables and they must be reproduced in full.

6. If the permission fee for the requested use of our material is waived in this instance, please be advised that your future requests for Elsevier materials may attract a fee.

7. Reservation of Rights: Publisher reserves all rights not specifically granted in the combination of (i) the license details provided by you and accepted in the course of this licensing transaction, (ii) these terms and conditions and (iii) CCC's Billing and Payment terms and conditions.

8. License Contingent Upon Payment: While you may exercise the rights licensed immediately upon issuance of the license at the end of the licensing process for the transaction, provided that you have disclosed complete and accurate details of your proposed use, no license is finally effective unless and until full payment is received from you (either by publisher or by CCC) as provided in CCC's Billing and Payment terms and conditions. If full payment is not received on a timely basis, then any license preliminarily granted shall be deemed automatically revoked and shall be void as if never granted. Further, in the event that you breach any of these terms and conditions or any of CCC's Billing and Payment terms and conditions, the license is automatically revoked and shall be void as if never granted. Use of materials as described in a revoked license, as well as any use of the materials beyond the scope of an unrevoked license, may constitute copyright infringement and publisher reserves the right to take any and all action to protect its copyright in the materials.

9. Warranties: Publisher makes no representations or warranties with respect to the licensed material.

10. Indemnity: You hereby indemnify and agree to hold harmless publisher and CCC, and their respective officers, directors, employees and agents, from and against any and all claims arising out of your use of the licensed material other than as specifically authorized pursuant to this license.

11. No Transfer of License: This license is personal to you and may not be sublicensed, assigned, or transferred by you to any other person without publisher's written permission.

12. No Amendment Except in Writing: This license may not be amended except in a writing signed by both parties (or, in the case of publisher, by CCC on publisher's behalf).

13. Objection to Contrary Terms: Publisher hereby objects to any terms contained in any purchase order, acknowledgment, check endorsement or other writing prepared by you, which terms are

inconsistent with these terms and conditions or CCC's Billing and Payment terms and conditions. These terms and conditions, together with CCC's Billing and Payment terms and conditions (which are incorporated herein), comprise the entire agreement between you and publisher (and CCC) concerning this licensing transaction. In the event of any conflict between your obligations established by these terms and conditions and those established by CCC's Billing and Payment terms and conditions, these terms and conditions shall control.

14. Revocation: Elsevier or Copyright Clearance Center may deny the permissions described in this License at their sole discretion, for any reason or no reason, with a full refund payable to you. Notice of such denial will be made using the contact information provided by you. Failure to receive such notice will not alter or invalidate the denial. In no event will Elsevier or Copyright Clearance Center be responsible or liable for any costs, expenses or damage incurred by you as a result of a denial of your permission request, other than a refund of the amount(s) paid by you to Elsevier and/or Copyright Clearance Center for denied permissions.

LIMITED LICENSE

The following terms and conditions apply only to specific license types:

15. **Translation**: This permission is granted for non-exclusive world **English** rights only unless your license was granted for translation rights. If you licensed translation rights you may only translate this content into the languages you requested. A professional translator must perform all translations and reproduce the content word for word preserving the integrity of the article.

16. **Posting licensed content on any Website**: The following terms and conditions apply as follows: Licensing material from an Elsevier journal: All content posted to the web site must maintain the copyright information line on the bottom of each image; A hyper-text must be included to the Homepage of the journal from which you are licensing at http://www.sciencedirect.com/science/journal/xxxxx or the Elsevier homepage for books at http://www.elsevier.com; Central Storage: This license does not include permission for a scanned version of the material to be stored in a central repository such as that provided by Heron/XanEdu. Licensing material from an Elsevier book: A hyper-text link must be included to the Elsevier homepage at http://www.elsevier.com . All content posted to the web site must maintain the copyright information line on the bottom of each image.

Posting licensed content on Electronic reserve: In addition to the above the following clauses are applicable: The web site must be password-protected and made available only to bona fide students registered on a relevant course. This permission is granted for 1 year only. You may obtain a new license for future website posting.

17. **For journal authors:** the following clauses are applicable in addition to the above:

Preprints:

A preprint is an author's own write-up of research results and analysis, it has not been peer-reviewed, nor has it had any other value added to it by a publisher (such as formatting, copyright, technical enhancement etc.).

Authors can share their preprints anywhere at any time. Preprints should not be added to or enhanced in any way in order to appear more like, or to substitute for, the final versions of articles however authors can update their preprints on arXiv or RePEc with their Accepted Author Manuscript (see below).

If accepted for publication, we encourage authors to link from the preprint to their formal publication via its DOI. Millions of researchers have access to the formal publications on ScienceDirect, and so links will help users to find, access, cite and use the best available version. Please note that Cell Press, The Lancet and some society-owned have different preprint policies. Information on these policies is available on the journal homepage.

Accepted Author Manuscripts: An accepted author manuscript is the manuscript of an article that has been accepted for publication and which typically includes author-incorporated changes suggested during submission, peer review and editor-author communications.
Authors can share their accepted author manuscript:

- immediately
  - via their non-commercial person homepage or blog
  - by updating a preprint in arXiv or RePEc with the accepted manuscript
  - via their research institute or institutional repository for internal institutional uses or as part of an invitation-only research collaboration work-group
  - directly by providing copies to their students or to research collaborators for their personal use
  - for private scholarly sharing as part of an invitation-only work group on commercial sites with which Elsevier has an agreement
- After the embargo period
  - via non-commercial hosting platforms such as their institutional repository
  - via commercial sites with which Elsevier has an agreement

In all cases accepted manuscripts should:

- link to the formal publication via its DOI
- bear a CC-BY-NC-ND license - this is easy to do
- if aggregated with other manuscripts, for example in a repository or other site, be shared in alignment with our hosting policy not be added to or enhanced in any way to appear more like, or to substitute for, the published journal article.

Published journal article (JPA): A published journal article (PJA) is the definitive final record of published research that appears or will appear in the journal and embodies all value-adding publishing activities including peer review co-ordination, copy-editing, formatting, (if relevant) pagination and online enrichment.
Policies for sharing publishing journal articles differ for subscription and gold open access articles:
Subscription Articles: If you are an author, please share a link to your article rather than the full-text. Millions of researchers have access to the formal publications on ScienceDirect, and so links will help your users to find, access, cite, and use the best available version.
Theses and dissertations which contain embedded PJAs as part of the formal submission can be posted publicly by the awarding institution with DOI links back to the formal publications on ScienceDirect.
If you are affiliated with a library that subscribes to ScienceDirect you have additional private sharing rights for others' research accessed under that agreement. This includes use for classroom teaching and internal training at the institution (including use in course packs and courseware programs), and inclusion of the article for grant funding purposes.
Gold Open Access Articles: May be shared according to the author-selected end-user license and should contain a CrossMark logo, the end user license, and a DOI link to the formal publication on ScienceDirect.
Please refer to Elsevier's posting policy for further information.
18. **For book authors** the following clauses are applicable in addition to the above: Authors are permitted to place a brief summary of their work online only. You are not allowed to download and post the published electronic version of your chapter, nor may you scan the printed edition to

- Associating advertising with the full text of the Article
- Charging fees for document delivery or access
- Article aggregation
- Systematic distribution via e-mail lists or share buttons

Posting or linking by commercial companies for use by customers of those companies.

20. **Other Conditions**:

v1.9

Chapter 3

Effect of Biofuel (E85) Addition on Lubricated Sliding Wear Mechanisms of a Eutectic Al-Si Alloy

ELSEVIER LICENSE
TERMS AND CONDITIONS

Mar 19, 2017

This Agreement between ANINDYA BANERJI ("You") and Elsevier ("Elsevier") consists of your license details and the terms and conditions provided by Elsevier and Copyright Clearance Center.

License Number	4072680453034
License date	Mar 19, 2017
Licensed Content Publisher	Elsevier
Licensed Content Publication	Wear
Licensed Content Title	Effect of bio-fuel (E85) addition on lubricated sliding wear mechanisms of a eutectic Al–Si alloy
Licensed Content Author	A. Banerji,A. Edrisy,V. Francis,A.T. Alpas
Licensed Content Date	15 March 2014
Licensed Content Volume	311
Licensed Content Issue	1-2
Licensed Content Pages	13
Start Page	1
End Page	13
Type of Use	reuse in a thesis/dissertation
Intended publisher of new work	other
Portion	full article
Format	both print and electronic
Are you the author of this Elsevier article?	Yes
Will you be translating?	No
Order reference number	
Title of your thesis/dissertation	Friction Reduction in Engine Materials: Role of Tribolayers
Expected completion date	Mar 2017
Estimated size (number of pages)	400
Elsevier VAT number	GB 494 6272 12
Requestor Location	ANINDYA BANERJI Canada Attn: ANINDYA BANERJI
Total	0.00 USD
Terms and Conditions	

INTRODUCTION

1. The publisher for this copyrighted material is Elsevier. By clicking "accept" in connection with completing this licensing transaction, you agree that the following terms and conditions apply to this transaction (along with the Billing and Payment terms and conditions established by Copyright Clearance Center, Inc. ("CCC"), at the time that you opened your Rightslink account and that are available at any time at http://myaccount.copyright.com).

GENERAL TERMS

2. Elsevier hereby grants you permission to reproduce the aforementioned material subject to the terms and conditions indicated.

3. Acknowledgement: If any part of the material to be used (for example, figures) has appeared in our publication with credit or acknowledgement to another source, permission must also be sought from that source. If such permission is not obtained then that material may not be included in your publication/copies. Suitable acknowledgement to the source must be made, either as a footnote or in a reference list at the end of your publication, as follows:

"Reprinted from Publication title, Vol /edition number, Author(s), Title of article / title of chapter, Pages No., Copyright (Year), with permission from Elsevier [OR APPLICABLE SOCIETY COPYRIGHT OWNER]." Also Lancet special credit - "Reprinted from The Lancet, Vol. number, Author(s), Title of article, Pages No., Copyright (Year), with permission from Elsevier."

4. Reproduction of this material is confined to the purpose and/or media for which permission is hereby given.

5. Altering/Modifying Material: Not Permitted. However figures and illustrations may be altered/adapted minimally to serve your work. Any other abbreviations, additions, deletions and/or any other alterations shall be made only with prior written authorization of Elsevier Ltd. (Please contact Elsevier at permissions@elsevier.com). No modifications can be made to any Lancet figures/tables and they must be reproduced in full.

6. If the permission fee for the requested use of our material is waived in this instance, please be advised that your future requests for Elsevier materials may attract a fee.

7. Reservation of Rights: Publisher reserves all rights not specifically granted in the combination of (i) the license details provided by you and accepted in the course of this licensing transaction, (ii) these terms and conditions and (iii) CCC's Billing and Payment terms and conditions.

8. License Contingent Upon Payment: While you may exercise the rights licensed immediately upon issuance of the license at the end of the licensing process for the transaction, provided that you have disclosed complete and accurate details of your proposed use, no license is finally effective unless and until full payment is received from you (either by publisher or by CCC) as provided in CCC's Billing and Payment terms and conditions. If full payment is not received on a timely basis, then any license preliminarily granted shall be deemed automatically revoked and shall be void as if never granted. Further, in the event that you breach any of these terms and conditions or any of CCC's Billing and Payment terms and conditions, the license is automatically revoked and shall be void as if never granted. Use of materials as described in a revoked license, as well as any use of the materials beyond the scope of an unrevoked license, may constitute copyright infringement and publisher reserves the right to take any and all action to protect its copyright in the materials.

9. Warranties: Publisher makes no representations or warranties with respect to the licensed material.

10. Indemnity: You hereby indemnify and agree to hold harmless publisher and CCC, and their respective officers, directors, employees and agents, from and against any and all claims arising out of your use of the licensed material other than as specifically authorized pursuant to this license.

11. No Transfer of License: This license is personal to you and may not be sublicensed, assigned, or transferred by you to any other person without publisher's written permission.

12. No Amendment Except in Writing: This license may not be amended except in a writing signed by both parties (or, in the case of publisher, by CCC on publisher's behalf).
13. Objection to Contrary Terms: Publisher hereby objects to any terms contained in any purchase order, acknowledgment, check endorsement or other writing prepared by you, which terms are inconsistent with these terms and conditions or CCC's Billing and Payment terms and conditions. These terms and conditions, together with CCC's Billing and Payment terms and conditions (which are incorporated herein), comprise the entire agreement between you and publisher (and CCC) concerning this licensing transaction. In the event of any conflict between your obligations established by these terms and conditions and those established by CCC's Billing and Payment terms and conditions, these terms and conditions shall control.
14. Revocation: Elsevier or Copyright Clearance Center may deny the permissions described in this License at their sole discretion, for any reason or no reason, with a full refund payable to you. Notice of such denial will be made using the contact information provided by you. Failure to receive such notice will not alter or invalidate the denial. In no event will Elsevier or Copyright Clearance Center be responsible or liable for any costs, expenses or damage incurred by you as a result of a denial of your permission request, other than a refund of the amount(s) paid by you to Elsevier and/or Copyright Clearance Center for denied permissions.

LIMITED LICENSE

The following terms and conditions apply only to specific license types:
15. **Translation**: This permission is granted for non-exclusive world **English** rights only unless your license was granted for translation rights. If you licensed translation rights you may only translate this content into the languages you requested. A professional translator must perform all translations and reproduce the content word for word preserving the integrity of the article.
16. **Posting licensed content on any Website**: The following terms and conditions apply as follows: Licensing material from an Elsevier journal: All content posted to the web site must maintain the copyright information line on the bottom of each image; A hyper-text must be included to the Homepage of the journal from which you are licensing at http://www.sciencedirect.com/science/journal/xxxxx or the Elsevier homepage for books at http://www.elsevier.com; Central Storage: This license does not include permission for a scanned version of the material to be stored in a central repository such as that provided by Heron/XanEdu. Licensing material from an Elsevier book: A hyper-text link must be included to the Elsevier homepage at http://www.elsevier.com . All content posted to the web site must maintain the copyright information line on the bottom of each image.

Posting licensed content on Electronic reserve: In addition to the above the following clauses are applicable: The web site must be password-protected and made available only to bona fide students registered on a relevant course. This permission is granted for 1 year only. You may obtain a new license for future website posting.
17. **For journal authors:** the following clauses are applicable in addition to the above:
Preprints:
A preprint is an author's own write-up of research results and analysis, it has not been peer-reviewed, nor has it had any other value added to it by a publisher (such as formatting, copyright, technical enhancement etc.).
Authors can share their preprints anywhere at any time. Preprints should not be added to or enhanced in any way in order to appear more like, or to substitute for, the final versions of articles however authors can update their preprints on arXiv or RePEc with their Accepted Author Manuscript (see below).

If accepted for publication, we encourage authors to link from the preprint to their formal publication via its DOI. Millions of researchers have access to the formal publications on ScienceDirect, and so links will help users to find, access, cite and use the best available version. Please note that Cell Press, The Lancet and some society-owned have different preprint policies. Information on these policies is available on the journal homepage.

Accepted Author Manuscripts: An accepted author manuscript is the manuscript of an article that has been accepted for publication and which typically includes author-incorporated changes suggested during submission, peer review and editor-author communications.

Authors can share their accepted author manuscript:

- immediately
  - via their non-commercial person homepage or blog
  - by updating a preprint in arXiv or RePEc with the accepted manuscript
  - via their research institute or institutional repository for internal institutional uses or as part of an invitation-only research collaboration work-group
  - directly by providing copies to their students or to research collaborators for their personal use
  - for private scholarly sharing as part of an invitation-only work group on commercial sites with which Elsevier has an agreement
- After the embargo period
  - via non-commercial hosting platforms such as their institutional repository
  - via commercial sites with which Elsevier has an agreement

In all cases accepted manuscripts should:

- link to the formal publication via its DOI
- bear a CC-BY-NC-ND license - this is easy to do
- if aggregated with other manuscripts, for example in a repository or other site, be shared in alignment with our hosting policy not be added to or enhanced in any way to appear more like, or to substitute for, the published journal article.

Published journal article (JPA): A published journal article (PJA) is the definitive final record of published research that appears or will appear in the journal and embodies all value-adding publishing activities including peer review co-ordination, copy-editing, formatting, (if relevant) pagination and online enrichment.

Policies for sharing publishing journal articles differ for subscription and gold open access articles:

Subscription Articles: If you are an author, please share a link to your article rather than the full-text. Millions of researchers have access to the formal publications on ScienceDirect, and so links will help your users to find, access, cite, and use the best available version.

Theses and dissertations which contain embedded PJAs as part of the formal submission can be posted publicly by the awarding institution with DOI links back to the formal publications on ScienceDirect.

If you are affiliated with a library that subscribes to ScienceDirect you have additional private sharing rights for others' research accessed under that agreement. This includes use for classroom teaching and internal training at the institution (including use in course packs and courseware programs), and inclusion of the article for grant funding purposes.

Gold Open Access Articles: May be shared according to the author-selected end-user license and should contain a CrossMark logo, the end user license, and a DOI link to the formal publication on ScienceDirect.

Chapter 5

High Temperature Tribological Behaviour of W Containing Diamond-Like Carbon (DLC) Coating against Titanium Alloys

ELSEVIER LICENSE
TERMS AND CONDITIONS

Mar 19, 2017

This Agreement between ANINDYA BANERJI ("You") and Elsevier ("Elsevier") consists of your license details and the terms and conditions provided by Elsevier and Copyright Clearance Center.

License Number	4072680785015
License date	Mar 19, 2017
Licensed Content Publisher	Elsevier
Licensed Content Publication	Surface and Coatings Technology
Licensed Content Title	High temperature tribological behavior of W containing diamond-like carbon (DLC) coating against titanium alloys
Licensed Content Author	A. Banerji,S. Bhowmick,A.T. Alpas
Licensed Content Date	25 February 2014
Licensed Content Volume	241
Licensed Content Issue	n/a
Licensed Content Pages	12
Start Page	93
End Page	104
Type of Use	reuse in a thesis/dissertation
Intended publisher of new work	other
Portion	full article
Format	both print and electronic
Are you the author of this Elsevier article?	Yes
Will you be translating?	No
Order reference number	
Title of your thesis/dissertation	Friction Reduction in Engine Materials: Role of Tribolayers
Expected completion date	Mar 2017
Estimated size (number of pages)	400
Elsevier VAT number	GB 494 6272 12
Requestor Location	ANINDYA BANERJI Canada Attn: ANINDYA BANERJI
Total	0.00 USD
Terms and Conditions	

INTRODUCTION

1. The publisher for this copyrighted material is Elsevier. By clicking "accept" in connection with completing this licensing transaction, you agree that the following terms and conditions apply to this transaction (along with the Billing and Payment terms and conditions established by Copyright Clearance Center, Inc. ("CCC"), at the time that you opened your Rightslink account and that are available at any time at http://myaccount.copyright.com).

GENERAL TERMS

2. Elsevier hereby grants you permission to reproduce the aforementioned material subject to the terms and conditions indicated.

3. Acknowledgement: If any part of the material to be used (for example, figures) has appeared in our publication with credit or acknowledgement to another source, permission must also be sought from that source. If such permission is not obtained then that material may not be included in your publication/copies. Suitable acknowledgement to the source must be made, either as a footnote or in a reference list at the end of your publication, as follows:

"Reprinted from Publication title, Vol /edition number, Author(s), Title of article / title of chapter, Pages No., Copyright (Year), with permission from Elsevier [OR APPLICABLE SOCIETY COPYRIGHT OWNER]." Also Lancet special credit - "Reprinted from The Lancet, Vol. number, Author(s), Title of article, Pages No., Copyright (Year), with permission from Elsevier."

4. Reproduction of this material is confined to the purpose and/or media for which permission is hereby given.

5. Altering/Modifying Material: Not Permitted. However figures and illustrations may be altered/adapted minimally to serve your work. Any other abbreviations, additions, deletions and/or any other alterations shall be made only with prior written authorization of Elsevier Ltd. (Please contact Elsevier at permissions@elsevier.com). No modifications can be made to any Lancet figures/tables and they must be reproduced in full.

6. If the permission fee for the requested use of our material is waived in this instance, please be advised that your future requests for Elsevier materials may attract a fee.

7. Reservation of Rights: Publisher reserves all rights not specifically granted in the combination of (i) the license details provided by you and accepted in the course of this licensing transaction, (ii) these terms and conditions and (iii) CCC's Billing and Payment terms and conditions.

8. License Contingent Upon Payment: While you may exercise the rights licensed immediately upon issuance of the license at the end of the licensing process for the transaction, provided that you have disclosed complete and accurate details of your proposed use, no license is finally effective unless and until full payment is received from you (either by publisher or by CCC) as provided in CCC's Billing and Payment terms and conditions. If full payment is not received on a timely basis, then any license preliminarily granted shall be deemed automatically revoked and shall be void as if never granted. Further, in the event that you breach any of these terms and conditions or any of CCC's Billing and Payment terms and conditions, the license is automatically revoked and shall be void as if never granted. Use of materials as described in a revoked license, as well as any use of the materials beyond the scope of an unrevoked license, may constitute copyright infringement and publisher reserves the right to take any and all action to protect its copyright in the materials.

9. Warranties: Publisher makes no representations or warranties with respect to the licensed material.

10. Indemnity: You hereby indemnify and agree to hold harmless publisher and CCC, and their respective officers, directors, employees and agents, from and against any and all claims arising out of your use of the licensed material other than as specifically authorized pursuant to this license.

11. No Transfer of License: This license is personal to you and may not be sublicensed, assigned, or transferred by you to any other person without publisher's written permission.

12. No Amendment Except in Writing: This license may not be amended except in a writing signed by both parties (or, in the case of publisher, by CCC on publisher's behalf).
13. Objection to Contrary Terms: Publisher hereby objects to any terms contained in any purchase order, acknowledgment, check endorsement or other writing prepared by you, which terms are inconsistent with these terms and conditions or CCC's Billing and Payment terms and conditions. These terms and conditions, together with CCC's Billing and Payment terms and conditions (which are incorporated herein), comprise the entire agreement between you and publisher (and CCC) concerning this licensing transaction. In the event of any conflict between your obligations established by these terms and conditions and those established by CCC's Billing and Payment terms and conditions, these terms and conditions shall control.
14. Revocation: Elsevier or Copyright Clearance Center may deny the permissions described in this License at their sole discretion, for any reason or no reason, with a full refund payable to you. Notice of such denial will be made using the contact information provided by you. Failure to receive such notice will not alter or invalidate the denial. In no event will Elsevier or Copyright Clearance Center be responsible or liable for any costs, expenses or damage incurred by you as a result of a denial of your permission request, other than a refund of the amount(s) paid by you to Elsevier and/or Copyright Clearance Center for denied permissions.

LIMITED LICENSE

The following terms and conditions apply only to specific license types:
15. **Translation**: This permission is granted for non-exclusive world **English** rights only unless your license was granted for translation rights. If you licensed translation rights you may only translate this content into the languages you requested. A professional translator must perform all translations and reproduce the content word for word preserving the integrity of the article.
16. **Posting licensed content on any Website**: The following terms and conditions apply as follows: Licensing material from an Elsevier journal: All content posted to the web site must maintain the copyright information line on the bottom of each image; A hyper-text must be included to the Homepage of the journal from which you are licensing at http://www.sciencedirect.com/science/journal/xxxxx or the Elsevier homepage for books at http://www.elsevier.com; Central Storage: This license does not include permission for a scanned version of the material to be stored in a central repository such as that provided by Heron/XanEdu. Licensing material from an Elsevier book: A hyper-text link must be included to the Elsevier homepage at http://www.elsevier.com . All content posted to the web site must maintain the copyright information line on the bottom of each image.

Posting licensed content on Electronic reserve: In addition to the above the following clauses are applicable: The web site must be password-protected and made available only to bona fide students registered on a relevant course. This permission is granted for 1 year only. You may obtain a new license for future website posting.
17. **For journal authors:** the following clauses are applicable in addition to the above:
Preprints:
A preprint is an author's own write-up of research results and analysis, it has not been peer-reviewed, nor has it had any other value added to it by a publisher (such as formatting, copyright, technical enhancement etc.).
Authors can share their preprints anywhere at any time. Preprints should not be added to or enhanced in any way in order to appear more like, or to substitute for, the final versions of articles however authors can update their preprints on arXiv or RePEc with their Accepted Author Manuscript (see below).

Please refer to Elsevier's posting policy for further information.

18. **For book authors** the following clauses are applicable in addition to the above: Authors are permitted to place a brief summary of their work online only. You are not allowed to download and post the published electronic version of your chapter, nor may you scan the printed edition to create an electronic version. **Posting to a repository:** Authors are permitted to post a summary of their chapter only in their institution's repository.

19. **Thesis/Dissertation**: If your license is for use in a thesis/dissertation your thesis may be submitted to your institution in either print or electronic form. Should your thesis be published commercially, please reapply for permission. These requirements include permission for the Library and Archives of Canada to supply single copies, on demand, of the complete thesis and include permission for Proquest/UMI to supply single copies, on demand, of the complete thesis. Should your thesis be published commercially, please reapply for permission. Theses and dissertations which contain embedded PJAs as part of the formal submission can be posted publicly by the awarding institution with DOI links back to the formal publications on ScienceDirect.

Elsevier Open Access Terms and Conditions

You can publish open access with Elsevier in hundreds of open access journals or in nearly 2000 established subscription journals that support open access publishing. Permitted third party re-use of these open access articles is defined by the author's choice of Creative Commons user license. See our open access license policy for more information.

Terms & Conditions applicable to all Open Access articles published with Elsevier:

Any reuse of the article must not represent the author as endorsing the adaptation of the article nor should the article be modified in such a way as to damage the author's honour or reputation. If any changes have been made, such changes must be clearly indicated.

The author(s) must be appropriately credited and we ask that you include the end user license and a DOI link to the formal publication on ScienceDirect.

If any part of the material to be used (for example, figures) has appeared in our publication with credit or acknowledgement to another source it is the responsibility of the user to ensure their reuse complies with the terms and conditions determined by the rights holder.

Additional Terms & Conditions applicable to each Creative Commons user license:

CC BY: The CC-BY license allows users to copy, to create extracts, abstracts and new works from the Article, to alter and revise the Article and to make commercial use of the Article (including reuse and/or resale of the Article by commercial entities), provided the user gives appropriate credit (with a link to the formal publication through the relevant DOI), provides a link to the license, indicates if changes were made and the licensor is not represented as endorsing the use made of the work. The full details of the license are available at http://creativecommons.org/licenses/by/4.0.

CC BY NC SA: The CC BY-NC-SA license allows users to copy, to create extracts, abstracts and new works from the Article, to alter and revise the Article, provided this is not done for commercial purposes, and that the user gives appropriate credit (with a link to the formal publication through the relevant DOI), provides a link to the license, indicates if changes were made and the licensor is not represented as endorsing the use made of the work. Further, any new works must be made available on the same conditions. The full details of the license are available at http://creativecommons.org/licenses/by-nc-sa/4.0.

CC BY NC ND: The CC BY-NC-ND license allows users to copy and distribute the Article, provided this is not done for commercial purposes and further does not permit distribution of the Article if it is changed or edited in any way, and provided the user gives appropriate credit (with a link to the formal publication through the relevant DOI), provides a link to the license, and that the licensor is not represented as endorsing the use made of the work. The full details of the license are

If accepted for publication, we encourage authors to link from the preprint to their formal publication via its DOI. Millions of researchers have access to the formal publications on ScienceDirect, and so links will help users to find, access, cite and use the best available version. Please note that Cell Press, The Lancet and some society-owned have different preprint policies. Information on these policies is available on the journal homepage.

Accepted Author Manuscripts: An accepted author manuscript is the manuscript of an article that has been accepted for publication and which typically includes author-incorporated changes suggested during submission, peer review and editor-author communications.

Authors can share their accepted author manuscript:

- immediately
  - via their non-commercial person homepage or blog
  - by updating a preprint in arXiv or RePEc with the accepted manuscript
  - via their research institute or institutional repository for internal institutional uses or as part of an invitation-only research collaboration work-group
  - directly by providing copies to their students or to research collaborators for their personal use
  - for private scholarly sharing as part of an invitation-only work group on commercial sites with which Elsevier has an agreement
- After the embargo period
  - via non-commercial hosting platforms such as their institutional repository
  - via commercial sites with which Elsevier has an agreement

In all cases accepted manuscripts should:

- link to the formal publication via its DOI
- bear a CC-BY-NC-ND license - this is easy to do
- if aggregated with other manuscripts, for example in a repository or other site, be shared in alignment with our hosting policy not be added to or enhanced in any way to appear more like, or to substitute for, the published journal article.

Published journal article (JPA): A published journal article (PJA) is the definitive final record of published research that appears or will appear in the journal and embodies all value-adding publishing activities including peer review co-ordination, copy-editing, formatting, (if relevant) pagination and online enrichment.

Policies for sharing publishing journal articles differ for subscription and gold open access articles:

Subscription Articles: If you are an author, please share a link to your article rather than the full-text. Millions of researchers have access to the formal publications on ScienceDirect, and so links will help your users to find, access, cite, and use the best available version.

Theses and dissertations which contain embedded PJAs as part of the formal submission can be posted publicly by the awarding institution with DOI links back to the formal publications on ScienceDirect.

If you are affiliated with a library that subscribes to ScienceDirect you have additional private sharing rights for others' research accessed under that agreement. This includes use for classroom teaching and internal training at the institution (including use in course packs and courseware programs), and inclusion of the article for grant funding purposes.

Gold Open Access Articles: May be shared according to the author-selected end-user license and should contain a CrossMark logo, the end user license, and a DOI link to the formal publication on ScienceDirect.

Chapter 6

Role of Temperature on Tribological Behaviour of Ti containing MoS_2 Coating

ELSEVIER LICENSE
TERMS AND CONDITIONS

Mar 19, 2017

This Agreement between ANINDYA BANERJI ("You") and Elsevier ("Elsevier") consists of your license details and the terms and conditions provided by Elsevier and Copyright Clearance Center.

License Number	4072680860924
License date	Mar 19, 2017
Licensed Content Publisher	Elsevier
Licensed Content Publication	Surface and Coatings Technology
Licensed Content Title	Role of temperature on tribological behaviour of Ti containing MoS2 coating against aluminum alloys
Licensed Content Author	A. Banerji,S. Bhowmick,A.T. Alpas
Licensed Content Date	25 March 2017
Licensed Content Volume	314
Licensed Content Issue	n/a
Licensed Content Pages	11
Start Page	2
End Page	12
Type of Use	reuse in a thesis/dissertation
Intended publisher of new work	other
Portion	full article
Format	both print and electronic
Are you the author of this Elsevier article?	Yes
Will you be translating?	No
Order reference number	
Title of your thesis/dissertation	Friction Reduction in Engine Materials: Role of Tribolayers
Expected completion date	Mar 2017
Estimated size (number of pages)	400
Elsevier VAT number	GB 494 6272 12
Requestor Location	ANINDYA BANERJI Canada Attn: ANINDYA BANERJI
Total	0.00 USD
Terms and Conditions	

INTRODUCTION

1. The publisher for this copyrighted material is Elsevier. By clicking "accept" in connection with completing this licensing transaction, you agree that the following terms and conditions apply to this transaction (along with the Billing and Payment terms and conditions established by Copyright Clearance Center, Inc. ("CCC"), at the time that you opened your Rightslink account and that are available at any time at http://myaccount.copyright.com).

GENERAL TERMS

2. Elsevier hereby grants you permission to reproduce the aforementioned material subject to the terms and conditions indicated.

3. Acknowledgement: If any part of the material to be used (for example, figures) has appeared in our publication with credit or acknowledgement to another source, permission must also be sought from that source. If such permission is not obtained then that material may not be included in your publication/copies. Suitable acknowledgement to the source must be made, either as a footnote or in a reference list at the end of your publication, as follows:

"Reprinted from Publication title, Vol /edition number, Author(s), Title of article / title of chapter, Pages No., Copyright (Year), with permission from Elsevier [OR APPLICABLE SOCIETY COPYRIGHT OWNER]." Also Lancet special credit - "Reprinted from The Lancet, Vol. number, Author(s), Title of article, Pages No., Copyright (Year), with permission from Elsevier."

4. Reproduction of this material is confined to the purpose and/or media for which permission is hereby given.

5. Altering/Modifying Material: Not Permitted. However figures and illustrations may be altered/adapted minimally to serve your work. Any other abbreviations, additions, deletions and/or any other alterations shall be made only with prior written authorization of Elsevier Ltd. (Please contact Elsevier at permissions@elsevier.com). No modifications can be made to any Lancet figures/tables and they must be reproduced in full.

6. If the permission fee for the requested use of our material is waived in this instance, please be advised that your future requests for Elsevier materials may attract a fee.

7. Reservation of Rights: Publisher reserves all rights not specifically granted in the combination of (i) the license details provided by you and accepted in the course of this licensing transaction, (ii) these terms and conditions and (iii) CCC's Billing and Payment terms and conditions.

8. License Contingent Upon Payment: While you may exercise the rights licensed immediately upon issuance of the license at the end of the licensing process for the transaction, provided that you have disclosed complete and accurate details of your proposed use, no license is finally effective unless and until full payment is received from you (either by publisher or by CCC) as provided in CCC's Billing and Payment terms and conditions. If full payment is not received on a timely basis, then any license preliminarily granted shall be deemed automatically revoked and shall be void as if never granted. Further, in the event that you breach any of these terms and conditions or any of CCC's Billing and Payment terms and conditions, the license is automatically revoked and shall be void as if never granted. Use of materials as described in a revoked license, as well as any use of the materials beyond the scope of an unrevoked license, may constitute copyright infringement and publisher reserves the right to take any and all action to protect its copyright in the materials.

9. Warranties: Publisher makes no representations or warranties with respect to the licensed material.

10. Indemnity: You hereby indemnify and agree to hold harmless publisher and CCC, and their respective officers, directors, employees and agents, from and against any and all claims arising out of your use of the licensed material other than as specifically authorized pursuant to this license.

11. No Transfer of License: This license is personal to you and may not be sublicensed, assigned, or transferred by you to any other person without publisher's written permission.

12. No Amendment Except in Writing: This license may not be amended except in a writing signed by both parties (or, in the case of publisher, by CCC on publisher's behalf).
13. Objection to Contrary Terms: Publisher hereby objects to any terms contained in any purchase order, acknowledgment, check endorsement or other writing prepared by you, which terms are inconsistent with these terms and conditions or CCC's Billing and Payment terms and conditions. These terms and conditions, together with CCC's Billing and Payment terms and conditions (which are incorporated herein), comprise the entire agreement between you and publisher (and CCC) concerning this licensing transaction. In the event of any conflict between your obligations established by these terms and conditions and those established by CCC's Billing and Payment terms and conditions, these terms and conditions shall control.
14. Revocation: Elsevier or Copyright Clearance Center may deny the permissions described in this License at their sole discretion, for any reason or no reason, with a full refund payable to you. Notice of such denial will be made using the contact information provided by you. Failure to receive such notice will not alter or invalidate the denial. In no event will Elsevier or Copyright Clearance Center be responsible or liable for any costs, expenses or damage incurred by you as a result of a denial of your permission request, other than a refund of the amount(s) paid by you to Elsevier and/or Copyright Clearance Center for denied permissions.

LIMITED LICENSE

The following terms and conditions apply only to specific license types:
15. **Translation**: This permission is granted for non-exclusive world **English** rights only unless your license was granted for translation rights. If you licensed translation rights you may only translate this content into the languages you requested. A professional translator must perform all translations and reproduce the content word for word preserving the integrity of the article.
16. **Posting licensed content on any Website**: The following terms and conditions apply as follows: Licensing material from an Elsevier journal: All content posted to the web site must maintain the copyright information line on the bottom of each image; A hyper-text must be included to the Homepage of the journal from which you are licensing at http://www.sciencedirect.com/science/journal/xxxxx or the Elsevier homepage for books at http://www.elsevier.com; Central Storage: This license does not include permission for a scanned version of the material to be stored in a central repository such as that provided by Heron/XanEdu. Licensing material from an Elsevier book: A hyper-text link must be included to the Elsevier homepage at http://www.elsevier.com . All content posted to the web site must maintain the copyright information line on the bottom of each image.

Posting licensed content on Electronic reserve: In addition to the above the following clauses are applicable: The web site must be password-protected and made available only to bona fide students registered on a relevant course. This permission is granted for 1 year only. You may obtain a new license for future website posting.
17. **For journal authors:** the following clauses are applicable in addition to the above:
Preprints:
A preprint is an author's own write-up of research results and analysis, it has not been peer-reviewed, nor has it had any other value added to it by a publisher (such as formatting, copyright, technical enhancement etc.).
Authors can share their preprints anywhere at any time. Preprints should not be added to or enhanced in any way in order to appear more like, or to substitute for, the final versions of articles however authors can update their preprints on arXiv or RePEc with their Accepted Author Manuscript (see below).

If accepted for publication, we encourage authors to link from the preprint to their formal publication via its DOI. Millions of researchers have access to the formal publications on ScienceDirect, and so links will help users to find, access, cite and use the best available version. Please note that Cell Press, The Lancet and some society-owned have different preprint policies. Information on these policies is available on the journal homepage.

Accepted Author Manuscripts: An accepted author manuscript is the manuscript of an article that has been accepted for publication and which typically includes author-incorporated changes suggested during submission, peer review and editor-author communications.

Authors can share their accepted author manuscript:

- immediately
  - via their non-commercial person homepage or blog
  - by updating a preprint in arXiv or RePEc with the accepted manuscript
  - via their research institute or institutional repository for internal institutional uses or as part of an invitation-only research collaboration work-group
  - directly by providing copies to their students or to research collaborators for their personal use
  - for private scholarly sharing as part of an invitation-only work group on commercial sites with which Elsevier has an agreement
- After the embargo period
  - via non-commercial hosting platforms such as their institutional repository
  - via commercial sites with which Elsevier has an agreement

In all cases accepted manuscripts should:

- link to the formal publication via its DOI
- bear a CC-BY-NC-ND license - this is easy to do
- if aggregated with other manuscripts, for example in a repository or other site, be shared in alignment with our hosting policy not be added to or enhanced in any way to appear more like, or to substitute for, the published journal article.

Published journal article (JPA): A published journal article (PJA) is the definitive final record of published research that appears or will appear in the journal and embodies all value-adding publishing activities including peer review co-ordination, copy-editing, formatting, (if relevant) pagination and online enrichment.

Policies for sharing publishing journal articles differ for subscription and gold open access articles:

Subscription Articles: If you are an author, please share a link to your article rather than the full-text. Millions of researchers have access to the formal publications on ScienceDirect, and so links will help your users to find, access, cite, and use the best available version.

Theses and dissertations which contain embedded PJAs as part of the formal submission can be posted publicly by the awarding institution with DOI links back to the formal publications on ScienceDirect.

If you are affiliated with a library that subscribes to ScienceDirect you have additional private sharing rights for others' research accessed under that agreement. This includes use for classroom teaching and internal training at the institution (including use in course packs and courseware programs), and inclusion of the article for grant funding purposes.

Gold Open Access Articles: May be shared according to the author-selected end-user license and should contain a CrossMark logo, the end user license, and a DOI link to the formal publication on ScienceDirect.

Please refer to Elsevier's posting policy for further information.

18. **For book authors** the following clauses are applicable in addition to the above: Authors are permitted to place a brief summary of their work online only. You are not allowed to download and post the published electronic version of your chapter, nor may you scan the printed edition to create an electronic version. **Posting to a repository:** Authors are permitted to post a summary of their chapter only in their institution's repository.

19. **Thesis/Dissertation**: If your license is for use in a thesis/dissertation your thesis may be submitted to your institution in either print or electronic form. Should your thesis be published commercially, please reapply for permission. These requirements include permission for the Library and Archives of Canada to supply single copies, on demand, of the complete thesis and include permission for Proquest/UMI to supply single copies, on demand, of the complete thesis. Should your thesis be published commercially, please reapply for permission. Theses and dissertations which contain embedded PJAs as part of the formal submission can be posted publicly by the awarding institution with DOI links back to the formal publications on ScienceDirect.

Elsevier Open Access Terms and Conditions

You can publish open access with Elsevier in hundreds of open access journals or in nearly 2000 established subscription journals that support open access publishing. Permitted third party re-use of these open access articles is defined by the author's choice of Creative Commons user license. See our open access license policy for more information.

Terms & Conditions applicable to all Open Access articles published with Elsevier:

Any reuse of the article must not represent the author as endorsing the adaptation of the article nor should the article be modified in such a way as to damage the author's honour or reputation. If any changes have been made, such changes must be clearly indicated.

The author(s) must be appropriately credited and we ask that you include the end user license and a DOI link to the formal publication on ScienceDirect.

If any part of the material to be used (for example, figures) has appeared in our publication with credit or acknowledgement to another source it is the responsibility of the user to ensure their reuse complies with the terms and conditions determined by the rights holder.

Additional Terms & Conditions applicable to each Creative Commons user license:

CC BY: The CC-BY license allows users to copy, to create extracts, abstracts and new works from the Article, to alter and revise the Article and to make commercial use of the Article (including reuse and/or resale of the Article by commercial entities), provided the user gives appropriate credit (with a link to the formal publication through the relevant DOI), provides a link to the license, indicates if changes were made and the licensor is not represented as endorsing the use made of the work. The full details of the license are available at http://creativecommons.org/licenses/by/4.0.

CC BY NC SA: The CC BY-NC-SA license allows users to copy, to create extracts, abstracts and new works from the Article, to alter and revise the Article, provided this is not done for commercial purposes, and that the user gives appropriate credit (with a link to the formal publication through the relevant DOI), provides a link to the license, indicates if changes were made and the licensor is not represented as endorsing the use made of the work. Further, any new works must be made available on the same conditions. The full details of the license are available at http://creativecommons.org/licenses/by-nc-sa/4.0.

CC BY NC ND: The CC BY-NC-ND license allows users to copy and distribute the Article, provided this is not done for commercial purposes and further does not permit distribution of the Article if it is changed or edited in any way, and provided the user gives appropriate credit (with a link to the formal publication through the relevant DOI), provides a link to the license, and that the licensor is not represented as endorsing the use made of the work. The full details of the license are

Chapter 7

Role of Humidity in Reducing Sliding Friction of Multilayered Graphene

ELSEVIER LICENSE
TERMS AND CONDITIONS

Mar 19, 2017

This Agreement between ANINDYA BANERJI ("You") and Elsevier ("Elsevier") consists of your license details and the terms and conditions provided by Elsevier and Copyright Clearance Center.

License Number	4072680941732
License date	Mar 19, 2017
Licensed Content Publisher	Elsevier
Licensed Content Publication	Carbon
Licensed Content Title	Role of humidity in reducing sliding friction of multilayered graphene
Licensed Content Author	Sukanta Bhowmick,Anindya Banerji,Ahmet T. Alpas
Licensed Content Date	June 2015
Licensed Content Volume	87
Licensed Content Issue	n/a
Licensed Content Pages	11
Start Page	374
End Page	384
Type of Use	reuse in a thesis/dissertation
Intended publisher of new work	other
Portion	full article
Format	both print and electronic
Are you the author of this Elsevier article?	Yes
Will you be translating?	No
Order reference number	
Title of your thesis/dissertation	Friction Reduction in Engine Materials: Role of Tribolayers
Expected completion date	Mar 2017
Estimated size (number of pages)	400
Elsevier VAT number	GB 494 6272 12
Requestor Location	ANINDYA BANERJI Canada Attn: ANINDYA BANERJI
Total	0.00 USD
Terms and Conditions	

INTRODUCTION

12. No Amendment Except in Writing: This license may not be amended except in a writing signed by both parties (or, in the case of publisher, by CCC on publisher's behalf).
13. Objection to Contrary Terms: Publisher hereby objects to any terms contained in any purchase order, acknowledgment, check endorsement or other writing prepared by you, which terms are inconsistent with these terms and conditions or CCC's Billing and Payment terms and conditions. These terms and conditions, together with CCC's Billing and Payment terms and conditions (which are incorporated herein), comprise the entire agreement between you and publisher (and CCC) concerning this licensing transaction. In the event of any conflict between your obligations established by these terms and conditions and those established by CCC's Billing and Payment terms and conditions, these terms and conditions shall control.
14. Revocation: Elsevier or Copyright Clearance Center may deny the permissions described in this License at their sole discretion, for any reason or no reason, with a full refund payable to you. Notice of such denial will be made using the contact information provided by you. Failure to receive such notice will not alter or invalidate the denial. In no event will Elsevier or Copyright Clearance Center be responsible or liable for any costs, expenses or damage incurred by you as a result of a denial of your permission request, other than a refund of the amount(s) paid by you to Elsevier and/or Copyright Clearance Center for denied permissions.

LIMITED LICENSE

The following terms and conditions apply only to specific license types:
15. **Translation**: This permission is granted for non-exclusive world **English** rights only unless your license was granted for translation rights. If you licensed translation rights you may only translate this content into the languages you requested. A professional translator must perform all translations and reproduce the content word for word preserving the integrity of the article.
16. **Posting licensed content on any Website**: The following terms and conditions apply as follows: Licensing material from an Elsevier journal: All content posted to the web site must maintain the copyright information line on the bottom of each image; A hyper-text must be included to the Homepage of the journal from which you are licensing at http://www.sciencedirect.com/science/journal/xxxxx or the Elsevier homepage for books at http://www.elsevier.com; Central Storage: This license does not include permission for a scanned version of the material to be stored in a central repository such as that provided by Heron/XanEdu. Licensing material from an Elsevier book: A hyper-text link must be included to the Elsevier homepage at http://www.elsevier.com . All content posted to the web site must maintain the copyright information line on the bottom of each image.

Posting licensed content on Electronic reserve: In addition to the above the following clauses are applicable: The web site must be password-protected and made available only to bona fide students registered on a relevant course. This permission is granted for 1 year only. You may obtain a new license for future website posting.
17. **For journal authors:** the following clauses are applicable in addition to the above:
Preprints:
A preprint is an author's own write-up of research results and analysis, it has not been peer-reviewed, nor has it had any other value added to it by a publisher (such as formatting, copyright, technical enhancement etc.).
Authors can share their preprints anywhere at any time. Preprints should not be added to or enhanced in any way in order to appear more like, or to substitute for, the final versions of articles however authors can update their preprints on arXiv or RePEc with their Accepted Author Manuscript (see below).

If accepted for publication, we encourage authors to link from the preprint to their formal publication via its DOI. Millions of researchers have access to the formal publications on ScienceDirect, and so links will help users to find, access, cite and use the best available version. Please note that Cell Press, The Lancet and some society-owned have different preprint policies. Information on these policies is available on the journal homepage.
Accepted Author Manuscripts: An accepted author manuscript is the manuscript of an article that has been accepted for publication and which typically includes author-incorporated changes suggested during submission, peer review and editor-author communications.
Authors can share their accepted author manuscript:

- immediately
    - via their non-commercial person homepage or blog
    - by updating a preprint in arXiv or RePEc with the accepted manuscript
    - via their research institute or institutional repository for internal institutional uses or as part of an invitation-only research collaboration work-group
    - directly by providing copies to their students or to research collaborators for their personal use
    - for private scholarly sharing as part of an invitation-only work group on commercial sites with which Elsevier has an agreement
- After the embargo period
    - via non-commercial hosting platforms such as their institutional repository
    - via commercial sites with which Elsevier has an agreement

In all cases accepted manuscripts should:

- link to the formal publication via its DOI
- bear a CC-BY-NC-ND license - this is easy to do
- if aggregated with other manuscripts, for example in a repository or other site, be shared in alignment with our hosting policy not be added to or enhanced in any way to appear more like, or to substitute for, the published journal article.

Published journal article (JPA): A published journal article (PJA) is the definitive final record of published research that appears or will appear in the journal and embodies all value-adding publishing activities including peer review co-ordination, copy-editing, formatting, (if relevant) pagination and online enrichment.
Policies for sharing publishing journal articles differ for subscription and gold open access articles:
Subscription Articles: If you are an author, please share a link to your article rather than the full-text. Millions of researchers have access to the formal publications on ScienceDirect, and so links will help your users to find, access, cite, and use the best available version.
Theses and dissertations which contain embedded PJAs as part of the formal submission can be posted publicly by the awarding institution with DOI links back to the formal publications on ScienceDirect.
If you are affiliated with a library that subscribes to ScienceDirect you have additional private sharing rights for others' research accessed under that agreement. This includes use for classroom teaching and internal training at the institution (including use in course packs and courseware programs), and inclusion of the article for grant funding purposes.
Gold Open Access Articles: May be shared according to the author-selected end-user license and should contain a CrossMark logo, the end user license, and a DOI link to the formal publication on ScienceDirect.

Please refer to Elsevier's posting policy for further information.

18. **For book authors** the following clauses are applicable in addition to the above: Authors are permitted to place a brief summary of their work online only. You are not allowed to download and post the published electronic version of your chapter, nor may you scan the printed edition to create an electronic version. **Posting to a repository:** Authors are permitted to post a summary of their chapter only in their institution's repository.

19. **Thesis/Dissertation**: If your license is for use in a thesis/dissertation your thesis may be submitted to your institution in either print or electronic form. Should your thesis be published commercially, please reapply for permission. These requirements include permission for the Library and Archives of Canada to supply single copies, on demand, of the complete thesis and include permission for Proquest/UMI to supply single copies, on demand, of the complete thesis. Should your thesis be published commercially, please reapply for permission. Theses and dissertations which contain embedded PJAs as part of the formal submission can be posted publicly by the awarding institution with DOI links back to the formal publications on ScienceDirect.

Elsevier Open Access Terms and Conditions

You can publish open access with Elsevier in hundreds of open access journals or in nearly 2000 established subscription journals that support open access publishing. Permitted third party re-use of these open access articles is defined by the author's choice of Creative Commons user license. See our open access license policy for more information.

Terms & Conditions applicable to all Open Access articles published with Elsevier:

Any reuse of the article must not represent the author as endorsing the adaptation of the article nor should the article be modified in such a way as to damage the author's honour or reputation. If any changes have been made, such changes must be clearly indicated.

The author(s) must be appropriately credited and we ask that you include the end user license and a DOI link to the formal publication on ScienceDirect.

If any part of the material to be used (for example, figures) has appeared in our publication with credit or acknowledgement to another source it is the responsibility of the user to ensure their reuse complies with the terms and conditions determined by the rights holder.

Additional Terms & Conditions applicable to each Creative Commons user license:

CC BY: The CC-BY license allows users to copy, to create extracts, abstracts and new works from the Article, to alter and revise the Article and to make commercial use of the Article (including reuse and/or resale of the Article by commercial entities), provided the user gives appropriate credit (with a link to the formal publication through the relevant DOI), provides a link to the license, indicates if changes were made and the licensor is not represented as endorsing the use made of the work. The full details of the license are available at http://creativecommons.org/licenses/by/4.0.

CC BY NC SA: The CC BY-NC-SA license allows users to copy, to create extracts, abstracts and new works from the Article, to alter and revise the Article, provided this is not done for commercial purposes, and that the user gives appropriate credit (with a link to the formal publication through the relevant DOI), provides a link to the license, indicates if changes were made and the licensor is not represented as endorsing the use made of the work. Further, any new works must be made available on the same conditions. The full details of the license are available at http://creativecommons.org/licenses/by-nc-sa/4.0.

CC BY NC ND: The CC BY-NC-ND license allows users to copy and distribute the Article, provided this is not done for commercial purposes and further does not permit distribution of the Article if it is changed or edited in any way, and provided the user gives appropriate credit (with a link to the formal publication through the relevant DOI), provides a link to the license, and that the licensor is not represented as endorsing the use made of the work. The full details of the license are

Chapter 8

Friction Behaviour of Multilayered Graphene against Steel

CAMBRIDGE UNIVERSITY PRESS LICENSE
TERMS AND CONDITIONS

Mar 19, 2017

This Agreement between ANINDYA BANERJI ("You") and Cambridge University Press ("Cambridge University Press") consists of your license details and the terms and conditions provided by Cambridge University Press and Copyright Clearance Center.

License Number	4072681042853
License date	Mar 19, 2017
Licensed Content Publisher	Cambridge University Press
Licensed Content Publication	MRS Online Proceedings Library
Licensed Content Title	Friction Behaviour of Multilayered Graphene against Steel
Licensed Content Author	A. Banerji, S. Bhowmick, M.J. Lukitsch, A.T. Alpas
Licensed Content Date	Mar 1, 2016
Licensed Content Volume	1812
Licensed Content Issue	undefined
Start page	1
End page	8
Type of Use	Dissertation/Thesis
Requestor type	Author
Portion	Full article
Author of this Cambridge University Press article	Yes
Author / editor of the new work	Yes
Order reference number	
Territory for reuse	World
Title of your thesis / dissertation	Friction Reduction in Engine Materials: Role of Tribolayers
Expected completion date	Mar 2017
Estimated size(pages)	400
Requestor Location	ANINDYA BANERJI Canada Attn: ANINDYA BANERJI
Publisher Tax ID	123258667RT0001
Billing Type	Invoice
Billing Address	ANINDYA BANERJI

Canada
Attn: ANINDYA BANERJI

Total 0.00 USD

Terms and Conditions

TERMS & CONDITIONS

Cambridge University Press grants the Licensee permission on a non-exclusive non-transferable basis to reproduce, make available or otherwise use the Licensed content 'Content' in the named territory 'Territory' for the purpose listed 'the Use' on Page 1 of this Agreement subject to the following terms and conditions.

1. The License is limited to the permission granted and the Content detailed herein and does not extend to any other permission or content.
2. Cambridge gives no warranty or indemnity in respect of any third-party copyright material included in the Content, for which the Licensee should seek separate permission clearance.
3. The integrity of the Content must be ensured.
4. The License does extend to any edition published specifically for the use of handicapped or reading-impaired individuals.
5. The Licensee shall provide a prominent acknowledgement in the following format: author/s, title of article, name of journal, volume number, issue number, page references, , reproduced with permission.

Other terms and conditions:

v1.0

Questions? customercare@copyright.com or +1-855-239-3415 (toll free in the US) or +1-978-646-2777.

VITA AUCTORIS

ANINDYA BANERJI
M.Sc., M.A.Sc.,
E-mail: banerjia@uwindsor.ca
Publications:https://scholar.google.ca/citations?user=an05GI8AAAAJ&hl=en&oi=sra

Refereed Journal Publications

1. A. Banerji, M. J. Lukitsch, B. McClory, D. R. White, A. T. Alpas, Effect of iron oxides on sliding friction of thermally sprayed 1010 steel coated cylinder bores, Wear (2017) (In Press).

2. M. O. Tas, A. Banerji, M. J. Lukitsch, A. T. Alpas, Roles of Mirror-like Surface Finish and DLC Coatings on Piston Rings on Increasing Scuffing Resistance of Cast Iron Cylinder Liners, Wear (2017) (In Press).

3. A. Banerji, M. J. Lukitsch, A. T. Alpas, Friction reduction mechanisms in cast iron sliding against DLC: Effect of biofuel (E85) diluted engine oil, Wear 368 (2016) 196-209.

4. S. Bhowmick, A. Banerji, A. T. Alpas, Friction reduction mechanisms in multilayer graphene sliding against hydrogenated diamond-like carbon, Carbon (2016) 109 795-804.

5. A. Banerji, S. Bhowmick, A. T. Alpas, Role of temperature on tribological behaviour of Ti containing MoS_2 coating against aluminum alloys, Surface and Coatings Technology, 314 (2016) 2-12.

6. S. Bhowmick, A. Banerji, A.T. Alpas, Role of Humidity in Reducing Sliding Friction of Multilayered Graphene, Carbon 87 (2015) 374-384.

7. A. Banerji, S. Bhowmick, MJ Lukitsch, AT Alpas, Friction Behaviour of Multilayered Graphene against Steel, MRS Proceedings, 1812 (2016), imrc2015s6b-o001, Cambridge University Press.

8. S. Bhowmick, A. Banerji, M.Z.U. Khan, M.J. Lukitsch, A.T. Alpas, High Temperature Tribological Behavior of Tetrahedral Amorphous Carbon (ta-C) and Fluorinated ta-C Coatings against Aluminum Alloys, Surface and Coatings Technology, 284 (2015) 14-25.

9. S. Bhowmick, A. Banerji, A.T. Alpas, Tribological behaviour of Al- 6.5%, - 12%, - 18.5% Si alloys during machining using CVD diamond and DLC coated tools, Surface and Coatings Technology, 284 (2015) 353-364.

10. A. Rahbar-kelishami, A. Abdollah-zadeh, M.M. Hadavi, A. Banerji, A. Alpas, A.P. Gerlich, Effects of friction stir processing on wear properties of WC–12%Co sprayed on 52100 steel, Materials and Design, 86 (2015) 98–104.

11. S. Bhowmick, A. Banerji, M.J. Lukitsch, A.T. Alpas, The high temperature tribological behaviour of Si, O containing hydrogenated diamond-like carbon (a-C:H/a-Si:O) coating against aluminum alloy, Wear 330-331 (2015) 261–271.

12. S. Bhowmick, F. G. Sen, A. Banerji, A. T. Alpas, Friction and adhesion of hydrophobic fluorine containing hydrogenated diamond-like carbon (F-H-DLC) coating against magnesium alloy AZ91, Surface & Coatings Technology 267 (2014) 21-31.

13. S. Bhowmick, A. Banerji, A.T. Alpas, Tribological behavior and machining performance of non-hydrogenated diamond-like carbon coating tested against Ti–6Al–4V: Effect of surface passivation by ethanol, Surface & Coatings Technology 260 (2014) 290–302.

14. A. Banerji, A. Edrisy, V. Francis, A.T. Alpas, Effect of biofuel (E85) addition on lubricated sliding wear mechanisms of a eutectic Al-Si alloy, Wear 311 (2014) 1–13.

15. A. Banerji, S. Bhowmick, A.T. Alpas, High temperature tribological behavior of W containing diamond-like carbon (DLC) coating against titanium alloys, Surface & Coatings Technology 241 (2014) 93-104.

16. A. Banerji, H. Hu, A.T. Alpas, Sliding wear mechanisms of magnesium composites AM60 reinforced with Al_2O_3 fibres under ultra-mild wear conditions, Wear 301 (2013) 626–635.

17. A. Banerji, H. Hu, A.T. Alpas, Ultramild wear of Al_2O_3 fibre and particle reinforced magnesium matrix composites. Advanced Materials Research 445 (2012) 503-508.

18. A. Banerji, H. Hu, A.T. Alpas, Sliding wear behaviour of squeeze cast magnesium composite AM60-9% $(Al_2O_3)_f$, Magnesium Technology Proceedings at TMS Annual Meeting and Exhibition, Orlando, Fl, USA, (2012) 169-174.

19. A. Banerji, H. Hu, A.T. Alpas, Sliding wear behaviour of Mg alloy (AM60) reinforced with different volume fractions of Al_2O_3 fibres, Mg 2012: 9th International Conference on Magnesium Alloys and their Applications, Vancouver, BC, Canada, (2012) 935-939.

Invited Oral Presentations

20. A. Banerji, A.T. Alpas, Friction reduction of non-hydrogenated DLC (NH-DLC) coatings in lubricated sliding contact against cast iron (CI), 7th Symposium on Functional Coatings and Surface Engineering, Montreal, QC, Canada (2014).

21. S. Bhowmick, F. G. Sen, A. Banerji, A.T. Alpas, Tribological Coatings for Energy Efficient Manufacturing, 57th Annual SVC Technical Conference, Providence, IL, USA (2014).

22. S. Bhowmick, A. Banerji, M. Lukitsch, A.T. Alpas, Tribological coatings for automotive powertrains and manufacturing processes, 2nd International Surface Treatment Symposium, Istanbul, Turkey (2014).

23. A. Banerji, S. Bhowmick, A.T. Alpas, Tribological and machining behaviour of diamond-like carbon coatings against Ti-6Al-4V, 56th Annual SVC Technical Conference, Chicago, RI, USA (2013).

24. A. Banerji, A. Edrisy, A.T. Alpas, Ethanol as biofuel for lubricated sliding of powertrain components, 3rd Annual general meeting of Green Auto PowerTrain, Windsor, ON, Canada, (2012).

Oral Presentations

25. A. Banerji, S. Bhowmick, A. T. Alpas, High temperature tribological behaviour of Ti containing multilayer MoS_2 coating against Aluminum alloys, 59th Society of Vacuum Coaters Annual Technical Conference, Indianapolis, IN, USA (2016).

26. A. Banerji, S. Bhowmick, A. T. Alpas , The high temperature tribological behaviour of Si, O containing hydrogenated diamond-like carbon (a-C:H/a-Si:O) coating against aluminum alloy, 20th International Conference on Wear of Materials, Toronto, Canada (2015).

27. S. Bhowmick, A. Banerji, A.T. Alpas, Tribological behaviour of Al-Si alloys with 6.5%, 12% and 18.5% Si during machining using CVD-diamond and DLC coated tools**,** 42nd International Conference on Metallurgical Coatings and Thin Films (ICMCTF), San Diego, CA, USA (2015).

28. S. Bhowmick, A. Banerji, A.T. Alpas, Sliding Wear Behaviour of Graphene against Ti-6Al-4V: A Comparison with Polycrystalline Diamond and Hydrogenated Diamond-Like Carbon Coatings, San Jose, CA, USA (2015).

29. A. Banerji, S. Bhowmick, A.T. Alpas, Tribological behavior and machining performance of non-hydrogenated diamond-like carbon coating tested against Ti–6Al–4V: Effect of surface passivation by ethanol, 41st International Conference on Metallurgical Coatings and Thin Films (ICMCTF), San Diego, CA, USA (2014).

30. A. Banerji, Md. F. Rahman, S. Bhowmick, A.T. Alpas, Chip formation mechanisms and deformation behaviour of Ti-6Al-4V alloy subjected to orthogonal cutting at ambient and cryogenic conditions, 3rd International Conference on Virtual Machining Process Technology (VMPT), Calgary, AB, Canada (2014).

31. A. Banerji, A. Edrisy, V. Francis, A.T. Alpas, Effect of ethanol on lubricated sliding wear of Al and Mg alloys and composites, 5th World Tribology Congress, Torino, Italy (2013).

32. A. Banerji, S. Bhowmick, A.T. Alpas, Effect of test atmosphere on tribological behaviour of diamond-like carbon coatings: Implications for Ti alloy machining, STLE 68th STLE Annual Meeting & Exhibition, Detroit, MI, USA (2013).

33. A. Banerji, S. Bhowmick, A.T. Alpas, Tribological and machining behaviour of diamond-like carbon coatings against a cast magnesium alloy, STLE 68th STLE Annual Meeting & Exhibition, Detroit, MI, USA (2013).

34. A. Banerji, H. Hu, A.T. Alpas, Sliding wear mechanisms of magnesium composites AM60 reinforced with Al_2O_3 fibres under ultra-mild wear conditions, 19th International Conference on Wear of Materials, Portland, OR, USA (2013).

35. A. Banerji, H. Hu, A.T. Alpas, Sliding Wear Behaviour of Squeeze Cast Magnesium Composite AM60-9% $(Al_2O_3)_f$, 141st TMS Annual Meeting and Exhibition, Orlando, Fl, USA (2012).

36. A. Banerji, H. Hu, A.T. Alpas, Sliding wear behaviour of squeeze cast Mg matrix composites, SAE World congress, Detroit, MI, USA (2012).

Poster Presentations

37. M.Z.U. Khan, A. Banerji, H. Hu, A.T. Alpas, Wear maps for magnesium Composite (AM60) reinforced with Ceramic (Al_2O_3) fibres, Materials Today Asia, Kowloon, Hong Kong (2014).

38. S. Bhowmick, F.G. Sen, A. Banerji, A. T. Alpas, Tribology of Diamond-like Carbon Coatings against Al and Mg Alloys: Experimental and Atomistic Mechanisms, 57th Annual SVC Technical Conference, Chicago, Illinois, USA (2014)

39. A. Banerji, A. Edrisy, A.T. Alpas, Ethanol as biofuel for lubricated sliding of powertrain components, 3rd Annual general meeting of Green Auto PowerTrain, Windsor, ON, Canada. (2012).

40. A. Banerji, H. Hu, A.T. Alpas, Micromechanisms of low load wear of AM60 reinforced by Al_2O_3 fibre (f) and Al_2O_3 particle (p) + fibre (f), poster presented at 18th International Conference on Wear of Materials, Philadelphia, PA, USA, (2011).